Escola Tècnica Superior d'Enginyeries
Industrial i Aeronàutica de Terrassa
UNIVERSITAT POLITÈCNICA DE CATALUNYA

Final Degree Project

# Study of the Martian environment for application to the design of a greenhouse

*Author:* David de la Torre Sangrà

*Supervisor:* Dr. Elena Fantino

*A thesis submitted in fulfilment of the requirements*
*for the degree of Aeronautical Engineering*

*in the*

Department of Aerospace Engineering

June 2014

This page intentionally left blank.

Universitat Politècnica de Catalunya

# *Abstract*

Escola Tècnica Superior d'Enginyeries Industrial i Aeronàutica de Terrassa
Department of Aerospace Engineering

Aeronautical Engineering

**Study of the Martian environment for application to the design of a greenhouse**

by David de la Torre Sangrà

The human exploration of Mars belongs to the current plans of NASA and ESA. Getting the astronauts to Mars and returning them safely to Earth imposes several engineering challenges. In particular, creating the conditions for living on the Martian surface requires in the first place a thorough understanding of the Martian environment. Installing a manned base would require the implementation of life support systems including the appropriate means to provide food to the astronauts. The word "appropriate" in this context suggests the idea of "plant cultivation". This study is a reconstruction of the environment and climate of Mars. It develops through a review of the observation and in-situ data collected over 50 years of study and exploration. The review is followed by the study, understanding, revision and implementation of the models based on such data and on the physics of the main processes that affect the environment and the climate. The final objective is to provide a solid basis for selecting one or more candidate sites for the installation and operation of a greenhouse. Such candidates should undergo further analyses concerning the geological and engineering issues inherent to the realization of such an ambitious project. These analyses are out of the scope of this work, which focuses on the physics of the environment and the climate of the red planet. It should also be noted that the implications of this project go much beyond the specific proposed application because they have a clear scientific value and an intrinsic originality. As a matter of fact, this work has implied collecting, understanding, organizing and elaborating data and models which are often heterogeneous and dispersed. The result is the first global model of the Martian environment. As such, this study can be of considerable help in the feasibility studies of future missions to Mars, be them manned or robotic.

# *Acknowledgements*

I would like to especially thank my tutor, Dr. Elena Fantino. Her support and enthusiasm have been a major incentive not only during the project, but also on the academic subjects imparted by her during the academic year. Moreover, her outstanding searching skills and expertise have proved to be exceedingly valuable on a practical basis. Thanks also to Arnau Miró and Manel Soria for kindly putting up with me during this project and also for providing useful tricks. Finally, my most sincere gratitude to my parents for their patience and understanding.

# Contents

**Abstract** ii

**Acknowledgements** iii

**Contents** iv

**List of Figures** vii

**List of Tables** xiii

**Abbreviations** xiv

**Physical Constants** xvii

**Introduction** xviii

**Scope** xx

**1 State of the Art** 1

1.1 The data . . . 1

1.1.1 Viking . . . 3

1.1.2 Mars Pathfinder . . . 5

1.1.2.1 Sojourner . . . 5

1.1.3 Mars Global Surveyor . . . 7

1.1.4 Mars Odyssey . . . 9

1.1.5 Mars Express . . . 11

1.1.6 Mars Exploration Rover . . . 15

1.1.6.1 Spirit . . . 16

1.1.6.2 Opportunity . . . 17

1.1.7 Mars Reconnaissance Orbiter . . . 18

1.1.8 Phoenix . . . 19

1.1.9 Mars Science Laboratory . . . 21

1.2 The models . . . 23

1.2.1 Pollack . . . 26

1.2.2 Meteors . . . 27

1.2.2.1 The model of Dycus . . . 27

1.2.2.2 The model of Divine . . . 29

1.2.2.3 The model of Bland and Smith . . . 30
1.2.2.4 The model of McNamara and Suggs . . . 30
1.2.3 MarsGRAM . . . 31
1.2.3.1 MarsRAD . . . 32
1.2.3.2 FindDate . . . 33
1.2.4 EMMREM . . . 33

**2 The Mars Environment Multi-Model 35**
2.1 Introduction . . . 35
2.2 The physical models . . . 36
2.2.1 MarsGRAM . . . 37
2.2.2 MarsRAD . . . 40
2.2.3 Pollack . . . 41
2.2.4 Meteoroids . . . 42
2.3 The implementation . . . 43
2.3.1 MarsGRAM . . . 44
2.3.2 MarsRAD . . . 45
2.3.3 Pollack . . . 45
2.3.4 Dycus . . . 46
2.3.5 Divine . . . 46
2.3.6 Pre-processing functions . . . 47
2.3.6.1 Determination of the Julian date . . . 48
2.3.7 Post-processing functions . . . 49
2.3.7.1 The thermodynamic properties of the atmosphere . . . 49
2.3.7.2 Azimuth and elevation coordinates of the Sun . . . 51
2.3.8 Output . . . 52
2.3.9 Model bugs . . . 54
2.4 A sample of results . . . 55

**3 Environment and climate: the results 65**
3.1 The Martian environment . . . 65
3.1.1 Orbit, seasons and global physical parameters . . . 66
3.1.2 Meteoroid flux . . . 67
3.1.3 Topography . . . 67
3.1.4 Soil . . . 68
3.1.5 Atmosphere . . . 69
3.1.6 Electromagnetic radiation . . . 75
3.1.7 Particle radiation . . . 77
3.2 Climatic areas . . . 80
3.3 Site analysis . . . 82
3.3.1 Valles Marineris . . . 82
3.3.2 Gale Crater . . . 83
3.3.3 Olympus Mons Crater . . . 85
3.3.4 Planum Australe . . . 86

**4 Conclusions and future work 88**

**A TES Mineral Maps** **91**

**B Daily and seasonal plots** **97**
B.1 Spring equinox . . . . . 97
B.2 Summer solstice . . . . . 108
B.3 Fall equinox . . . . . 118
B.4 Winter solstice . . . . . 128
B.5 Annual simulation . . . . . 138

**C Budget** **148**

**Bibliography** **150**

# List of Figures


1.1 Science strategies timeline within the Mars Exploration Program. . . . . 3
1.2 Viking landers: daily average pressure measurements. . . . . 4
1.3 Viking orbiters IRTM raw temperature data (top) and simulated map (bottom). . . . . 4
1.4 Temperature measured by the Pathfinder ASI/MET instrument. . . . . 6
1.5 Pressure measured by the Pathfinder ASI/MET instrument. . . . . 6
1.6 Plausible minerals from the Sojourner APXS chemical analyses of Barnacle Bill and Yogi. . . . . 7
1.7 Evidence of soil layering from the Sojourner rover soil mechanics experiment. . . . . 7
1.8 TES data multi-year plot displaying dust opacity, temperatures, water-ice opacities and water vapour column. . . . . 10
1.9 TES observations of the planet-encircling dust storm in 2001. . . . . 11
1.10 TES measurement of Mars south cap temperature. . . . . 12
1.11 Topographic map of Mars from the MOLA instrument. . . . . 12
1.12 Radial magnetic field data from the MGS MAG/ER instrument. . . . . 13
1.13 THEMIS dust opacity map: raw measurements (left) and extrapolated map (right). . . . . 13
1.14 GRS map based on gamma rays from the hydrogen element. . . . . 13
1.15 MARIE daily average dose rates. . . . . 14
1.16 Ice-rich layered deposits at the South pole from the MARSIS instrument data. . . . . 15
1.17 Spirit Mini-TES temperature measurements at 30 meters from the surface. 17
1.18 Spirit (top) and Opportunity (bottom) dust aerosol optical depth measurements at 1075 cm-1. . . . . 18
1.19 SHARAD radar map of buried ice layers at the North pole. . . . . 20
1.20 Atmospheric water vapour measured by the TECP probe: the black circles refer to measurements made close to the surface. . . . . 21
1.21 REMS ground and air temperature measurements. . . . . 23
1.22 Atmospheric abundances by element as measured by SAM. . . . . 24
1.23 SAM chemical analysis of a drilled sample from John Klein rock. . . . . 24
1.24 RAD measurements during the interplanetary transfer. Five solar events were observed. . . . . 25
1.25 RAD measurements on the surface of Mars. The surface is partially shielded from radiation when the atmosphere is thicker (higher REMS pressure). . . . . 25

1.26 Solar irradiance at the Viking Lander 1 site. Summer season with minimal dust (left) and winter season with heavy dust (right). In the two cases, the solid line represents the available irradiance at the top of the atmosphere, the dotted line indicates the total irradiance at surface level, the dashed line refers to the direct irradiance, whereas the solid-dotted line is the diffuse irradiance. . . . . 27
1.27 Meteoroid mass loss and deceleration through the Martian atmosphere according to the Dycus model. . . . . 29
1.28 Speed distribution of $10^{-6}$ grams meteoroids at 1 AU. . . . . 31
1.29 MarsGRAM: distribution of temperatures 5 m above the surface. . . . . 32
1.30 EMMREM: simulated ion intensities at different energies. The simulations refer to the year 2005 at Mars orbit. . . . . 33

2.1 Solar zenith angle ($z$) and "tilted" solar zenith angle ($z_t$) when the reference is moved to a tilted plane ($t_p$). Note that this figure is only illustrative and assumes a solar azimuth angle of 0°; the $z_t$ value for an arbitrary azimuth angle is computed as noted in Eq. 2.19. . . . . 52
2.2 MarsGRAM bug concerning the daily density values. . . . . 54
2.3 Original MarsGRAM code results with TES scenario. Dust-free scenario (blue circle) versus dust storm (red cross). Note that the temperature and density are not affected by the dust storm but the radiation fluxes are actually modified, thus yielding results not coherent with the simulated TES scenario. . . . . 55
2.4 Fixed MarsGRAM code results with TES scenario. Dust-free scenario (blue circle) versus dust storm (red cross). Now the code ignores the dust storm, forcing the radiation flux values to comply with the simulated TES scenario. . . . . 55
2.5 Faulty value in Pollack albedo 0.1 database. . . . . 56
2.6 Faulty value in Pollack albedo 0.4 database. . . . . 56
2.7 MEMM simulation results multiplot. Atmospheric quantities and general parameters. . . . . 57
2.8 MEMM simulation results multiplot. Atmospheric constituents concentration in volume percentage. . . . . 58
2.9 MEMM simulation results multiplot. Atmospheric constituents concentration in mass percentage. . . . . 59
2.10 MEMM simulation results multiplot. Daily values, surface ice and dust optical depth. . . . . 60
2.11 MEMM simulation results multiplot. Radiation fluxes from MarsRAD. . . . 61
2.12 MEMM simulation results multiplot. Planet albedo, sky temperature, and heat rate values from MarsRAD, and radiation fluxes from Pollack. . . . . 62
2.13 MEMM simulation results multiplot. Dust properties and scale heights. . . 63
2.14 Results from the Dycus and Divine meteoroid models, and comparison between them. . . . . 64

3.1 The orbit of Mars and the definition of $L_s$. . . . . 66
3.2 Meteoroid flux at top of the atmosphere, according to Dycus and Divine. . 67
3.3 Map with the main features of Mars in Latin nomenclature. . . . . 68
3.4 Combined TES plot of the Martian surface mineralogy. . . . . 68
3.5 Evolution of the polar surface ice throughout one Martian year. . . . . 69

3.6 Surface dust coverage measured by the TES/MGS instrument. . . . . 70
3.7 TES bolometric albedo global map. . . . . 70
3.8 Evolution of atmospheric $CO_2$ throughout one Martian year. Samples are taken at midday (12:00h local solar time). The contrast between clear sky conditions and a localised dust storm appears at $L_s \approx$270°. . . . . 71
3.9 Evolution of atmospheric $H_2O$ throughout one Martian year. Samples are taken at midday (12:00h local time). The contrast between clear sky conditions and a localised dust storm appears at $L_s \approx$270°. . . . . 71
3.10 Evolution of the atmospheric mean pressure throughout one Martian year. Samples are taken at midday (12:00h local time). Note the contrast between clear sky conditions and a localised dust storm at $L_s \approx$270°. 71
3.11 Evolution of the atmospheric mean density throughout one Martian year. Samples are taken at midday (12:00h local time). Note the contrast between clear sky conditions and a localised dust storm at $L_s \approx$270°. . . . . 72
3.12 Evolution of the atmospheric mean temperature throughout one Martian sol. . . . . 72
3.13 Evolution of the atmospheric maximum daily temperature throughout one Martian year. Clear sky conditions and a localised dust storm at $L_s \approx$270°. 73
3.14 Evolution of the atmospheric minimum daily temperature throughout one Martian year. Clear sky conditions and a localised dust storm at $L_s \approx$270°. 73
3.15 Evolution of the atmospheric maximum daily temperature throughout one Martian year. . . . . 73
3.16 Evolution of soil mean temperature throughout one Martian sol. . . . . 74
3.17 Vertical profiles for atmospheric temperature, density, pressure and wind speed. Solid line for midday values, dashed line for midnight values. . . . 74
3.18 Wind speed magnitude. . . . . 75
3.19 Downwards direct Solar irradiation throughout one Martian sol. Comparison between clear sky and dust storm scenarios. . . . . 76
3.20 Downwards diffuse Solar irradiation throughout one Martian sol. Comparison between clear sky and dust storm scenarios. . . . . 76
3.21 Downwards infrared irradiation throughout one Martian sol. Comparison between clear sky and dust storm scenarios. . . . . 76
3.22 Absorptivity of various gases of the atmosphere as a function of the wavelength of radiation. . . . . 77
3.23 MARIE/Odyssey radiation dose measurements, March 2002. . . . . 78
3.24 MARIE/Odyssey radiation dose measurements, October 2003. . . . . 78
3.25 RAD/MSL radiation dose measurements on the surface, 2012-2013. . . . 79
3.26 Calculations of the skin dose equivalent (cSv) for astronauts on the surface of Mars near solar minimum. Note that the centi-Sievert (cSv) refers to a biological effect, as opposed to the millirad which refers to a physical quantity. . . . . 79
3.27 Climate areas, Spring equinox ($L_s$=0°). . . . . 81
3.28 Climate areas, Summer solstice ($L_s$=90°). . . . . 82
3.29 Climate areas, Fall equinox ($L_s$=90°). . . . . 83
3.30 Climate areas, Winter solstice ($L_s$=270°). . . . . 84
3.31 Climatic areas, annual simulation. . . . . 84
3.32 Multiplot of Melas Chasma environment, for a full Martian year. . . . . 85
3.33 Multiplot of the environment at Gale Crater over one Martian year. . . . . 85

3.34 Multiplot of the environment at Olympus Mons crater over one Martian year. . . . 86
3.35 Multiplot of the environment at Planum Australe over a full Martian year. . 86

A.1 TES plot of the Martian surface mineralogy. Quartz . . . 91
A.2 TES plot of the Martian surface mineralogy. K-feldspar . . . 92
A.3 TES plot of the Martian surface mineralogy. Plagioclase . . . 92
A.4 TES plot of the Martian surface mineralogy. Amphibole . . . 93
A.5 TES plot of the Martian surface mineralogy. Low-Ca Pyroxene . . . 93
A.6 TES plot of the Martian surface mineralogy. High-Ca Pyroxene . . . 94
A.7 TES plot of the Martian surface mineralogy. Olivine . . . 94
A.8 TES plot of the Martian surface mineralogy. Hematite . . . 95
A.9 TES plot of the Martian surface mineralogy. Sulfates . . . 95
A.10 TES plot of the Martian surface mineralogy. Carbonates . . . 96
A.11 TES plot of the Martian surface mineralogy. Sheet Silicates and High-Si glass . . . 96

B.1 Average daily atmospheric temperature . . . 98
B.2 Maximum daily atmospheric temperature . . . 98
B.3 Minimum daily atmospheric temperature . . . 99
B.4 Average daily ground temperature . . . 99
B.5 Maximum daily ground temperature . . . 100
B.6 Minimum daily ground temperature . . . 100
B.7 Average daily sky temperature . . . 101
B.8 Maximum daily sky temperature . . . 101
B.9 Minimum daily sky temperature . . . 102
B.10 Average daily SW downwards flux (surface) . . . 102
B.11 Maximum daily SW downwards flux (surface) . . . 103
B.12 Average daily SW upwards flux (surface) . . . 103
B.13 Maximum daily SW upwards flux (surface) . . . 104
B.14 Average daily LW upwards flux (surface) . . . 104
B.15 Maximum daily LW upwards flux (surface) . . . 105
B.16 Minimum daily LW upwards flux (surface) . . . 105
B.17 Average daily wind speed . . . 106
B.18 Maximum daily wind speed . . . 106
B.19 Minimum daily wind speed . . . 107
B.20 Average daily atmospheric temperature . . . 108
B.21 Maximum daily atmospheric temperature . . . 108
B.22 Minimum daily atmospheric temperature . . . 109
B.23 Average daily ground temperature . . . 109
B.24 Maximum daily ground temperature . . . 110
B.25 Minimum daily ground temperature . . . 110
B.26 Average daily sky temperature . . . 111
B.27 Maximum daily sky temperature . . . 111
B.28 Minimum daily sky temperature . . . 112
B.29 Average daily SW downwards flux (surface) . . . 112
B.30 Maximum daily SW downwards flux (surface) . . . 113

B.31 Average daily SW upwards flux (surface) . . . 113
B.32 Maximum daily SW upwards flux (surface) . . . 114
B.33 Average daily LW upwards flux (surface) . . . 114
B.34 Maximum daily LW upwards flux (surface) . . . 115
B.35 Minimum daily LW upwards flux (surface) . . . 115
B.36 Average daily wind speed . . . 116
B.37 Maximum daily wind speed . . . 116
B.38 Minimum daily wind speed . . . 117
B.39 Average daily atmospheric temperature . . . 118
B.40 Maximum daily atmospheric temperature . . . 118
B.41 Minimum daily atmospheric temperature . . . 119
B.42 Average daily ground temperature . . . 119
B.43 Maximum daily ground temperature . . . 120
B.44 Minimum daily ground temperature . . . 120
B.45 Average daily sky temperature . . . 121
B.46 Maximum daily sky temperature . . . 121
B.47 Minimum daily sky temperature . . . 122
B.48 Average daily SW downwards flux (surface) . . . 122
B.49 Maximum daily SW downwards flux (surface) . . . 123
B.50 Average daily SW upwards flux (surface) . . . 123
B.51 Maximum daily SW upwards flux (surface) . . . 124
B.52 Average daily LW upwards flux (surface) . . . 124
B.53 Maximum daily LW upwards flux (surface) . . . 125
B.54 Minimum daily LW upwards flux (surface) . . . 125
B.55 Average daily wind speed . . . 126
B.56 Maximum daily wind speed . . . 126
B.57 Minimum daily wind speed . . . 127
B.58 Average daily atmospheric temperature . . . 128
B.59 Maximum daily atmospheric temperature . . . 128
B.60 Minimum daily atmospheric temperature . . . 129
B.61 Average daily ground temperature . . . 129
B.62 Maximum daily ground temperature . . . 130
B.63 Minimum daily ground temperature . . . 130
B.64 Average daily sky temperature . . . 131
B.65 Maximum daily sky temperature . . . 131
B.66 Minimum daily sky temperature . . . 132
B.67 Average daily SW downwards flux (surface) . . . 132
B.68 Maximum daily SW downwards flux (surface) . . . 133
B.69 Average daily SW upwards flux (surface) . . . 133
B.70 Maximum daily SW upwards flux (surface) . . . 134
B.71 Average daily LW upwards flux (surface) . . . 134
B.72 Maximum daily LW upwards flux (surface) . . . 135
B.73 Minimum daily LW upwards flux (surface) . . . 135
B.74 Average daily wind speed . . . 136
B.75 Maximum daily wind speed . . . 136
B.76 Minimum daily wind speed . . . 137
B.77 Average annual atmospheric temperature . . . 138

B.78 Maximum annual atmospheric temperature . . . . . 138
B.79 Minimum annual atmospheric temperature . . . . . 139
B.80 Average annual ground temperature . . . . . 139
B.81 Maximum annual ground temperature . . . . . 140
B.82 Minimum annual ground temperature . . . . . 140
B.83 Average annual sky temperature . . . . . 141
B.84 Maximum annual sky temperature . . . . . 141
B.85 Minimum annual sky temperature . . . . . 142
B.86 Average annual SW downwards flux (surface) . . . . . 142
B.87 Maximum annual SW downwards flux (surface) . . . . . 143
B.88 Average annual SW upwards flux (surface) . . . . . 143
B.89 Maximum annual SW upwards flux (surface) . . . . . 144
B.90 Average annual LW upwards flux (surface) . . . . . 144
B.91 Maximum annual LW upwards flux (surface) . . . . . 145
B.92 Minimum annual LW upwards flux (surface) . . . . . 145
B.93 Average annual wind speed . . . . . 146
B.94 Maximum annual wind speed . . . . . 146
B.95 Minimum annual wind speed . . . . . 147

# List of Tables

C.1 Budget of the *Study of the Martian environment for application to the design of a greenhouse*. . . . . 149

# Abbreviations

| | |
|---|---|
| **APXS** | **A**lpha **P**article **X**-Ray **S**pectrometer |
| **APXS** | **A**lpha **P**roton **X**-Ray **S**pectrometer |
| **ASI** | **A**tmospheric **S**tructure **I**nstrument |
| **AU** | **A**stronomical **U**nit |
| **BRYNTRYN** | **B**ar**y**o**n** **Tra**n**s**port |
| **CRISM** | **C**ompact **R**econnaissance **I**maging **S**pectrometer for **M**ars |
| **CheMin** | **Chem**istry and **Min**eralogy X-Ray Diffraction/X-Ray Fluorescence Instrument |
| **ChemCam** | **Chem**istry and **Cam**era |
| **DAN** | **D**ynamic **A**lbedo of **N**eutrons |
| **EMMREM** | **E**arth-**M**oon-**M**ars **R**adiation **E**nvironment **M**odule |
| **ER** | **E**lectron **R**eflectometer |
| **ESA** | **E**uropean **S**pace **A**gency |
| **GCR** | **G**alactic **C**osmic **R**ays |
| **GRS** | **G**amma **R**ay **S**pectrometer |
| **GTS** | **G**round **T**emperature **S**ensor |
| **HAZCAM** | **Haz**ard Avoidance **Cam**eras |
| **HETC-HEDS** | **H**igh **E**nergy **T**ransport **C**ode – **H**uman **E**xploration and **D**evelopment in **S**pace |
| **HRSC** | **H**igh/Super **R**esolution **S**tereo **C**olour Imager |
| **HZETRN** | High-Charge-and-Energy (**HZE**) **Tra**n**s**port |
| **HiRISE** | **Hi**gh **R**esolution **I**maging **S**cience **E**xperiment |
| **ISRO** | **I**ndian **S**pace **R**esearch **O**rganisation |
| **ISS** | **I**nternational **S**pace **S**tation |
| **JAXA** | **J**apan **A**erospace E**x**ploration **A**gency |
| **JD** | **J**ulian **D**ay |
| **LRO** | **L**unar **R**econnaissance **O**rbiter |

| | |
|---|---|
| **LTST** | **L**ocal **T**rue **S**olar **T**ime |
| **LW** | **L**ong-**W**ave |
| **MAHLI** | **Ma**rs **H**and **L**ens **I**mager |
| **MARCI** | **Mar**s **C**olor **I**mager |
| **MARDI** | **Mar**s **D**escent **I**mager |
| **MARIE** | **Ma**rs **R**adi**i**ation **E**nvironment Experiment |
| **MCS** | **M**ars **C**limate **S**ounder |
| **MECA** | **M**icroscopy, **E**lectrochemistry, and **C**onductivity **A**nalyzer |
| **MEDLI** | **M**ars Science Laboratory **E**ntry **D**escent and **L**anding **I**nstrument |
| **MEM** | **M**eteoroid **E**ngine **M**odel |
| **MEMM** | **M**ars **E**nvironment **M**ulti **M**odel |
| **MER** | **M**ars **E**xploration **R**over |
| **MGCM** | **M**ars **G**eneral **C**irculation **M**odel |
| **MGS** | **M**ars **G**lobal **S**urveyor |
| **MOC** | **M**ars **O**rbiter **C**amera |
| **MOLA** | **M**ars **O**rbiter **L**aser **A**ltimeter |
| **MRO** | **M**ars **R**econnaissance **O**rbiter |
| **MSL** | **M**ars **S**cience **L**aboratory |
| **MTGCM** | **M**ars **T**hermospheric **G**eneral **C**irculation **M**odel |
| **MY** | **M**ars **Y**ear |
| **Mastcam** | **Mast Cam**era |
| **Mini-TES** | **Mini**ature **T**hermal **E**mission **S**pectrometer |
| **NASA** | **N**ational **A**eronautics and **S**pace **A**dministration |
| **NAVCAM** | **Nav**igation **Cam**eras |
| **NMS** | **N**eutral **M**ass **S**pectrometer |
| **PANCAM** | **Pan**oramic **Cam**eras |
| **RA** | **R**obotic **A**rm |
| **RAD** | **R**adiation **A**ssessment **D**etector |
| **REMS** | **R**over **E**nvironmental **M**onitoring **S**tation |
| **RPA** | **R**etarding **P**otential **A**nalyzer |
| **SAM** | **S**ample **A**nalysis at **M**ars Instrument Suite |
| **SHARAD** | **Sha**llow **Rad**ar |
| **SPE** | **S**olar **P**roton **E**vents |

| | |
|---|---|
| **SSI** | **S**urface **S**tereo **I**mager |
| **SW** | **S**hort-**W**ave |
| **TECP** | **T**hermal and **E**lectrical **C**onductivity **P**robe |
| **TEGA** | **T**hermal and **E**volved **G**as **A**nalyzer |
| **TES** | **T**hermal **E**mission **S**pectrometer |
| **THEMIS** | **Th**ermal **E**mission **I**maging **S**ystem |
| **UHF** | **U**ltra **H**igh **F**requency |
| **USA** | **U**nited **S**tates of **A**merica |
| **USSR** | **U**nion of **S**oviet **S**ocialist **R**epublics |
| **UTC** | **U**niversal **T**ime **C**oordinated |
| **XRFS** | **X**-**R**ay **F**luorescence **S**pectrometer |

# Physical Constants

| | | | |
|---|---|---|---|
| Mars Tropical Year | $t_y$ | = | $686.9725$ days |
| Sutherland's Constant for $CO_2$ | $C_{CO_2}$ | = | $240$ |
| Reference Temperature for $CO_2$ | $T_{0_{CO_2}}$ | = | $686.9725$ °R |
| Reference Viscosity for $CO_2$ at $T_{0_{CO_2}}$ | $\mu_{0_{CO_2}}$ | = | $0.0148$ cP |

# Introduction

Detailed knowledge of the Martian environment is fundamental to any future exploration mission to the red planet. And it is even more so in the case of a manned mission. Sending humans to Mars is a huge technological challenge. Among many other issues, a human base shall possess a self-sustainable life support system to provide the necessary nutrients to the astronauts. Most reasonably, a greenhouse. In order to design and deploy such a system, the environment of the planet must be known with high accuracy.

In this work we have developed a model, the Mars Environment Multi-Model (MEMM), that provides the most complete and up-do-date description of the Martian environment. This scientific and engineering tool is built on existing models, each one describing a specific physical aspect of the environment. These models are based on physical laws and tuned with the experimental measurements taken by the several missions that have flown to Mars. The simulations run with this model will eventually lead to the definition of climatic zones and to a global quantitative picture of the environment offered by the red planet.

This report is organized as follows:

- Chapter 1 reviews the space missions to Mars that have provided relevant data for the understanding of its environment. It also gives the state of the art of the data that were obtained by those missions. This is done by following the timeline of the progress and evolution of the Mars exploration missions, from the initial probes carrying simple equipment to the latest missions characterized by advanced technological instrumentation. Then we review the main models relevant to the subject, especially those which are most employed to describe the Martian climate

and environment: the majority of these models make use of the data returned from the missions.

- Chapter 2 presents and describes the integration made to obtain one macro-model from several existing models. MEMM is first illustrated from the physical point of view and then it is analysed in terms of its implementation and structure.

- Chapter 3 deals with the simulations made with MEMM: several simulations have been executed providing a wide range of results and encompassing different scenarios (e.g., in each of the four seasons, with clear sky or under dust storms). This yields a global picture of the environment on Mars that will help characterise the atmospheric, electromagnetic and particle radiation and meteoroid conditions. The chapter ends with the determination of the climatic zones on the Martian surface. The results allow a better global understanding of the Martian environment, while providing all the physical quantities (e.g., temperature, pressure, density, winds, radiation fluxes, etc.) required for the design of a greenhouse. Specifically, the results of MEMM are foreseen to be employed as input to the thermodynamical model of a greenhouse, which is the subject of another final year's project.

The report ends with a series of conclusions and with a list of possible future improvements.

# Scope

The scope of the present work is structured as follows:

- To discuss the most relevant and prominent missions to Mars in terms of
  - mission time-line, objectives and scientific goals;
  - spacecraft scientific instruments;
  - missions results.
- To present the current models describing the Martian environment in terms of
  - physical quantities and underlying physical laws;
  - scope of each model;
  - results of each model.
- To develop a gobal model (MEMM) of the Martian environment. This item shall develop through:
  - the selection of suitable models for inclusion into MEMM;
  - the modification of each model for integration into MEMM;
  - the development of an interface to expand the models functionality, and to properly treat and format the final results.
- To obtain a global description of the Martian environment through
  - the characterization of its geography, topography, seasons, atmospheric composition and characteristics, winds, temperature, radiation fluxes, meteoroid fluxes, soil composition;
  - the simulation of the full environment in the best- and worst-case scenarios;
  - the identification of the Martian climatic areas.

# Chapter 1

# State of the Art

This chapter starts with a presentation of the missions that have delivered useful data concerning the Martian environment. For each we discuss the objectives, the science instruments carried onboard and the most relevant results. The physical models and the available software that have been considered for inclusion in MEMM are introduced in the second part of the chapter. As a whole, this part of the report contains the state of the art of our knowledge and modelling capabilities concerning the environment on Mars.

## 1.1 The data

Since 1960, 44 space missions have been flown to Mars. Of these, only 22 reached Mars orbit and fulfilled their objectives. The first attempt to reach Mars was made by USSR's 1M No. 1 spacecraft in 1960, but the launcher suffered a third stage failure at $T + 300$ seconds and the mission was lost. The first spacecraft to actually fly to Mars was USA's Mariner 4 in 1964, which performed a successful flyby and sent imagery back. The Soviet Union was the first country to land a capsule on the surface of Mars with its M-73 No. 50 (Mars 6) mission in 1973. NASA's Mars Pathfinder delivered Sojourner, the first rover, in 1996.

Up to present time, five space agencies (USSR/Russia, NASA, ESA, JAXA and ISRO) have designed and flown missions to Mars.[1,2] The USA have been the most prolific country with 14 successful missions out of 21 sent (while this report is being written,

MAVEN is en route to its destination). The USSR succeeded only in three of its 19 missions. Europe succeeded in both its two missions, i.e., Mars Express and Rosetta. Japan's only mission to Mars, Nozomi, failed during the interplanetary cruise, whereas the first Indian mission, Mangalyaan, is currently on its way to the red planet.

Since 1997 (Mars Pathfinder), all of NASA's Martian missions have belonged to the Mars Exploration Program, a space programme that defines a global set of goals[3] that all the missions must fulfil within their own specific objectives. These goals are

- to determine whether life ever developed on Mars: the mission shall search for evidence of past liquid water and present water ice, and biosignatures of current and past life.
- to characterize the climate of Mars: monitoring the present seasonal climate changes and the global dust storms will help understand the planet climate changes along millions of years.
- to characterize the geology of Mars: analysing the soil and the rocks provides information to understand how activities like wind, water and volcanism have modelled the surface. Studying the magnetism also helps understand the internal structure of the planet.
- to prepare for the human exploration of Mars: before sending any manned mission to Mars, the issue of the radiation environment on the surface must be addressed and the availability of water and several other resources must be assessed. Furthermore, robotic spacecraft must be deployed well in advance to sending human crews.

As shown in Fig. 1.1, the main strategy within the Mars Exploration Program is to "Follow the Water", thus directing all the efforts towards the search and analysis of water indices on Mars. However, since the Mars Science Laboratory mission, this strategy has been progressively overlapped by another, i.e., to "Seek Signs of Life", which means focussing on the search and analysis of present or past biological traces on the planet.

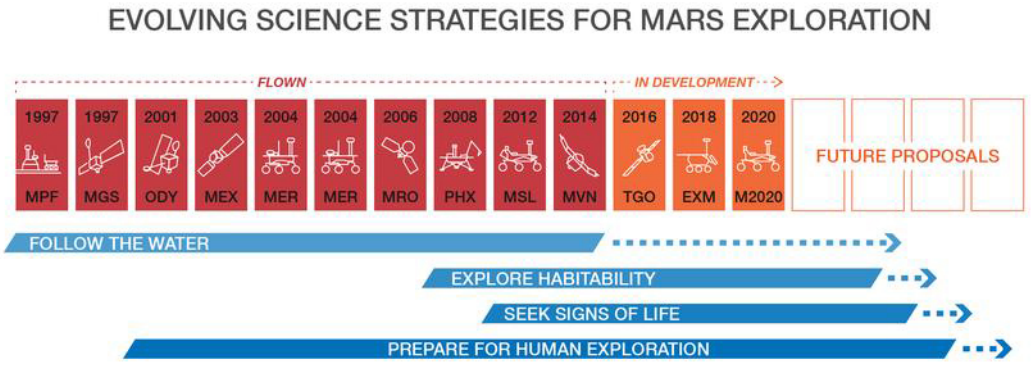


Figure 1.1: Science strategies timeline within the Mars Exploration Program.

The missions that belong to the Mars Exploration Program are: Mars Pathfinder, Mars Global Surveyor, Mars Odyssey, Mars Express, Mars Exploration Rovers, Mars Reconnaissance Orbiter, Phoenix, Mars Science Laboratory, and Mars Atmosphere and Volatile Evolution Mission.

### 1.1.1 Viking

The Viking mission consisted of two spacecraft, Viking 1 and Viking 2, each carrying an orbiter and a lander. In both cases, the objective was to soft-land on Mars and search for evidence of life.[4] The two s/c were launched on August 20, 1975 and on September 9, 1975, respectively. The launch dates were selected to provide minimum-energy transfers. The lander of Viking 1 touched down at Chryse Planitia on July 20, 1976, whereas the lander of the second mission landed at Utopia Planitia on August 7, 1976. The two vehicles concluded their operational life in 1982 and 1980, respectively, and the orbiters were shut down in 1980 and 1978. The orbiters mapped the surface of Mars at a 150-300 meter resolution. The landers were equipped with two 360-degree Imaging Cameras, a Gas Chromatograph, a Mass Spectrometer, a Neutral Mass Spectrometer (NMS), an X-Ray Fluorescence Spectrometer (XRFS), a Retarding Potential Analyzer (RPA), magnetometers, a Radio Science device, thermometers, wind sensors and seismometers.[5,6] The mission provided extensive data on atmospheric pressure (Fig. 1.2), temperature, winds and atmospheric dust. The orbiters mapped the global atmospheric temperatures of the planet (Fig. 1.3).[7] No evidence of life was found.[8]

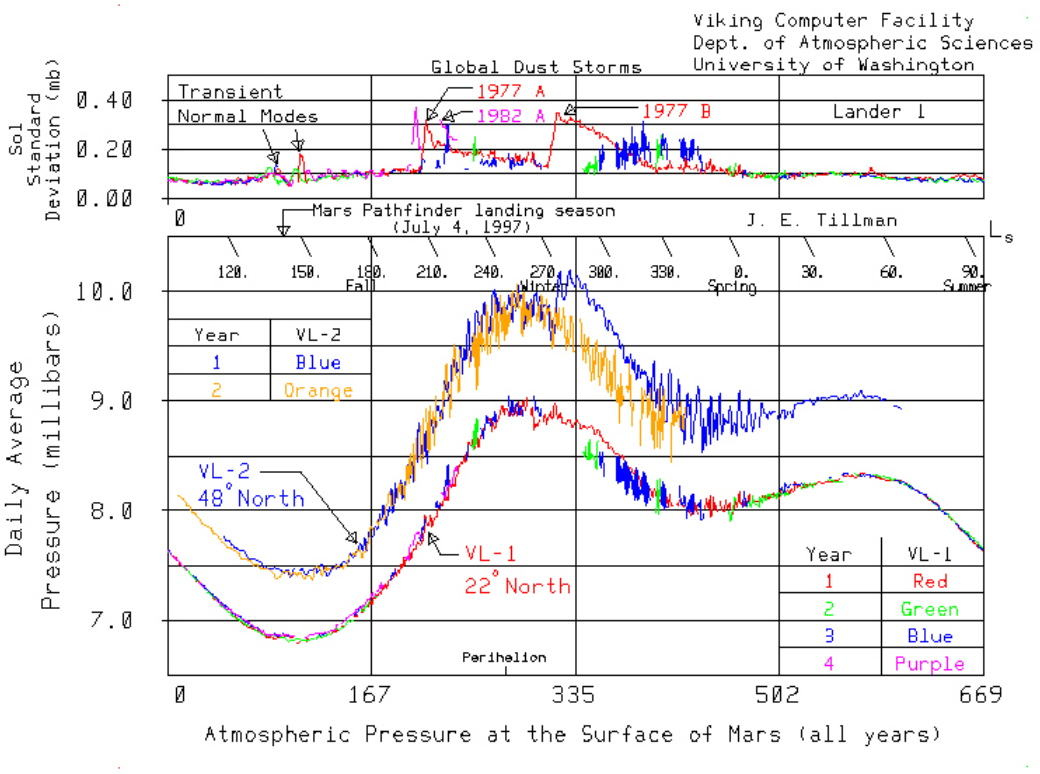


Figure 1.2: Viking landers: daily average pressure measurements.

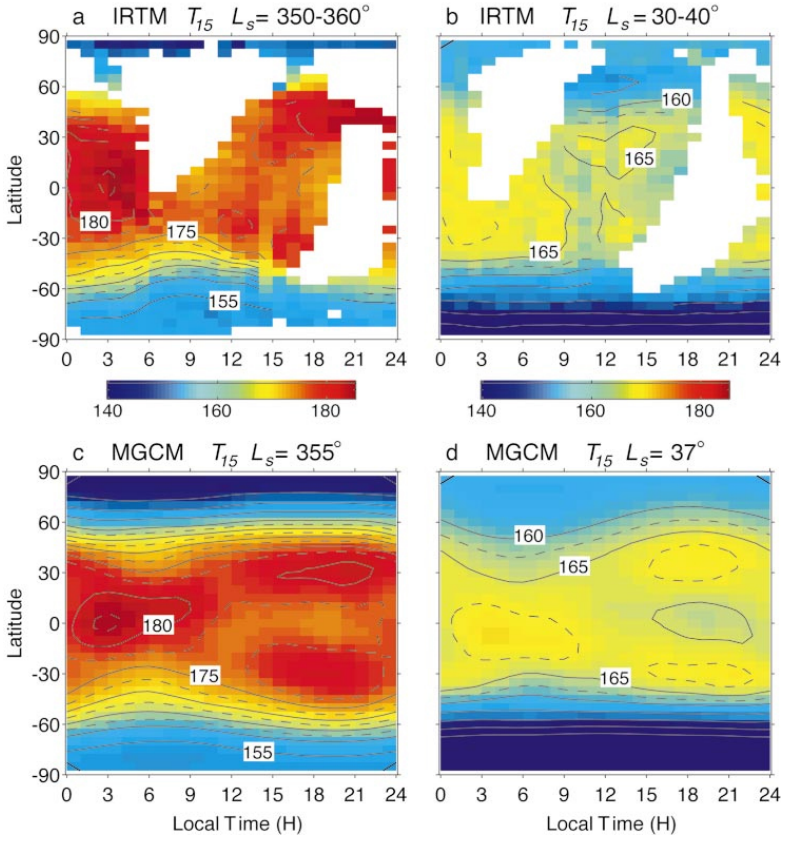


Figure 1.3: Viking orbiters IRTM raw temperature data (top) and simulated map (bottom).

### 1.1.2 Mars Pathfinder

The Mars Pathfinder mission was developed as a technology demonstration project for future missions. The mission objective was to develop a “faster, better, and cheaper” system to place a science payload on Mars. It also aimed at demonstrating the usefulness of a rover on the surface. The science objectives were to study the surface geology, petrology, geochemistry and magnetic properties, as well as the atmospheric characteristics, their daily and seasonal variations, and orbital dynamics.[9] The mission included one lander (Pathfinder) and one micro-rover (Sojourner). It was launched on December 4, 1996, and landed at Ares Vallis (Chryse Planitia) on July 4, 1997. The lander carried three scientific instruments: the Stereoscopic Imager (IMP), the Alpha Proton X-Ray Spectrometer (APXS) mounted on the Sojourner rover, and the Atmospheric Structure Instrument/Meteorology package (ASI/MET). The ASI/MET instrument performed measurements of temperature (Fig. 1.4), pressure (Fig. 1.5) and winds during descent, landing and throughout the mission. The temperature data showed turbulent convection in the morning and in the afternoon due to the rapid surface heating. The temperature is stable at sunrise and at sunset as well as during the night, with small variations caused by down-slope winds.[10]

#### 1.1.2.1 Sojourner

The Sojourner rover was a six-wheel vehicle with a total mass of 10.5 kg. It was designed to operate within 500 meters of the Pathfinder lander, as the data transfer was performed via UHF link. The rover main objective was to test new technology in order to improve the design of future surface vehicles.[11] The rover carried the APXS instrument on the rear side. The main objective of the APXS was to provide a chemical elemental analysis of the Martian soil and rocks, thus completing the analysis made by the Viking landers which did not have capability to detect C, N, O, and Na compounds. The APXS analysis executed at two sites, i.e., Barnacle Bill and Yogi (Fig. 1.6), revealed that the samples were not basalts, and that not all had volcanic origin, some of them being sedimentary rocks. The presence of rounded pebbles and cobbles also suggests the possible presence of liquid water in the past.[12]

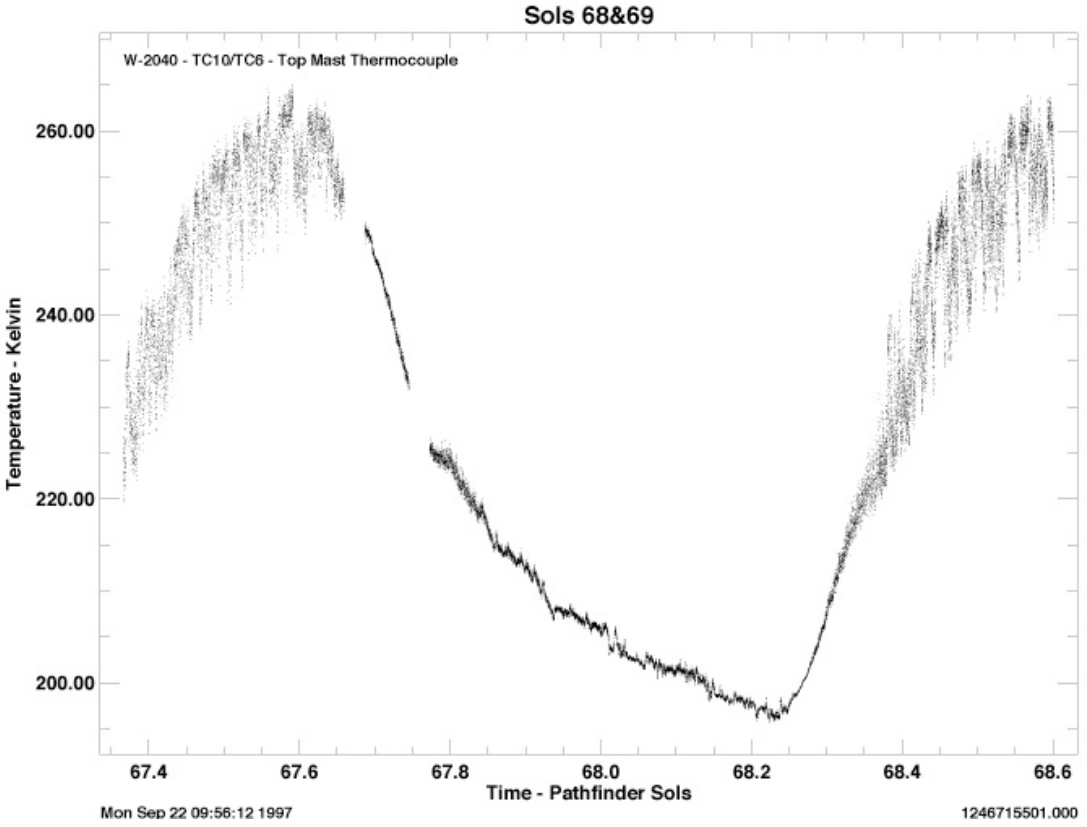


Figure 1.4: Temperature measured by the Pathfinder ASI/MET instrument.

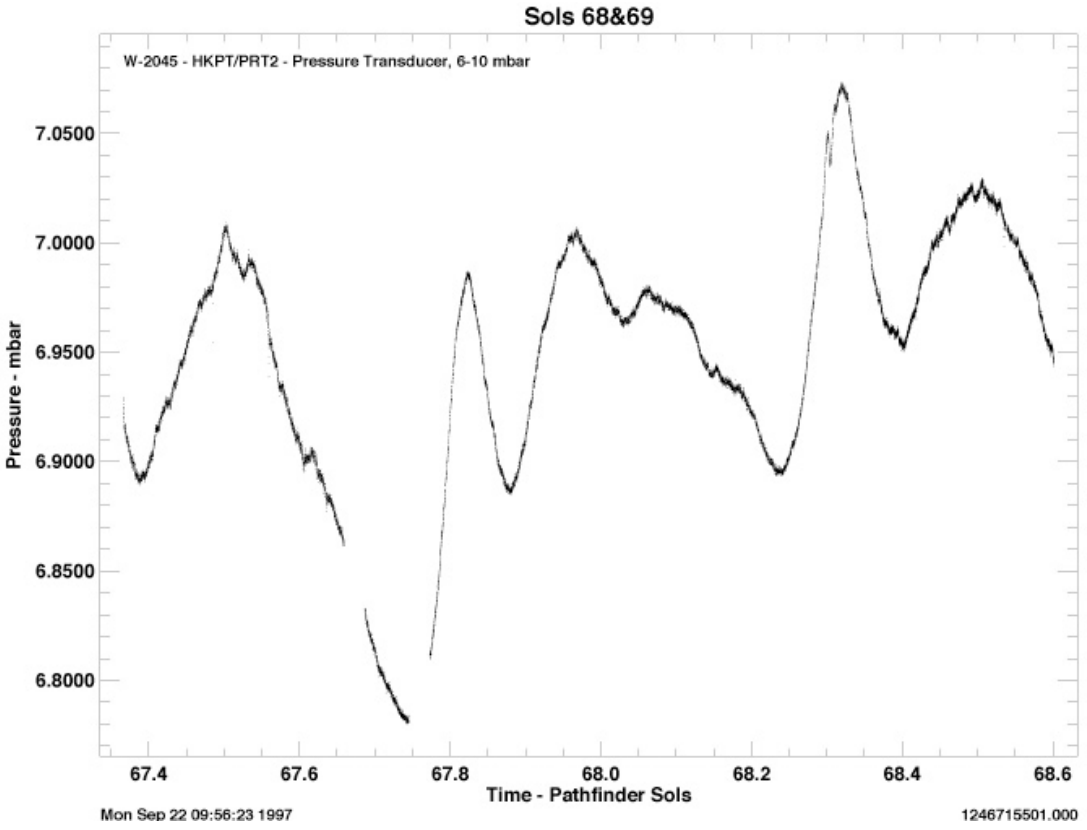


Figure 1.5: Pressure measured by the Pathfinder ASI/MET instrument.

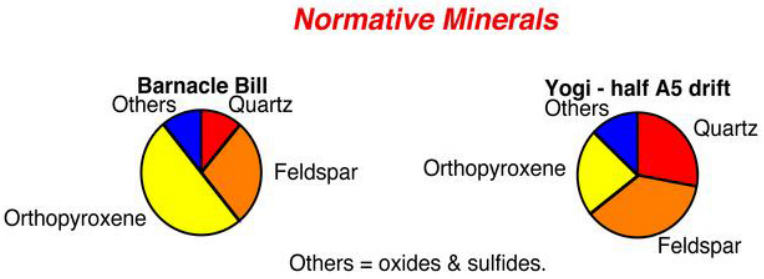


Figure 1.6: Plausible minerals from the Sojourner APXS chemical analyses of Barnacle Bill and Yogi.

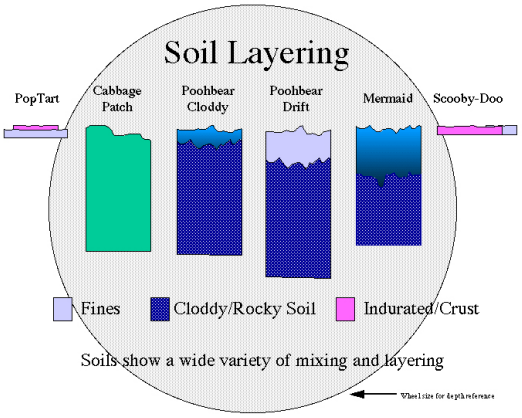


Figure 1.7: Evidence of soil layering from the Sojourner rover soil mechanics experiment.

The rover also used its wheels to carry out an indirect analysis of the soil.[13] The vehicle spun the wheels while electric current and temperature were being recorded. From these data the shear force at the soil/wheel interface could be estimated and this information was then used to characterize the soil layering (Fig. 1.7).

### 1.1.3 Mars Global Surveyor

The Mars Global Surveyor mission consisted in an orbiter designed to gather data on the surface morphology, topography, composition, gravity, atmospheric dynamics, and magnetic field of Mars. The orbiter was the successor of Mars Orbiter, lost shortly before orbit insertion in 1993. Mars Global Surveyor was launched on November 7, 1996. It arrived at Mars on September 12, 1997. After a series of issues during the aerobraking manoeuvre, the orbiter reached the final near-circular orbit in February 1999. The orbit was Sun-synchronous and almost circular. The primary mission lasted one Martian year since the summer of the Northern hemisphere. The orbiter performed

an extended mission until April 2002. In 2003, the orbiter provided relaying support for other missions (Mars Odyssey, Mars Exploration Rovers). It finally went silent in 2006 following a software update bug.

The mission science objectives were

- to characterize the surface features and geological processes;
- to determine the composition, distribution and physical properties of surface minerals, rocks and ice;
- to determine the global topography, planet shape, and gravitational field;
- to map the magnetic and crustal remnant field;
- to monitor the global weather and the thermal structure of the atmosphere;
- to study the seasonal interactions between the surface and the atmosphere.

The extended mission objectives were:

- to continue monitoring the weather so as to provide continuity with the Mars Reconnaissance Orbiter mission;
- to provide imaging of possible landing sites for the Phoenix lander and the Mars Science Laboratory rover;
- to observe and analyse key sites of scientific interest;
- to continue monitoring the surface changes caused by wind and ice.

The Mars Global Surveyor's orbiter carried several instruments: the Mars Orbiter Camera (MOC) that provided daily wide-angle images as well as specific location narrow-angle images, the Mars Orbiter Laser Altimeter (MOLA) that measured the surface height, the Thermal Emission Spectrometer (TES) that studied the atmosphere and mapped the mineral composition of the surface, the Electron Reflectometer (MAG/ER) that studied the magnetic properties of Mars, and the Gravity Field Experiment (RSS) that mapped variations in the gravity field. It also carried a UHF antenna to relay communications from the surface landers and rovers. MOC provided a vast range of images from the surface, allowing detailed investigation of Mars geological processes.

Some of these images suggest the existence of liquid water in the past.[14] The images have also been used to determine the landing sites for future missions (Phoenix, Opportunity). TES systematically measured and monitored the surface and atmosphere of Mars, greatly improving the data previously gathered by Mariners 6, 7, and 9 and Vikings 1 and 2. The instrument collected more than 206 million spectra throughout the mission.[15] The results produced the first several mineral maps of the surface.[16] The TES monitored the atmosphere during three years, gathering information on daily/seasonal variations of temperature, pressure, water concentration, dust levels and winds (Fig. 1.8).[17–22] It also monitored the dust storm that broke in Hellas Planitia in June 2001, which ultimately engulfed the whole planet in a global dust storm (Fig. 1.9).[23] It then traced[24] the disappearance of the polar caps (Fig. 1.10), and provided temperature measurements of the southern polar cap, which allowed the development of a model to explain the dust ejection jets from $CO_2$ sublimation during the spring.[25] MOLA provided the first complete topographic model of Mars with a resolution better than 100 meters and typical accuracies of 30 meters (Fig. 1.11).[26] MAG/ER was the first instrument to systematically map the magnetic field of Mars (Fig. 1.12). The results of this experiment indicated that Mars once had a magnetic field which is not evident today. This suggests that the magnetic dynamo of the core is extinct for yet unknown reasons.[26] RSS greatly improved the gravity models from Mariner 9 and Viking, leading to a more accurate understanding of the planet's interior.[26]

### 1.1.4 Mars Odyssey

The Mars Odyssey orbiter was launched on April 7, 2001. It reached Mars on October 24, 2001. Upon completion of the primary mission on August 24, 2004, the extended mission began. The mission objectives were[27]

- to map the composition of the surface elements on a global scale;
- to determine the abundance of hydrogen in the shallow subsurface;
- to acquire multi-spectral images of the surface mineralogy;
- to characterize the morphology of the surface;
- to measure the near-space radiation environment.

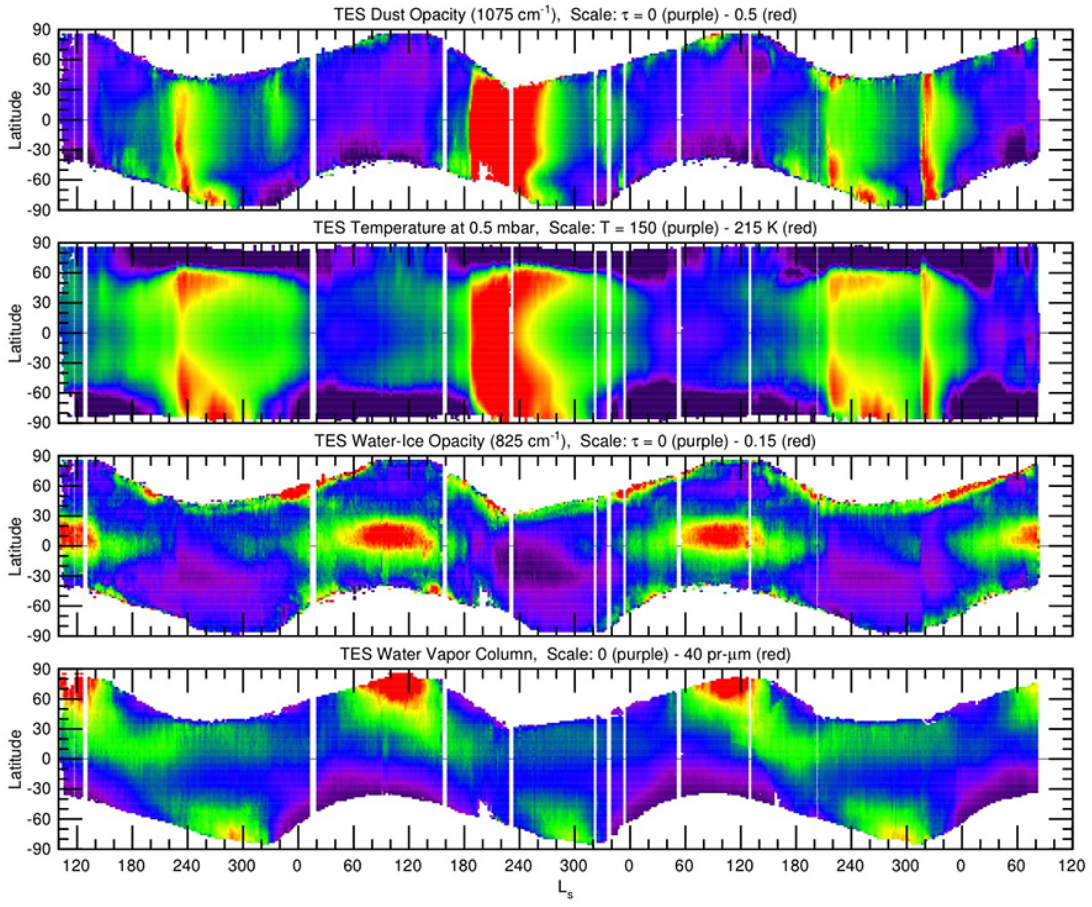


Figure 1.8: TES data multi-year plot displaying dust opacity, temperatures, water-ice opacities and water vapour column.

Additionally, the orbiter acted as communications relay for the surface landers and rovers (Mars Exploration Rovers, Mars Phoenix Lander) by transmitting nearly 95% of their data back to Earth.

The orbiter carried three main instruments: THEMIS (Thermal Emission Imaging System) to determine the distribution of surface minerals at visible and infrared wavelengths, GRS (Gamma Ray Spectrometer) to determine the presence of 20 chemical elements on the surface of Mars, and MARIE (Mars Radiation Environment Experiment) to study the radiation environment.[28] The data of the THEMIS instrument greatly improved the resolution of the MGS/TES instrument. THEMIS also monitored[29] the the amount of dust in the Martian atmosphere (Fig. 1.13). The images were also used to choose the landing sites for the Phoenix lander, the Mars Exploration Rovers and the Mars Science Laboratory rover.[30–32] The results of the GRS instrument indicated, among other results, the presence of water in the polar caps (Fig. 1.14).

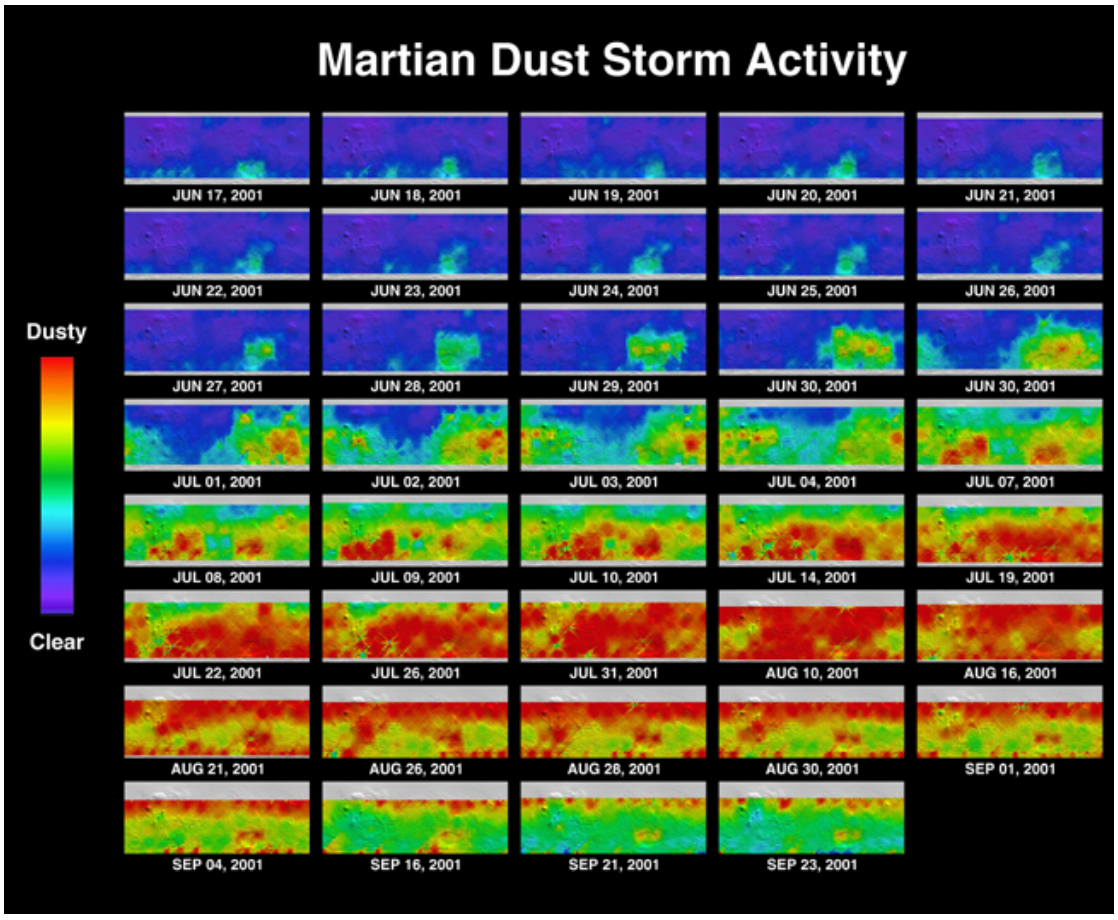


Figure 1.9: TES observations of the planet-encircling dust storm in 2001.

The MARIE instrument collected radiation data during the interplanetary transfer until its shutdown in 2001. After the orbiter reached a stable orbit in 2002, the instrument was resumed (Fig. 1.15). It started malfunctioning shortly after a series of strong solar flares in Autumn 2003. The radiation dose results prove to be a major threat to any human exploration of Mars.[33]

### 1.1.5 Mars Express

Mars Express represents the first European attempt to send a spacecraft to Mars. The mission included an orbiter and a lander (Beagle-2). The launch took place on June 2, 2003 and the arrival occurred in December 25 of the same year. The lander failed during the descent, whereas the orbiter performed five successful extended missions, the last of which is scheduled to end in December 2014. The mission scientific objectives were[34]

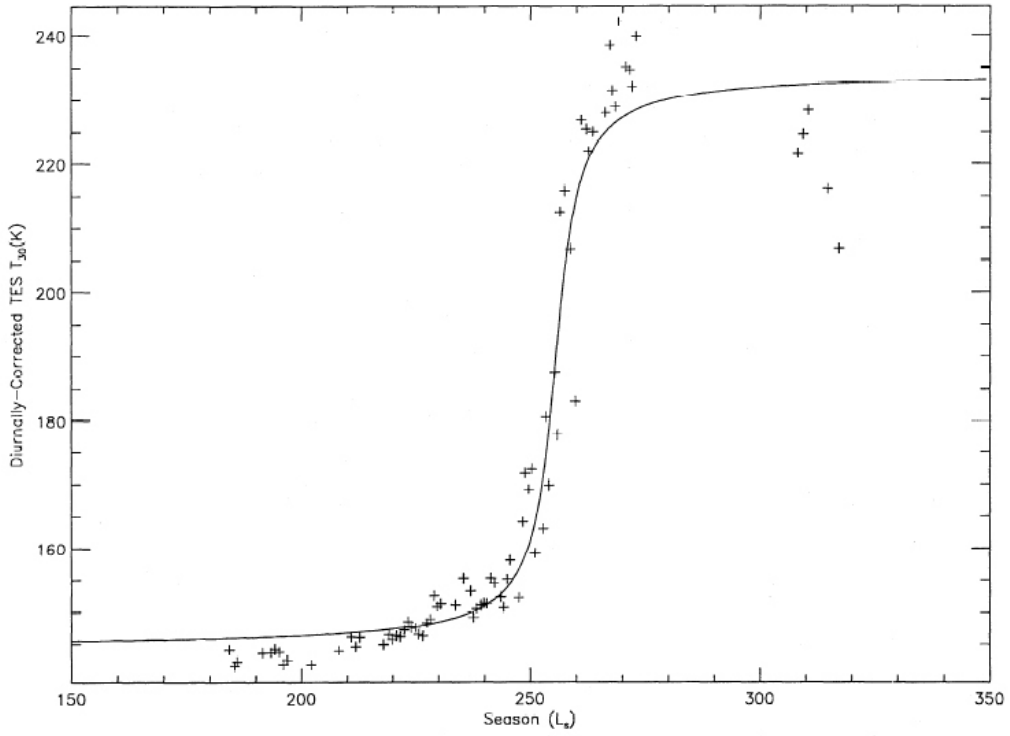


Figure 1.10: TES measurement of Mars south cap temperature.

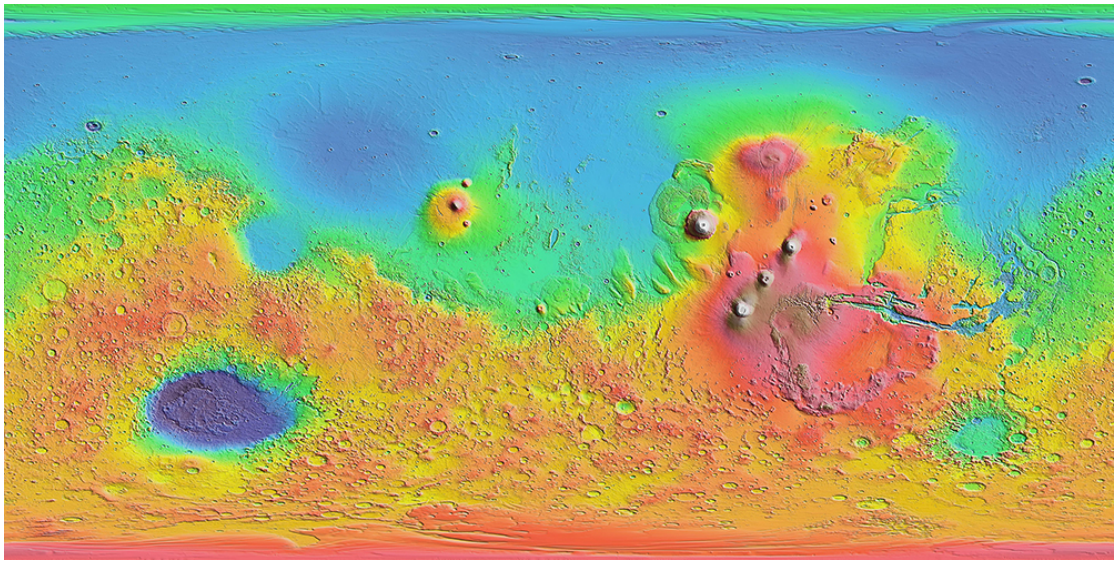

Figure 1.11: Topographic map of Mars from the MOLA instrument.

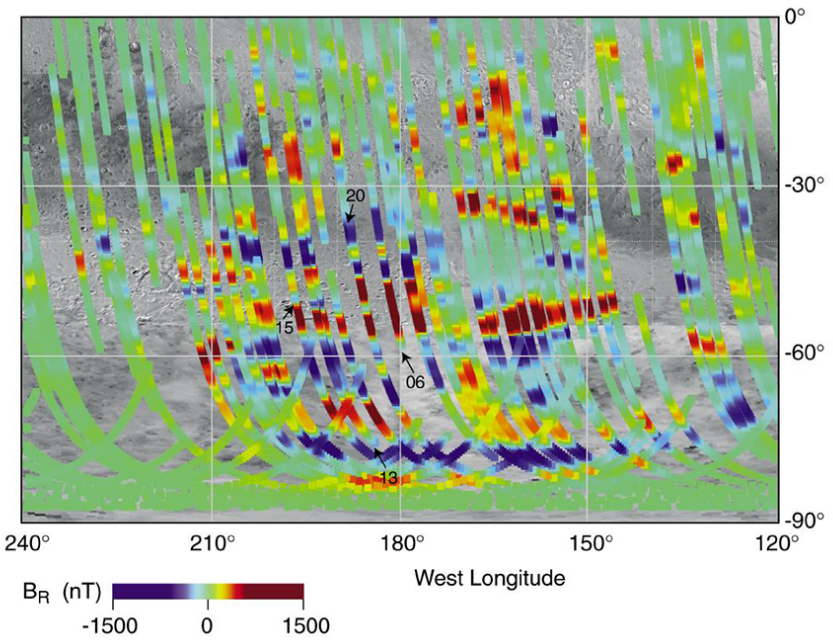


Figure 1.12: Radial magnetic field data from the MGS MAG/ER instrument.

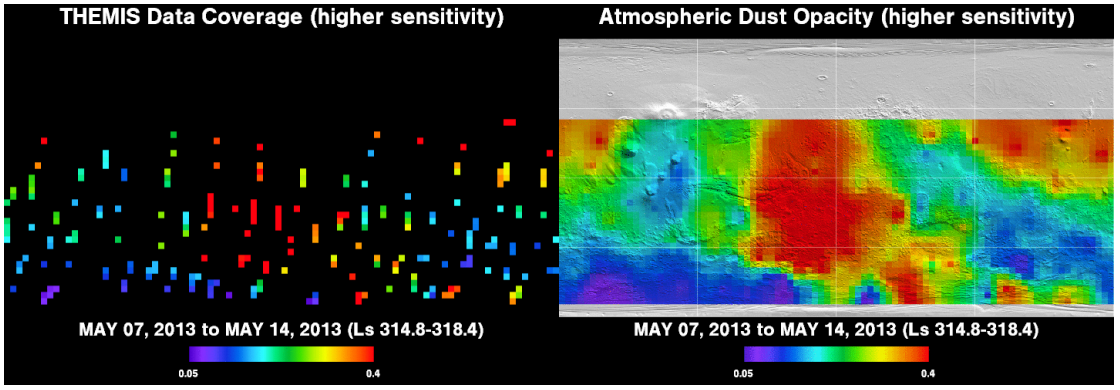


Figure 1.13: THEMIS dust opacity map: raw measurements (left) and extrapolated map (right).

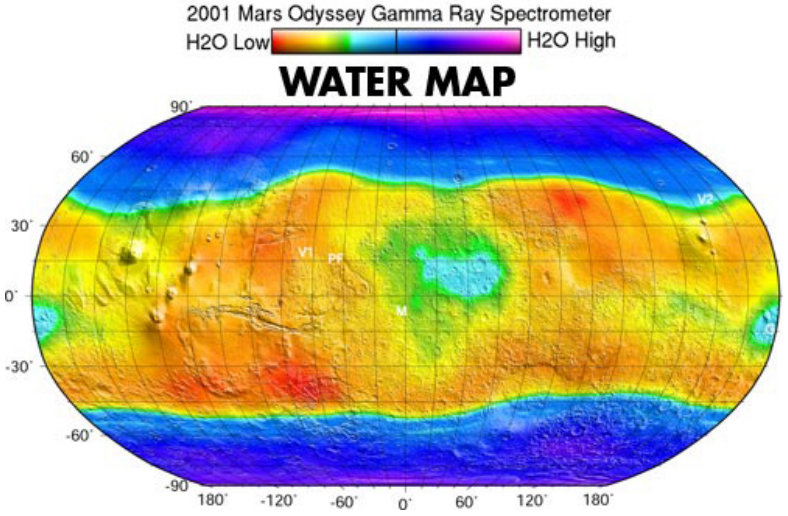


Figure 1.14: GRS map based on gamma rays from the hydrogen element.

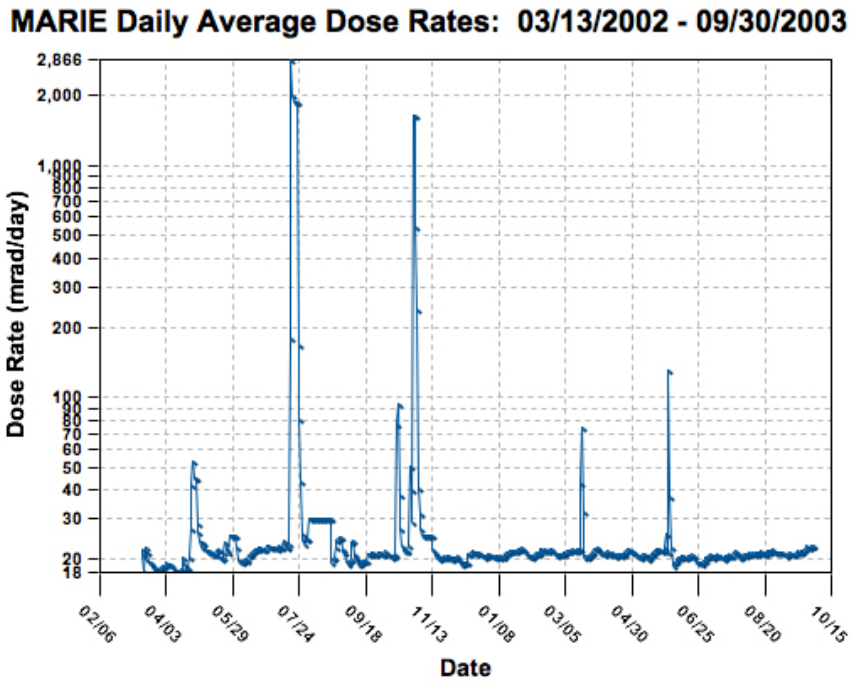


Figure 1.15: MARIE daily average dose rates.

- to globally map the surface with imagery at 2-10 meters resolution, and to obtain mineralogical maps at 100-1000 meters scale;
- to characterise the global atmospheric circulation and composition;
- to characterise the subsurface structure at the kilometer scale;
- to characterise the surface-atmosphere interaction;
- to measure the structure of the interior, atmosphere and environment via radio science;
- to perform surface geochemistry and exobiology.

The Mars Express orbiter carried the following instruments: the Energetic Neutral Atoms Analyser (ASPERA-3) to visualise the charged and neutral gas environments around Mars, the High/Super Resolution Stereo Colour Imager (HRSC) to photograph the surface of Mars, the Radio Science Experiment (MaRS) to measure local variations in the gravity field, the Subsurface Sounding Radar/Altimeter (MARSIS) to map the distribution of water and ice on the surface, the IR Mineralogical Mapping Spectrometer (OMEGA) to determine the mineral composition of the surface, the Planetary Fourier Spectrometer (PFS) to measure the global atmospheric concentration of water vapour,

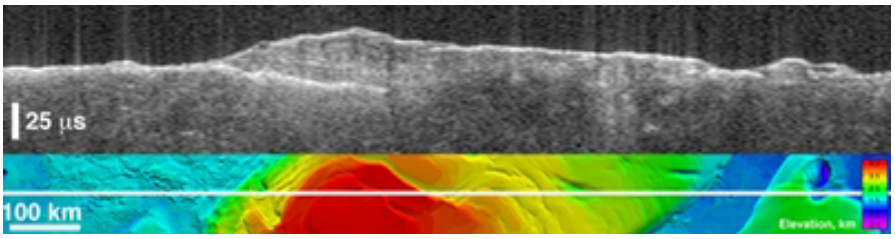


Figure 1.16: Ice-rich layered deposits at the South pole from the MARSIS instrument data.

and the UV and IR Atmospheric Spectrometer (SPICAM) to measure the vertical profiles of the atmosphere with greater resolution than PFS.[35]

HRSC provided improved resolution images of the surface of Mars. The HRSC Digital Terrain Models have allowed better insight into the geological processes and have been used to select the landing sites for the Mars Science Laboratory. HRSC has also acquired sharp images of Phobos, and has improved the orbit determination of the Martian moons. OMEGA carried out an extensive mapping of water-ice and carbon dioxide-ice in the polar regions[36] and it identified high altitude carbon-dioxide clouds in the atmosphere. MARSIS detected water-ice deposits in the subsurface of the polar regions (Fig. 1.16). PFS produced temperature maps from the surface up to an altitude of 50 km. It also detected the presence of methane, which could indicate the presence of active geological or biological processes.[37] SPICAM provided the first complete vertical distribution of carbon-dioxide in the atmosphere of Mars.[38] ASPERA made measurements of the escape ratio of several ions (among which those of hydrogen and oxygen) from the atmosphere of Mars. It also gave insight into the interactions between the solar wind and the atmospheres of planets without a magnetic field. The MaRS experiment studied the surface roughness. It also discovered and observed a previously-unknown ionosphere layer[39] and a seasonal ozone layer[40] near the South pole.

### 1.1.6 Mars Exploration Rover

The Mars Exploration Rover mission consisted in two twin rover vehicles deployed at different locations. The design was based on an improved, bigger and better equipped version of the Sojourner rover.[41] The scientific objectives of the mission were[42]

- to search and characterise soils and rocks to find evidence of past water activity;

- to determine the composition of soils and rocks near the landing site;
- to determine the geological processes that shaped the local terrain;
- to perform ground measurements in order to calibrate and validate the data gathered by the several orbiters;
- to search for minerals with iron content and minerals that were formed in water;
- to characterize the mineralogy of soils and rocks;
- to search for geological signs of the environmental conditions of the epoch in which liquid water was present.

The onboard scientific instruments were: a Miniature Thermal Emission Spectrometer (Mini-TES) to determine the mineralogy of the soil and rocks, a Mössbauer Spectrometer (MB) to study iron-bearing minerals, an Alpha Particle X-Ray Spectrometer (APXS) to determine the chemistry of the soil and rocks, a Rock Abrasion Tool (RAT) mounted on the arm to grind a small hole into rocks to later study their internal structure, and three sets of Magnet Arrays to collect atmospheric dust for analysis. Each rover also carried several cameras: four Hazard Avoidance Cameras (HAZCAM) to capture three-dimensional imagery used for autonomous navigation, two Navigation Cameras (NAVCAM) to provide three-dimensional panoramic images of the scenery, two Panoramic Cameras (PANCAM) to provide multi-spectral imagery with human-like field of vision, and one Microscopic Imager mounted on the robotic arm to take close-up pictures of soil and rocks.[42]

#### 1.1.6.1 Spirit

Mars Exploration Rover A, better known as Spirit, was launched on June 10, 2003. It landed on Mars on January 4, 2004. The planned mission duration was of 90 days, but thanks to a number of solar panel clearing operations, the rover continued working until May 1, 2009, thus exceeding by more than 21 times the foreseen mission duration. The cause of the failure was a front wheel that got sand-trapped in soft soil at Troy crater. Attempts to free the rover proved ineffective. Then, the batteries did not survive their fourth Martian winter, and the rover went silent on March 22, 2010.[43,44] The chosen landing site was Gusev Crater (14.59°S, 175.3°W), a giant impact crater believed to

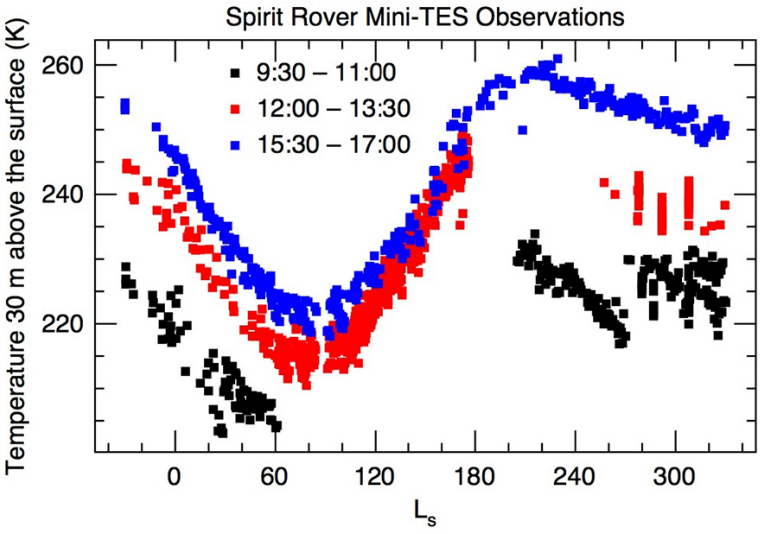


Figure 1.17: Spirit Mini-TES temperature measurements at 30 meters from the surface.

be a possible former lake.[45] Furthermore, during descent the onboard accelerometers gathered data that were later used to improve the atmospheric models of Mars.[46] Spirit found evidence of a volcanic explosion at the Home Plate plateau which suggested that Mars had experienced an active volcanic period.[47,48] At Columbia Hills Spirit discovered several bedrock components that showed complex geological processes, some of which appeared to be alterations caused by water.[49,50] However, one of the most surprising findings was made at Troy crater: when the rover got sand-trapped, it found a patch of nearly pure silica. This brought evidence of a past wetter environment because the silica had likely been produced during hot springs or thanks to the action of steam vents.[44] The rover autonomous detection algorithms[51] captured several movies of dust devils, proving the dynamic behaviour of the Martian atmosphere. The data gathered by the Mini-TES instrument provided the temperature (Fig. 1.17) and dust optical depth (Fig. 1.18) profiles of the planetary boundary layer, i.e., from the surface up to 2 km height.[52] It also helped study the permafrost layer of the Martian surface while improving several existing models.[53]

#### 1.1.6.2 Opportunity

Mars Exploration Rover B (Opportunity) left the Earth on July 7, 2003 and landed on Mars on January 25, 2004. Also in this case, the foreseen mission duration was of 90 days, but as of 2014 the rover is still operating. The selected landing site was Meridiani Planum (0.2°N, 357.5°E), where mineral deposits suggested the presence of water in

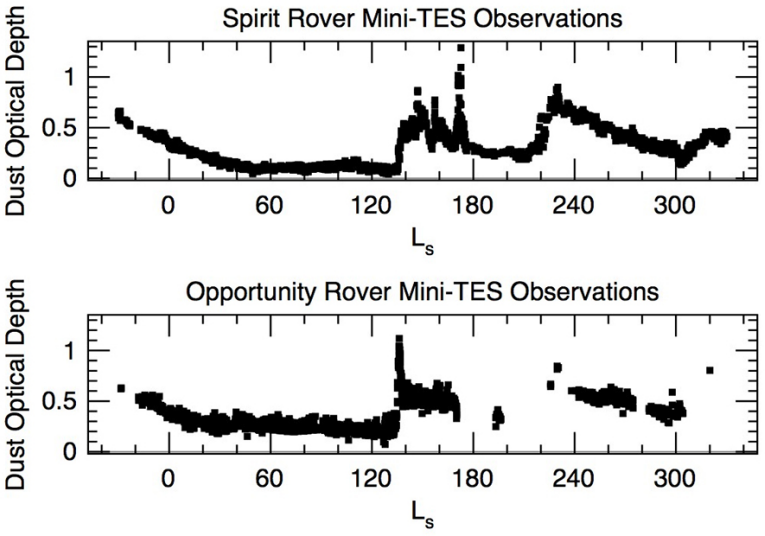


Figure 1.18: Spirit (top) and Opportunity (bottom) dust aerosol optical depth measurements at 1075 cm-1.

the past.[45] Like Spirit, the Opportunity rover also obtained valuable accelerometer data during the descent. Over these ten years, the rover has monitored the daily and seasonal temperature changes in the planetary boundary layer, it has taken images of water-ice particles clouds in the Martian sky, and has also detected a thin layer of frost on the rover calibration peg. The observations made by Opportunity at Meridiani Planum gave insight into the concentration variations of argon over the seasons. The aeolian ripples in the North-South direction suggest that in the past the tilt of the Martian rotation axis was larger and this produced strong eastward winds. The analysis of the bedrock suggests sand deposition by wind, with subsequent alteration by water.[54] Both Spirit and Opportunity also observed several meteorite rocks, mainly composed of iron, nickel and silicates.[54,55]

### 1.1.7 Mars Reconnaissance Orbiter

The Mars Reconnaissance Orbiter mission was designed after the Mars Global Surveyor. It was launched on August 12, 2005 and arrived at Mars on March 10, 2006. As of 2014, the mission is still operational. The mission objectives are[56]

- to characterise the mechanisms of seasonal climate change of Mars;
- to identify water-related terrain features;

- to search for evidence of aqueous or hydrothermal activity sites;
- to identify potential candidate sites for future lander missions;
- to relay communications from the surface landers to Earth.

The orbiter carried six instruments: the High Resolution Imaging Science Experiment (HiRISE) that took high-resolution visible wavelength imagery, the Context Camera (CTX) that provided wide-range context views for the HiRISE and CRISM instruments, the Mars Color Imager (MARCI) that monitored clouds and dust storms, the Compact Reconnaissance Imaging Spectrometer for Mars (CRISM) that analysed the visible and near-infrared spectra of the surface, the Mars Climate Sounder (MCS) that detected vertical profiles of temperature, dust and water, and the Shallow Radar (SHARAD) that sounded the surface to determine the presence of water ice at depths of 1 meter and greater.[57] The mission experienced a substantial improvement in the data transfer speeds: in 2010 the orbiter had sent more than 100 Terabytes of data back to Earth, three times the total amount sent from all the previous missions.[58] This allowed critical relay support for the rovers on the surface (Spirit, Opportunity, Curiosity). HiRISE has taken high resolution imagery to help in the selection of landing sites for the Mars Science Laboratory and for future landers.[59] The Mars Climate Sounder has validated a model that predicted a particular daily morning clouds pattern.[60] It has also been monitoring the atmosphere aiming at improving the models in view of the design of the descent trajectory for Mars Science Laboratory.[61] The data provided by SHARAD on the North polar ice layers confirms the models[62] that theorize several global climate cycles that have been taking place during the last million years (Fig. 1.19).

### 1.1.8 Phoenix

Phoenix was the first lander to successfully return data from the northern polar regions of Mars. It was launched on August 4, 2007 and landed at Green Valley in May 25, 2008. After five months of operation, the lander ended communications in November 29, 2008 due to battery depletion during winter. The mission objectives were[63,64]

- to study the history of water in the Martian Arctic;

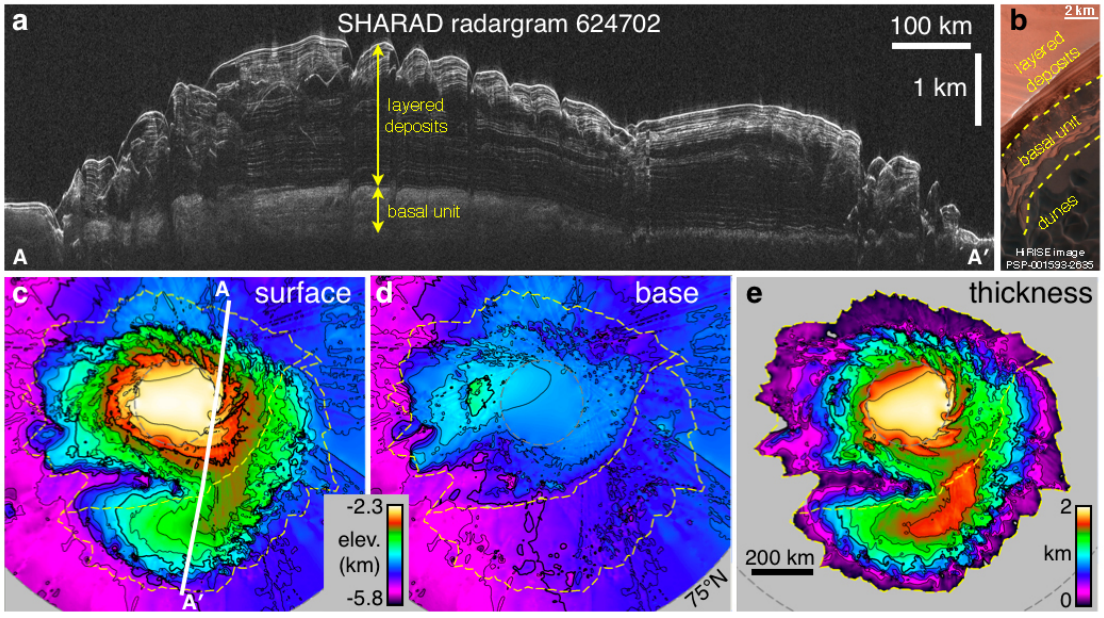


Figure 1.19: SHARAD radar map of buried ice layers at the North pole.

- to search for evidence of an habitable zone and assess the biological potential of the ice-soil boundary.

The Phoenix lander carried three of the instruments previously used by the Mars Polar Lander: the Surface Stereo Imager (SSI), the Robotic Arm (RA) and the Thermal and Evolved Gas Analyzer (TEGA). Additional instruments were the Mars Descent Imager (MARDI), the Microscopy, Electrochemistry, and Conductivity Analyzer (MECA), the Wet Chemistry Experiment, the Optical Microscope and the Atomic Force Microscope, the Thermal and Electrical Conductivity Probe (TECP), and a meteorological station (MET).[65] The results returned by the mission provide evidence[66] of water ice at the Phoenix landing site (Fig. 1.20), as well as water snow precipitation[67] from cirrus ice clouds. Further analysis has pointed to the existence of climate cycles that may make the landing area warmer and wetter, thus favourable to life of microbes.[68] The lander also analysed the atmospheric dust.[69] The instruments on the robotic arm have returned extensive data from the several collected soil samples.[70,71] The Phoenix orbiter also collaborated with the Mars Reconnaissance Orbiter to perform a combined mapping of the polar regions of Mars.[72]

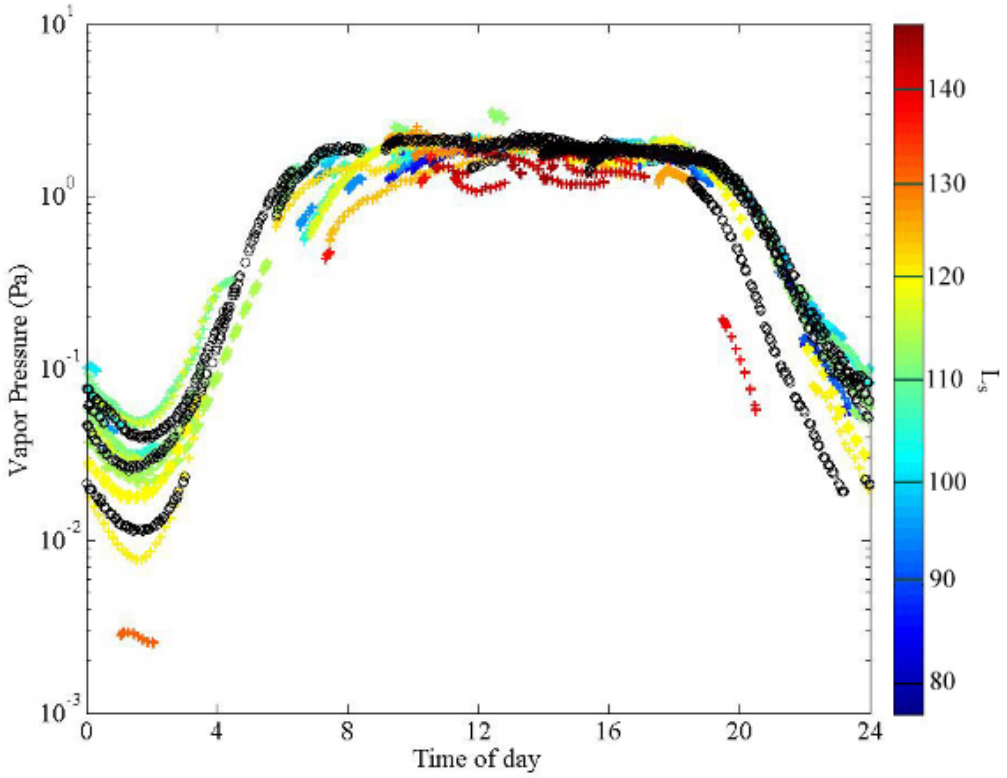


Figure 1.20: Atmospheric water vapour measured by the TECP probe: the black circles refer to measurements made close to the surface.

### 1.1.9 Mars Science Laboratory

The Mars Science Laboratory mission consists in one rover, Curiosity, that is a car-sized mobile laboratory designed from an improved version of the Mars Exploration Rovers. The spacecraft was launched on November 26, 2011, and landed at Aeolis Palus in Gale Crater on August 6, 2012. The Gale Crater location was selected by its deposit of layered materials at the central mountain.[73] The rover is powered by a Radioisotope Thermal Generator, and is still operating as of April 2014.

The mission objectives are[74]

- to perform an inventory of organic carbon compounds;
- to perform an inventory of the chemical building blocks of life (carbon, hydrogen, nitrogen, oxygen, phosphorous and sulphur);
- to identify features that could be related to the effects of biological processes;

- to investigate the chemical, isotopic, and mineralogical composition of the surface;
- to interpret the geological processes that have formed the soil and rocks;
- to assess long-timescale atmospheric processes;
- to determine the present seasonal distribution of water and carbon dioxide;
- to characterise the surface radiation levels, including galactic cosmic radiation, solar particle events and secondary neutrons.

The Curiosity rover is loaded with a wide range of instruments, including Cameras (the Mast Camera Mastcam, the Mars Hand Lens Imager MAHLI and the Mars Descent Imager MARDI), Spectrometers (the Alpha Particle X-Ray Spectrometer APXS, the Chemistry and Camera ChemCam, the Chemistry and Mineralogy X-Ray Diffraction/X-Ray Fluorescence Instrument CheMin and the Sample Analysis at Mars Instrument Suite SAM), Radiation Detectors (the Radiation Assessment Detector RAD and the Dynamic Albedo of Neutrons DAN), Environmental Sensors (the Rover Environmental Monitoring Station REMS) and Atmospheric Sensors (Mars Science Laboratory Entry Descent and Landing Instrument MEDLI).[75] Curiosity has already provided a wide range of results of which here below we give a short summary.

- The REMS instrument has taken measurements of the near surface atmospheric boundary layer temperature, and the Ground Temperature Sensor (GTS) has obtained values for the ground temperature.[76] The results show that the air is warmer than the ground at night and colder than the ground in the morning (Fig. 1.21). REMS has also measured the humidity[77], which is of the order of 2% between -30$^{\circ}$C and -10$^{\circ}$C and of 10% between -80$^{\circ}$C and -60$^{\circ}$C, wind magnitude and direction which are being used to improve the current atmosphere circulation models[78], and the direct and diffuse UV irradiance[79].
- The topography of Gale crater induces local winds of 3-5 m/s that produce a one hour and a half shift of the daily pressure values, which in turn causes variation in the ground temperature measurements.[79] Besides, the solar heating causes a daily global pressure tidal wave that sweeps across the planet.[76,80]
- SAM has measured the composition of the atmosphere (Fig. 1.22).[81] The presence of methane has not been confirmed, thus contradicting previous results.[76]

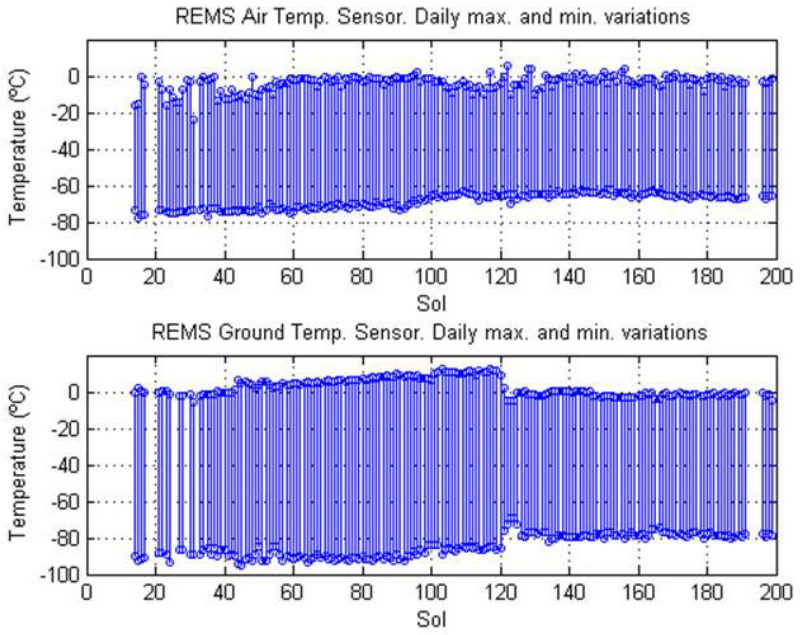


Figure 1.21: REMS ground and air temperature measurements.

Besides, the presence of heavy isotopes suggests that atmospheric loss has occurred in the past.[76]

- SAM and CheMin have analysed the soil chemistry. Predominant crystalline components similar to basalt have been found in Gusev Crater[82], as well as evidence of water, sulphates, carbonates, and potential perchlorates (Fig. 1.23).[76,83]
- RAD has detected galactic cosmic radiation and several solar particle events[76,84] during the orbital transfer (Fig. 1.24) and on the surface (Fig. 1.25). The measured values exceed the maximum safety levels for humans. As shown in Fig. 1.25, a thicker atmosphere can partially shield the surface from radiation.
- The overall data from the rover are also being used to calibrate and validate the data taken by the orbiters.[85]

## 1.2 The models

Several efforts have been made in the past 40 years[86] to model the environment, the atmosphere, the radiative processes, the geological phenomena, etc. of Mars. These efforts have resulted in models that are used to predict the physical conditions on the

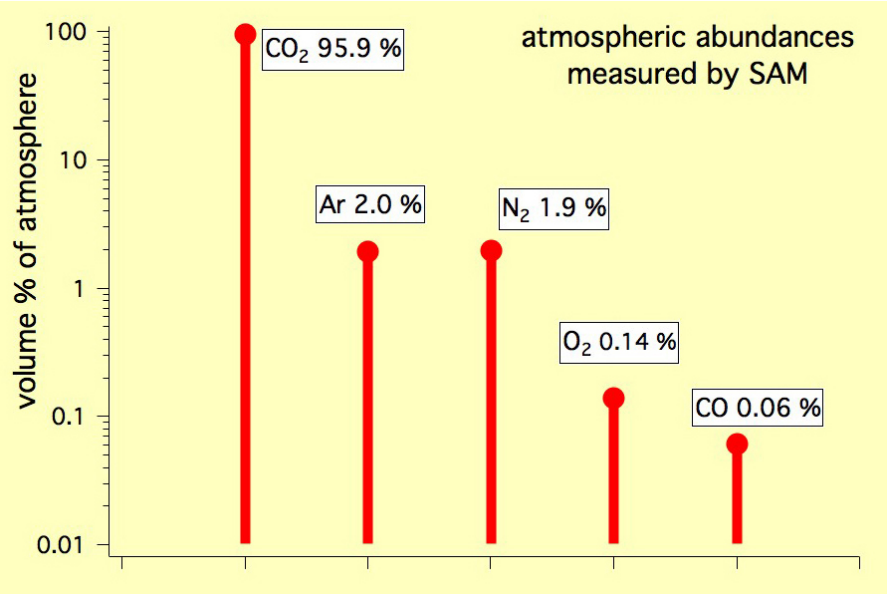


Figure 1.22: Atmospheric abundances by element as measured by SAM.

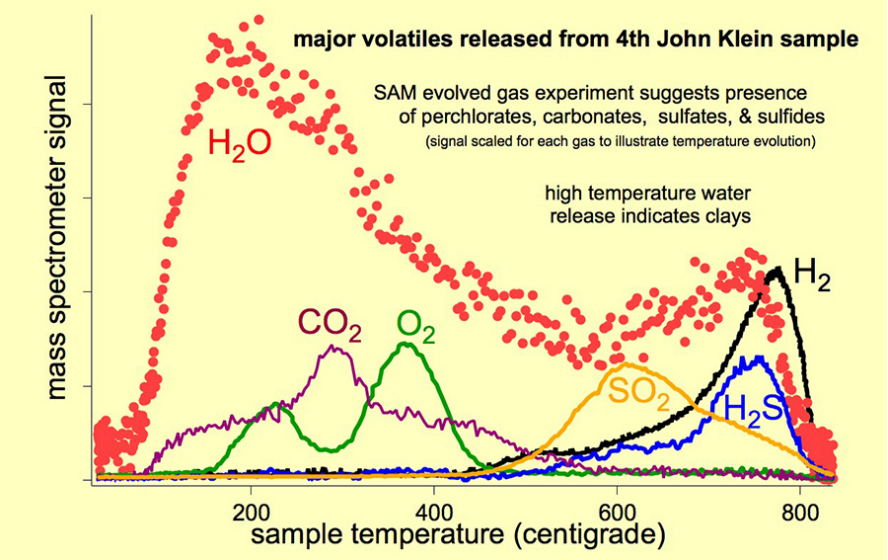


Figure 1.23: SAM chemical analysis of a drilled sample from John Klein rock.

planet. Among their several applications, such models constitute a very useful scientific tool in the design of future exploration missions since they allow to improve the accuracy and thus to reduce the associated risks (e.g., think of the design of entry trajectories). For the purpose of this study, only the models that deal with the environmental and climatic factors have been considered, i.e., those aspects that would influence the design of a greenhouse for operation on the surface of the planet: temperature, atmospheric pressure, atmospheric density, winds, radiative processes, impacts of meteoroids. We now provide a synthesis of the physical contents of those models.

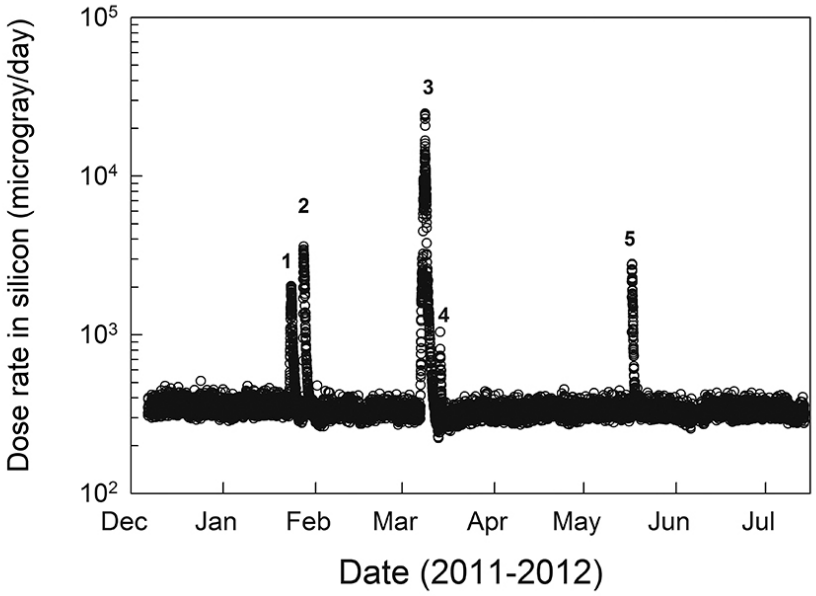


Figure 1.24: RAD measurements during the interplanetary transfer. Five solar events were observed.

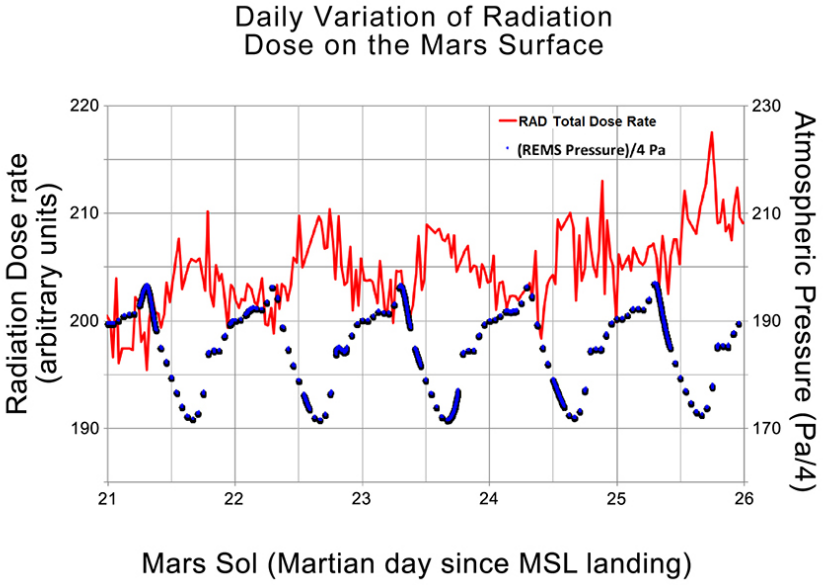


Figure 1.25: RAD measurements on the surface of Mars. The surface is partially shielded from radiation when the atmosphere is thicker (higher REMS pressure).

### 1.2.1 Pollack

The study made by Robert M. Haberle and James B. Pollack[87] aims to obtain the solar irradiance (the electromagnetic energy incident on the unit surface perpendicularly in the unit of time) at the surface of Mars. In general, when a beam of sunlight propagates through an atmosphere, its irradiance $F_{dir}$ is attenuated according to an exponential law that reads as follows:

$$F_{dir} = Se^{-\tau/\nu}, \tag{1.1}$$

where $S$ is the solar irradiance at the top of the atmosphere, $\tau$ is the optical depth, and $\nu$ is the cosine of the zenith angle $z$ of the Sun. $F_{dir}$ is called direct irradiance. However, part of the incoming radiation is scattered by the atmospheric dust and propagates omni-directionally. This scattered component is called diffuse irradiance. The sum of direct and diffuse components is called total or net irradiance.

Pollack[88] modelled the net solar irradiance at Mars as a function of altitude, optical depth, surface albedo and zenith angle. Harbele[87] then extracted the values of the net irradiance at surface level, and produced a three-dimensional table with the irradiance as a function of optical depth, surface albedo and zenith angle. To further simplify the results, Haberle computed a normalized irradiance from the tables corresponding to the albedo values 0.1 and 0.4, and compiled each set of results in a two-dimensional table with the normalized irradiance as a function of optical depth and surface albedo. The normalized irradiance corresponding to any albedo value between 0.1 and 0.4 had to be interpolated. This normalized irradiance is then used to calculate the total solar irradiance $F_{tot}$:

$$F_{tot} = \frac{Sf(\tau, z, A)}{1 - A}. \tag{1.2}$$

Subtracting the direct irradiance calculated with the exponential law (Eq. 1.1) from the total irradiance calculated by Pollack (Eq. 1.2) provides the diffuse irradiance $F_{diff}$:

$$F_{diff} = S\left[\frac{f(\tau, \nu, A)}{1 - A} - e^{-\tau/\nu}\right]. \tag{1.3}$$

As illustrated in Fig. 1.26, the diffuse irradiance cannot be ignored, especially in scenarios in which $\tau$ is high.

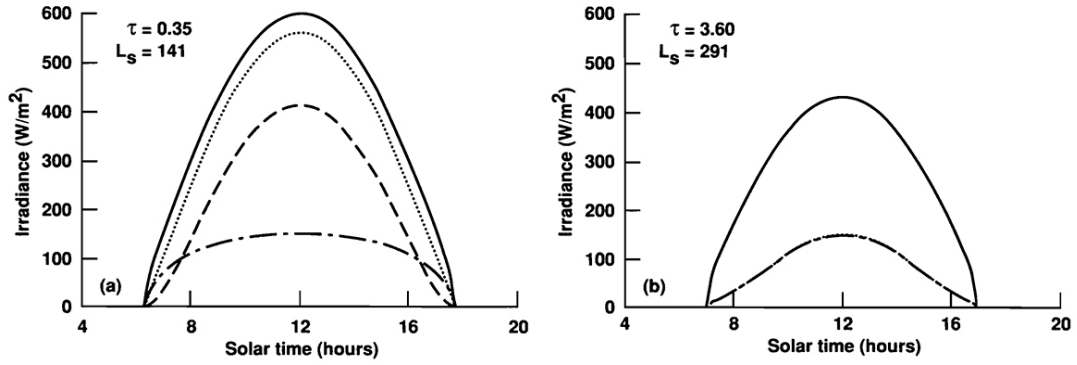


Figure 1.26: Solar irradiance at the Viking Lander 1 site. Summer season with minimal dust (left) and winter season with heavy dust (right). In the two cases, the solid line represents the available irradiance at the top of the atmosphere, the dotted line indicates the total irradiance at surface level, the dashed line refers to the direct irradiance, whereas the solid-dotted line is the diffuse irradiance.

### 1.2.2 Meteors

The Mars Exploration Rovers encountered and identified several meteorite rocks on the surface of Mars.[55] Also, the crater population of Mars indicates a moderate meteor impact history. Thus, an assessment of the possible threat of meteoroid impacts to a future Martian surface facility is required. A wide range of meteoroid models are available in the literature. However, most of them were written for the Earth or, more generally, for distance of 1 AU from the Sun. In this study, only the models dealing with Mars or the Martian orbit are considered.

#### 1.2.2.1 The model of Dycus

Robert D. Dycus[89] proposed a model to estimate the meteoroid flux at the surface of Mars. The meteoroid flux in the Solar System can be modelled using the following mass flux:

$$N_{DS} = km^s, \tag{1.4}$$

where $m$ is the mass of the meteoroid and $k$ and $s$ are parameters adjusted on experimental measurements of meteorite fall, asteroid databases, and Lunar and Martian crater data. $N_{DS}$ constitutes the deep-space flux, i.e., valid far from the planets. A specialized form of Eq. 1.4 describes the meteoroid flux $N_{DSe}$ near the ecliptic plane,

where most of the planets reside:

$$\log N_{DSe} = -18.97 + 4.44r - 0.89r^2 - 0.8 \log m, \tag{1.5}$$

where $r$ is the distance from the Sun in AU, m is expressed in grams, and the flux is given in [$\#$ m$^{-2}$ s$^{-1}$].

The presence of a massive body like a planet modifies the meteoroid flux locally: the planet's gravitational field attracts the meteoroids, thus producing an enhancement of the flux in its vicinity. This effect is called *planet focussing*. On the other hand, the planet also geometrically shields the incoming flux, which results in a reduction of the flux. This effect is called *geometrical shielding*. The combined effects of planet focusing and geometrical shielding can be expressed by the following factor:

$$I = 1 + \frac{2GM}{RV_p^3}. \tag{1.6}$$

Here, $M$ is the planet's mass in $kg$, $R$ is the effective capture radius (sum of the equatorial planet radius and the atmosphere scale height) in km, and $V_p$ is the planetocentric velocity of the object, in $km\ s^{-1}$. The factor $I$ for the case of Marts ($I = 1.6$) is then introduced in the deep-space flux $N_{DSe}$ to yield the meteoroid flux $N_e$ on top of the Martian atmosphere, at Mars' mean distance from the Sun ($r = 1.52AU$):

$$\log N_M = -14.08 - 0.8 \log m. \tag{1.7}$$

Then, the flux at the surface is obtained by numerical integration through the atmosphere taking into account the rate of mass loss $dm/dt$ and the deceleration $dv/dt$:

$$\frac{dm}{dt} = (-\lambda A/2\psi)(m/\rho_m)^{2/3}\rho_a^{v^3} \tag{1.8}$$

$$\frac{dv}{dt} = -(\Gamma A/\rho_m^{2/3} m^{1/3})\rho_a^{v^2} \tag{1.9}$$

where $\lambda$ is the heat transfer coefficient, $\psi$ is the heat of ablation of the meteoritic material, $A$ is the dimensionless shape factor, $\rho_m$ is the atmospheric density, $v$ is the meteoroid velocity, and $\Gamma$ is the drag coefficient. The model used to calculate the properties of the atmosphere is based on data from the Mariner 4 mission. The results indicate complete deceleration to terminal velocity for bodies less massive than of 10 g, various

METEORITE MASS LOSS AND DECELERATION IN THE MARTIAN ATMOSPHERE*

| Mass at Top of Atmosphere (gm) | Calculated Mass Reaching Surface (gm) | Calculated Surface Impact Velocity (km/sec) |
|---|---|---|
| $10^{10}$ | $9.96 \times 10^{9}$ | 8.18 |
| $10^{9}$ | $9.91 \times 10^{8}$ | 8.16 |
| $10^{8}$ | $9.81 \times 10^{7}$ | 8.10 |
| $10^{7}$ | $9.60 \times 10^{6}$ | 8.00 |
| $10^{6}$ | $9.19 \times 10^{5}$ | 7.77 |
| $10^{5}$ | $8.45 \times 10^{4}$ | 7.28 |
| $3.16 \times 10^{4}$ | $2.51 \times 10^{4}$ | 6.87 |
| $10^{4}$ | $7.39 \times 10^{3}$ | 6.29 |
| $3.16 \times 10^{3}$ | $2.17 \times 10^{3}$ | 5.49 |
| $10^{3}$ | $6.44 \times 10^{2}$ | 4.42 |
| $3.16 \times 10^{2}$ | $1.97 \times 10^{2}$ | 3.10 |
| $10^{2}$ | $6.20 \times 10^{1}$ | 1.66 |
| $3.16 \times 10^{1}$ | $1.96 \times 10^{1}$ | 0.43 |
| $10^{1}$ | $6.20 \times 10^{0}$ | ** |

*Meteorite entering atmosphere vertically at 8.2 km/sec
**Meteorite completely decelerated to impact at free fall terminal velocity

Figure 1.27: Meteoroid mass loss and deceleration through the Martian atmosphere according to the Dycus model.

levels of deceleration for meteoroids of mass between 10 g and 1 t (metric ton), and little to no deceleration for bodies of larger mass (see Fig. 1.27).

#### 1.2.2.2 The model of Divine

Neil Divine[90] proposed a description of the interplanetary meteoroid population in terms of five distinct populations, each one with separable distributions in particle mass and in orbital inclination, eccentricity, and perihelion distance. These five populations are labelled eccentric, inclined, halo, core, and asteroidal. The model proposed by Divine makes use of classical Keplerian dynamics, and the parameters for mass and orbital distributions are adjusted with experimental data from radar, the zodiacal light, and fluxes from impact detectors aboard the Pioneer 10 and 11, Helios 1, Galileo, and Ulysses spacecraft.

A specific[91] application of the model to the orbit of Mars yields the following equation to calculate the meteoroid flux ($F_d$) at the perihelion:

$$\log(F_d) = a + b\ \log m + c\ (\log m)^2 + d\ (\log m)^3 + e\ (\log m)^4 + f\ (\log m)^5 \qquad (1.10)$$

where $a = -14.187$, $b = -1.3164$, $c = 4.1347\ 10^{-3}$, $d = -1.3871\ 10^{-2}$, $e = -8.1004\ 10^{-3}$, $f = -7.9186\ 10^{-4}$, and $m$ is the meteoroid mass in [g].

#### 1.2.2.3 The model of Bland and Smith

P. A. Bland and T. B. Smith[92] have modelled the accumulation of meteorites on the surface of Mars. The model calculates the survivability of meteoroids, calculated as the ratio between the objects entering the atmosphere and the objects reaching the surface with a final mass greater than a specific value and below a given impact speed (due to an excessive impact speed, most of the meteorite material would vaporize). A single-body meteoroid simulation integrates the trajectory through the atmosphere taking into account the effects of drag and ablation (mass loss without fragmentation). The results show that a small range of meteoroids, those with masses between 20-50 grams, could enter the atmosphere and decelerate to a speed lower than 1.6 km $s^{-1}$ (their survival speed), impacting the surface without vaporizing. However, given the initial flux of 440-1760 meteorites per $10^6$ $km^{-2}$ $year^{-1}$ at the top of the atmosphere, only 10% are actually able to impact at survival speeds and conserve at least 10 grams of mass intact.

#### 1.2.2.4 The model of McNamara and Suggs

H. McNamara, R. Suggs et al.[93] created a physics-based sporadic meteoroid model called Meteoroid Engine Model (MEM). The sporadic meteoroid flux consists in a diffuse distribution of meteoroids of cometary or asteroidal origin. This diffuse flux constitutes a continuous threat to spacecraft, unlike the regular meteoroid showers that last for short periods of time. The MEM calculates the sporadic meteoroid flux and its directionality between 0.5 AU and 2.0 AU. The model includes the generation of new meteoroids from natural sources (comets, asteroids), and the resulting velocity distributions are validated with experimental observations. The model is oriented to help in the design of spacecraft structures and impact damage evaluation. The model provides the meteoroid flux and the impact speed at the surface of an arbitrary cubic object, as shown in Fig. 1.28.

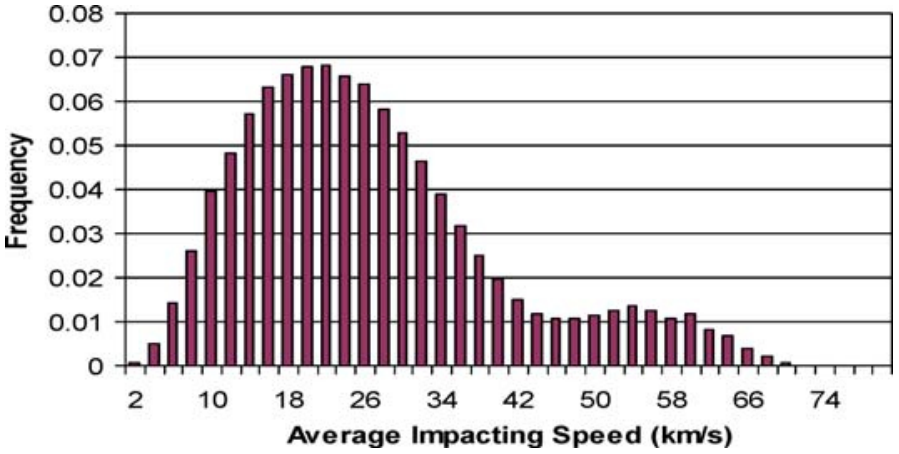


Figure 1.28: Speed distribution of $10^{-6}$ grams meteoroids at 1 AU.

### 1.2.3 MarsGRAM

The Mars Global Reference Atmospheric Model (Mars-GRAM)[94] models the properties of the atmosphere of Mars (temperature, pressure, density, winds, and others). MarsGRAM interpolates data tables built on mathematical models and experimental measurements. The data tables provide daily average values for each atmospheric parameter, as well as the amplitudes and phases of their diurnal and semi-diurnal wave components. These values are then used as parameters in the so-called *tidal equation* which provides the tide $T$ as

$$T = A_0 + A_1 \cos\left[\frac{\pi}{12}(t - \phi_1)\right] + A_2 \cos\left[\frac{\pi}{6}(t - \phi_2)\right] \tag{1.11}$$

where $A_0$ is the daily average and $A_1$, $A_2$, $\phi_1$ and $\phi_2$ are the diurnal and semi-diurnal amplitudes and phases, respectively. $t$ is time.

The first MarsGRAM versions were based on parametrizations of the data collected by the Mariner and Viking missions. Later versions were improved with the results from the NASA Ames Mars General Circulation Model[95] (MGCM) for altitudes between 0 and 80 km, and the University of Arizona Mars Thermospheric General Circulation Model[96] (MTGCM) for higher altitudes. The MGCM and MTGCM are global-circulation models based on atmospheric thermodynamics and atmospheric circulation. They are being constantly updated by fitting to the data from later missions to Mars (currently Mars Pathfinder and Mars Global Surveyor, up to year 2006). MarsGRAM has been used in mission design applications such as in the computation of the aerobraking manoeuvres

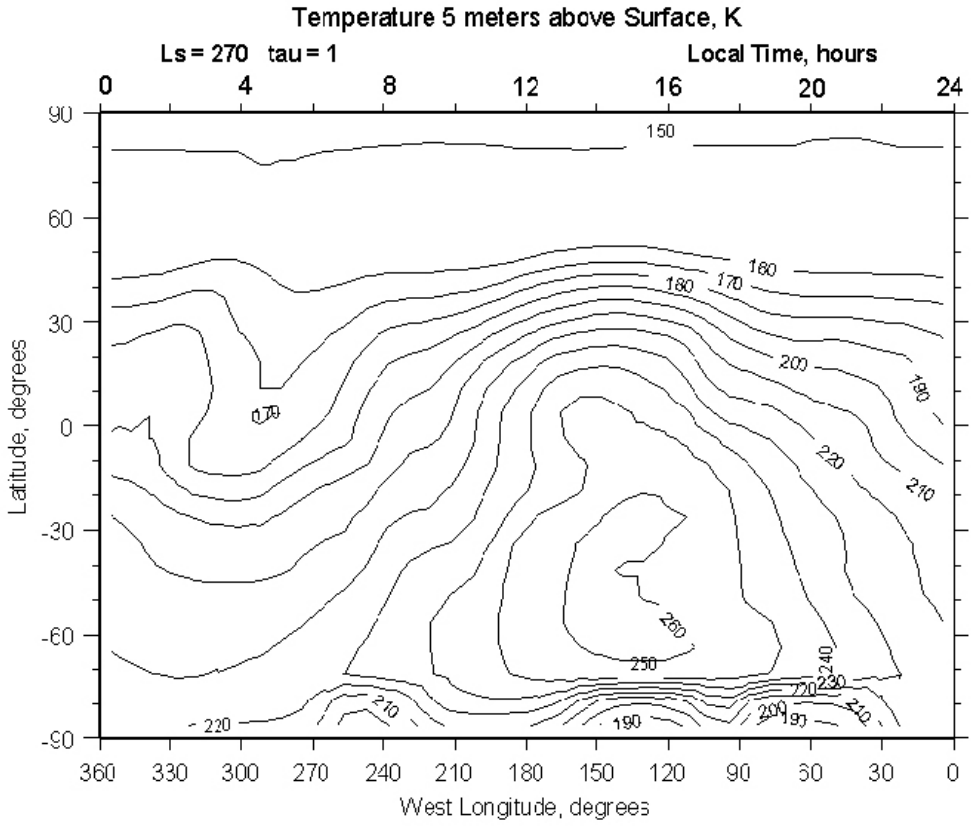


Figure 1.29: MarsGRAM: distribution of temperatures 5 m above the surface.

of Mars Global Surveyor, in the prediction and validation of Mars Pathfinder hypersonic aerodynamics, and in studies of the aerothermodynamic entry of Mars Polar Lander.[94] As an example, Fig. 1.29 shows the distribution of temperatures 5 m above the surface.

MarsGRAM also includes several auxiliary modules which allow the computation of trajectory input profiles, radiation-related quantities, and several time conversion routines. Two of these modules, i.e., MarsRAD and FindDate, are discussed below due to their relevance in this context.

#### 1.2.3.1 MarsRAD

MarsRAD is an auxiliary program of MarsGRAM. It computes solar (i.e., shortwave) and planetary thermal (i.e, longwave) irradiation at the surface and on top of the atmosphere. Shortwave fluxes are computed with a delta-Eddington method[97] using total

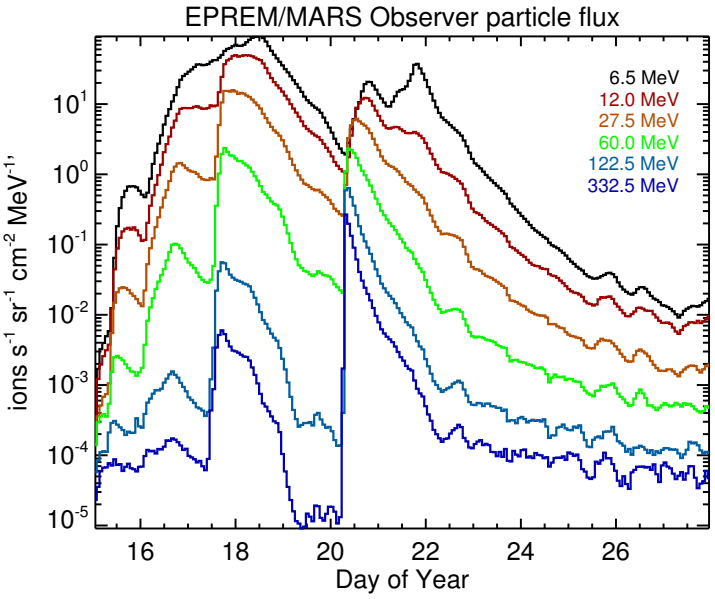


Figure 1.30: EMMREM: simulated ion intensities at different energies. The simulations refer to the year 2005 at Mars orbit.

dust optical depth values, whereas longwave fluxes are computed with a broad-band (emissivity) method[98] using the infrared emissivities of $CO_2$ and water vapour.

#### 1.2.3.2 FindDate

FindDate is an auxiliary program of MarsGRAM. It calculates the calendar date corresponding to a given longitude $L_s$ of the Sun and a given local true solar time LTST at Mars. The algorithm determines $L_s$ based on an arbitrary initial date, then propagates the Martian orbit with a value of true anomaly equal to the difference between the calculated $L_s$ and its target value. The new position gives a new value of $L_s$, and the process is repeated until convergence (for a selected tolerance on $L_s$). The final orbital position is iterated again so that LTST for a given solar longitude coincides with the target value.

### 1.2.4 EMMREM

The Earth-Moon-Mars Radiation Environment Module (EMMREM) is a software that aims to model the Earth-Moon-Mars and Interplanetary space radiation environment.[99] EMMREM returns radiation dose exposure values, as illustrated in Fig. 1.30. The code makes use of several already existing models, specifically:

- the BRYNTRYN (Baryon Transport) code[100] developed at NASA, which simulates charged proton particles through a shielding surface (it was developed to study the effects of cosmic radiation on astronauts, mainly due to SEPs (Solar energetic particles)).
- the HZETRN (High-Charge-and-Energy (HZE) Transport) code[101] developed at NASA, which uses a one-dimensional simplification of the Boltzmann transport equation to obtain radiation dosimetry.
- the HETC-HEDS (High Energy Transport Code – Human Exploration and Development in Space) Monte Carlo code[102] developed at Oak Ridge National Laboratory and the University of Tennessee, which simulates particle cascades to determine the trajectories of all the primary and secondary particles produced in a nuclear collision.

Additionally, EMMREM uses experimental observations (ISS/STO for Earth scenarios, LRO/CRaTER for Lunar scenarios, and MSL/RAD and Odyssey/MARIE for Mars scenarios) to reduce the uncertainty of the simulated results.

# Chapter 2

# The Mars Environment Multi-Model

In this chapter, the Mars Environment Multi-Model (MEMM) is illustrated in detail. MEMM integrates and merges several existing models in one scientific and engineering tool. Section 2.1 introduces and explains the model in general. The physical quantities that it provides are illustrated in Sect. 2.2, together with the input and output parameters required by each of the constituent models. Sect. 2.3 deals with the implementation of MEMM, including the description of auxiliary routines. An overview of the physical output of MEMM is provided in Sect. 2.4.

## 2.1 Introduction

MEMM is a macro-model that merges a number of existing models of the Martian environment. MEMM is a global scientific tool that provides the user with a set of physical quantities. The model currently computes the following parameters:

- atmosphere: temperature, pressure, density, concentration of components, wind speed;
- surface: ground temperature, albedo, polar ice, dust optical depth, altitude of local surface with respect to the *datum* (the elevation at which the atmosphere pressure is 610 Pascals);

- positioning: Mars orbital radius, areocentric longitude of the Sun from Mars, local true solar time, solar zenith angle, azimuth and elevation of the Sun from a user-defined tilted plane;
- radiation: longwave flux, shortwave flux, equivalent sky temperature, planetary albedo, atmosphere heating rates;
- meteoroid flux at the top of the atmosphere;
- thermodynamic properties of $CO_2$: specific heat, dynamic viscosity, heat convection coefficient.

MEMM was originally conceived as part of the study of the Martian environment for the design of a greenhouse. In other words, MEMM shall be used to provide quantitative information about the thermodynamic feasibility of the design of a greenhouse, with all its implications: site choice, most favourable season, best epoch, restrictions, risks and uncertainties. However, the development of the work has gone much further than this: what we have now is a scientific tool that can be employed in many other applications, including studies and designs of future missions to Mars. Therefore, MEMM can be interesting to the global scientific community devoted to the study of Mars.

## 2.2 The physical models

MEMM is built around the idea of modularity. This means that it hosts several independent models and makes them work together as a single cooperative unit. The outputs of one model are used as inputs to others, thus improving the accuracy of the results (e.g., MarsGRAM provides accurate albedo, dust optical depth, and zenith angle values to the Pollack model), or limiting the intrinsic scope of the model to the scenario of interest (e.g., MarsGRAM provides the range of orbital radius of Mars to the Dycus model). In order to ensure the consistency of the results and the performance of the code, we have carried out a selection among many of the available models, in particular those presented in Chapter 1. The eligibility criteria adopted are to provide a description of the Martian environment as complete as possible, without redundancy and by

focussing on the parameters of interest to us: atmospheric temperature, pressure, density and winds speed, solar and planetary electromagnetic radiation, particle radiation, surface composition, and meteoroid fluxes.

The implemented models provide a complete description of the atmospheric characteristics, the solar and thermal radiation environment, and the meteoroid flux. Unfortunately, no models of the Martian soil have been found, and the EMMREM code was unavailable when this project was carried out. Further work on these aspects should be made in preparation for an upgraded, future version of MEMM. However, provisional results for the soil composition and the particle radiation environment are adopted, respectively, from the TES instrument (MGS mission) and from MSL/Curiosity. An overview of the implemented models as well as their flow of input and output data are given below.

### 2.2.1 MarsGRAM

MarsGRAM evaluates the atmosphere of Mars and returns the temperature, density, pressure, wind intensity and direction, chemical composition and concentration, dust properties, and several orbital parameters of Mars. MarsGRAM has been selected as a model for MEMM because it provides the most complete description of the Martian atmosphere to date, and therefore it constitutes a scientific and engineering reference. Additionally, the fact that the outputs can be used as inputs to the majority of the other models turns MarsGRAM into the main component of MEMM.

MarsGRAM requires an extensive set of inputs and configuration parameters, namely:

- Date (Year, Month, Day, Hour, Minute, Seconds), in Mars-event time (date/time of an event on Mars) or Earth-Receive time (date/time once the information from the event on Mars has travelled back to Earth), and as Coordinated Universal Time (UTC) or Terrestrial (Dynamical) Time.
- Optical depth of the background dust, as well as its minimum and maximum seasonal values.
- Dust particle diameter [$\mu$m] and density [kg m$^{-3}$].

- Dust storms: solar longitude $L_s$ [°] at beginning of storm, duration [°] in $L_s$, intensity (in terms of dust optical depth), radius [km], latitude [°] and longitude [°] of the centroid.
- Data set used to perform the simulations (MarsGRAM 2001 GCM dataset, or TES mapping year 1 and 2 datasets).
- 10.7 cm solar flux at 1 AU [$10^{-22}$ W cm$^{-2}$].
- Observer's latitude [°], longitude [°] and altitude [km].
- Equatorial and Polar radius [km] of the reference ellipsoid.

Additionally, MarsGRAM makes use of several external databases that contain topographic models, albedo and dust opacity values, and the simulated data from the MGCM and MTGCM models (see Sect. 1.2.3).

MarsGRAM writes the results into a number of text files in tabulated format. The number of outputs of each simulation can vary according to the user configuration. The most complete list of outputs that can be extracted from the model is:

- Atmosphere:
  - mean temperature, in [K] and [°C],
  - mean pressure, in [N m$^{-2}$] and [mb],
  - pressure scale height [km],
  - density (total, daily average, daily minimum and daily maximum values) [kg m$^{-3}$],
  - density scale height [km],
  - mole fraction of atmospheric components ($CO_2$, $N_2$, Ar, $O_2$, CO, He, $H_2$, H and $H_2O$) [% by volume],
  - mass fraction of atmospheric components ($CO_2$, $N_2$, Ar, $O_2$, CO, He, $H_2$, H and $H_2O$) [% by mass],
  - local daily average temperature [K],
  - local daily average pressure [N m$^{-2}$],
  - local daily average density [kg m$^{-3}$],

  - local daily minimum and maximum temperature [K],
  - local daily minimum and maximum density [kg $m^{-3}$].

- Dust:
  - dust optical depth,
  - dust column areal density [kg $m^{-2}$],
  - dust mixing ratio [kg dust $kg^{-1}$ air],
  - dust mass density [$\mu$g dust $m^{-3}$],
  - dust number density [number of dust particles $m^{-3}$].

- Ground:
  - ground (soil) surface temperature [K],
  - surface albedo,
  - surface polar ice indication (presence or absence of surface ice),
  - altitude of local surface above MOLA 1/2-degree areoid [km].

- Winds:
  - eastward wind speed (total, mean and perturbed values) [m $s^{-1}$],
  - northward wind speed (total, mean and perturbed values) [m $s^{-1}$],
  - vertical wind perturbation [m $s^{-1}$],
  - local daily average of the eastward wind speed [m $s^{-1}$],
  - local daily average of the northward wind speed [m $s^{-1}$].

- Others:
  - solar zenith angle [°],
  - local gravitational acceleration [m $s^{-2}$],
  - radial distance from planet's center of mass to observer's position (areoid radius plus altitude) [km],
  - Mars orbital radius [AU],
  - areocentric longitude of the Sun with respect to Mars [°],
  - local true solar time [Mars hours].

### 2.2.2 MarsRAD

MarsRAD evaluates the solar and thermal radiation environment of Mars, and returns the shortwave (SW: wavelengths 0.1-10$\mu$m from solar origin) and longwave (LW: wavelengths 10-1000$\mu$m from planetary, solar and atmospheric origin) fluxes at the surface and on top of the atmosphere, the heating rates at the surface and the sky temperature. MarsRAD has been selected as a model for MEMM because it gives the total solar and thermal radiation fluxes at the surface.

MarsRAD originally gets its inputs from several of MarsGRAM's output files, although not all the extracted values are effectively used. The specific inputs required by MarsRAD are:

- atmospheric mean temperature [K],
- atmospheric mean pressure [N m$^{-2}$],
- ground surface temperature [K],
- dust optical depth,
- local acceleration of gravity [m s$^{-2}$],
- Mars orbital radius [AU],
- surface albedo,
- cosine of solar zenith angle,
- dust mixing ratio [kg dust kg$^{-1}$ air],
- surface polar ice indicator.

MarsRAD also writes the results into tabulated text files. The physical quantities that can be obtained from the results are the following:

- downwelling LW flux at the surface [W m$^{-2}$],
- upwelling LW flux at the surface [W m$^{-2}$],
- upwelling LW flux at the top of the atmosphere [W m$^{-2}$],

- LW flux emitted by the atmosphere [W $m^{-2}$],
- downwelling SW flux at the surface [W $m^{-2}$],
- upwelling SW flux at the surface [W $m^{-2}$],
- upwelling SW flux at the top of the atmosphere [W $m^{-2}$],
- net SW flux absorbed by the atmosphere [W $m^{-2}$],
- solar flux at the top of the atmosphere [W $m^{-2}$],
- planetary albedo,
- equivalent sky temperature [K],
- ground surface temperature [K],
- effective black-body temperature at the top of the atmosphere [K],
- downwelling SW+LW flux absorbed at the surface [W $m^{-2}$],
- upwelling SW+LW flux at the top of the atmosphere [W $m^{-2}$],
- diffuse transmittance for diffuse irradiance,
- diffuse transmittance for beam irradiance,
- beam transmittance,
- LW, SW and total (LW+SW) heating rate values at the surface [W $m^{-2}$ $s^{-1}$].

### 2.2.3 Pollack

The model by Pollack deals with the solar electromagnetic radiation. It has been included in MEMM as a supplement to MarsRAD since the latter only provides the total flux, whereas Pollack outputs the direct and diffuse components as well. Tests have been executed in order to ensure compatibility between the two models.

In order to solve the physical equations, Pollack requires the following input:

- areocentric longitude of the Sun with respect to Mars [°],

- solar zenith angle [$^\circ$],
- dust optical depth,
- surface albedo.

Additionally, the model makes use of two tables that contain the normalized solar flux as a function of dust optical depth, solar zenith angle, and surface albedo. The output consists in:

- solar direct flux at the surface [W m$^{-2}$],
- solar diffuse flux at the surface [W m$^{-2}$],
- solar total (direct + diffuse) flux at the surface [W m$^{-2}$],
- solar ground (upwards) flux at the surface [W m$^{-2}$].

### 2.2.4 Meteoroids

Two models have been selected for implementation in MEMM, i.e., the model due to Dycus and that published by Divine. Other models were available, but their inclusion in the code would have required a commitment that was judged beyond the scope of the present project. The Dycus model dates back to the year 1969, it is a simplified model (for example, it assumes an unrealistic omnidirectional diffuse flux), and it is based upon experimental measurements that are outdated. As part of the integration into MEMM, the Dycus model has been modified as explained in Sect. 2.3.4: instead of integrating the meteoroid trajectory through the atmosphere, only the flux at the top of the atmosphere is considered. The reason is that any meteoroid hitting the atmosphere is potentially dangerous (in particular, to the greenhouse), thus MEMM must provide the (full) incoming flux of meteoroids. An important extension of the Dycus model is the determination of the meteoroid flux as a function of distance from the Sun, and the application of the corrections for gravitational focussing and geometrical shielding due to the planets. This upgrade converts the modified Dycus model into a general model valid for all the Solar System, capable of computing the meteoroid flux in deep space (i.e., far from the planets) and in the vicinity of the planets. The input required by the modified version of Dycus are:

- the asteroid mass [g],
- the distance from the Sun [AU],
- the planet's mass [kg],
- the planet's equatorial radius [km],
- the planet's atmospheric scale height [km].

The user is left the option to ignore the parameters related to the planet (i.e, mass, equatorial radius and atmospheric scale height) in which case the code returns the deep space flux. The output of the modified model is the meteoroid flux on top of the atmosphere (or in deep space if required) [$m^{-2}$ $s^{-1}$].

The model by Divine is built on a much longer data span (up to 1993) which lends it a higher accuracy than in the previous case. This model has been improved in MEMM by taking into account the real distance from the Sun as described in Sect. 2.3.5. Furthermore, the velocity of the meteoroid has been included in the calculations. The required input consists in:

- the asteroid mass [g],
- the distance from the Sun [AU].

The output is the meteoroid flux hitting the atmosphere [$m^{-2}$ $s^{-1}$] and the approximated meteoroid speed relative to Mars [km $s^{-1}$].

We recall that both models deal with omnidirectional fluxes. A future improvement of MEMM should include a more realistic treatment of this issue.

## 2.3 The implementation

The models that compose MEMM are written in Fortran. They have been compiled into MEX modules to be used by Matlab. This choice, on the one hand, benefits from the high performance of the compilation in Fortran, and from the convenience of the Matlab environment, on the other. The latter is especially useful in the pre- and post-processing phases.

Each model is a stand-alone function and can be executed independently. However, several scripts have been prepared to automatically link each model with the others in order to provide the required inputs and handle/organize the outputs.

The implementation of MEMM is not a mere compilation of existing codes: a careful analysis was carried out on the original modules which resulted in the application of corrections, improvements and modifications. As a whole, a large amount of preparatory work lies at the foundations of MEMM. This effort is illustrated separately for each model in the following subsections.

### 2.3.1 MarsGRAM

MarsGRAM is freely distributed by NASA upon request as Fortran source code. It is designed to be executed as a stand-alone program that requires a series of inputs via command prompt, reads the simulation parameters from a text file and writes the output to a series of text files. The implementation into MEMM has required an extensive conversion towards automatic operation. However, we emphasize that the corresponding changes have been applied with the minimum interference with the original code. In this way, the code behaves inside MEMM like it did in its previous form. This guarantees stability, while at the same time it allows to easily track the changes and to quickly upgrade the model with a new release.

The most critical modification has been the suppression of the input command prompts. Currently, the code runs without any prompt-type interruption because all inputs are either provided by the Matlab script or hard-coded. The input/output flow is now handled through an external module which has a program-global scope. This global module contains a mirrored copy of the variables from the input text file and the variables from the output text files. The input variables are collected from the Matlab workspace into the global module, and then the values are translated into MarsGRAM's internal variables at the point of the input reading. Similarly, the values of the internal variables which were written into the output files are now copied into the global module at the end of the program, and then fed back to the Matlab workspace. This ensures that absolutely no additional flow exists across the original MarsGRAM subroutines, thus minimizing the risk and leaving the code as clean as possible.

The error-type program interruptions (i.e., STOP) have been left as they were, although the proper way of handling them should be to return the execution control to Matlab with a specific error code, instead of force-terminating the whole environment. Also, the code does not currently check for validity and internal consistency of the input data; if the data is non-consistent, the program crashes. Further work on these aspects is encouraged in future versions of MEMM.

### 2.3.2 MarsRAD

Being an auxiliary program of MarsGRAM, MarsRAD is also distributed as Fortran source code. The code was designed to read the input from some of MarsGRAM's output text files and write the results in more text files. As in MarsGRAM, the integration into MEMM has been made without altering the structure of the code. All the prompts have been suppressed or hard-coded. The same strategy involving the usage of a global scope module to store all the required input/output variables has been applied. In this case, however, a further set of physical variables (i.e., the heating rates) is added to the original output.

### 2.3.3 Pollack

The original Pollack/Harbele model (see Sec. 1.2.1) uses a series of albedo-dependent tables to interpolate the value of the normalized solar irradiance as a function of the solar zenith angle and the dust optical depth. This discretized information is handled by a routine of MEMM that linearly interpolates in three-dimensions, thus turning the solar irradiance into a function of three parameters, namely the solar zenith angle $z$, the dust optical depth $\tau$ and the surface albedo $a$. Furthermore, the off-bounds values for $z$ and $\tau$ have been limited in order to avoid potential errors: for example, if the input value exceeds a limit, it is set at that limit. As an additional safety measure, if the input value for the solar azimuth angle exceeds $90^{\circ}$, the value for the total irradiance is manually set at $F_{tot} = 0$ [W m$^{-2}$] (i.e., night-time). Note that the linear interpolation suffers from an intrinsic low accuracy. Implementing high-order interpolation methods should be considered. The algorithm implements Pollack's[87] model equations.

### 2.3.4 Dycus

The original Dycus model described in Sect. 1.2.2.1 is valid for the orbit of Mars. During the implementation in MEMM, it has been extended to provide general results valid for the entire Solar System, both far from the planets (i.e., in deep space) and in their vicinity (i.e., including corrections for geometrical shielding and gravitational focussing). Note that the original model has an intrinsic low accuracy, which means that its output should be handled with care. Let us consider Eq. (1.5) which describes the meteoroid flux near the ecliptic plane, and Eq. (1.6) that gives the focussing and shielding factors for a planetary body. Combining the two equations yields the meteoroid flux near the ecliptic plane and under the influence of the planet:

$$\log N_e = -18.97 + 4.44r - 0.89r^2 - 0.8 \log m + \log I \tag{2.1}$$

The factor $I$ is a function of the magnitude of the mean unperturbed planetocentric orbital velocity $V_{p_r}$ [km s$^{-1}$] of the meteoroids at the given heliocentric distance $r$. Such velocity accounts for the kinematics of the meteoroids as if the planets did not perturb their motion. It is obtained by means of a $r^{-1/2}$ dependence from the heliocentric distance $r$:

$$V_{p_r} = \frac{V_{p_0}}{\sqrt{r}}, \tag{2.2}$$

where $V_{p_0} = 8.0$ [km s$^{-1}$] is the mean unperturbed planetocentric orbital velocity at 1 AU.

For the meteoroid flux in deep space (i.e., far from the influence of a planet) $I$ = 1, which makes the last term in the sum of Eq. (2.1) disappear ($\log(1.0)$=0). Then, the result is converted to absolute magnitude $N$ [m$^{-2}$ s$^{-1}$]:

$$N = 10^{N_e}. \tag{2.3}$$

### 2.3.5 Divine

The original model by Divine has also been modified to provide results for any position of Mars in its orbit. However, the algorithm does not provide a functional dependence of the flux from the heliocentric distance: it gives the value at perihelion and estimates that

it is 25% lower than the flux at aphelion. A simple linear interpolation has been applied to estimate the correction factor $d_f(r)$ to approximate the flux at any other distance $r$ (in AU):

$$d_f(r) = 1.0 - 0.25 \left( \frac{r - r_\pi}{r_\alpha - r_\pi} \right), \tag{2.4}$$

where $r_\alpha$ = 1.665861 AU is the aphelion radius and $r_\pi$ = 1.381497 AU is the perihelion radius. Eventually, the flux $F(r)$ is obtained according to Eq. (1.10) and corrected by $d_f(r)$:

$$F(r) = d_f(r) F_d. \tag{2.5}$$

Note that using a linear interpolation in a non-linear model induces an approximation error, although this error should never exceed the difference between the values at the perihelion and aphelion. Further work on this issue belongs to the future improvements of MEMM.

Eventually, the speed of the meteoroid relative to Mars $v$ [km s$^{-1}$] is approximated by:

$$v = 0.010775 \exp(-0.866 \log m) + 9.63, \tag{2.6}$$

where $m$ is the meteoroid mass in [g].

### 2.3.6 Pre-processing functions

Several functions are required in order to prepare and organize the input for a simulation with MEMM. Most of them are date conversion functions (for example, from Martian sols to Earth days). When organizing the content for this report we judged that the most standard functions did not deserve space in the present chapter and that the most appropriate location for their description was the user manual. An exception to this is the algorithm to compute the Julian date given the longitude of the Sun (which is an expression of the position of Mars in its orbit) due to its wide application and usefulness. The corresponding function is illustrated here below.

#### 2.3.6.1 Determination of the Julian date

It is sometimes useful to define the initial date of a simulation by means of an arbitrary value for the longitude of the Sun (i.e., the position of Mars in its orbit). A set of auxiliary functions have been implemented to provide such functionality to MEMM.

The Mars Climate Database Projects[103] provides an algorithm which first computes the Julian day corresponding to a given Martian Year (based on an arbitrary convention proposed by R. Todd Clancy[104]); then, the number of sols corresponding to the input solar longitude $L_s$ is added to the Julian day which is eventually converted into a calendar date (year, month, day, hours, minutes, seconds). The problem with this algorithm is its extremely low precision because it does not account for mid and long-term orbital perturbations. As a consequence, the equations must be constantly adjusted manually to prevent wrong settings of the year when $L_s$ is close to 0° or 360°. This has been considered unacceptable for MEMM and the algorithm has been rejected.

The option chosen has consisted in translating into Matlab scripts the internal routines of MarsGRAM. This allows to achieve the same precision as MarsGRAM and to avoid discrepancies with MarsGRAM's own internal calculations. The algorithm develops through two routines:

- the computation of the Julian day corresponding to a given calendar date (CAL2JD),
- the computation of the solar longitude $L_s$ corresponding to a given Julian day (JD2LS).

In practice, the Julian day $JD_{ref}$ corresponding to the Mars Year 1 is determined first. Then, the Julian day $JD_0$ corresponding to the required Mars Year $MY$ is obtained through

$$JD_0 = (MY - 1)t_y + JD_{ref}, \tag{2.7}$$

where $t_y$ is the duration of the Martian tropical year [days] ($t_y = 686.9725 days$). The zero of the difference between the solar longitude computed with the obtained Julian day and the target solar longitude is sought iteratively by using $JD_0$ as initial guess. Upon convergence, the Julian date $JD$ is converted to calendar date.

At a later stage, one of MarsGRAM's specialized routines has been incorporated as a MEX module to improve the previous computation and provide an additional piece of information, i.e., the local true solar time at a given geographical longitude. As a whole, the routine performs the following operations:

1. computes the Julian day $JD$ from an input calendar date using CAL2JD;
2. finds the corresponding solar longitude $L_s$ by means of JD2LS;
3. iterates on $JD = JD + q \times \Delta L_s$, where $q$ equals the Martian tropical year [days]/360° and $\Delta L_s$ is the difference between the current computed $L_s$ and the target value;
4. iterates on the local time at the specified longitude;
5. converts $JD$ into a calendar date.

### 2.3.7 Post-processing functions

The raw output of MEMM needs further treatment in order to provide the physical quantities that are required for a complete environment and climate model of Mars. This holds especially for the application of the present work, i.e., the definition of the external conditions for the operation of the greenhouse. All the additional physical parameters are computed in the post-processing of MEMM. They can be grouped into the two categories: the thermodynamic properties of the atmosphere and the azimuth and elevation coordinates of the Sun as seen from a user-defined location and orientation (in practice for our purposes, a tilted plane).

#### 2.3.7.1 The thermodynamic properties of the atmosphere

The thermodynamic simulation of the greenhouse requires the following properties of the atmosphere: the convection heat transfer coefficient, the dynamic viscosity and the specific heat. Since the Martian atmosphere is almost entirely composed of $CO_2$ ($> 95\%$ in volume), the properties are assumed to be those of a pure $CO_2$ atmosphere.

The specific heat $c_p$ [J kg$^{-1}$ K$^{-1}$] of $CO_2$ as a function of temperature can be extracted from an interpolated polynomial:

$$c_p = a + bT + cT^2 + dT^3, \tag{2.8}$$

where the parameters are $a$ = 0.564 [J kg$^{-1}$ K$^{-1}$], $b$ = 4.526 $\times$ 10$^{-4}$ [J kg$^{-1}$ K$^{-2}$], $c$ = 2.829 $\times$ 10$^{-6}$ [J kg$^{-1}$ K$^{-3}$], $d$ = -4.053 $\times$ 10$^{-9}$ [J kg$^{-1}$ K$^{-4}$] and $T$ is the temperature in [K]. The polynomial approximation is valid for the temperature range $175K < T < 400K$.

The dynamic viscosity $\mu$ is calculated as:

$$\mu = \mu_0 \frac{a}{b} \left( \frac{T_r}{T_0} \right)^{\frac{3}{2}} \tag{2.9}$$

and the units are centipoise [cP]. In Eq. (2.9)

$$a = 0.555T_0 + C, \tag{2.10}$$

$$b = 0.555T_r + C, \tag{2.11}$$

and the parameters $T_0$, $T_r$ and $C$ are fluid-dependent: for $CO_2$, $C$ = 240, $T_0$ = 527.67 [$R$], $\mu_0$ = 0.01480 [cP]. Note also that $T_r$ is the temperature in degrees Rankine [°R]:

$$T_r = \frac{9}{5}T, \tag{2.12}$$

$T$ being the temperature in Kelvin. The result of Eq. (2.9) can be expressed in Pascals [Pa] by multiplication by 10$^{-3}$.

The equations to be employed for the determination of the convection heat transfer coefficient $h$ must be chosen according to the turbulence (defined by the Reynolds number $Re$) and diffusivity (defined by the Prandtl number $Pr$) of the fluid. $Re$ is obtained from

$$Re = \rho \, v \frac{L}{\mu}, \tag{2.13}$$

where $\rho$ is the density of the atmosphere [kg m$^{-3}$], $v$ is the wind speed magnitude [m s$^{-1}$], $L$ is the reference length of the given object (i.e., the greenhouse) in [m], and $\mu$ is calculated with Eq. (2.9).

$Pr$ is given by:

$$Pr = c_p \frac{\mu}{k}, \tag{2.14}$$

where $k$ is the thermal conductivity of the atmosphere (again under the simplification of being made entirely of $CO_2$), and $c_p$ and $\mu$ are given by Eqs. (2.9) and (2.8), respectively. The $Re$ and $Pr$ numbers are used to compute the Nusselt number $Nu$ which, in the case of a laminar flow ($Re < 3.3 \times 10^5$) is

$$Nu = \begin{cases} 0.5\sqrt{Re \cdot Pr} & \text{if } Pr < 0.1, \\ 0.332\sqrt{Re}\sqrt[3]{Pr} & \text{if } Pr > 0.1. \end{cases} \tag{2.15}$$

The case of turbulent flow is not included in MEMM because the $Re$ number in the atmosphere of Mars (approximately $5 \times 10^4$) is much smaller than the turbulent limit ($3.3 \times 10^5$).

Finally, the convection heat transfer coefficient $h$ [W m$^{-2}$ K$^{-1}$] is computed as:

$$h = k \frac{Nu}{L}. \tag{2.16}$$

#### 2.3.7.2 Azimuth and elevation coordinates of the Sun

As a requirement for the greenhouse model, the azimuth and elevation of the Sun as viewed from a tilted plane (i.e., the walls of the greenhouse) must be calculated. MEMM implements a combination of the algorithms proposed by D.Rapp[105] and Allison[106]. First, the solar declination $\delta$ is computed in degrees [°] as

$$\delta = \sin^{-1}\left(0.42565 \sin L_s\right) + 0.25 \sin L_s, \tag{2.17}$$

where $L_s$ is the aerocentric longitude of the Sun expressed in degrees.

The Solar hour angle $H$ [°] is obtained by

$$H = \lambda - \lambda_s, \tag{2.18}$$

where $\lambda$ is the geographical longitude of the observer and $\lambda_s$ is the geographical longitude of the sub-solar point.

The solar zenith angle $z_t$ when the reference frame is moved to an arbitrary plane (see Fig. 2.1) can be calculated as follows:

$$\cos z_t = \sin\delta \sin(\phi - t_p) + \cos\delta \cos(\phi - t_p) \cos H, \tag{2.19}$$

where $\phi$ is the geographical latitude of the observer and $t_p$ is the plane tilt angle with respect to the horizontal reference (i.e., local horizon).

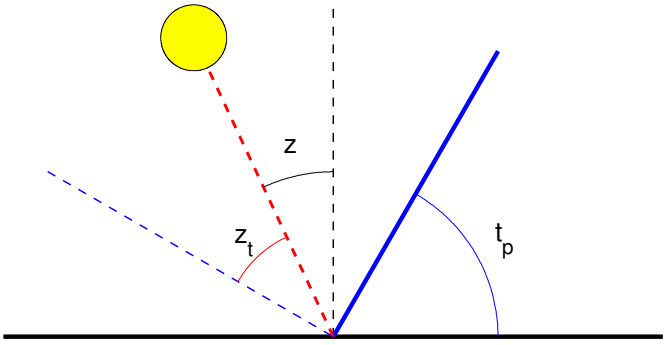


Figure 2.1: Solar zenith angle ($z$) and "tilted" solar zenith angle ($z_t$) when the reference is moved to a tilted plane ($t_p$). Note that this figure is only illustrative and assumes a solar azimuth angle of 0°; the $z_t$ value for an arbitrary azimuth angle is computed as noted in Eq. 2.19.

The elevation $el$ can be computed from Eq. (2.19) as

$$el = \pi/2 - z_t. \tag{2.20}$$

Eventually, the azimuth $a$ is given by

$$\tan a = \frac{\sin H}{\cos\phi \tan\delta - \sin\phi \cos H}. \tag{2.21}$$

### 2.3.8 Output

The results of a simulation with MEMM are stored in a structure, named *RAW* for convenience, the internal structure of which is:

$$RAW.model.group.variable.$$

The $model$ field is the identifier of the specific model: MarsGRAM, MarsRAD, Pollack, Dycus or Divine. The $group$ is an optional, arbitrary field of results. It is used whenever

the complexity or the amount of results from a particular model requires further organization of its variables (currently this applies to MarsGRAM and MarsRAD). If no groups are defined for a given model, its variables are stored directly under the model field (i.e., RAW.model.variable). Each $group$ and $variable$ name and shape will be heavily dependent on the model they belong to. The reader is referred to the specific model documentation for further information.

This scheme helps keep the results organized and virtually isolated among modules, which allows an easy and straightforward implementation of new models into MEMM (i.e., there will be no conflicts between variables). However, it also requires an extensive post-processing work when compiling multi-array simulations (think of longitude/latitude maps, time simulations, for example). A trade-off has been conducted between scalability and code efficiency, and the former has been recognized a higher priority, given the modular nature of MEMM.

If the results of the simulations of MEMM are used as input to an external code, the user must take care of extracting the necessary parameters from the internal structure of the RAW object. In the specific case of the greenhouse model, one must:

1. obtain a MEMM simulation for the selected site (longitude,latitude) during a certain period of time, thus obtaining a RAW array in time (i.e., RAW(t));
2. create the input structure array (e.g., Mars(t)) containing the required inputs (temperature, pressure, etc.);
3. execute a loop through the RAW array and copy the desired parameters to the Mars(t) structure;
4. carry out the additional calculations concerning the specific heat, the dynamic viscosity and the heat transfer coefficient (Sect. 2.3.7.1).

More complex input structures might require additional processing (e.g., statistical treatment).

### 2.3.9 Model bugs

During the implementation of the models, several errors and bugs have been found in the original codes. These bugs have been successfully fixed in MEMM. A report is provided here below.

In MarsGRAM, a redefinition of a variable caused the daily density to take erroneous values. The bug was solved by removing the redefinition command. A comparison between the values before and after the fix is shown in Fig. 2.2:

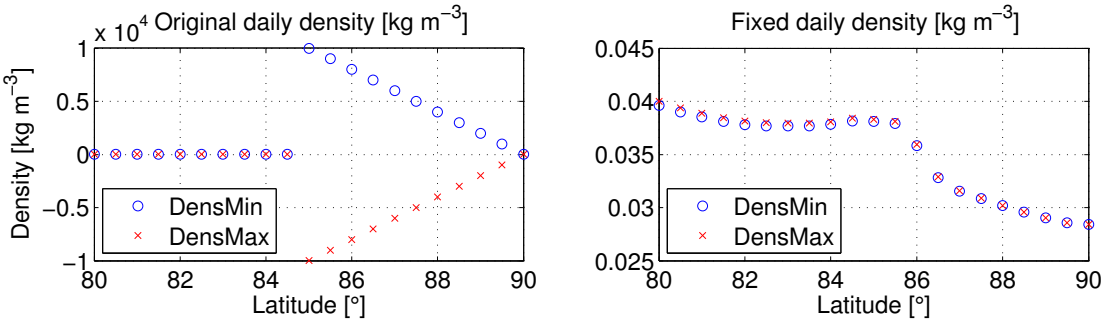


Figure 2.2: MarsGRAM bug concerning the daily density values.

In MarsGRAM, the user can optionally input an arbitrary dust storm on Mars. The user can also select the source data from a simulation made to reproduce the environmental conditions measured during the first two TES mapping years. If the TES data are selected, the values for the temperature, density, etc. are not affected by the input dust storm. However, in the original code the value of the dust optical depth was still affected by the dust storm parameters. When the results were fed into MarsRAD, the resulting irradiation levels were modified accordingly by the optical dust depth, which made the radiation results unrealistic according to the TES scenario (Fig. 2.3). The MarsGRAM code has been modified to ignore the user dust storm when the TES data is selected. Currently, the radiation levels match the atmospheric quantities of a TES scenario (Fig. 2.4).

In MarsRAD, the code tried to access the position 0 in a vector which started at position 1. This triggered a segmentation fault that force-terminated the program. The code has been modified to prevent the access to any position outside the array's allowed range.

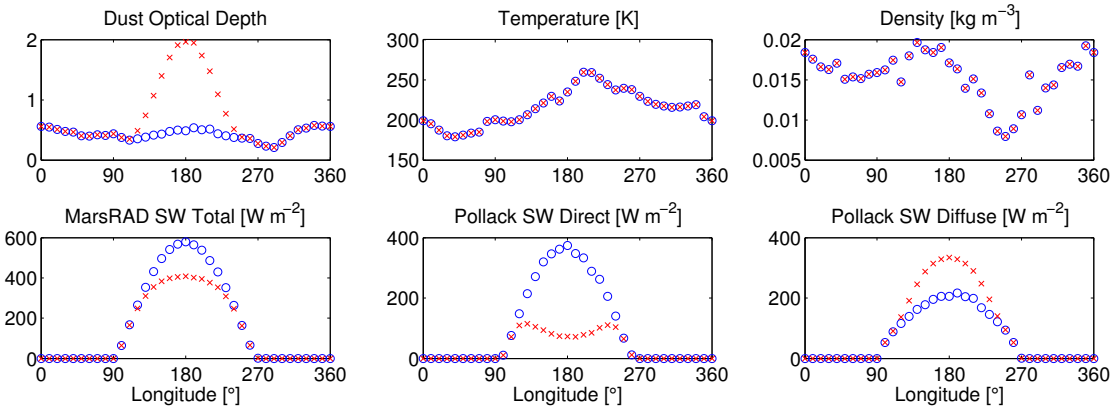


Figure 2.3: Original MarsGRAM code results with TES scenario. Dust-free scenario (blue circle) versus dust storm (red cross). Note that the temperature and density are not affected by the dust storm but the radiation fluxes are actually modified, thus yielding results not coherent with the simulated TES scenario.

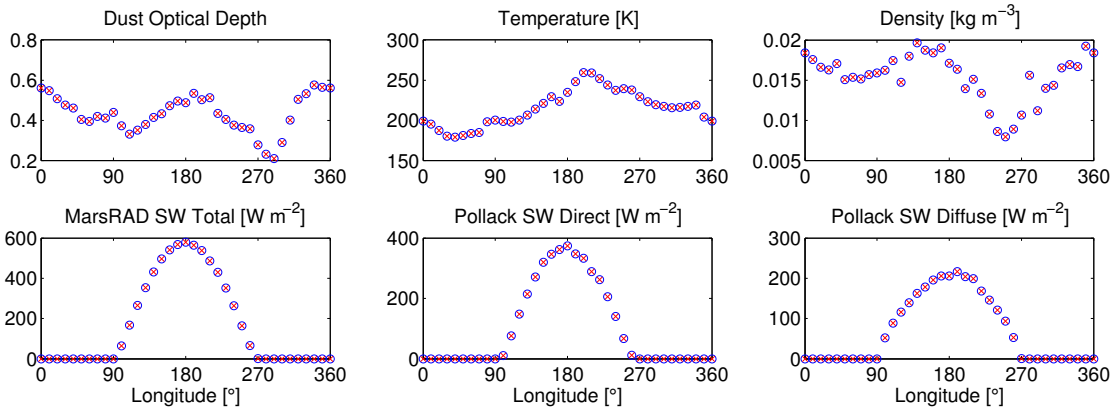


Figure 2.4: Fixed MarsGRAM code results with TES scenario. Dust-free scenario (blue circle) versus dust storm (red cross). Now the code ignores the dust storm, forcing the radiation flux values to comply with the simulated TES scenario.

A value in the two tables of Pollack (Fig. 2.5 and Fig. 2.6) was incorrectly interpreted, which produced a small error in the results. The faulty value has been corrected by a $5^{th}$ degree polynomial function.

## 2.4 A sample of results

In Fig. 2.7 to 2.14 we provide a sample of the results of a simulation executed with MEMM.

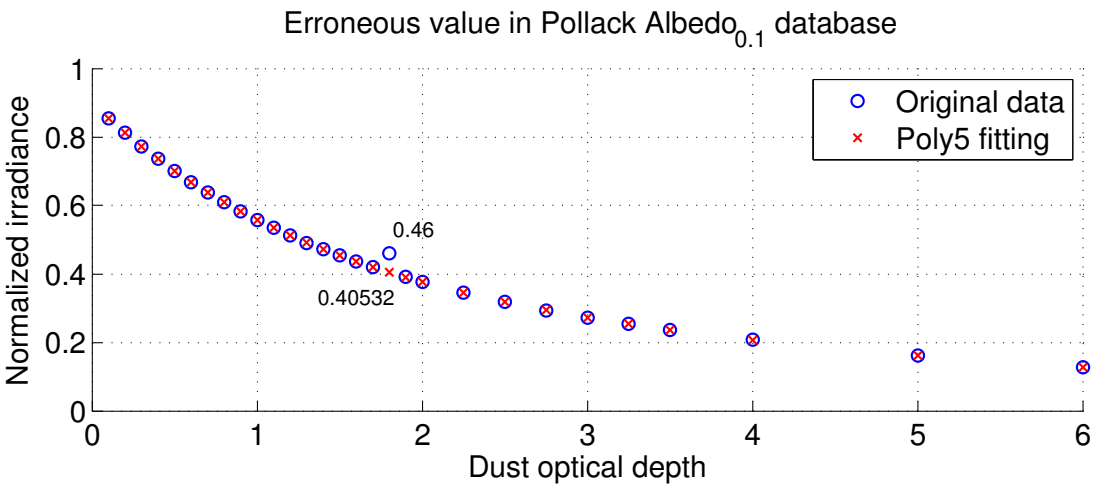


Figure 2.5: Faulty value in Pollack albedo 0.1 database.

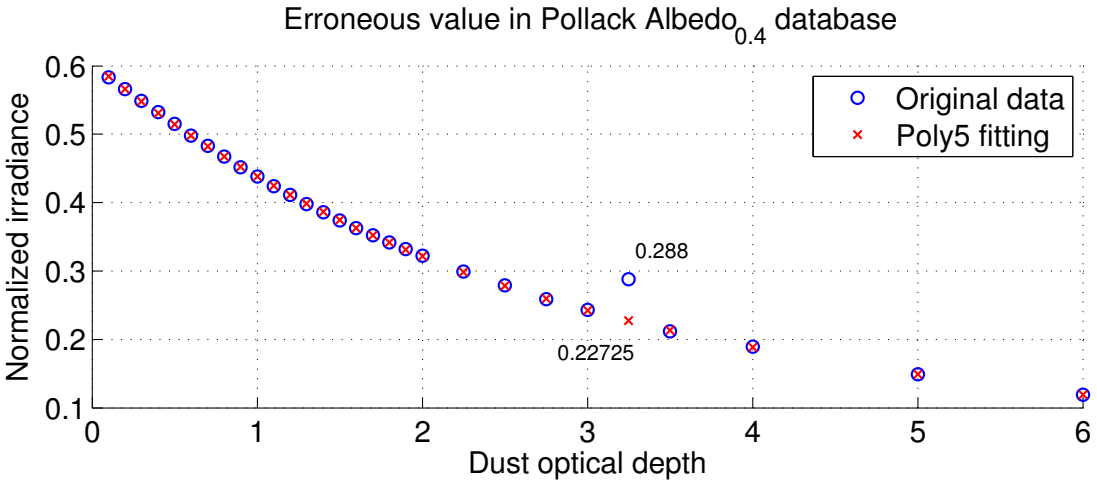


Figure 2.6: Faulty value in Pollack albedo 0.4 database.

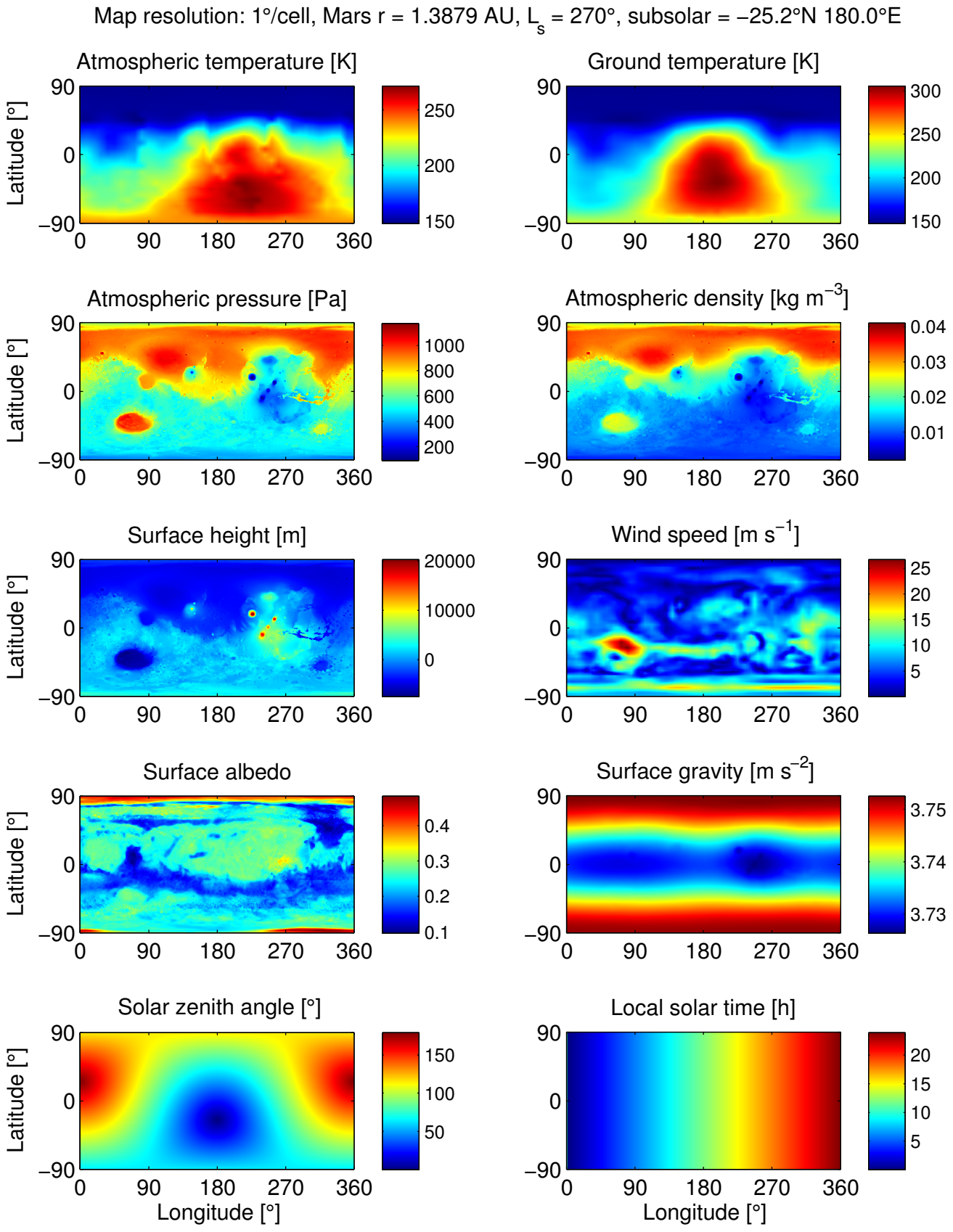


Figure 2.7: MEMM simulation results multiplot. Atmospheric quantities and general parameters.

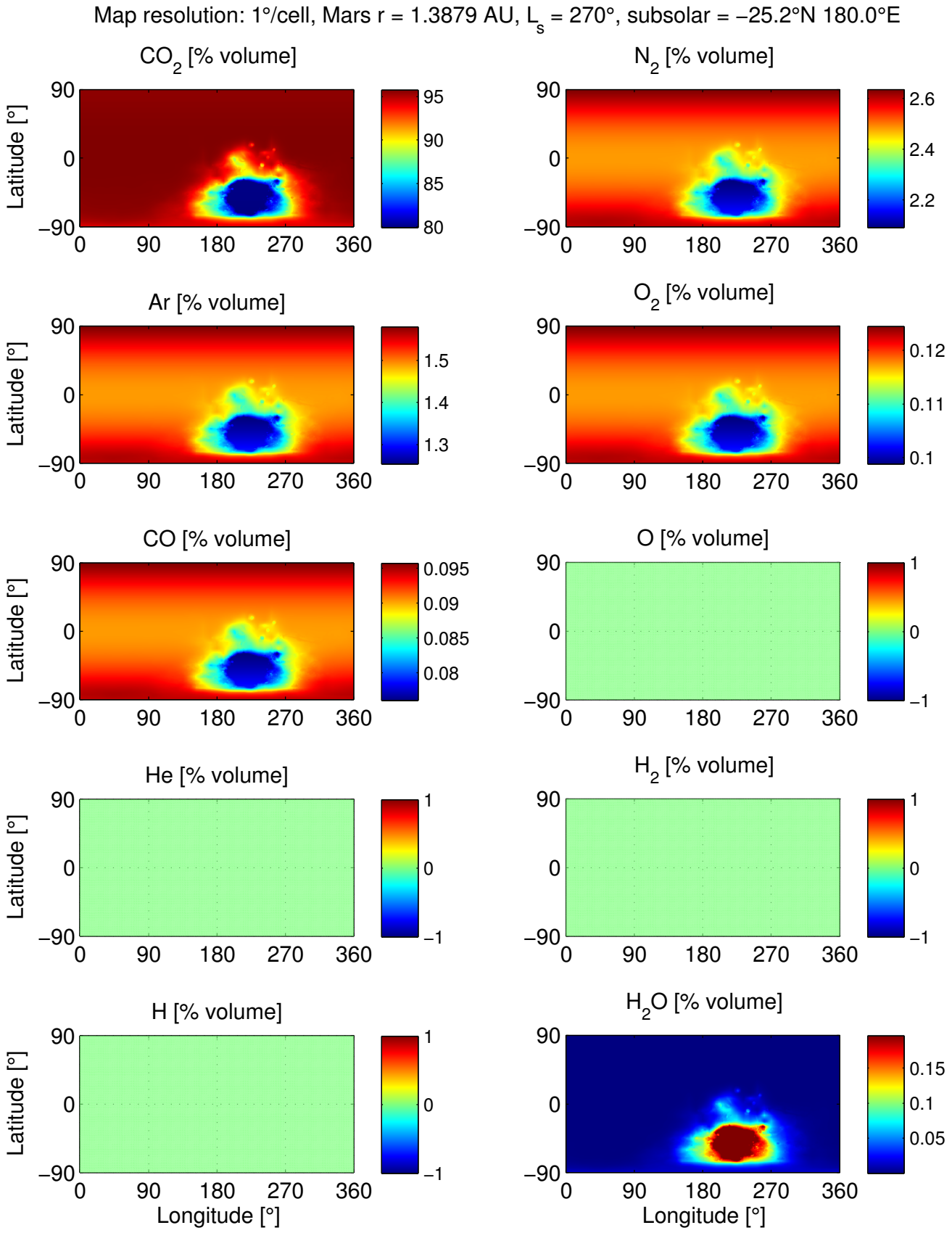


Figure 2.8: MEMM simulation results multiplot. Atmospheric constituents concentration in volume percentage.

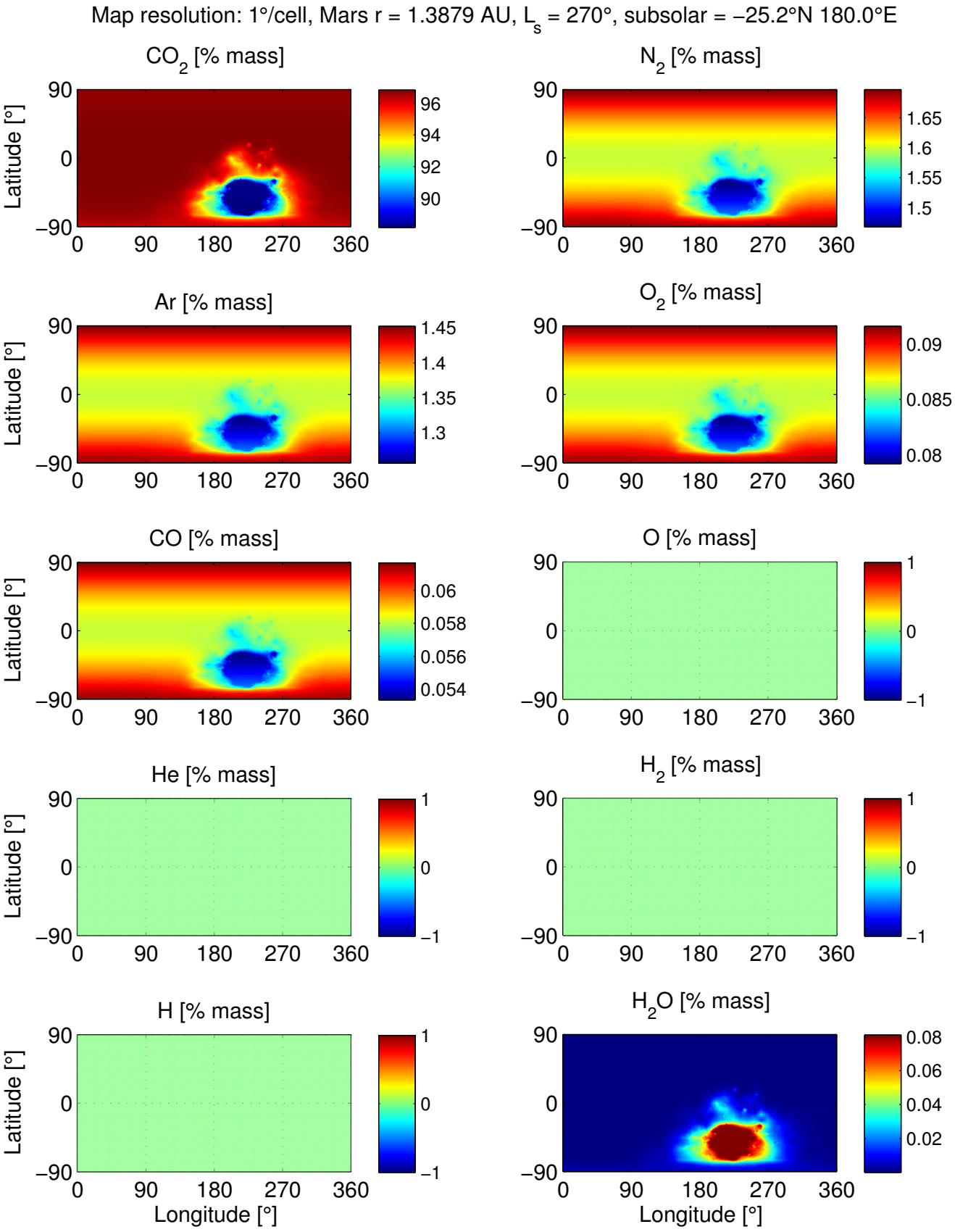


Figure 2.9: MEMM simulation results multiplot. Atmospheric constituents concentration in mass percentage.

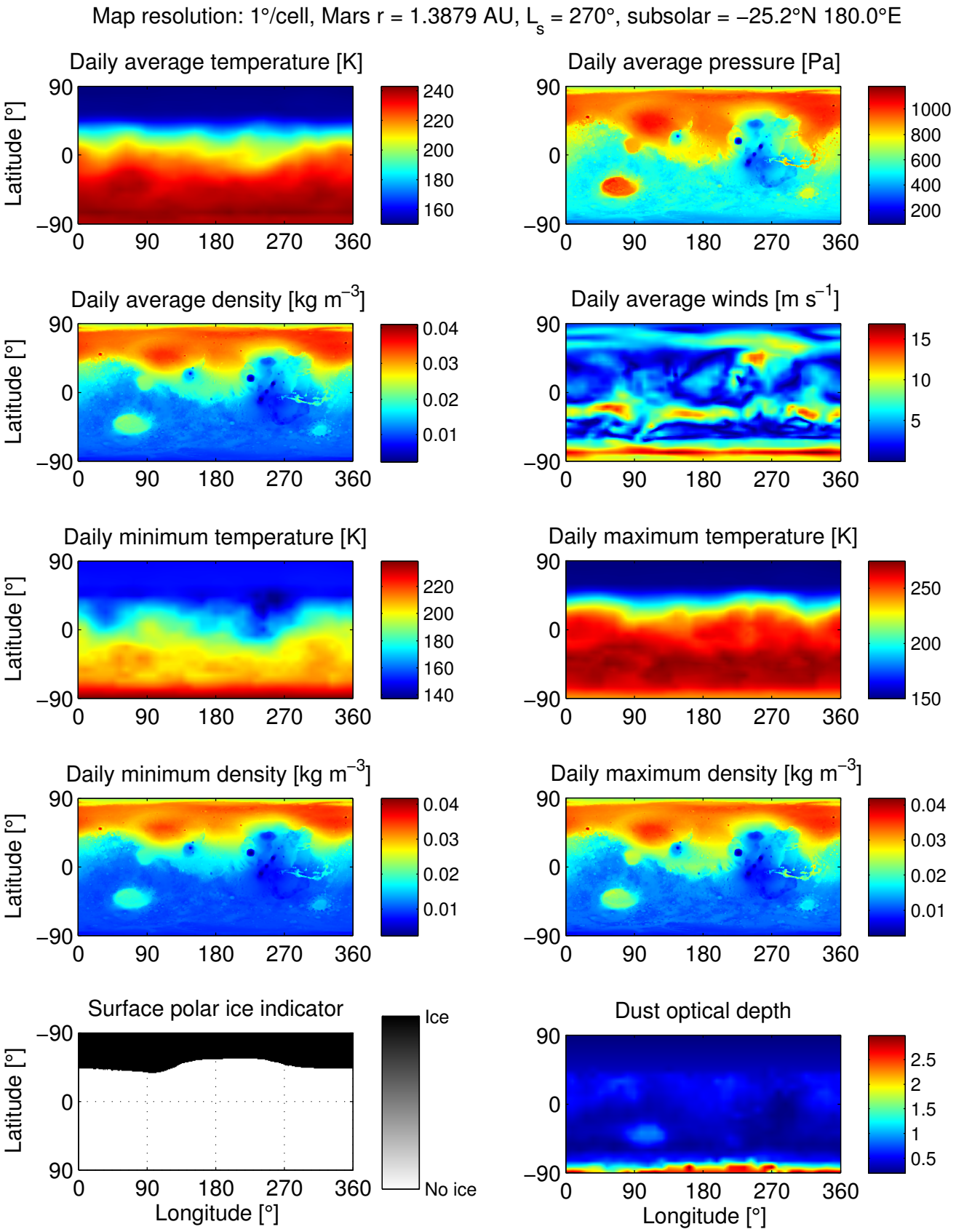


Figure 2.10: MEMM simulation results multiplot. Daily values, surface ice and dust optical depth.

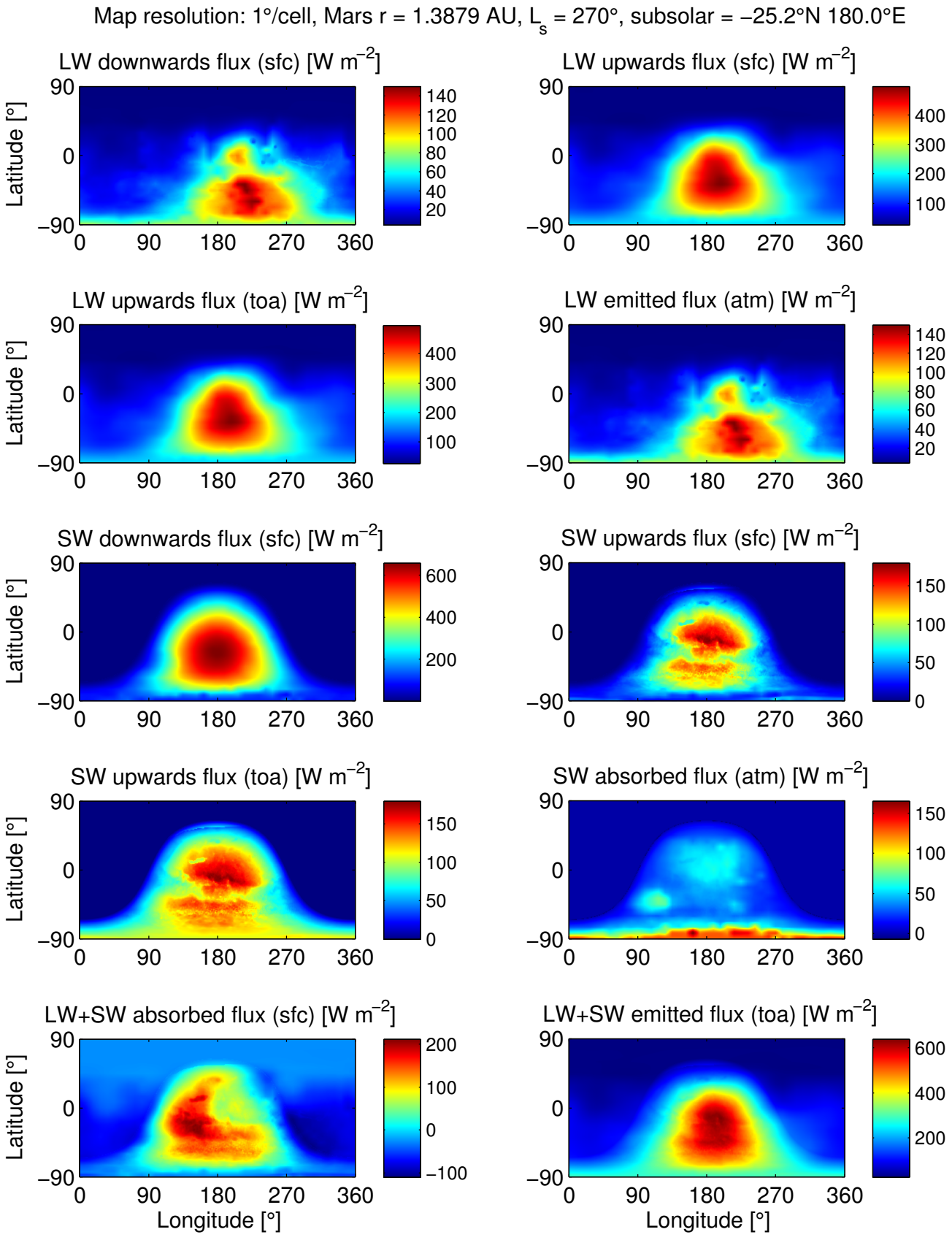


Figure 2.11: MEMM simulation results multiplot. Radiation fluxes from MarsRAD.

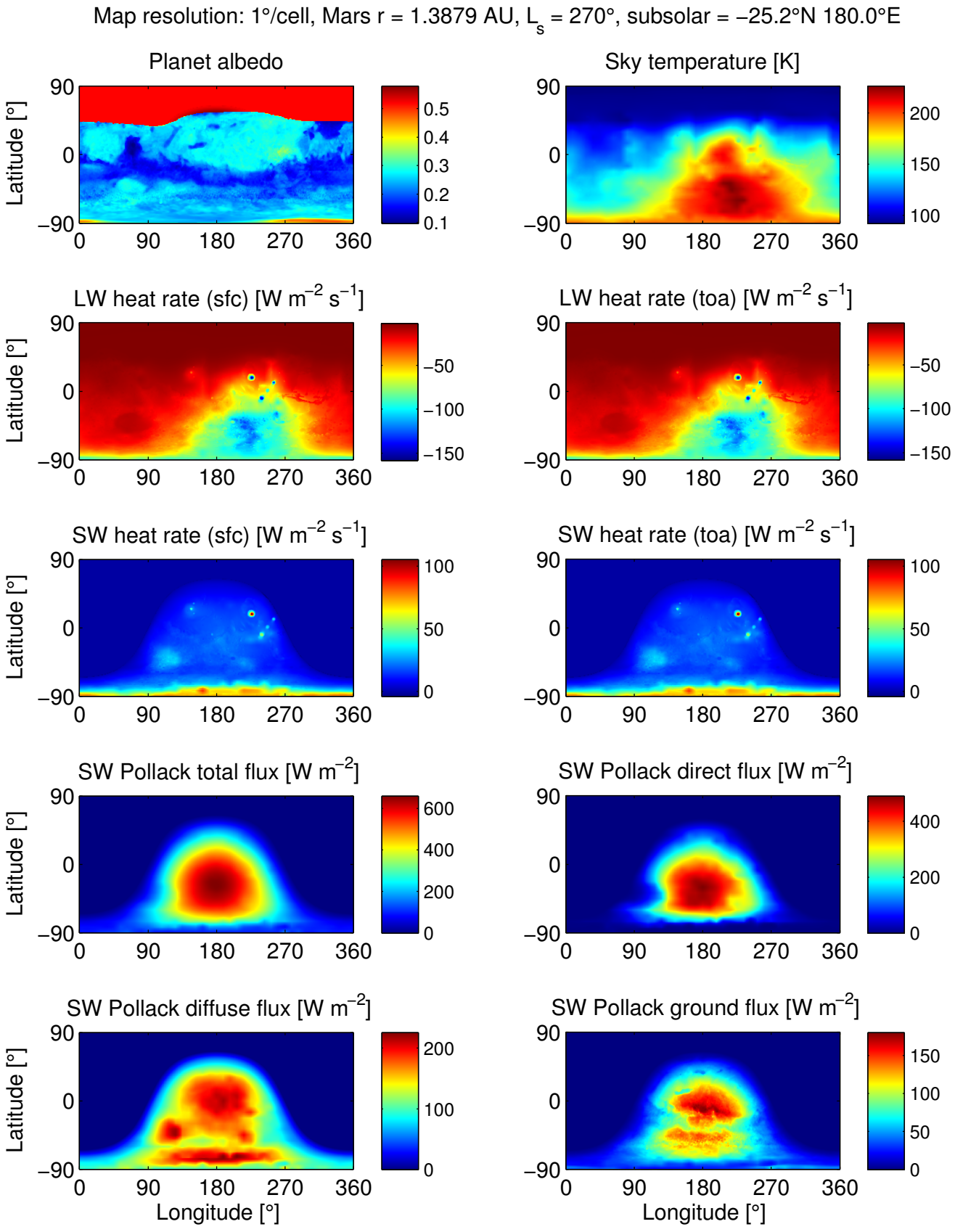


Figure 2.12: MEMM simulation results multiplot. Planet albedo, sky temperature, and heat rate values from MarsRAD, and radiation fluxes from Pollack.

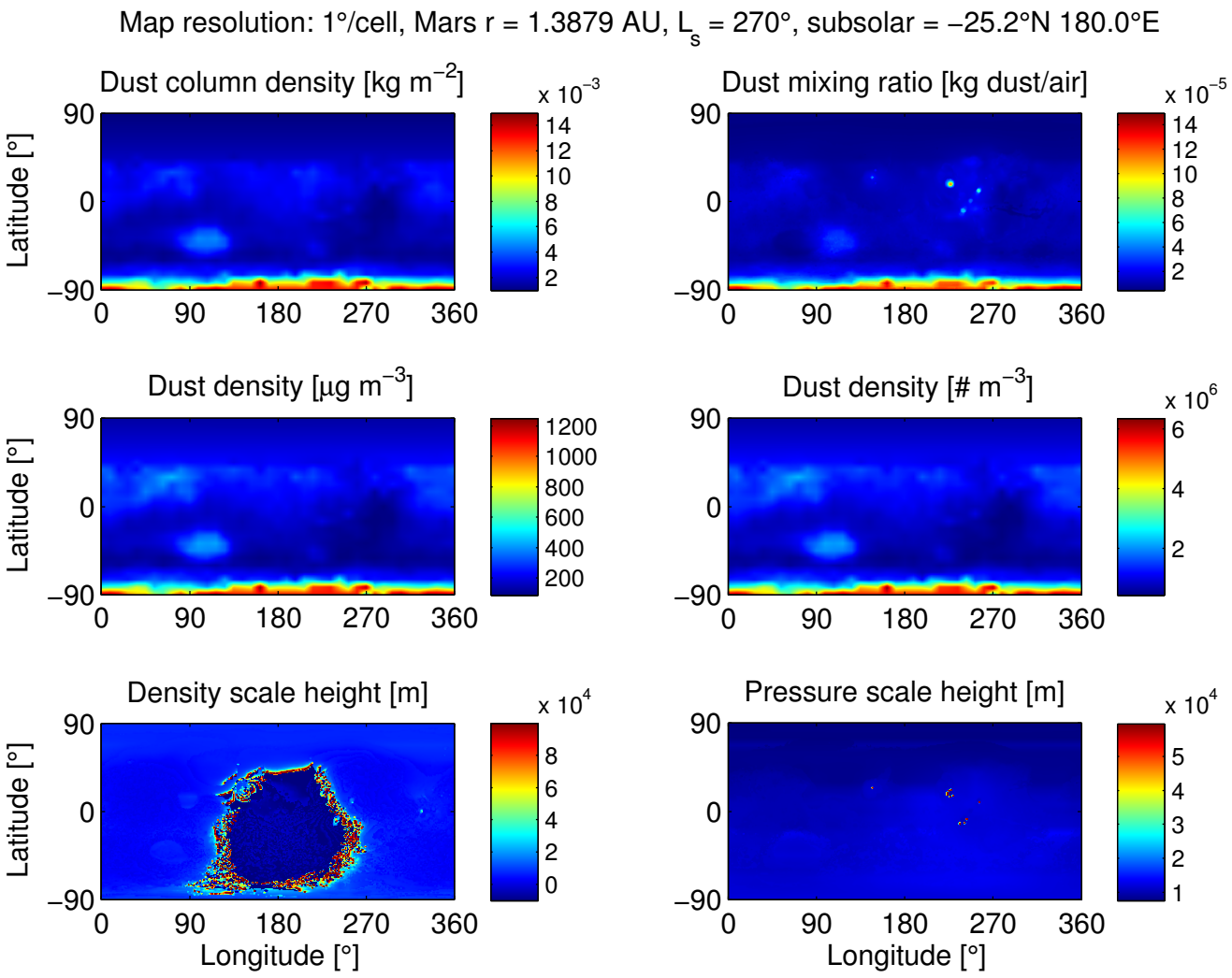


Figure 2.13: MEMM simulation results multiplot. Dust properties and scale heights.

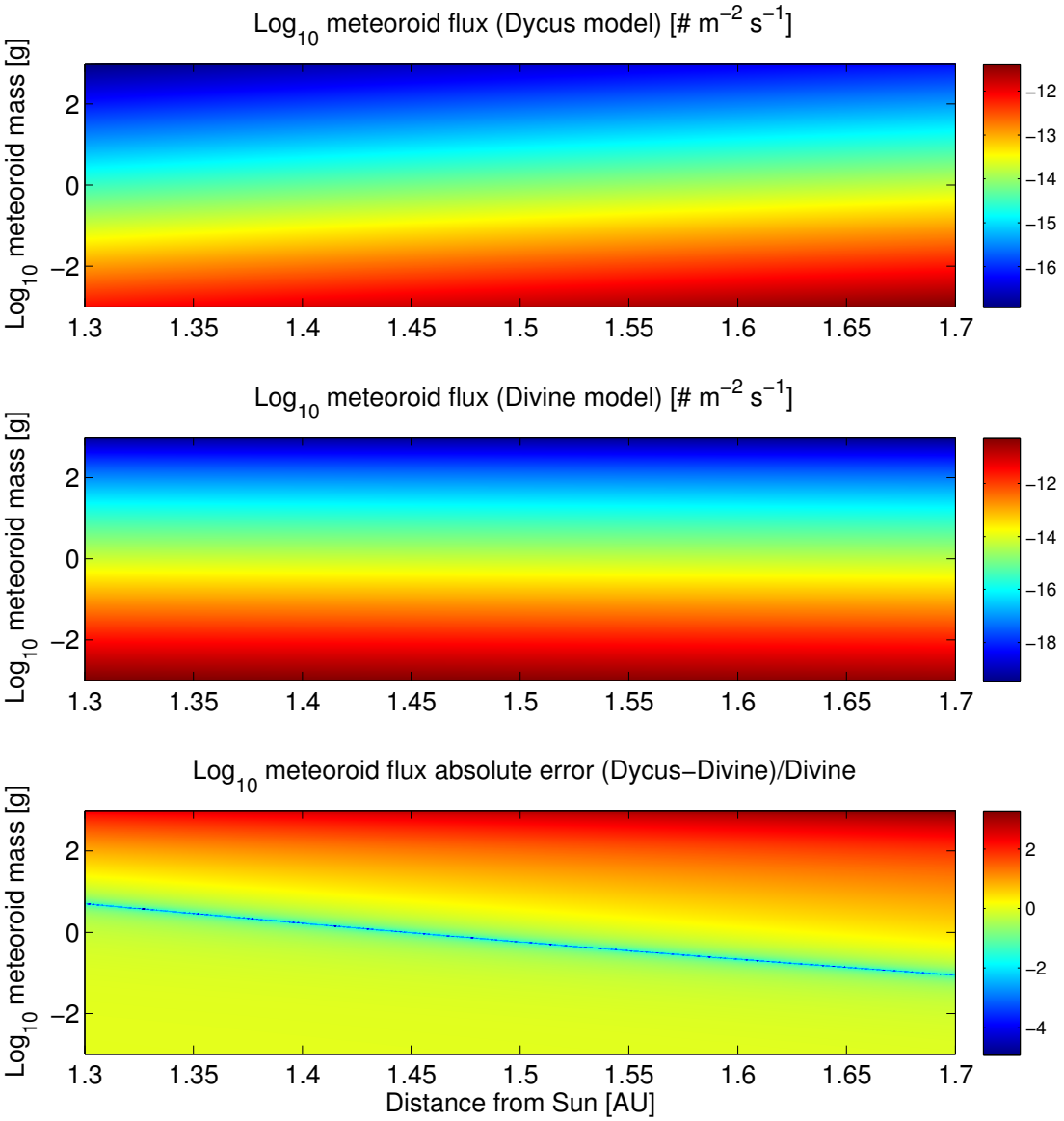


Figure 2.14: Results from the Dycus and Divine meteoroid models, and comparison between them.

# Chapter 3

# Environment and climate: the results

In this chapter, we present the environment and the climate of Mars. In Sect. 3.1 we illustrate the information concerning the climate and the environment of the red planet as derived from in-situ observations and from the models presented in Chapter 2. The section also contains a general introduction to the physics of Mars as a planet. The results of the global simulations performed with MEMM are discussed in Sect. 3.2. Such results are employed in the analysis and identification of climatic areas, based on temperature, pressure and air density. The most favourable zones shall be selected for further analyses and follow-up studies to identify candidate sites for the installation and operation of the greenhouse.

## 3.1 The Martian environment

In order to provide a complete view of the Martian environment, a combination of results from MEMM and experimental data is used. The MEMM simulations are made by considering a scenario with no atmospheric dust and another scenario with a dust storm during the northern winter. This allows to determine the best-case and worst-case situations, as well as to characterize the behaviour of the several physical parameters in the presence of a dust storm.

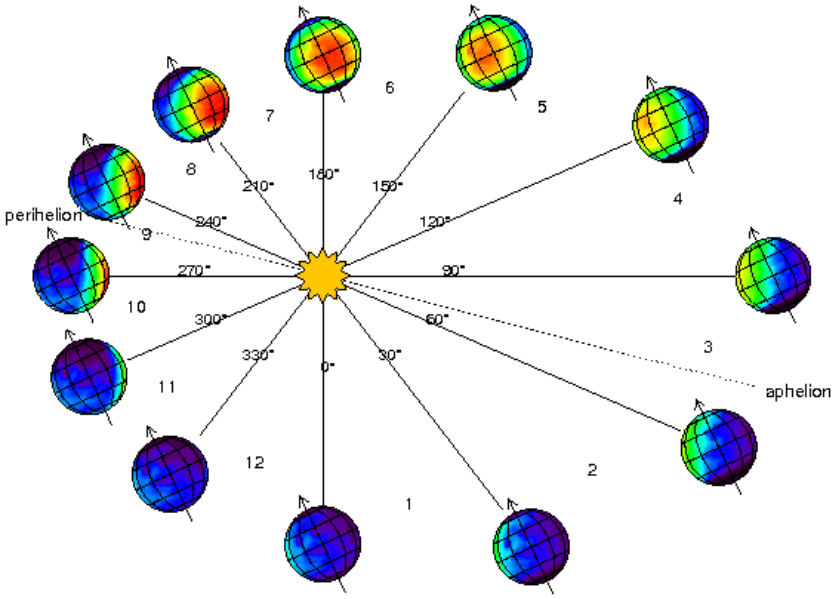


Figure 3.1: The orbit of Mars and the definition of $L_s$.

### 3.1.1 Orbit, seasons and global physical parameters

Mars is the fourth planet of the Solar System in terms of distance to the Sun. Its orbit has a semi-major axis of 227,939,100 km and an eccentricity of 0.093315, which gives a distance between aphelion (the most distant point of the orbit from the Sun) and perihelion (the closest point to the Sun) of 42,540,300 km. The orbital period is of 686.971 Earth days or 668.5991 Martian days, also called *sols*. Seasons are defined according to the longitude of the Sun $L_s$ (see Fig. 3.1). The latter is defined as the Mars-Sun angle, measured on the orbital plane of Mars from the Spring equinox (where $L_s$ = 0°), i.e., one of the nodes of the orbital plane with the equatorial plane. As such, the Summer solstice occurs at $L_s$ = 90°, the Fall equinox at $L_s$ = 180°, and the Winter solstice at $L_s$ = 270°. Note that like for our planet, the equinoxes and solstices are named after the seasons of the northern hemisphere.

Martian months too are defined by $L_s$: in this case, the subdivision is in intervals of 30° each. However, because of the relatively high eccentricity of the orbit, the duration of each month (and hence of each season) varies appreciably: the longest month corresponds to 60° $< L_s <$90° and has a duration of 66.7 sols, whereas the shortest month occupies the longitude interval 240° $< L_s <$270° and lasts 46.1 sols. The mass of Mars is of 0.64174 $\times$ $10^{24}$ kg and its radius (3396 km) is approximately half that of the Earth.

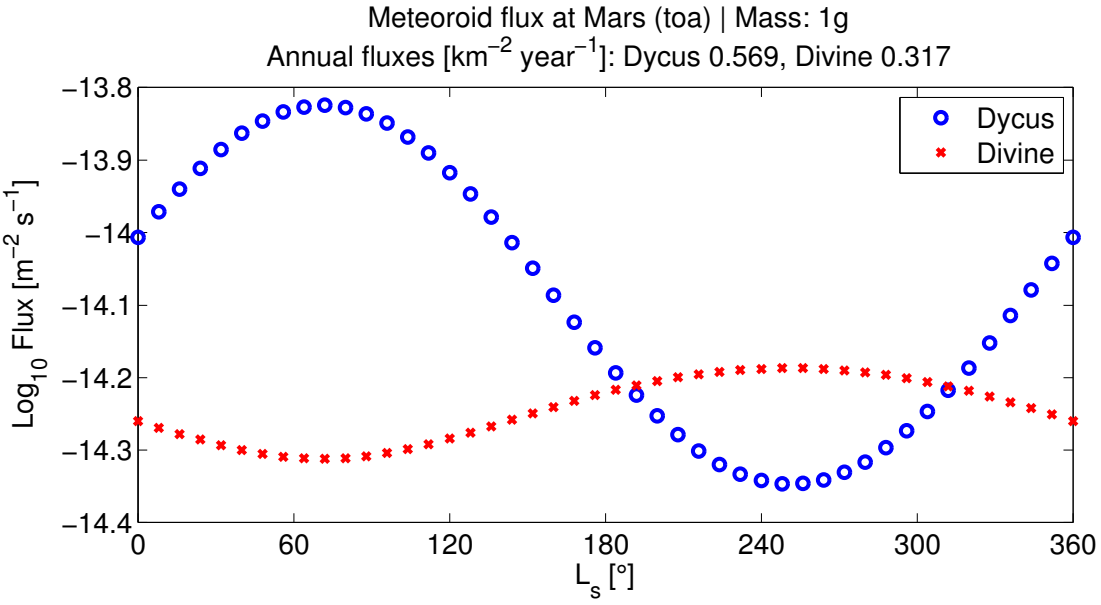


Figure 3.2: Meteoroid flux at top of the atmosphere, according to Dycus and Divine.

The sidereal period of rotation is of 24.7 hours and the obliquity of the equator to the orbital plane is of 25.9 degrees.

### 3.1.2 Meteoroid flux

The annual flux of 1 gram mass meteoroids according to the Dycus and Divine models (see Fig. 3.2) is of 0.57 and 0.32 meteoroids km$^{-2}$ year$^{-1}$ respectively. Note the fundamental discrepancy between the two meteoroid models: while Dycus assumes a direct relationship between distance and flux (the flux increases with distance to the Sun), Divine employs an inverse relationship (the flux decreases with heliocentric distance).

### 3.1.3 Topography

Mars is a rocky planet. Its surface can be divided into two topographical regions: the geologically ancient cratered southern highlands and the younger northern plains. Several accidents are notorious: the Tharsis bulge, containing the Tharsis Montes and the nearly 22km-high Olympus Mons (which is also the highest volcano in the Solar System), the Hellas and Argyre basins, and Valles Marineris (a huge series of equatorial canyons). Many dune fields extend on the poles and within the craters. A more detailed map can be seen in Fig. 3.3.

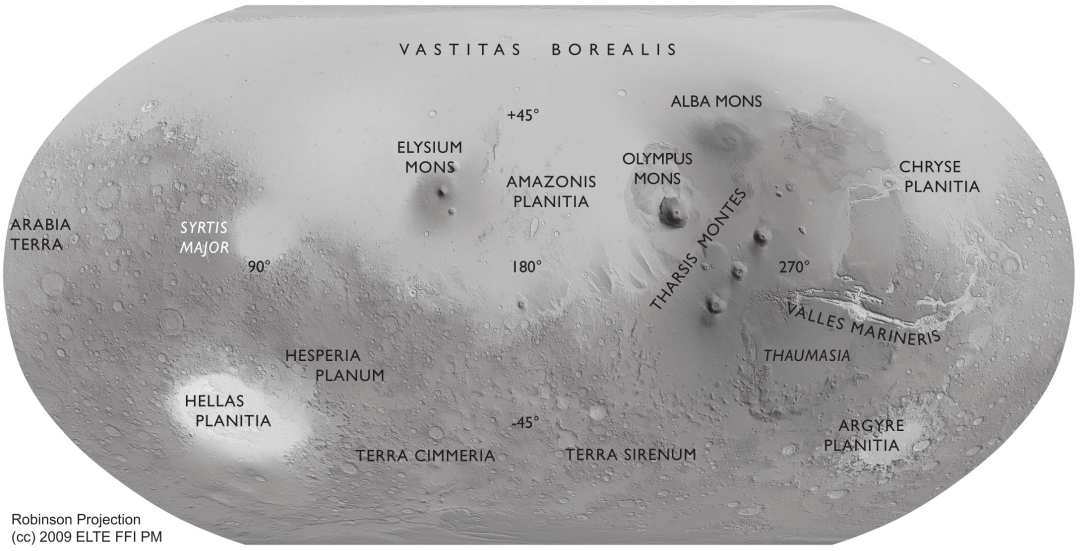


Figure 3.3: Map with the main features of Mars in Latin nomenclature.

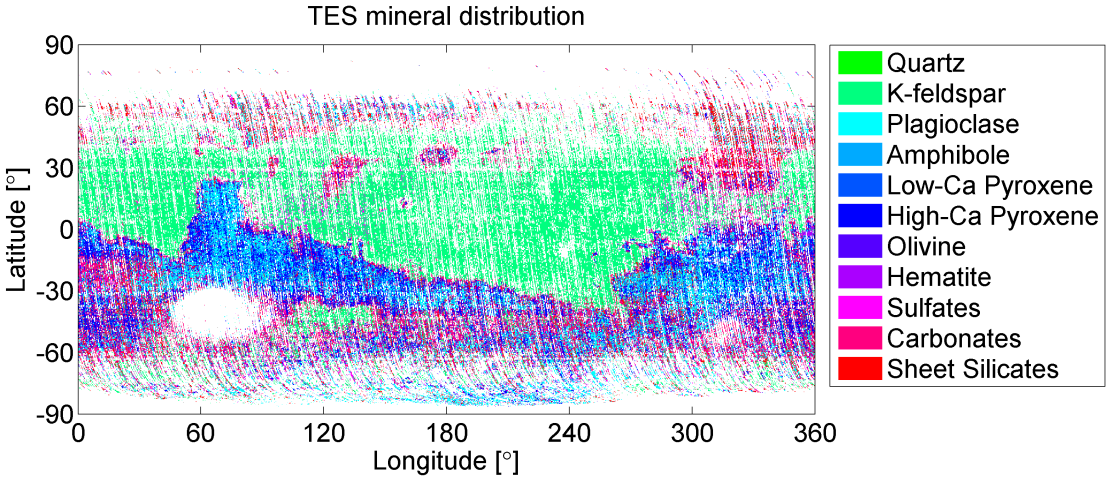


Figure 3.4: Combined TES plot of the Martian surface mineralogy.

### 3.1.4 Soil

The Martian soil is composed of silica ($SiO_2$, 58.2%), iron oxide ($Fe_2O_3$, 23.7%), magnesium oxide (MgO, 10.8%) and calcium oxide (CaO, 7.3%). A more accurate geographical distribution of the mineralogical components in the soil is presented in Fig. 3.4 which refers to data from the TES/MGS mission,. More illustrations for each separate mineral can be found in Appendix A.

The polar caps are usually covered by frozen $CO_2$ ice. The $CO_2$ sublimates to the atmosphere during the Summer due to the increased soil temperature, and it precipitates

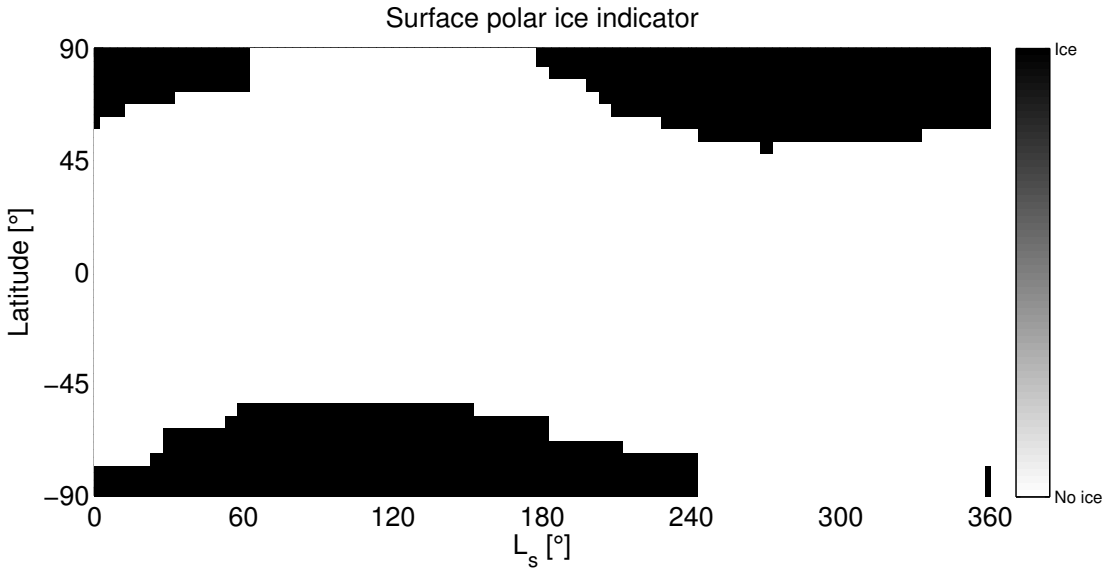


Figure 3.5: Evolution of the polar surface ice throughout one Martian year.

again in the form of ice in Winter. The resulting seasonal extension variation of the northern and southern polar caps is shown in Fig. 3.5.

A thick permafrost (i.e., soil permanently at or below the freezing point of water) is present in the entire planet's subsurface. The permafrost layer can extend down to a depth of 1 km at the equator and several km at the poles. However, the layer in contact with the atmosphere at latitudes between 40°S and 40°N is dehydrated from the surface down to 1 m depth. This occurs because water ice can only exist in equilibrium with the Martian atmosphere if the atmospheric temperature is below the frost point of atmospheric water vapour (198K).

The surface is covered mainly by rocks and fine dust. The darker areas of Fig. 3.6 are indicative of dust-free exposed rocks, while the brighter regions usually indicate dust accumulation.

The albedo global map measured by the TES/MGS instrument can be seen in Fig. 3.7

### 3.1.5 Atmosphere

The atmosphere is made up of carbon dioxide ($CO_2$, 95%), molecular nitrogen ($N_2$, 2.7%), argon (Ar, 1.6%), molecular oxygen ($O_2$, 0.13%), carbon oxide (CO, 0.08%),

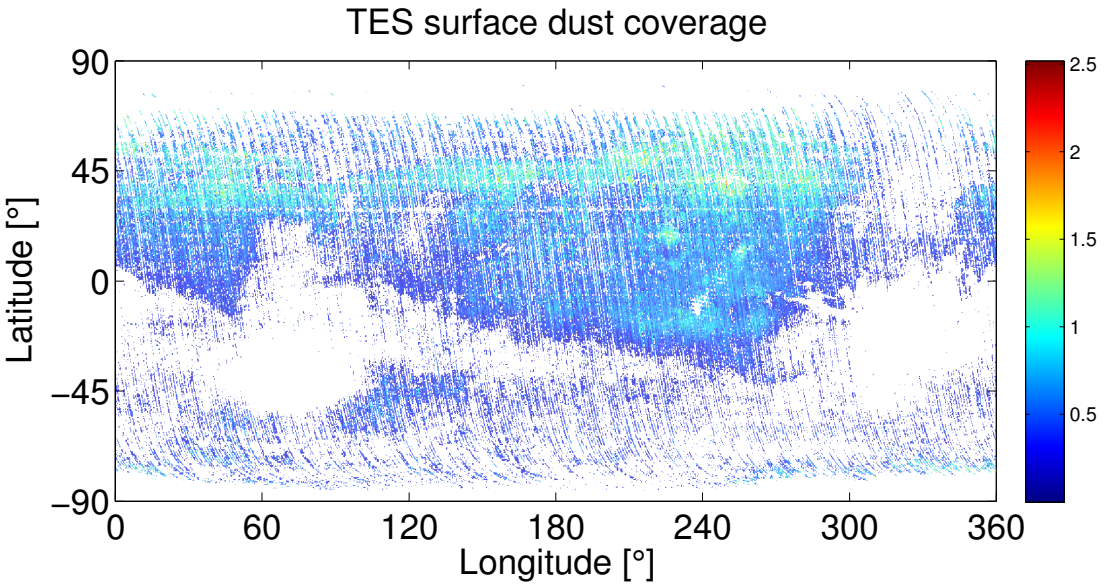


Figure 3.6: Surface dust coverage measured by the TES/MGS instrument.

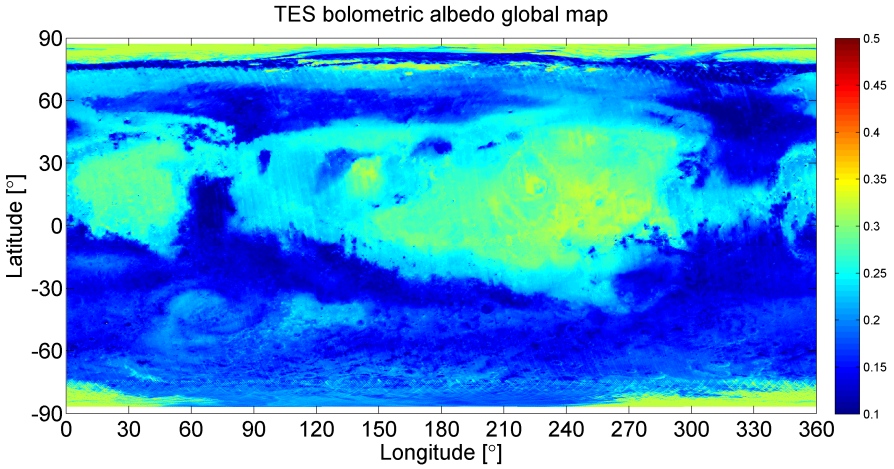


Figure 3.7: TES bolometric albedo global map.

water vapour ($H_2O$, 0.01%). The atmosphere becomes drier and richer in $CO_2$ during a dust storm, as shown in Fig. 3.8 and Fig. 3.9.

The atmospheric pressure is extremely low compared with that of the Earth. The maximum values are of 1kPa at Hellas basin, 800Pa at northern plains, 500Pa at the southern highlands, and as low as 200Pa at the Tharsis bulge. The daily variation is not significant (5%), however a dust storm can increase the pressure levels by up to 25%, as illustrated in Fig. 3.10.

The atmospheric density has a noticeable variation throughout the year, with a 40% difference between the lowest and the highest values. The daily variations are also

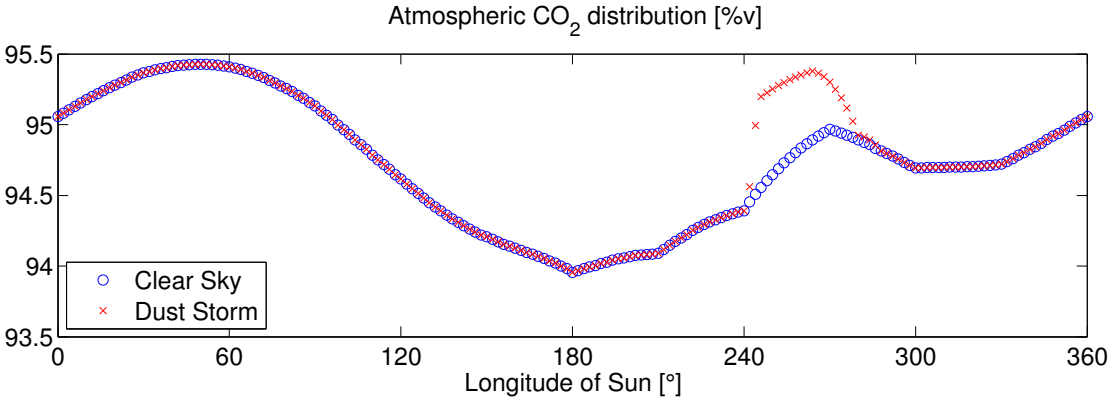


Figure 3.8: Evolution of atmospheric $CO_2$ throughout one Martian year. Samples are taken at midday (12:00h local solar time). The contrast between clear sky conditions and a localised dust storm appears at $L_s$ ≈270°.

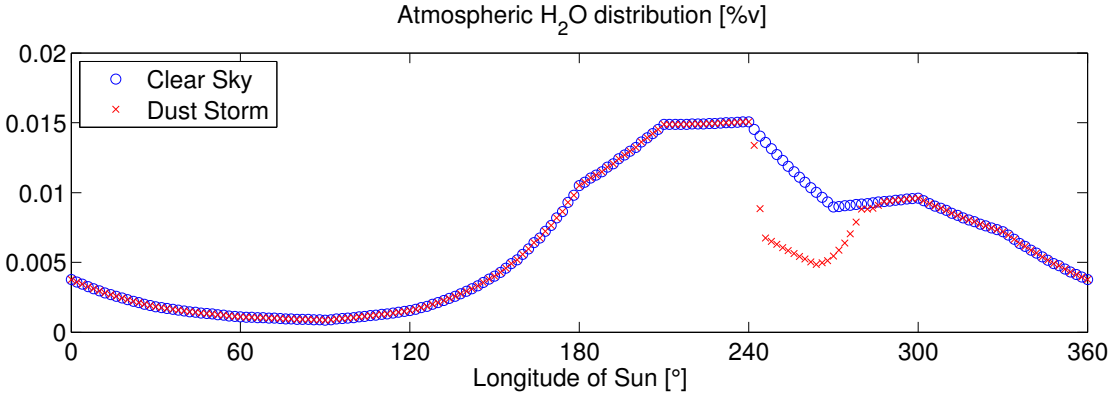


Figure 3.9: Evolution of atmospheric $H_2O$ throughout one Martian year. Samples are taken at midday (12:00h local time). The contrast between clear sky conditions and a localised dust storm appears at $L_s$ ≈270°.

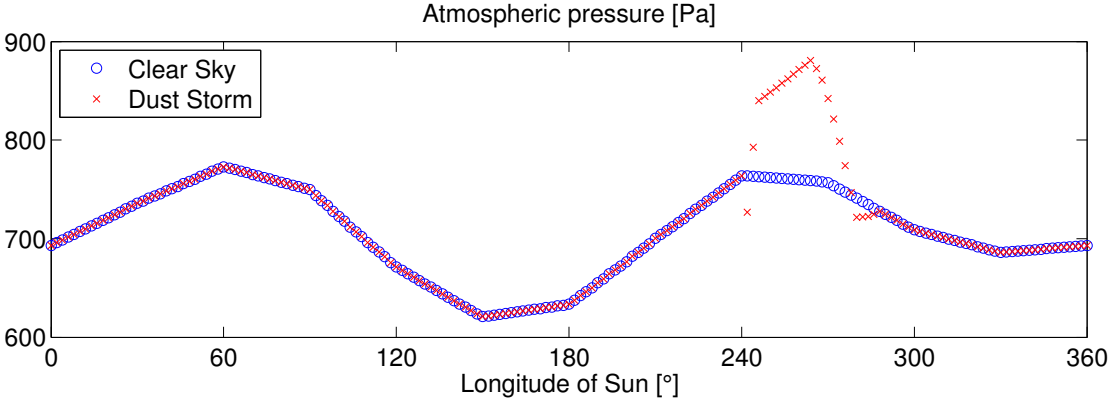


Figure 3.10: Evolution of the atmospheric mean pressure throughout one Martian year. Samples are taken at midday (12:00h local time). Note the contrast between clear sky conditions and a localised dust storm at $L_s$ ≈270°.

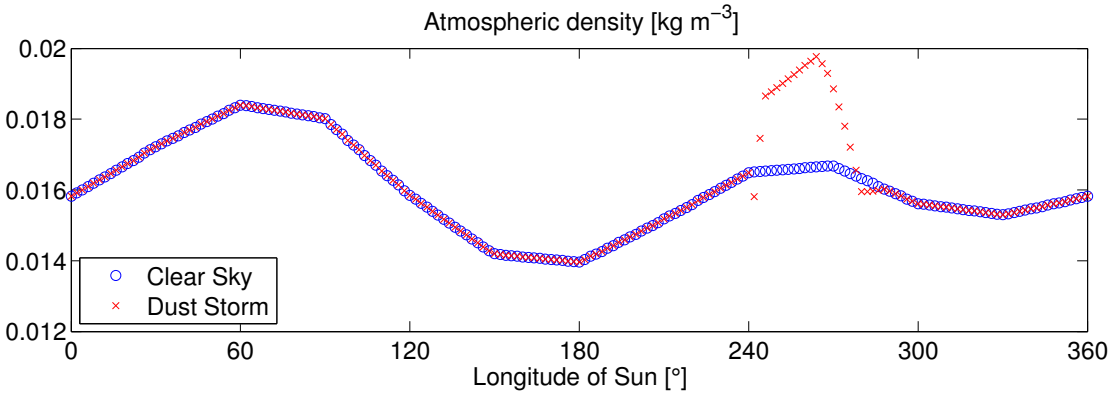


Figure 3.11: Evolution of the atmospheric mean density throughout one Martian year. Samples are taken at midday (12:00h local time). Note the contrast between clear sky conditions and a localised dust storm at $L_s \approx 270°$.

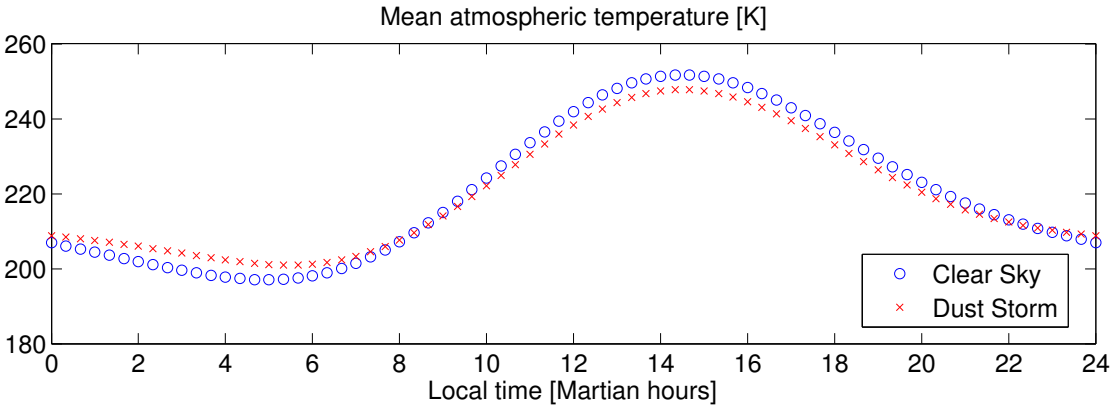


Figure 3.12: Evolution of the atmospheric mean temperature throughout one Martian sol.

appreciable (50%), and a dust storm can increase this parameter by an additional 30% (Fig. 3.11).

Mars exhibits strong day-night temperature variations (50%). Such gradients are due to the low atmospheric density which is responsible for the loss of the heat received during daytime. As shown in Fig. 3.13 and Fig. 3.14, a dust storm can smooth the daily variations. The seasonal variations can be as large as 60%. An interesting issue is that, due to the non-zero eccentricity of the orbit, the Summer in the northern hemisphere is 15% colder than the Winter. This phenomenon is further clarified in Fig. 3.15.

Since the Martian soil has a low thermal inertia and the atmosphere has a low heat capacity, the ground temperature cycles are even stronger than those of the atmosphere, with daily variations of almost 80% (Fig. 3.16).

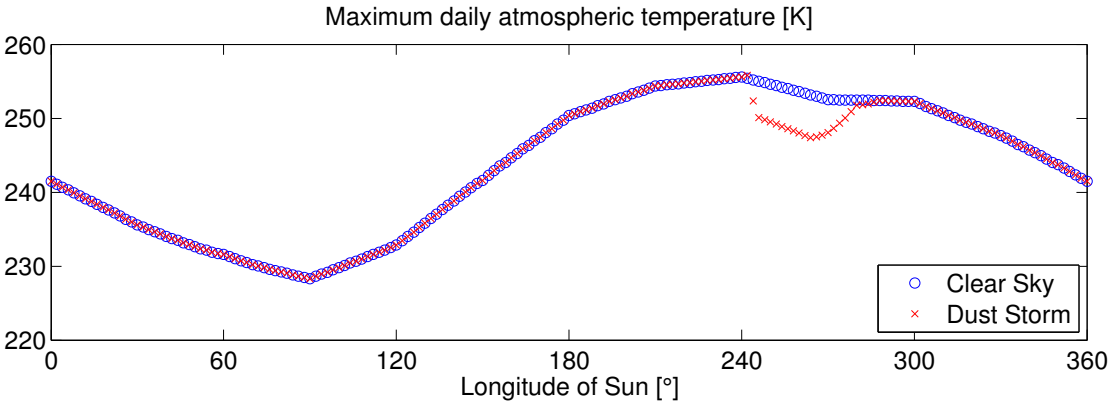


Figure 3.13: Evolution of the atmospheric maximum daily temperature throughout one Martian year. Clear sky conditions and a localised dust storm at $L_s$ ≈270°.

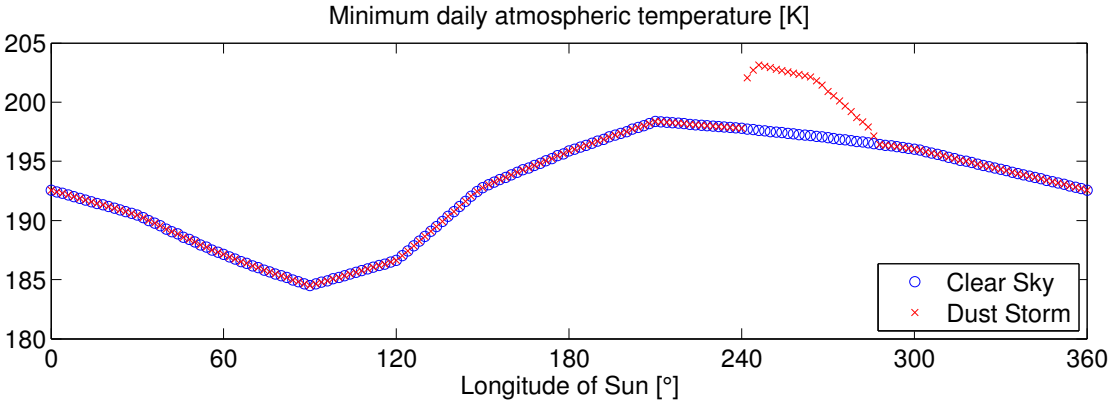


Figure 3.14: Evolution of the atmospheric minimum daily temperature throughout one Martian year. Clear sky conditions and a localised dust storm at $L_s$ ≈270°.

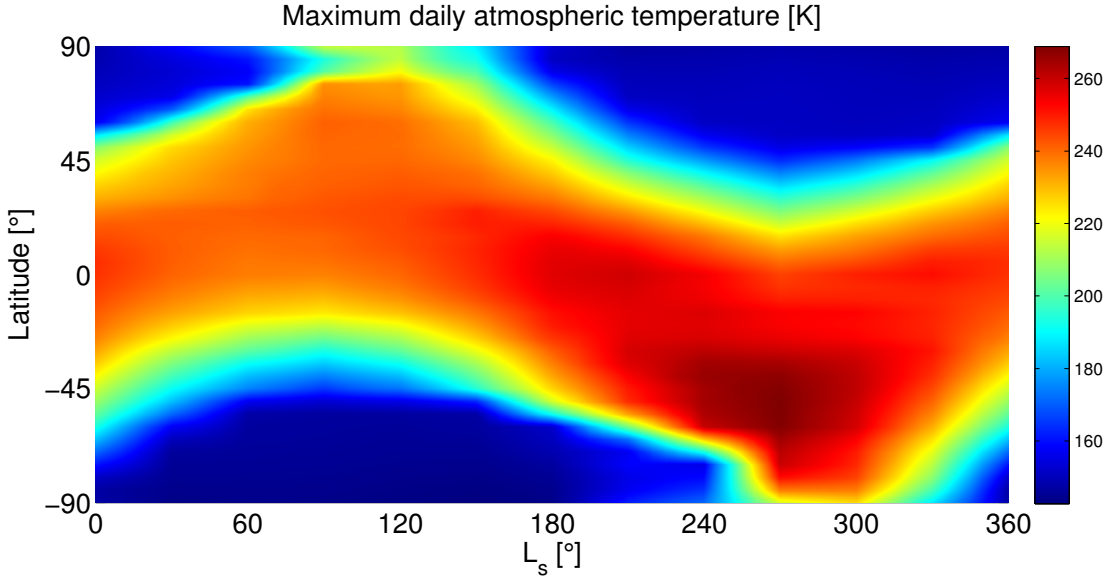


Figure 3.15: Evolution of the atmospheric maximum daily temperature throughout one Martian year.

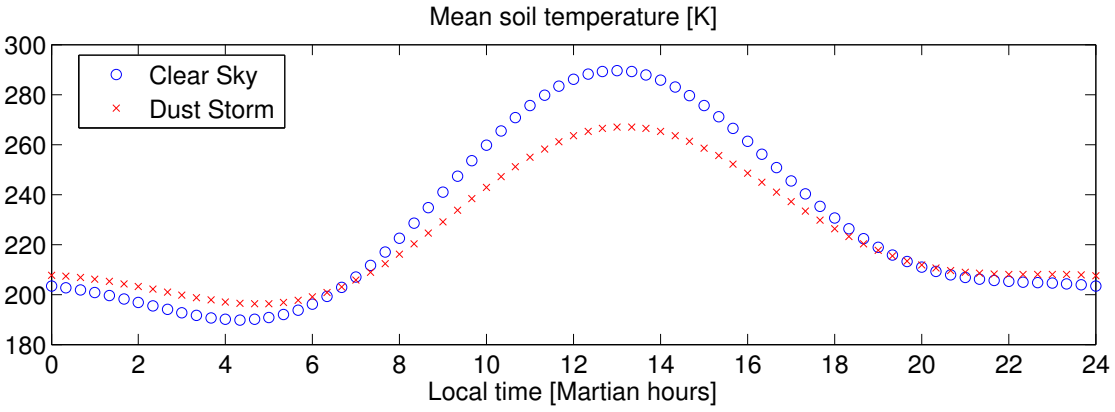


Figure 3.16: Evolution of soil mean temperature throughout one Martian sol.

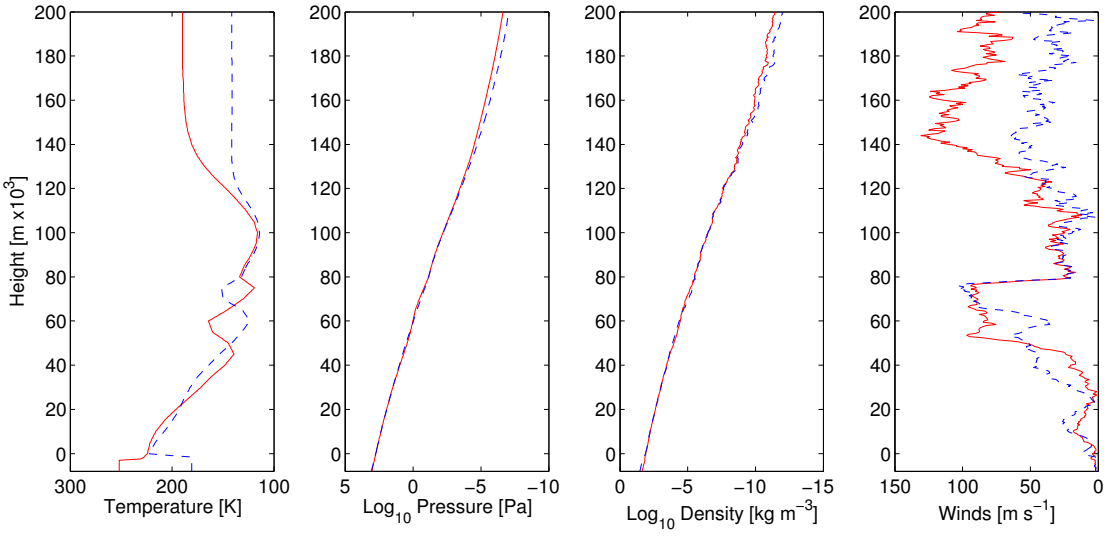


Figure 3.17: Vertical profiles for atmospheric temperature, density, pressure and wind speed. Solid line for midday values, dashed line for midnight values.

The atmospheric vertical profile is similar to that of the Earth: temperature decreases rapidly up to an altitude of 100-120km, then it increases again in the thermosphere. Pressure and density decrease in a logarithmic pattern. Winds become faster up to an altitude of 80km, then decrease in speed up to 120km, and increase again in the thermosphere.

Boundary layer models indicate that local winds may approach speeds of 20 to 30 m/s in areas of significant topographic slope. Average winds on the surface are in the range of 3 to 10 m/s (Fig. 3.18).

During Winter, roughly between 200° $< L_s <$330° in the southern hemisphere the stronger winds caused by the soil heating (recall that at perihelion Mars receives 45% more irradiation than at aphelion) can raise the accumulated dust from the surface,

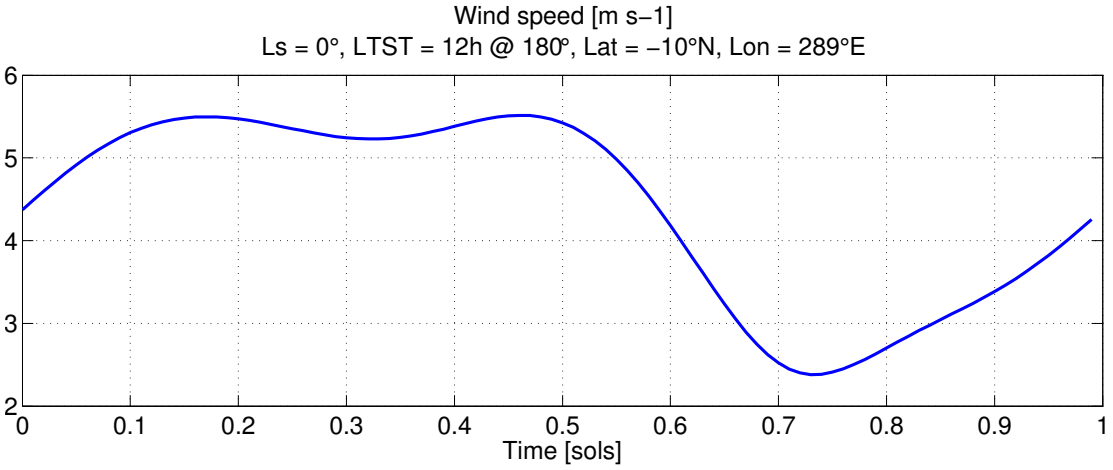


Figure 3.18: Wind speed magnitude.

creating dust storms ranging from simple dust devils to global-encompassing storms: if the dust storm grows to a significant size, the heating from the storm itself causes it to grow to global dimensions. The distribution, duration and frequency of the dust storms is highly irregular and not well understood. A major dust storm can cause the atmospheric dust to deposit and accumulate on any exposed surface. Dust devils (and normal wind gusts) can blow the accumulated dust away.

### 3.1.6 Electromagnetic radiation

The solar irradiance at the top of the atmosphere varies between 493 W m$^{-2}$ at aphelion ($L_s$=70°) and 716 W m$^{-2}$ at perihelion ($L_s$=250°). Although part of the incoming solar irradiance is scattered by the atmosphere, in clear sky conditions the total value at the surface is very similar to the value at the top of the atmosphere. However, dust storms may cause high values of the optical depths ($\tau$ >3.0), blocking almost all the direct solar irradiance (Fig. 3.19) and yielding diffuse solar irradiance values (Fig. 3.20) which are nevertheless still lower than the values at the top of the atmosphere. The infrared irradiance emitted by the Martian atmosphere varies from about 80 W m$^{-2}$ under clear sky conditions to about 120 W m$^{-2}$ during a major dust storm (Fig. 3.21).

The atmospheric $CO_2$ has two minor absorption bands in the near infrared (at 1.9$\mu$m and 2.7$\mu$m), and two major absorption bands in the thermal infrared (at 4$\mu$m and 15$\mu$m). It is transparent to the visible and near-UV. Fig. 3.22 shows the absorptivity of various

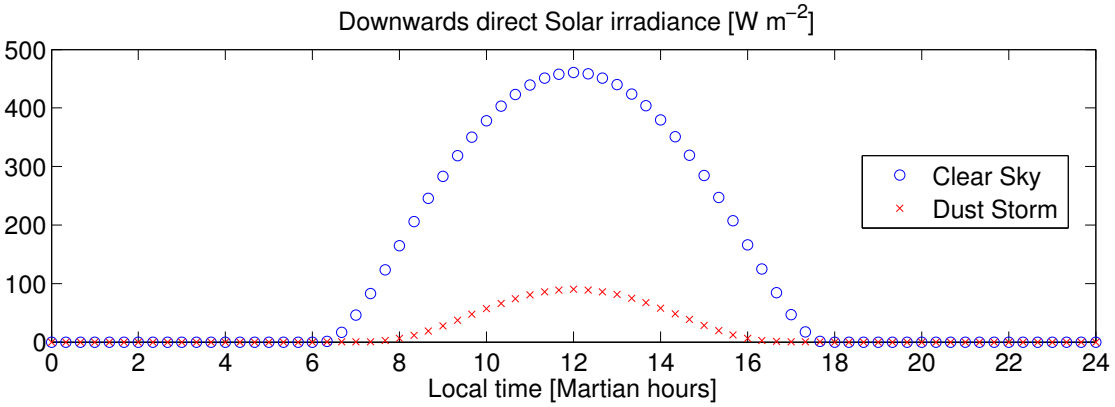


Figure 3.19: Downwards direct Solar irradiation throughout one Martian sol. Comparison between clear sky and dust storm scenarios.

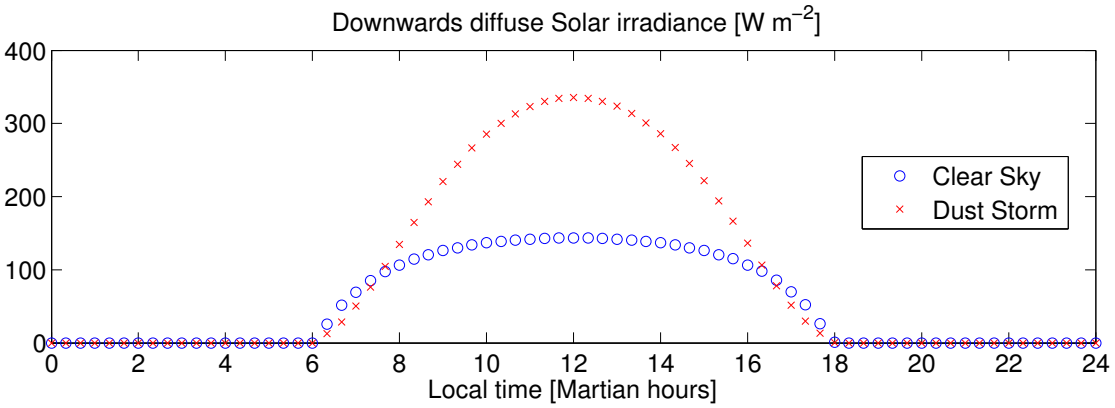


Figure 3.20: Downwards diffuse Solar irradiation throughout one Martian sol. Comparison between clear sky and dust storm scenarios.

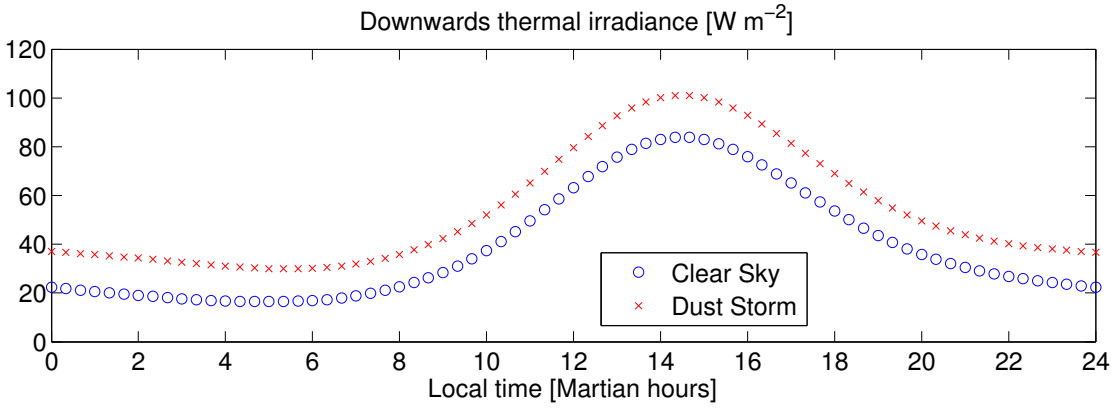


Figure 3.21: Downwards infrared irradiation throughout one Martian sol. Comparison between clear sky and dust storm scenarios.

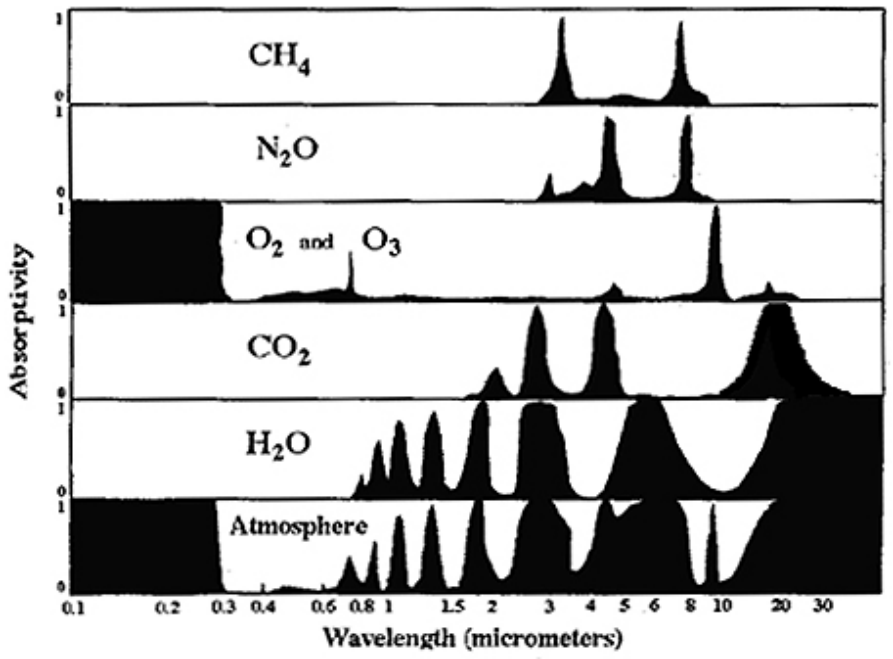


Figure 3.22: Absorptivity of various gases of the atmosphere as a function of the wavelength of radiation.

gases on the atmosphere of Earth; the phenomena is replicated on Mars considering a 95% $CO_2$ atmosphere.

Under normal conditions, the sky appears blue like on Earth. This is explained by the Rayleigh law about the elastic scattering of light by particles being much smaller than the wavelength of the radiation. Rayleigh scattering of sunlight in the atmosphere causes diffuse sky radiation, which is the reason for the blue color of the sky and the yellow tone of the sun itself. The Rayleigh scattering cross-section has a strong wavelength dependence ($\lambda^{-4}$) meaning that shorter (blue) wavelengths are scattered more strongly than longer (red) wavelengths. Despite all this, at high optical depths on Mars the atmospheric dust scatters the longer wavelengths, thus making the sky appear orange-reddish.

### 3.1.7 Particle radiation

The main sources of the Martian particle radiation environment are galactic cosmic rays (GCR) and solar proton events (SPE). Mars has no appreciable magnetic field and this is responsible for virtually no protection against flows of energetic particles. The most threatening radiation is the SPE produced during a solar flare, which typically

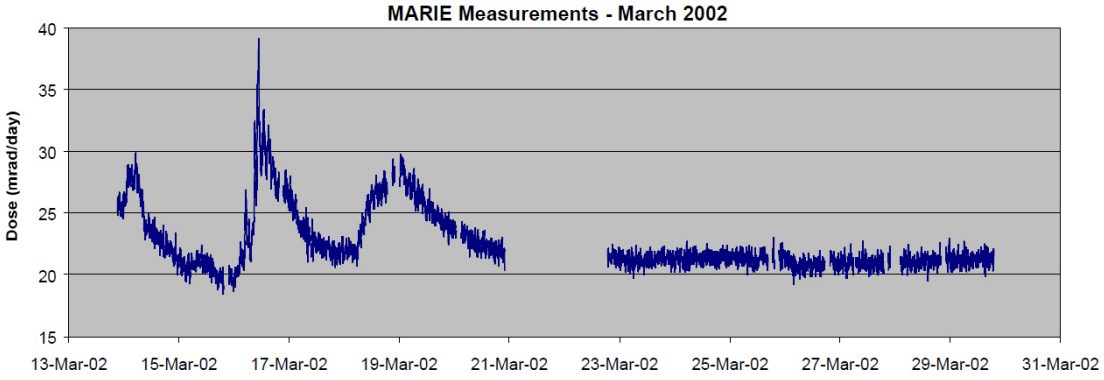


Figure 3.23: MARIE/Odyssey radiation dose measurements, March 2002.

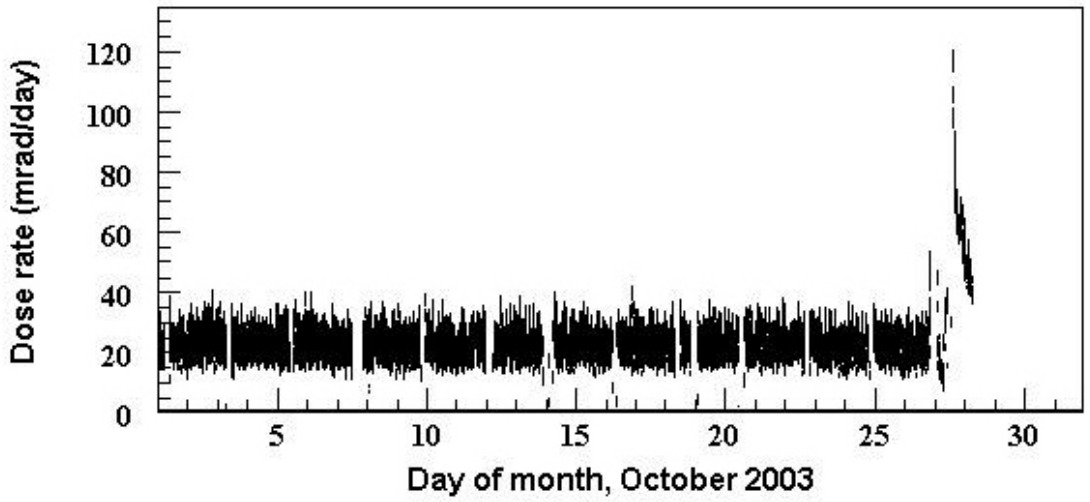


Figure 3.24: MARIE/Odyssey radiation dose measurements, October 2003.

lasts only a few days but can raise the radiation levels by several orders of magnitude with respect to the nominal values. Solar events (solar flares) are highly irregular and difficult to predict, although their occurrence follows the 11-year cycle of alternating high and low solar activity. The JPL-SPE model[107] currently divides this 11-year cycle into four inactive and seven active years.

There exist very few data sources of particle radiation environment on Mars. Currently two missions (MARIE/Odyssey and RAD/MSL) have provided data. The results are summarized in Fig. 3.23, 3.24 and 3.25. The measurements indicate a mean radiation level of 20 to 30 mrad/day, but any solar event may make these values increase by several orders of magnitude (one of the solar flares did actually break the MARIE instrument).

Calculations[108] made by Saganti and Cucinotta with the HZTERN model indicate variations in the dose with altitude (Fig. 3.26): higher altitudes offer less shielding (30 cSv

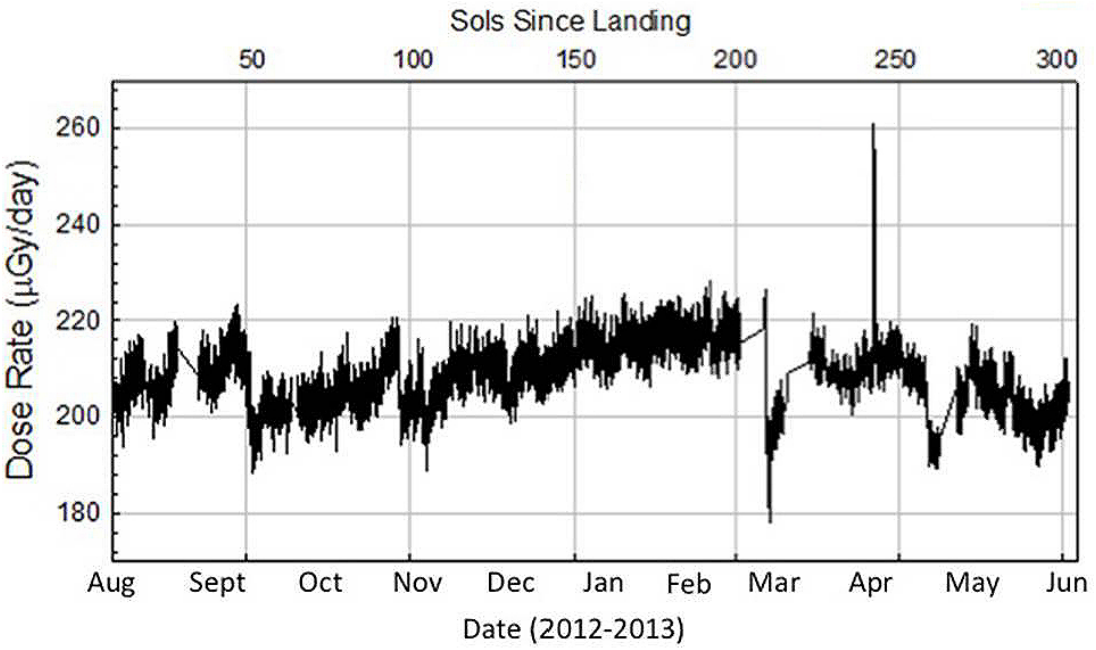


Figure 3.25: RAD/MSL radiation dose measurements on the surface, 2012-2013.

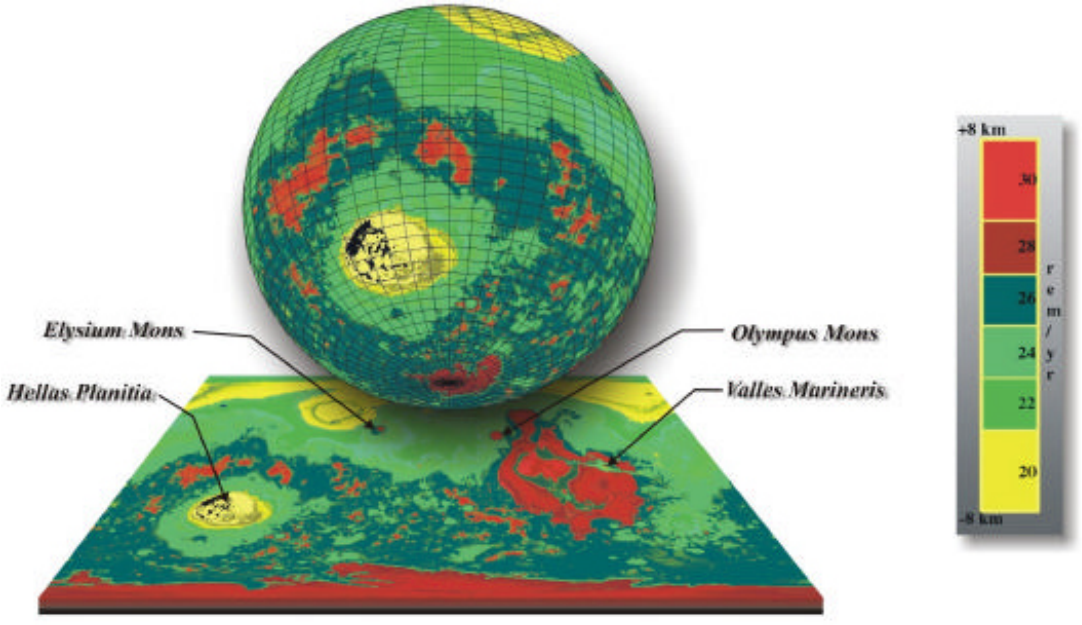


Figure 3.26: Calculations of the skin dose equivalent (cSv) for astronauts on the surface of Mars near solar minimum. Note that the centi-Sievert (cSv) refers to a biological effect, as opposed to the millirad which refers to a physical quantity.

$yr^{-1}$) and lower altitudes offer higher shielding (20 cSv $yr^{-1}$).

## 3.2 Climatic areas

In the following we present the results of the simulations made with MEMM. They represent the geographical distributions of the maxima, minima and averages of all the physical parameters of interest: atmospheric temperature, ground temperature, sky temperature, SW downwards and upwards fluxes, LW upwelling irradiance, and wind speed. In order for the scenario to be realistic, a simple seasonal variation of the atmospheric dust (dust optical range between 0.3 and 0.6) has been implemented in the simulation. An alternative approach should consider a best-case and a worst-case scenario (i.e., minimum and maximum expected dust levels). However this is left as a future improvement of the model. Note also that this study takes into account only the environmental (read: atmospheric) conditions. Geological issues are excluded and the same holds for any local atmospheric phenomena. Any future greenhouse design project, however, should deal with all these parameters for an accurate assessment.

In order to provide the reader with a clear and concise report of the results, only the plots concerning the final climatic areas are included in this chapter. The plots showing averages, maxima and minima are contained in Appendix B.

Several simulations have been run for the four reference dates of the year, i.e., the equinoxes and the solstices. In this way, we intend to address the best-case and worst-case scenarios. The results appear in Figs. 3.27 to 3.30: they show the average atmospheric temperature and allow to identify areas or zones characterized by the same value of this parameter. This constitutes a first attempt to draw a climatic map, since a complete picture should include several other quantities (e.g., topography, polar ice caps extension, mineralogy, surface dust, etc.).

Due to the eccentricity of the orbit of Mars, northern summers (e.g., Fig. 3.28) are colder than southern summers (Fig. 3.30). Spring and Fall equinoxes (Fig. 3.27,3.29) stand somewhere in the middle. Recall, however, that the Winter is shorter than the Summer. This means that apparently the most favourable southern Summer lasts less than the apparently least favourable northern Summer, whereas for the Winter the opposite is true, i.e., the southern Winter is longer and harsher than the northern Winter, which in turn is shorter and more temperate. The Spring equinox is also relatively colder than the

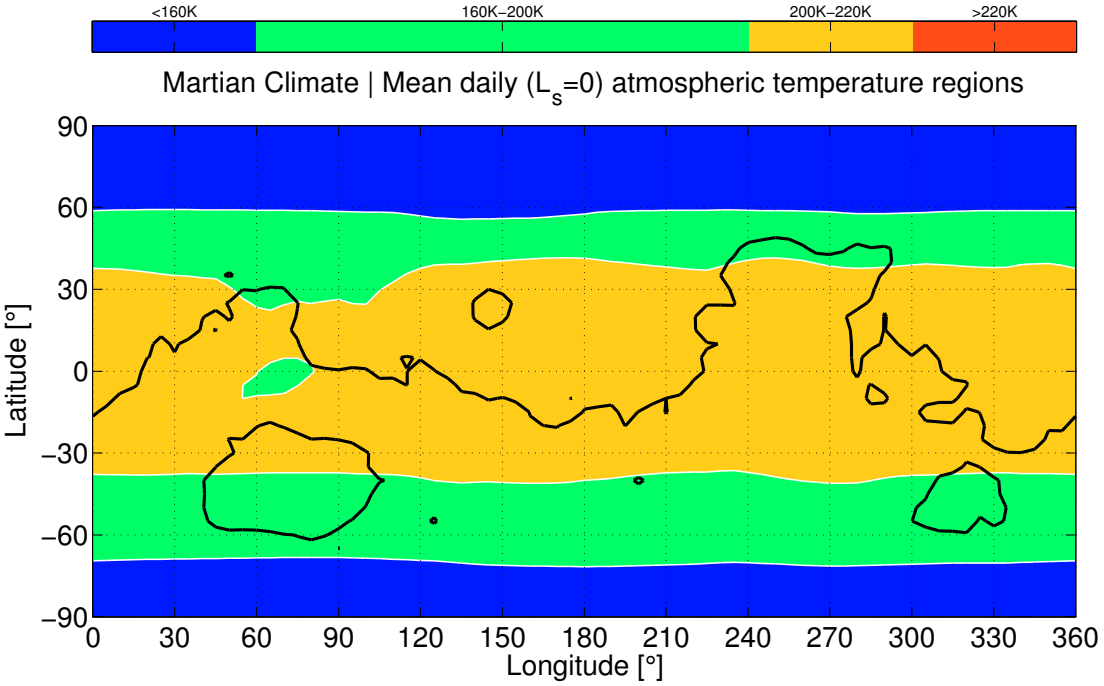


Figure 3.27: Climate areas, Spring equinox ($L_s$=0°).

Fall equinox, as the aphelion ($L_s$=70°) is closer to the Spring equinox and the perihelion ($L_s$=250°) is closer to the Fall equinox (see Fig. 3.1).

The lack of oceans is responsible for the periodicity of the climate and this ensures that the simulations performed over one year are representative of the conditions that can be found on a higher scale. In order to properly determine the climate over long periods of time (i.e., several Martian years), the simulation must be made by averaging the data from at least a full Martian year. This allows to take the aforementioned seasonal effects into account. The resulting annual climatic areas can be observed in Fig. 3.31. On a latitude basis, the polar regions between 60° and 90° and between -90° to -60° latitude in general are not favourable for long stays. The equatorial region between -30° and 30° latitude appear to be the most favourable. The most prominent feature of the Martian climatic map is perhaps its variability in longitude: regions between 120-190° (Elysium Planitia) and 240-330° (east of the Tharsis bulge) are slightly warmer. This fact is not entirely evident in Fig. 3.31 because of the colormap and scale adopted, but it can be clearly seen in the *Annual* plots contained in Appendix B). On the contrary, the region between 30° and 90° longitude (Tyrrena Terra) is colder as it lays on a low-albedo terrain.

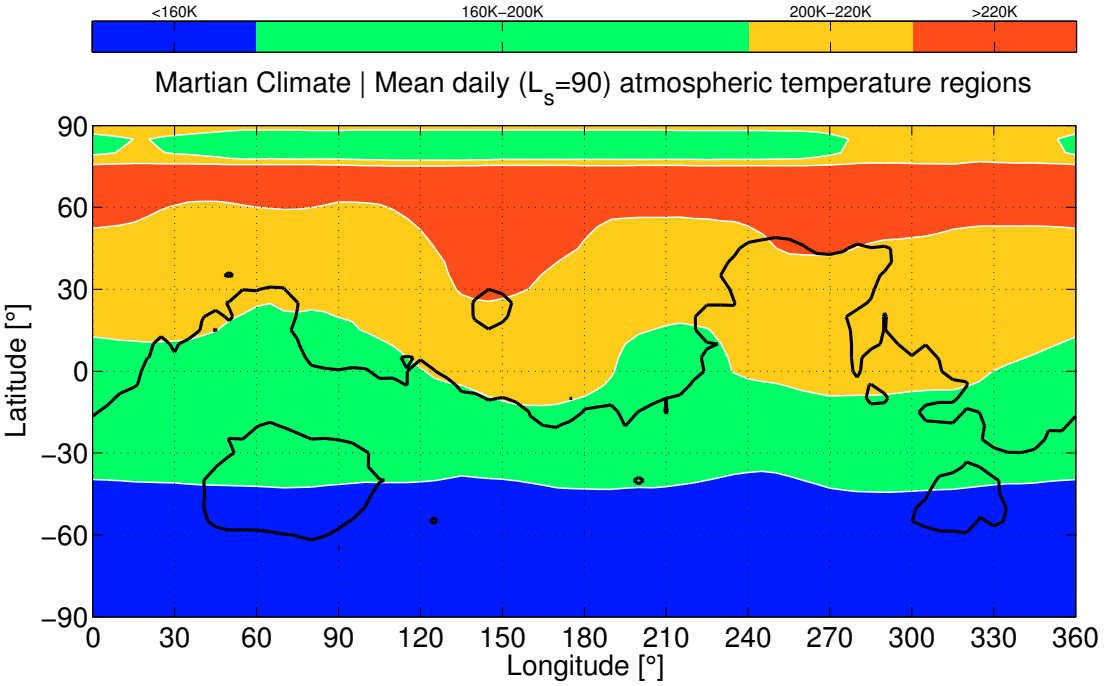


Figure 3.28: Climate areas, Summer solstice ($L_s$=90°).

## 3.3 Site analysis

Several sites have been selected for further analysis: they are either locations visited by past missions or sites that have been previously considered for sending landers and/or rovers. We wish to emphasise that the final selection of the most suitable site for the installation of the greenhouse is out of the scope of this work, since it requires the evaluation of additional aspects concerning geology, mineralogy, local terrain orography and in terms of scientific objectives.

### 3.3.1 Valles Marineris

Valles Marineris is a set of canyons near the equator, east of the Tharsis bulge (≈290° longitude). The central part, named Melas Chasma, was considered as landing site for the MSL mission. It is located in one of the most favourable climatic zones, and the low terrain (-4km) provides protection against particle radiation (≈20cSv). The main drawback is that the canyon has an altitude gap of 8km between the lowest basin and the surrounding highlands, which may obstruct the Sun at low elevation angles (in the morning and in the evening). In its current version, MEMM does not take such effect into account: it should be either separately assessed or implemented in a future release

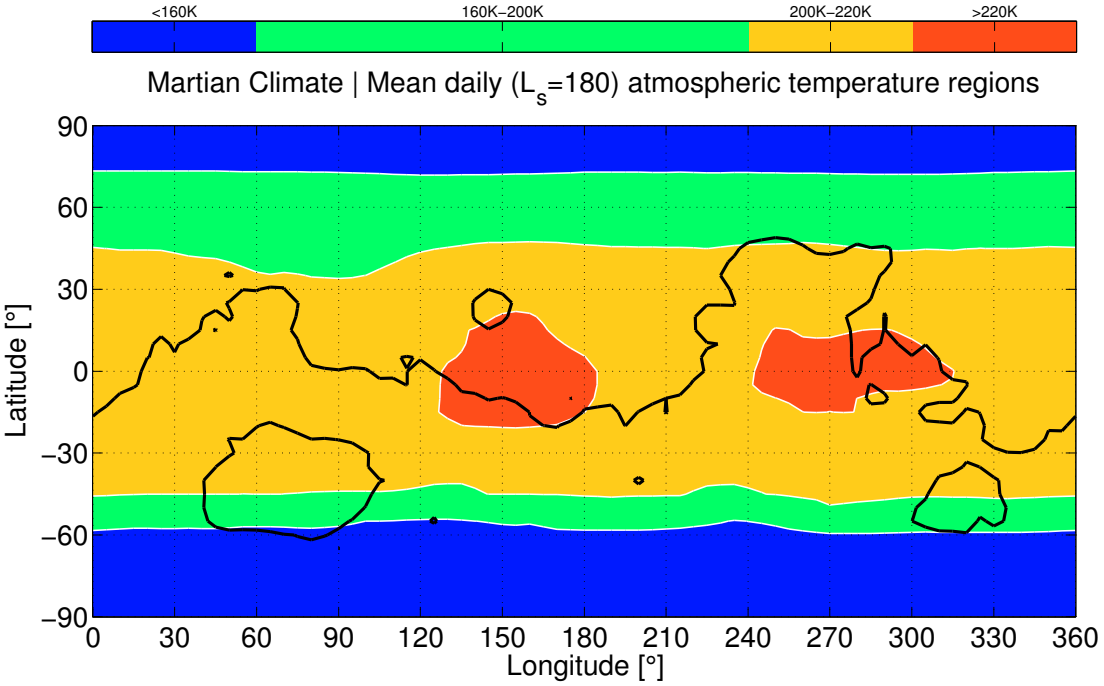


Figure 3.29: Climate areas, Fall equinox ($L_s$=90°).

of MEMM. The annual evolution of several parameters of interest is shown in Fig. 3.32.

Melas Chasma exhibits annual atmospheric temperature variations of 30K and a daily variation of 50K. The mean temperature is 215K, with a global maximum at nearly 260K and a global minimum of 180K. Ground temperatures can reach positive values in degrees Celsius throughout the Winter. The pressure ranges from 700Pa to 1kPa, and the density remains fairly constant at 0.02 kg m$^{-3}$. This site receives a maximum downwards radiation flux of 700 W m$^{-2}$ and is characterized by a maximum upwards flux of 520 W m$^{-2}$.

### 3.3.2 Gale Crater

The Gale crater is the landing site of the MSL/Curiosity rover. It is located south of the Elysium Planitia in one of the most favourable climatic zones. The terrain height (-4km to -3km, similar to Vallis Marineris) offers protection against particle radiation, and the moderate height offset of the surrounding terrain (≈2km) does not obstruct the Sun as much as in Valles Marineris. The annual evolution of several parameters of interest is provided in Fig. 3.33.

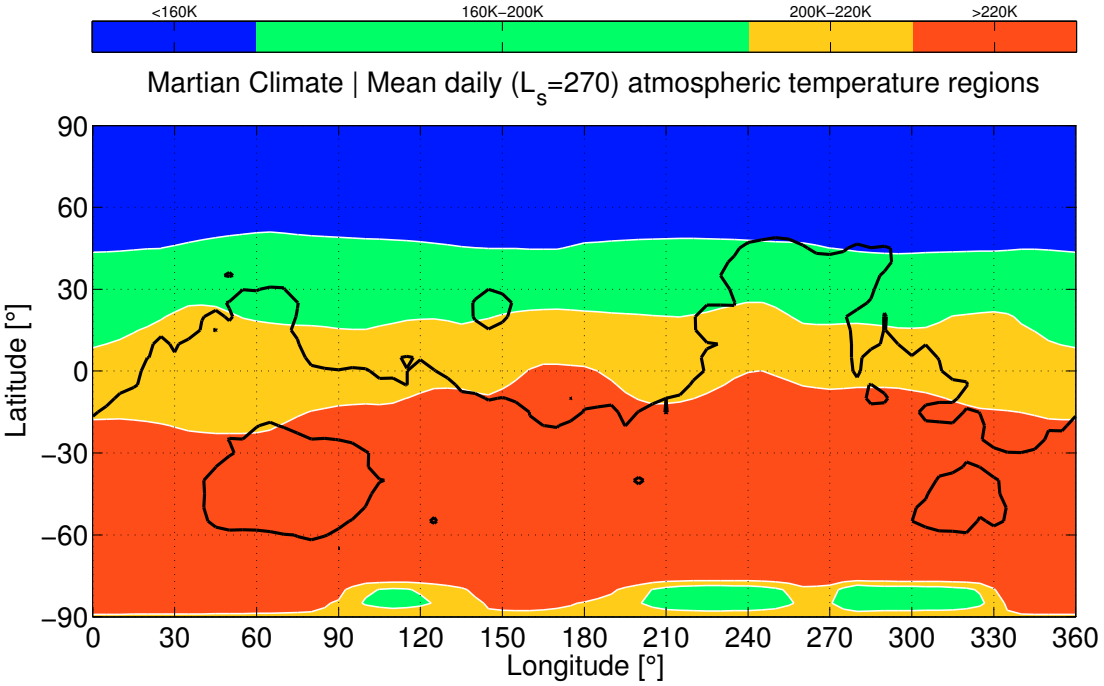


Figure 3.30: Climate areas, Winter solstice ($L_s$=270°).

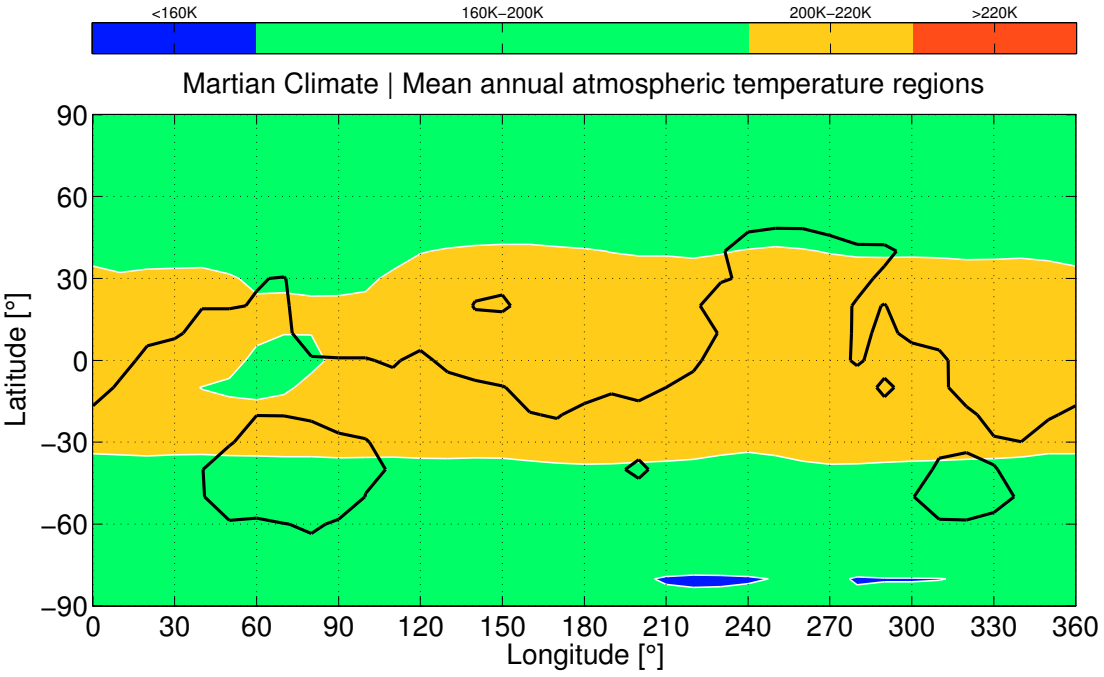


Figure 3.31: Climatic areas, annual simulation.

The conditions at Gale Crater are extremely similar to those found at Melas Chasma, except for the pressure and the density which are lower on a general scale (-200Pa and -5 g $m^{-3}$, respectively). The ground temperature is slightly lower and the same holds for the wind speed during Winter.

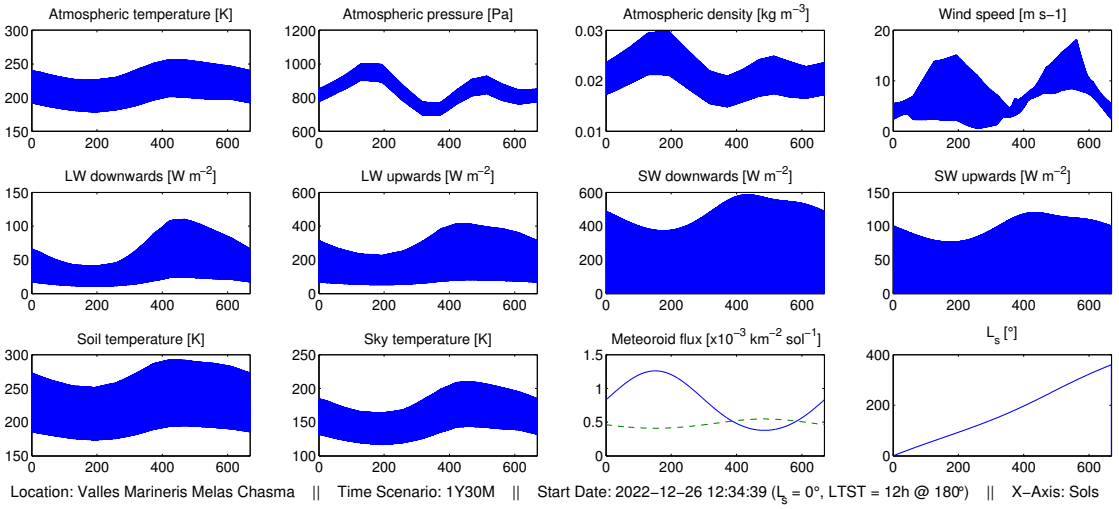


Figure 3.32: Multiplot of Melas Chasma environment, for a full Martian year.

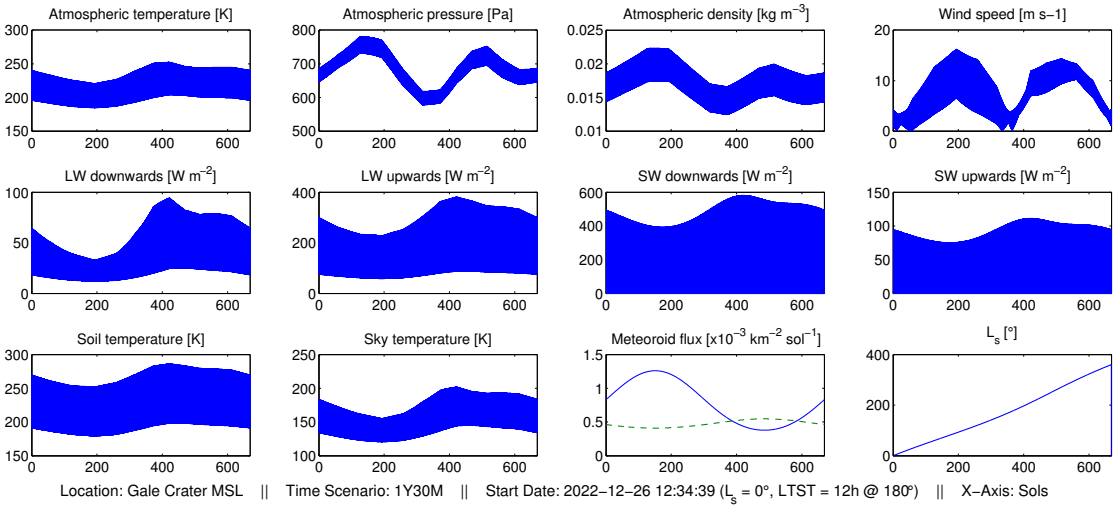


Figure 3.33: Multiplot of the environment at Gale Crater over one Martian year.

### 3.3.3 Olympus Mons Crater

The Olympus Mons is located north-west of the Tharsis bulge. With its 18km, it is the highest mountain of Mars and the second highest mountain of the Solar System. Its characteristics are discussed here for the sake of comparison with more favourable environments in the lower lands. The annual evolution of several quantities of interest can be found in Fig. 3.34.

The conditions at the crater of Olympus Mons are far more extreme than in the lower lands. The atmospheric mean temperature remains fairly constant throughout the year (10K variations), whereas the daily variations are large (80K). The density and pressure

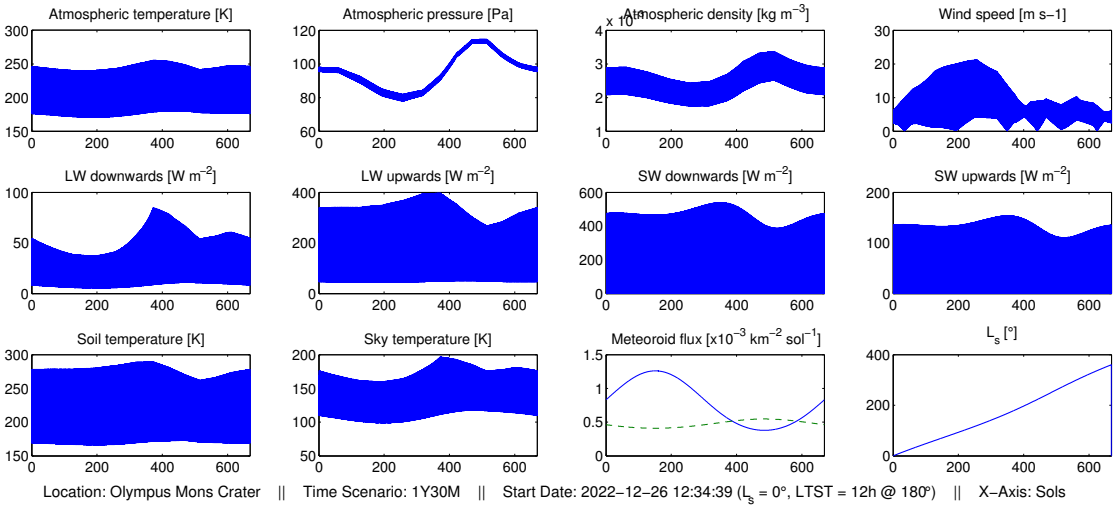


Figure 3.34: Multiplot of the environment at Olympus Mons crater over one Martian year.

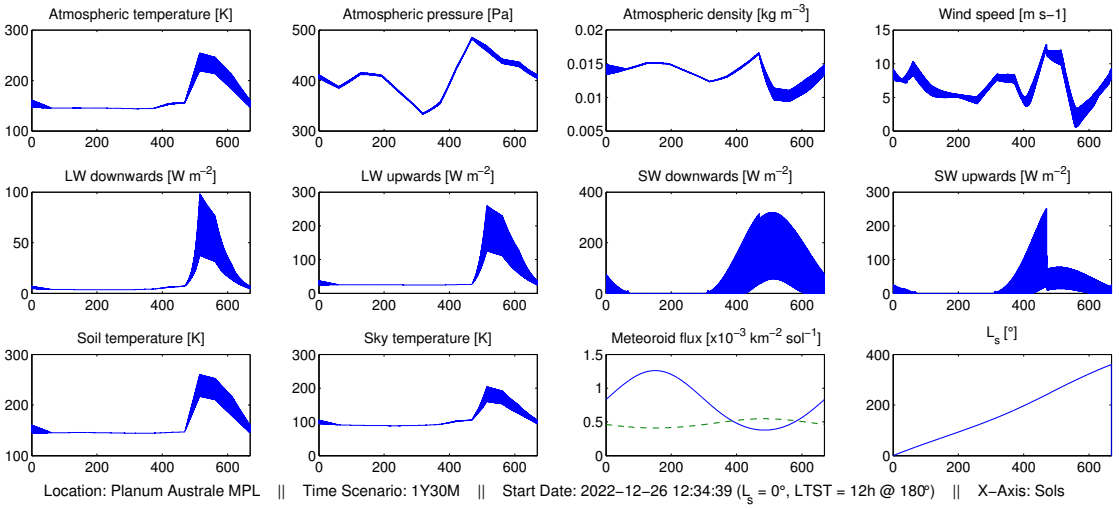


Figure 3.35: Multiplot of the environment at Planum Australe over a full Martian year.

are one order of magnitude lower than at Melas Chasma. As the dim atmosphere provides virtually no protection, the particle radiation flux is almost that of free space.

### 3.3.4 Planum Australe

Planum Australe, located almost at the south pole, was selected as the landing site for the Mars Polar Lander mission. The lander failed during descent and the mission was lost. The Martian poles are interesting due to their extreme conditions.

As illustrated in Fig. 3.35, if Olympus Mons is extreme on a daily basis then the south pole is extreme on an annual basis. During 60% of the year, the pole remains at a

constant temperature of 150K, and virtually no SW irradiation reaches or is reflected by the surface. Then, close to the Winter solstice (i.e., in the southern Summer), the temperature drastically rises to a daily range between 220K and 260K. Note also that during this period the Sun never sets, thus providing a continuous radiation flux although with a maximum which is half that found at Melas Chasma. Temperature and pressure are also half those at Melas Chasma throughout the year. There is virtually no daily variation of pressure and density, not even in Winter.

# Chapter 4

# Conclusions and future work

In this chapter, we draw the conclusions of the study and we discuss its possible future developments. The objective of this work was to obtain a quantitative picture of the environment and climate of Mars in a way which could be useful to the design of a greenhouse.

Over the past 50 years an impressive technological and design progress has characterized the missions sent to Mars. From the first probes that carried only few simple atmospheric measurement devices (thermometers, pressure sensors and anemometers) to the MSL/Curiosity rover, a car-sized mobile laboratory loaded with several cameras, spectrometers, radiation detectors, and of course, improved atmospheric and environmental sensors. Nevertheless, the mission that has provided the most complete global-scale data about Mars is Mars Global Surveyor, whose information is used nowadays in most of the environmental models available (e.g., MarsGRAM). The data collected by the in-situ missions have allowed to obtain a fairly good understanding of the present Martian atmospheric properties (temperature, pressure, density, and composition), the global-scale soil properties (albedo and composition), and the topography. However, many aspects (e.g., winds and dust storms, UV radiation, particle radiation, local soil, dust and rocks composition, etc.) are still not well known and thus require further and more accurate measurements and physical models.

This study has led to the construction of a macro-model called MEMM that provides an up-to-date physical description of the Martian environment. It can be employed both as a scientific tool and an engineering tool. MEMM has been successfully implemented by

integrating some of the most complete models available (i.e., MarsGRAM, MarsRAD, Pollack, Divine), by adding functionalities and interfaces among the original modules, by implementing further physical treatment, and by identifying discrepancies among the components, improving their sinergy and correcting bugs. Data from the MGS/TES and MSL/Curiosity have been added to supplement information concerning the soil mineralogical composition and the particle radiation environment, respectively. As a result, MEMM provides all the environmental quantities required as input to the thermodynamic study of a greenhouse.

The Martian environment is quite different from the Earth's environment. Due to the higher eccentricity of the Martian orbit, the seasons differ much in terms of duration: the northern hemisphere has long, relatively warm winters and short, mild summers, while the southern hemisphere has long, cold winters and short, relatively hot summers. Note that the concept of hot here is relative: atmospheric temperatures on Mars rarely exceed 0°C can be as low as -120°C during the coldest winters. Ground temperatures, however, can sometimes reach 25°C during the Summer. The atmosphere is very weak and light, not far from vacuum, exhibiting less than 1% of the Earth's atmospheric pressure and about 2% of its density. Any future habitat/greenhouse shall therefore implement a certain degree of pressurization. Moreover, the thin atmosphere together with the lack of planetary magnetic fields make the particle radiation levels on the surface extremely high, especially during solar particle events. Any future settlement shall actively shield the habitats, settle on the lowest regions where the atmosphere mildly attenuates the radiation dose, or search for protection inside caves in the highlands where the atmosphere offers virtually no protection. The Martian dust may also constitute a serious enemy, as the winds and the occasional storms can accumulate dust on nearly horizontal surfaces, thus covering equipment and reducing the amount of effective absorbed solar fluxes. Surface dust, in turn, make the terrain soft and unstable, which is bad for building stable structures. Generally, areas with high albedo are potentially covered with dust and are therefore not attractive as landing sites. The solar flux at Mars is nearly half that reaching the Earth, and during a major dust storm the sunlight is almost completely blocked, although the diffuse component boosts up the resulting flux levels to nearly 60% of the clear-sky values. On a climate basis, the polar regions from 60° to 90° and from -90° to -60° latitude in general are not favourable for long stays due to

the average low temperatures. The equatorial region between -30° and 30° latitude appears to be the most favourable choice, with daily average temperatures ranging from -50°C to -70°C. Longitude-wise, the regions between 120-190° (Elysium Planitia) and 240-330° (east of the Tharsis bulge) are slightly warmer. On the contrary, the region between 30 and 90° (Tyrrena Terra) is colder as it lays on a low-albedo terrain.

Despite the huge amount of work and effort spent to prepare MEMM and to give it a self-standing structure, several improvements and extensions can be envisaged. MEMM is a modular software and as such it easily lends itself to upgrades and replacement of models. MarsGRAM should be updated as soon as new versions become available, refined using the experimental data from the most recent missions (e.g., MER, MSL, etc.). The meteoroid models (Dycus and Divine) should be replaced by a more advanced and sophisticated description, preferably one giving the directionality of the meteoroid flux. Models depicting the particle radiation environment and the mineralogical composition of the ground should also be implemented as soon as they are available. Finally, the climate maps described in Sect.3.2 should be improved by taking into account the global topography, the extension of the polar ice caps, the mineralogy and the surface dust distribution.

As a final concluding remark, we wish to point out that several models of the Martian environment exist, but to the author's knowledge none gives the global view provided by MEMM. Therefore this work has a strong character of originality.

# Appendix A

# TES Mineral Maps

We present several mineralogical maps extracted from the TES/MGS mission RAW data.

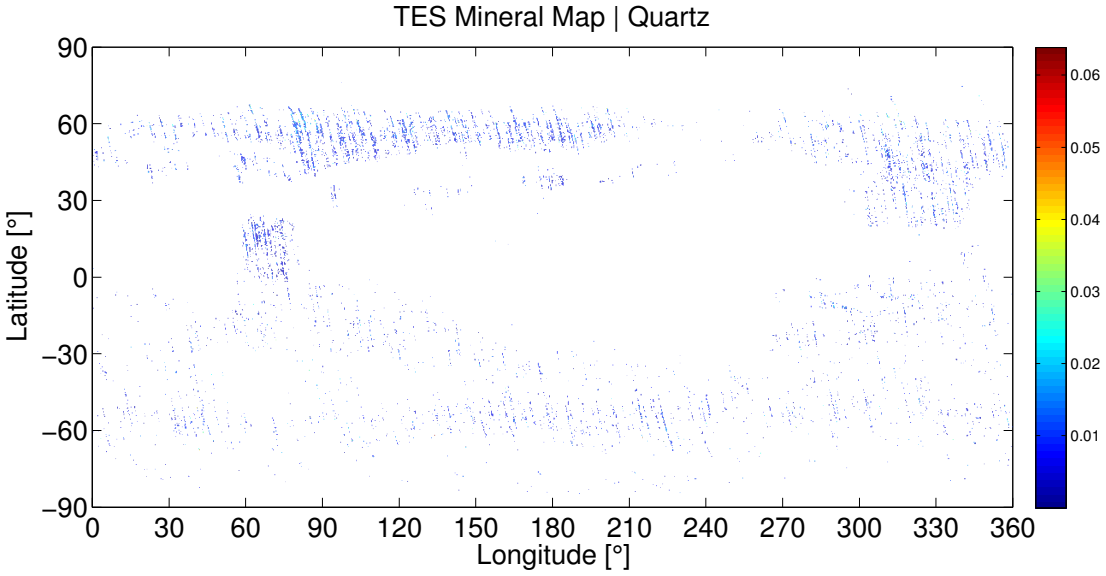


Figure A.1: TES plot of the Martian surface mineralogy. Quartz

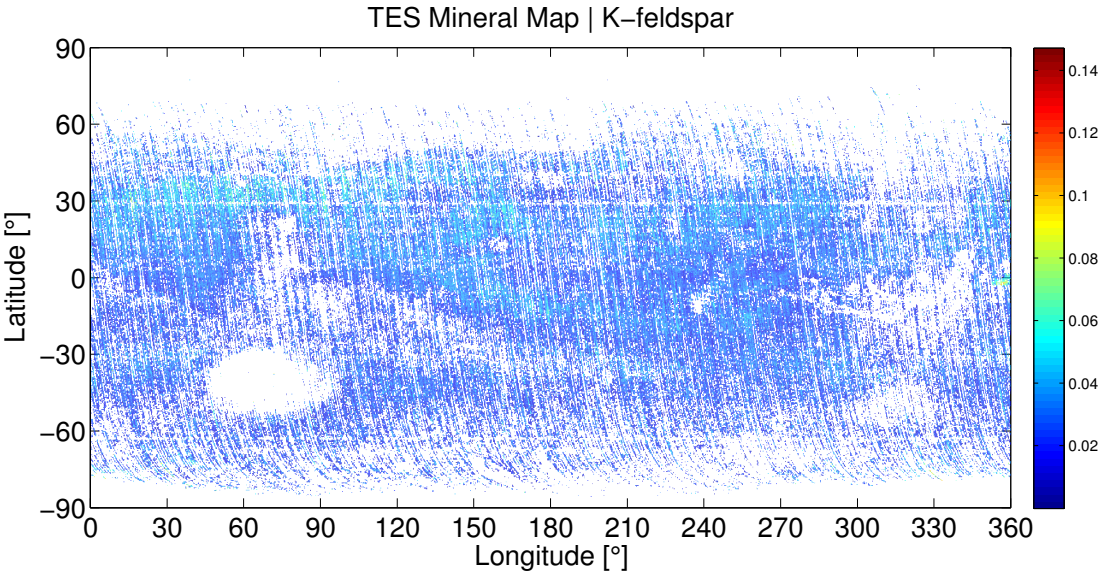


Figure A.2: TES plot of the Martian surface mineralogy. K-feldspar

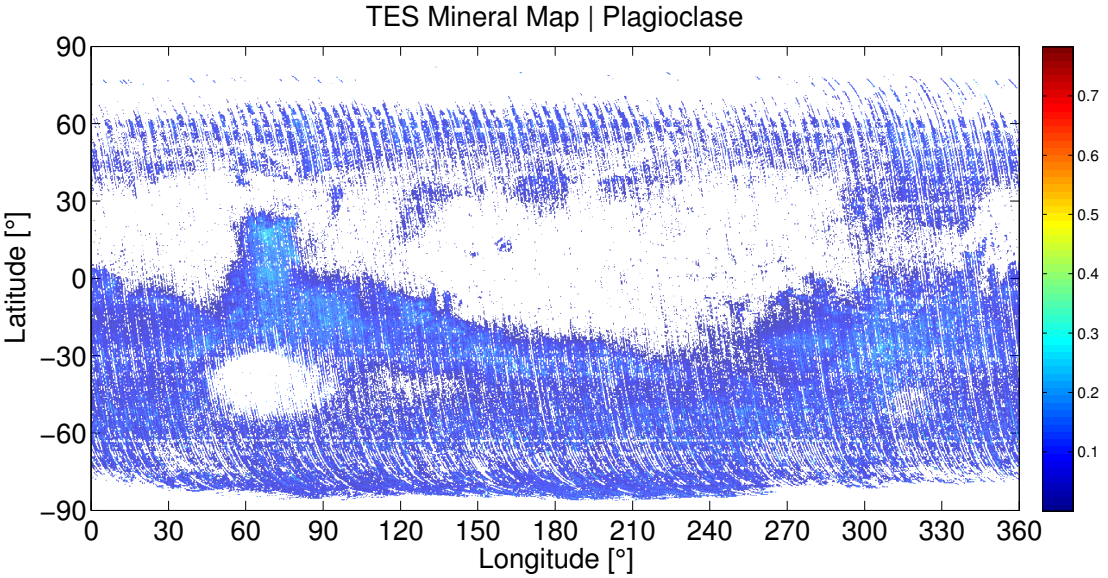


Figure A.3: TES plot of the Martian surface mineralogy. Plagioclase

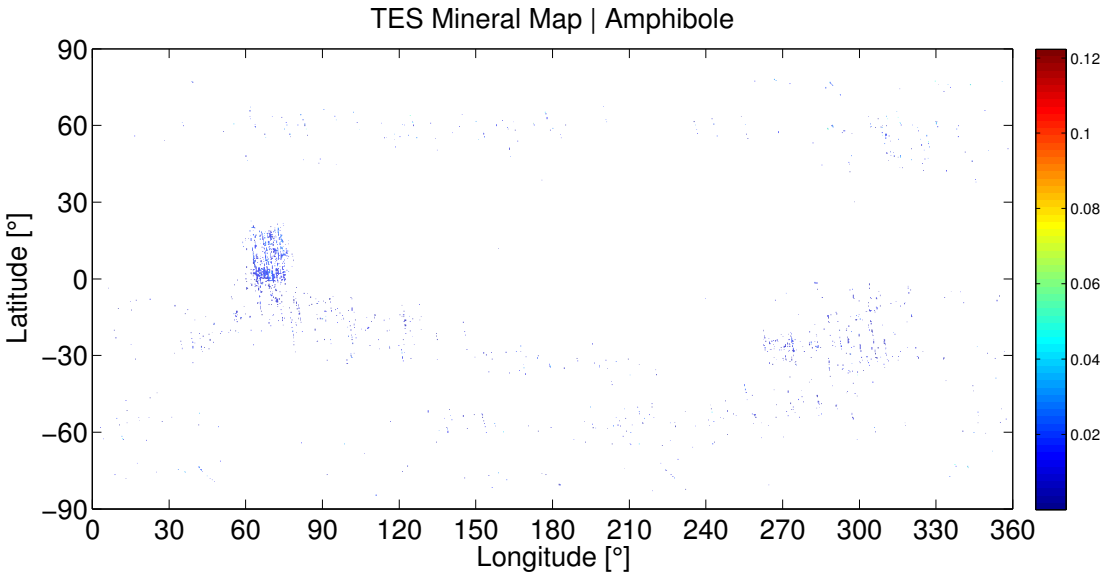


Figure A.4: TES plot of the Martian surface mineralogy. Amphibole

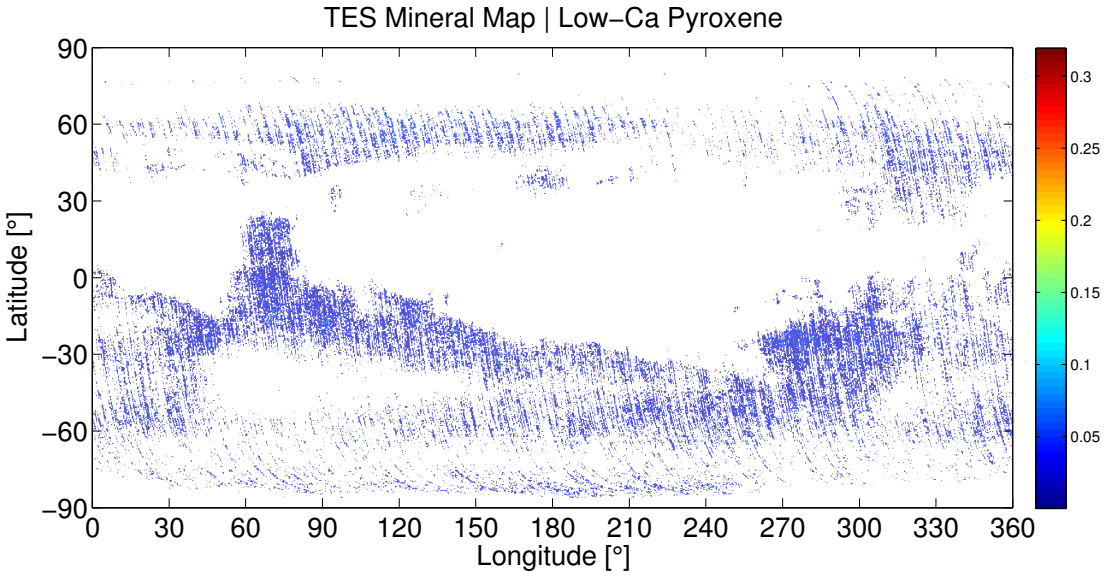


Figure A.5: TES plot of the Martian surface mineralogy. Low-Ca Pyroxene

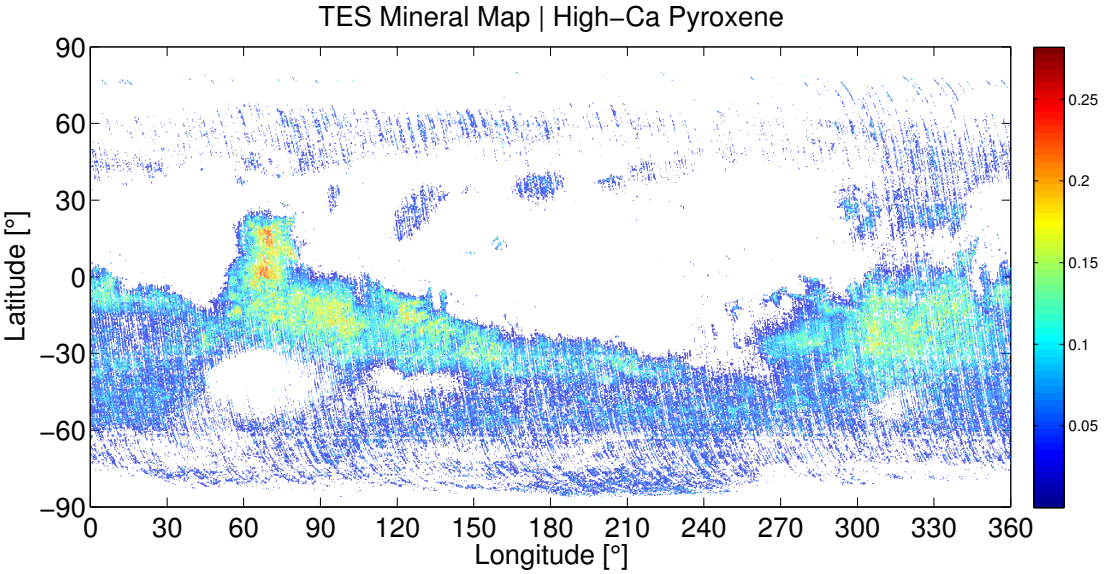


Figure A.6: TES plot of the Martian surface mineralogy. High-Ca Pyroxene

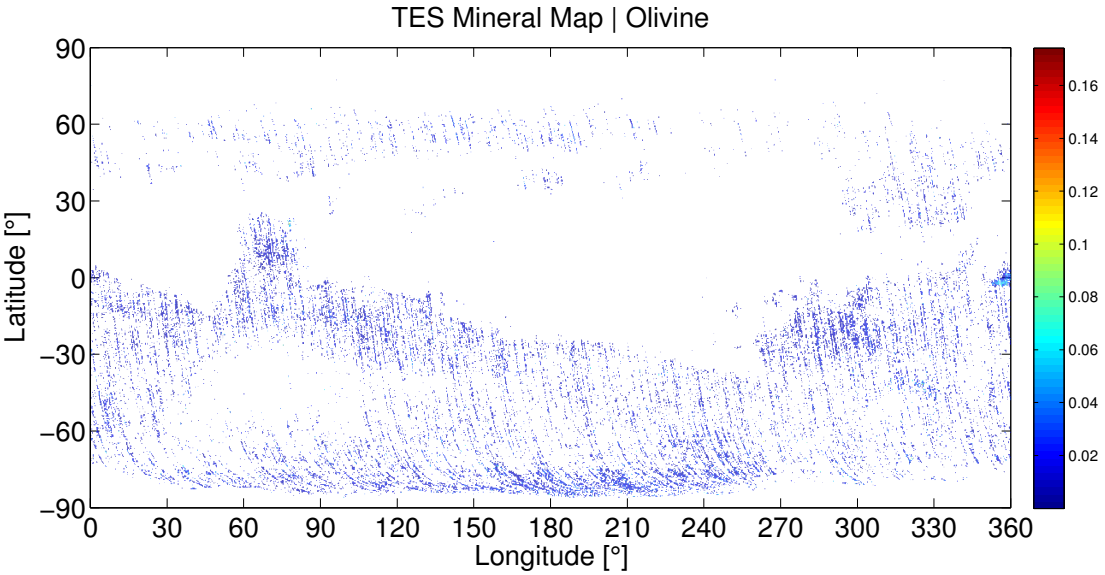


Figure A.7: TES plot of the Martian surface mineralogy. Olivine

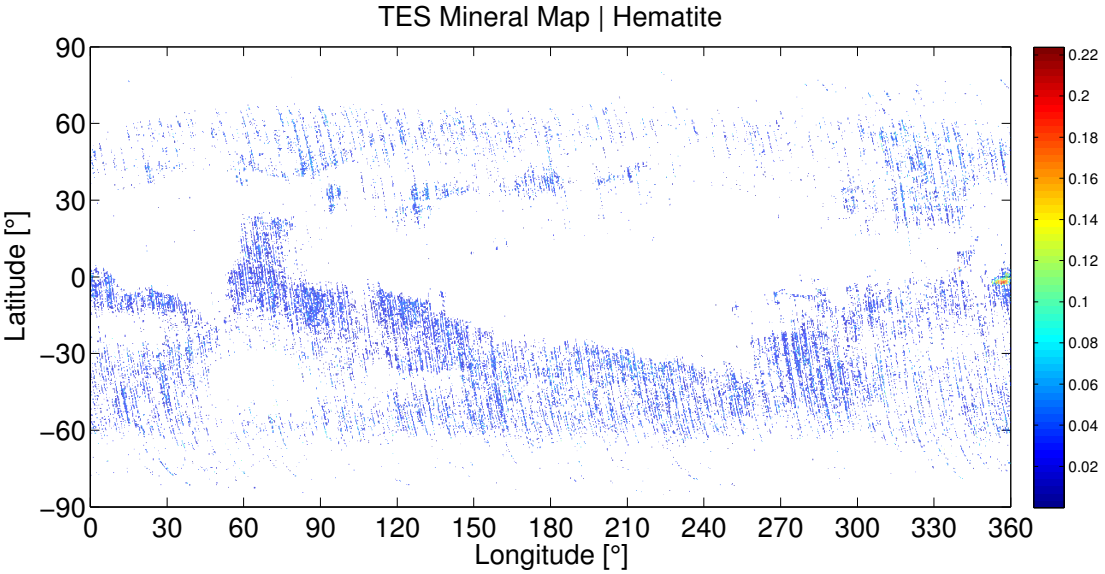


Figure A.8: TES plot of the Martian surface mineralogy. Hematite

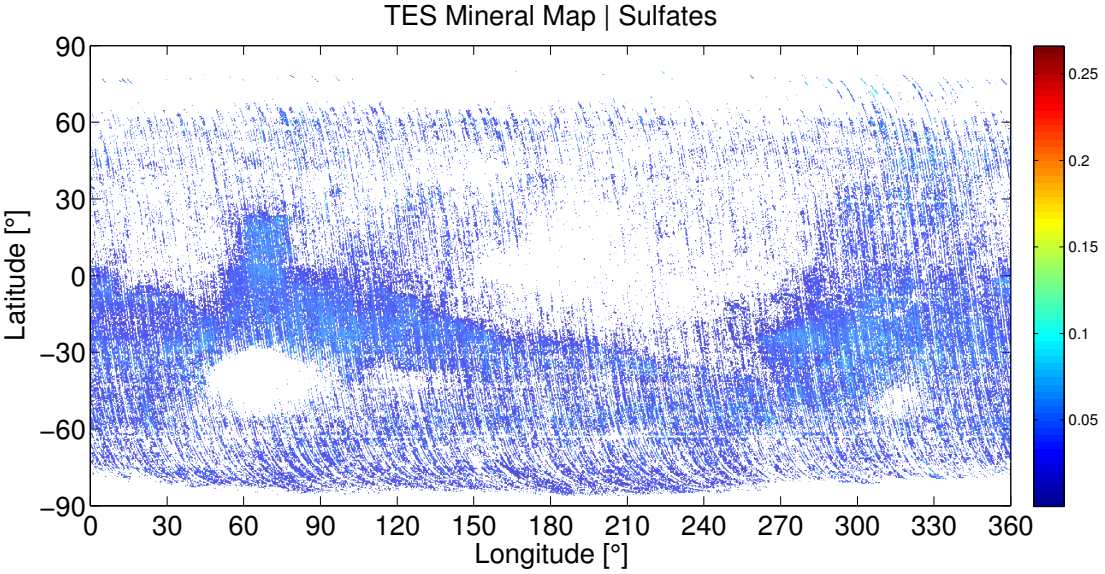


Figure A.9: TES plot of the Martian surface mineralogy. Sulfates

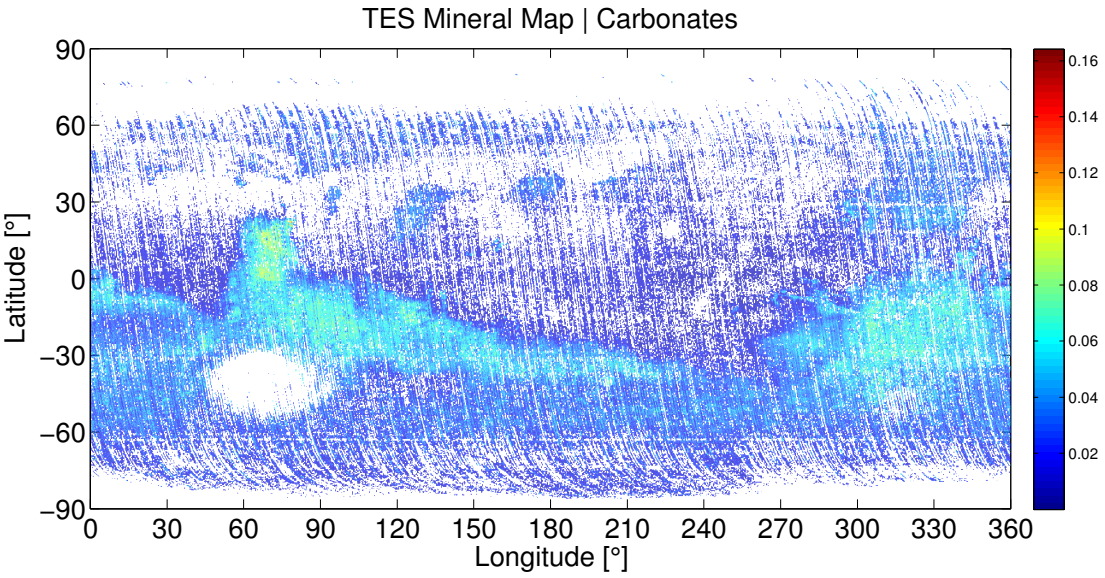


Figure A.10: TES plot of the Martian surface mineralogy. Carbonates

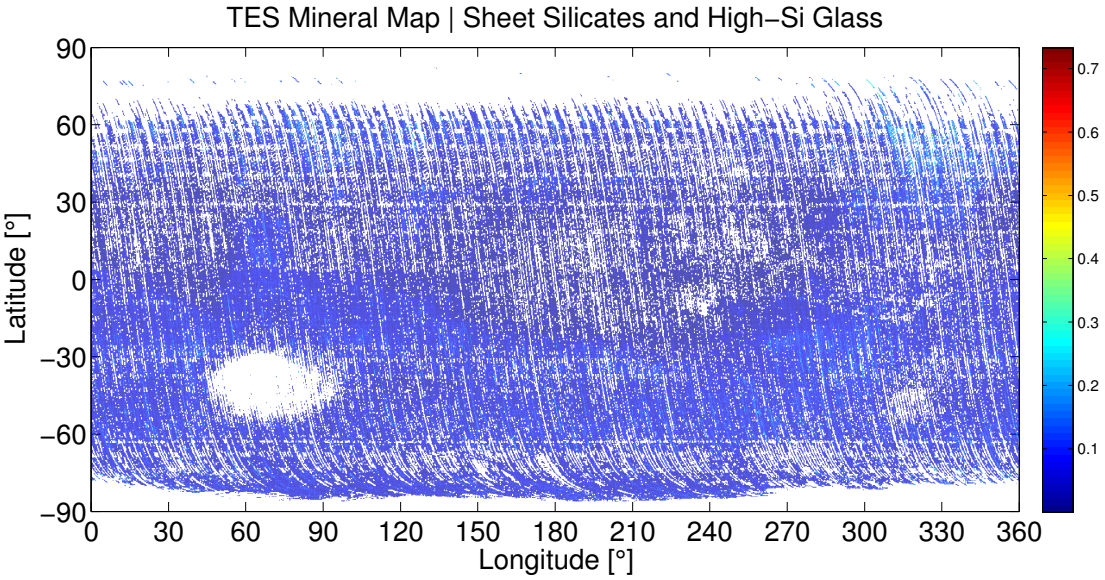


Figure A.11: TES plot of the Martian surface mineralogy. Sheet Silicates and High-Si glass

# Appendix B

# Daily and seasonal plots

We present the additional results of MEMM simulation, as exposed in Sect. 3.2. All the plots represent the average, maximum, and minimum values for each of the quantity of interest (atmospheric temperature, ground temperature, sky temperature, SW downwards and upwards irradiance, LW upwelling irradiance, and wind speed). Note that no LW downwards irradiance has been included due to its relatively low impact (less than 4%) in the total irradiance. Also, the minimum values for the SW components are not included, being always 0 (night-time).

## B.1 Spring equinox

The results for the Spring equinox ($L_s$=0°) are presented below.

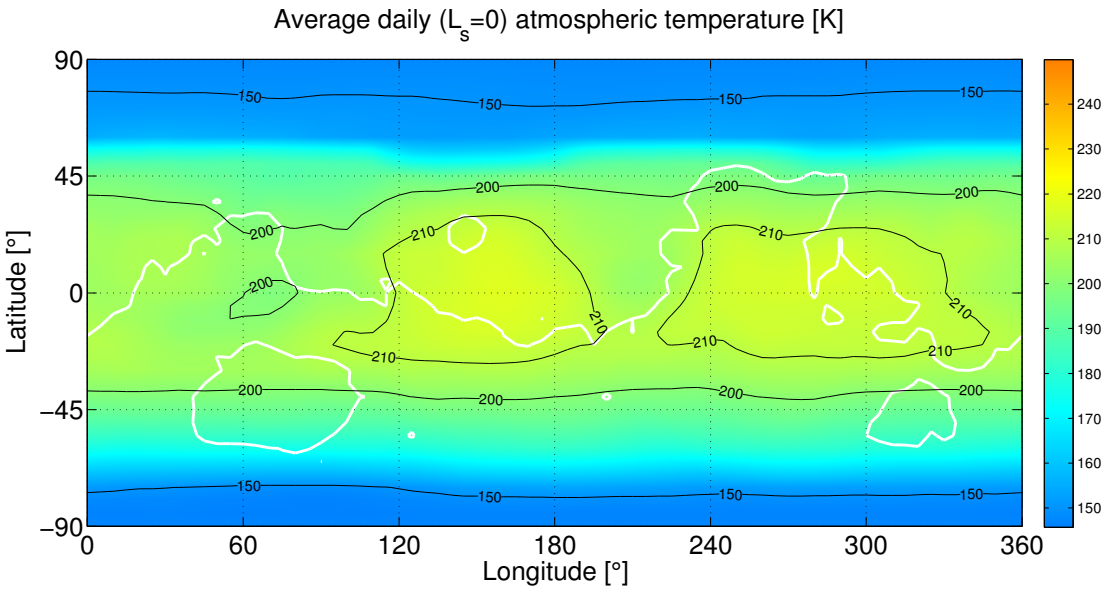


Figure B.1: Average daily atmospheric temperature

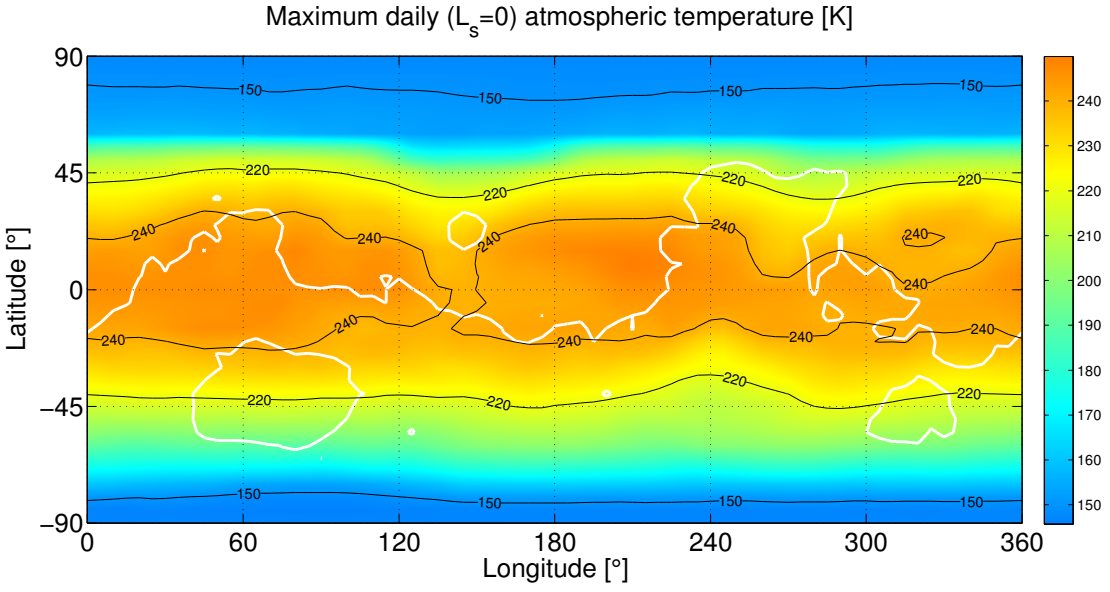


Figure B.2: Maximum daily atmospheric temperature

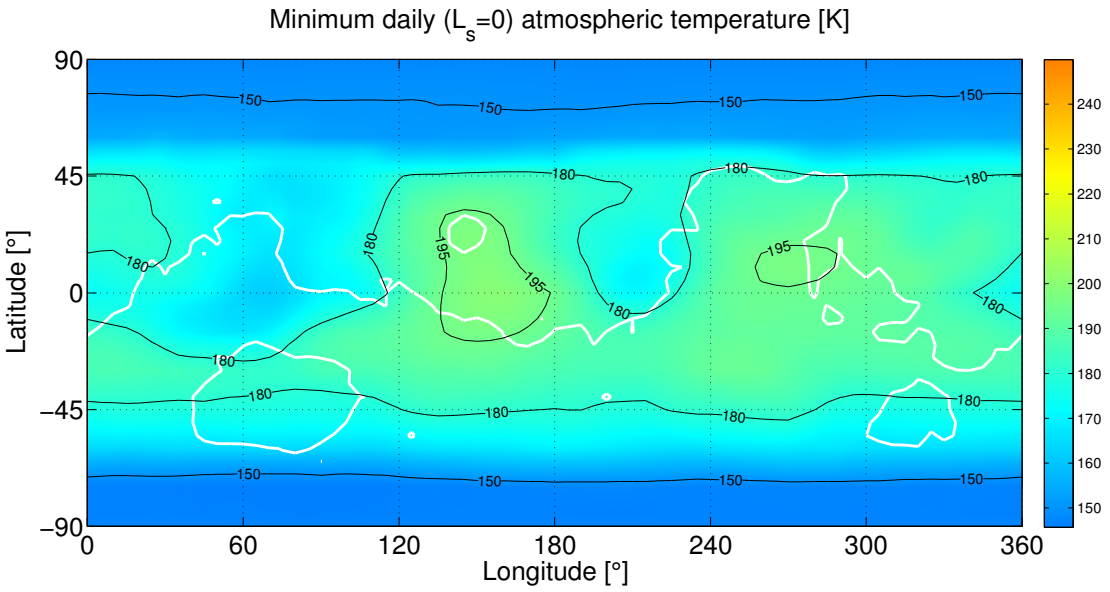


Figure B.3: Minimum daily atmospheric temperature

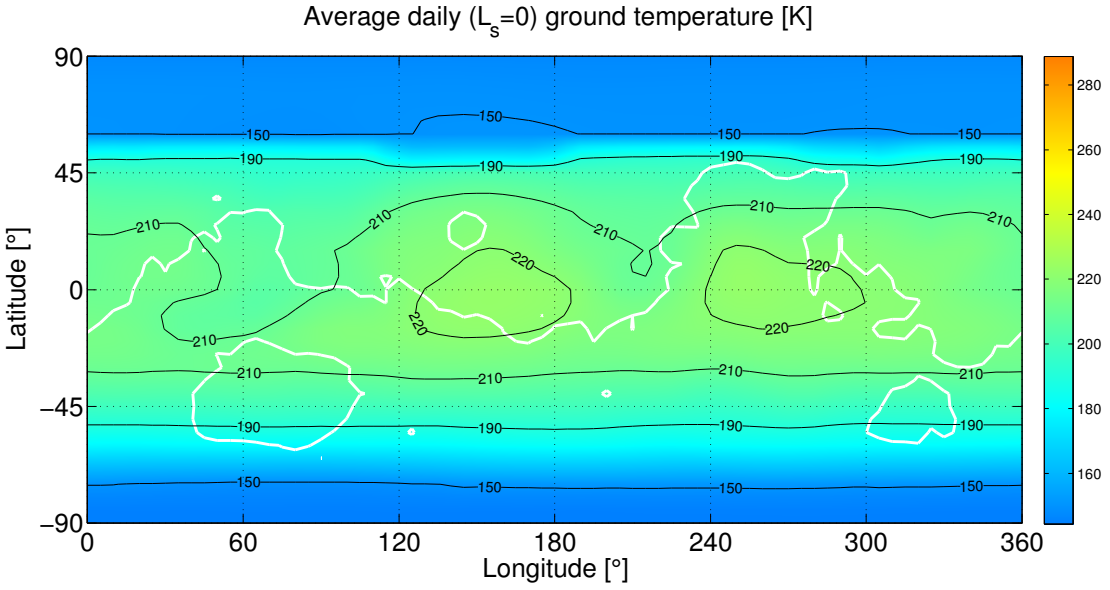


Figure B.4: Average daily ground temperature

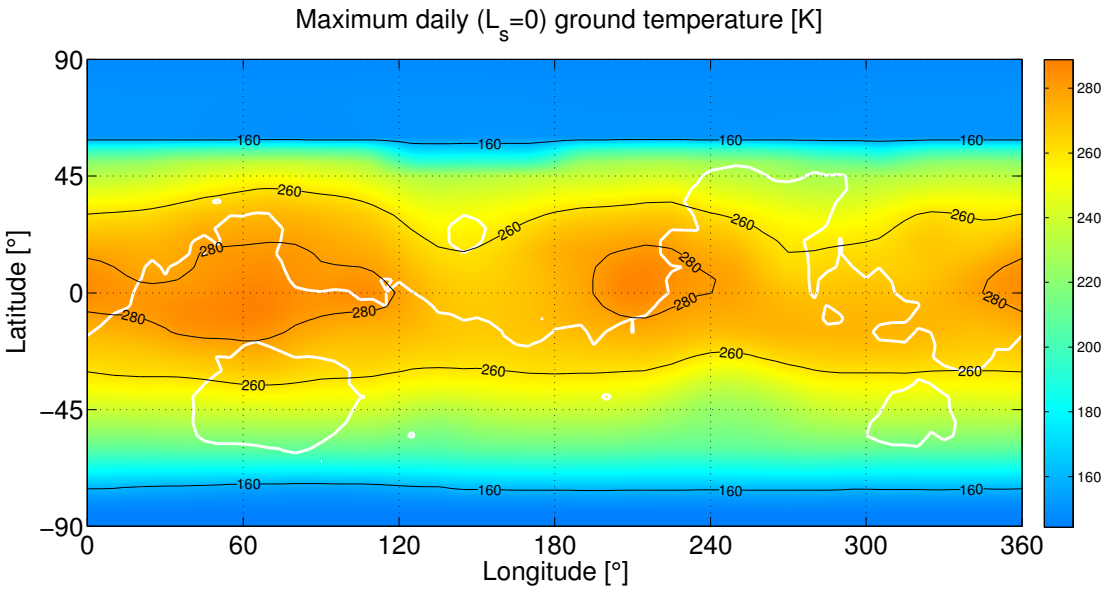


Figure B.5: Maximum daily ground temperature

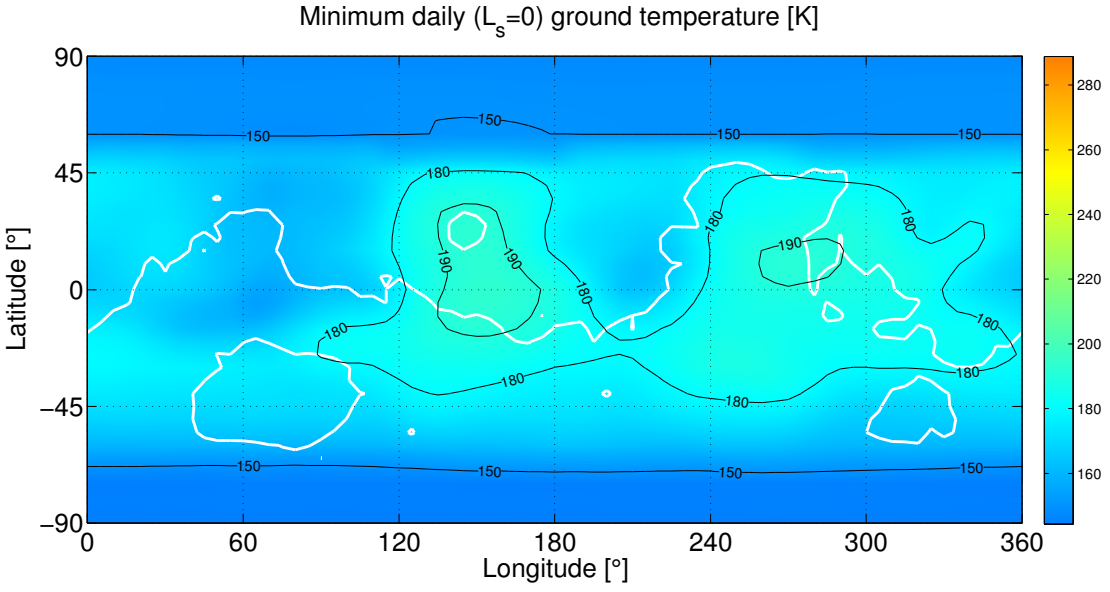


Figure B.6: Minimum daily ground temperature

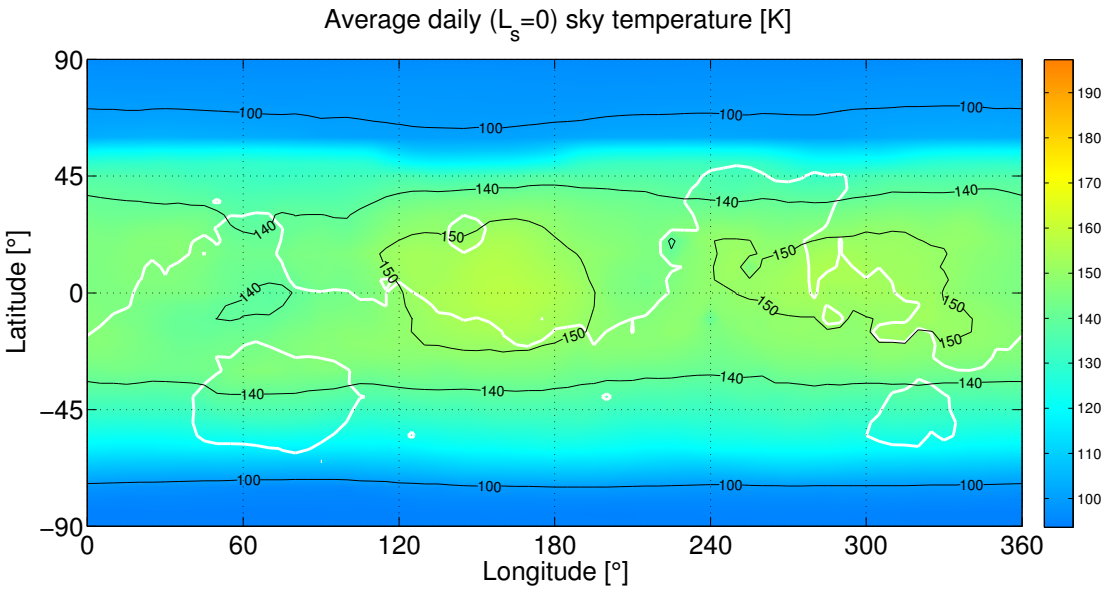


Figure B.7: Average daily sky temperature

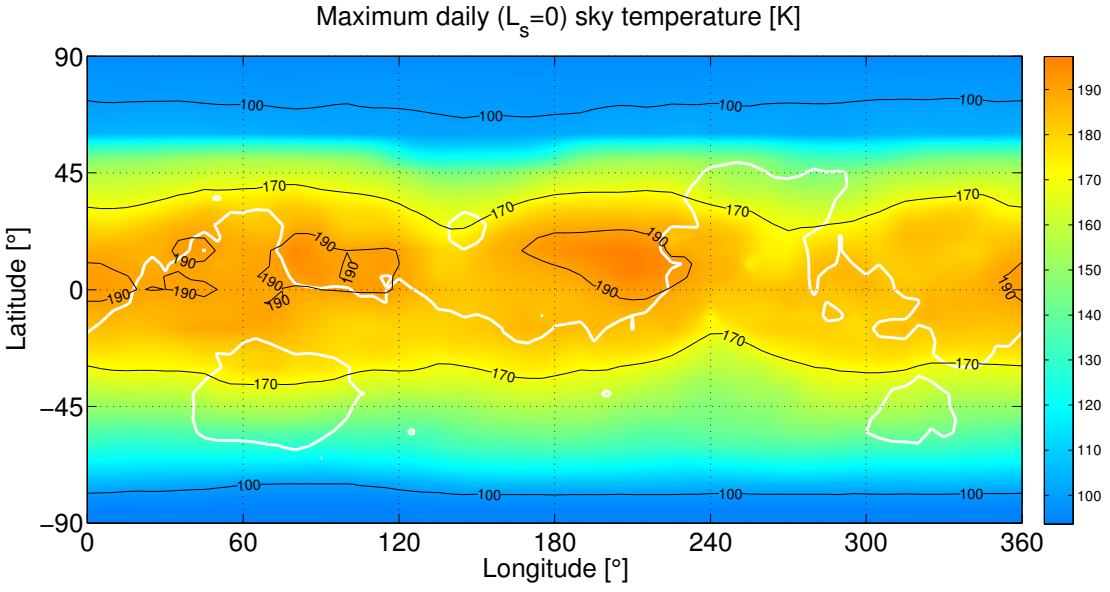


Figure B.8: Maximum daily sky temperature

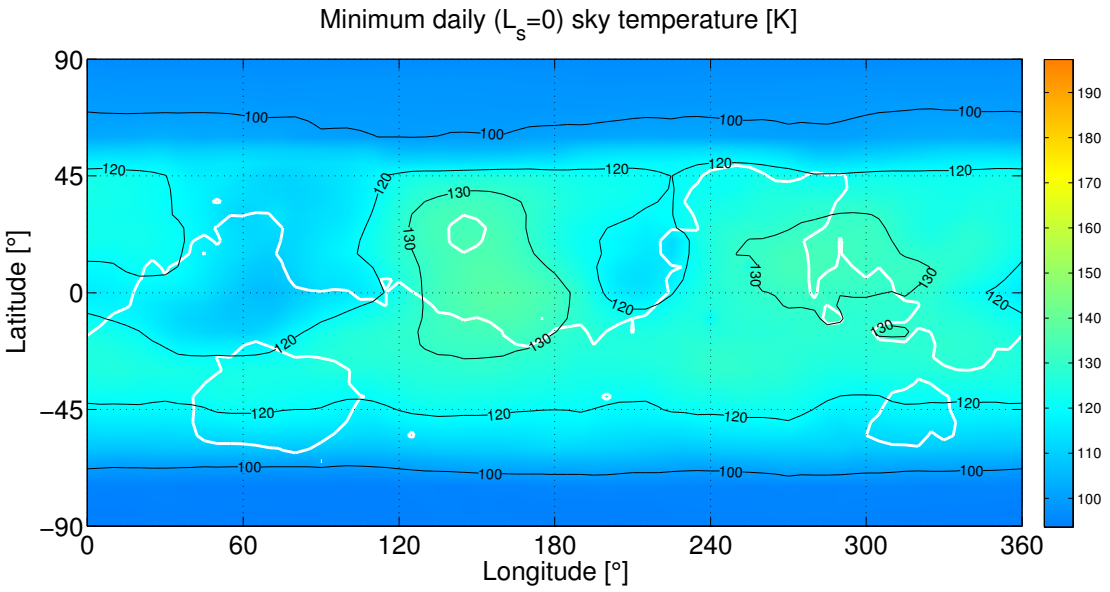


Figure B.9: Minimum daily sky temperature

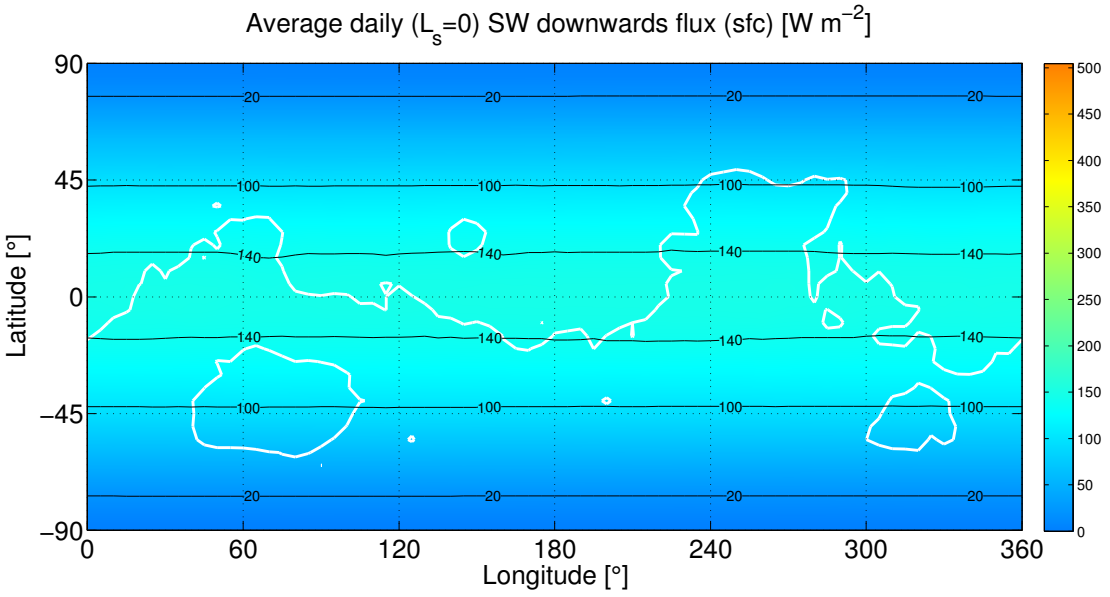


Figure B.10: Average daily SW downwards flux (surface)

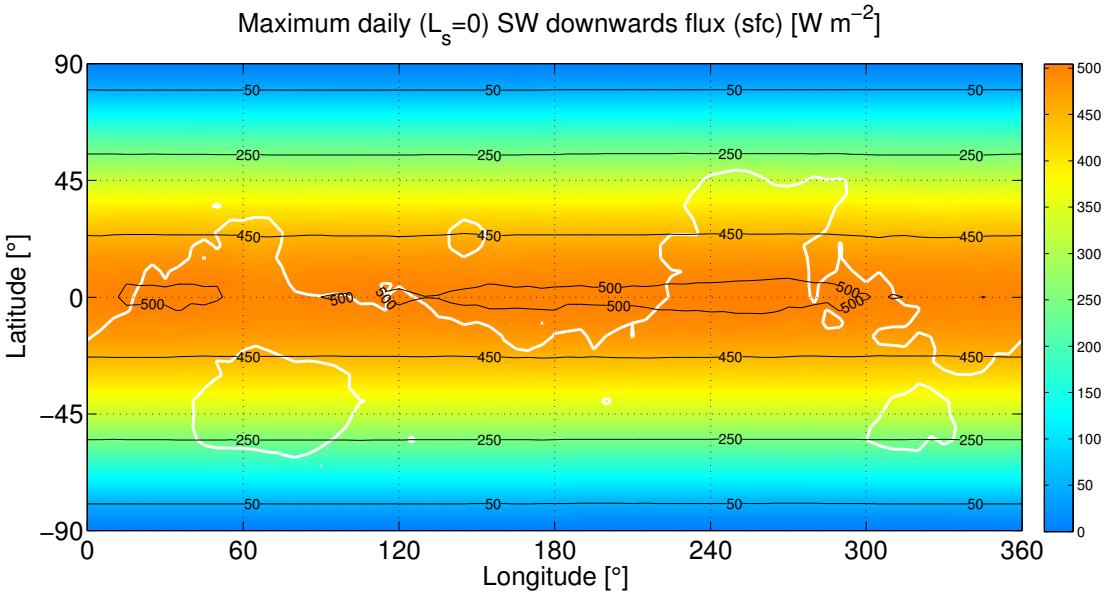


Figure B.11: Maximum daily SW downwards flux (surface)

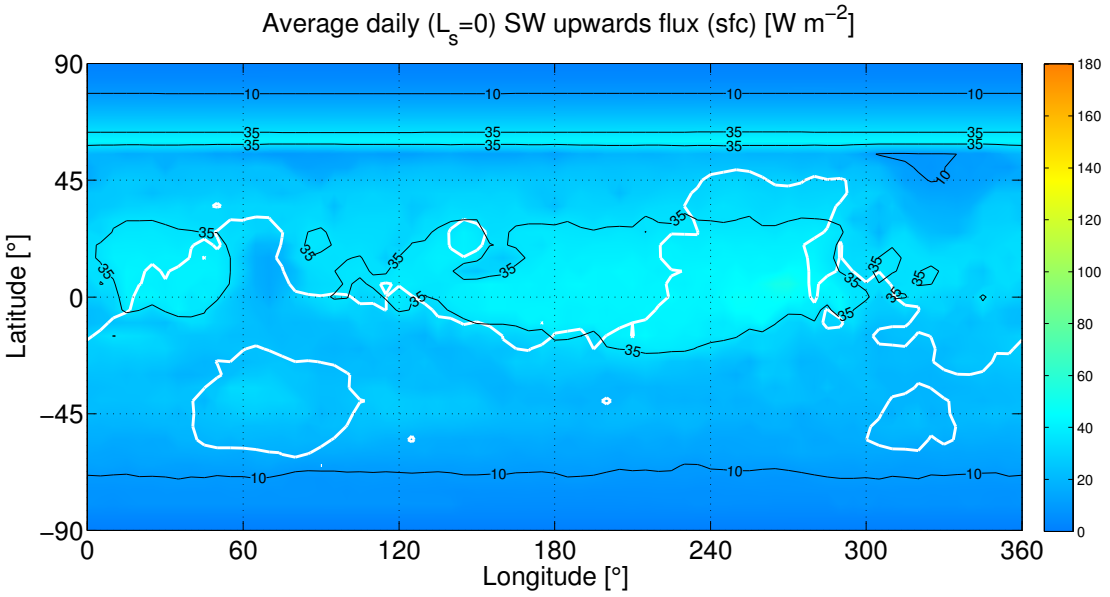


Figure B.12: Average daily SW upwards flux (surface)

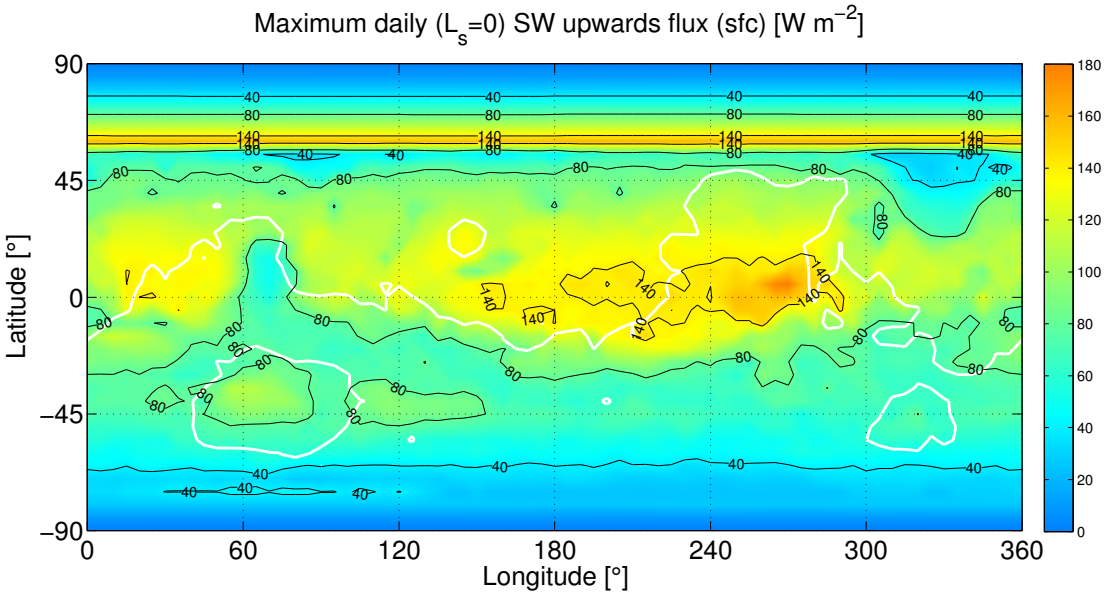


Figure B.13: Maximum daily SW upwards flux (surface)

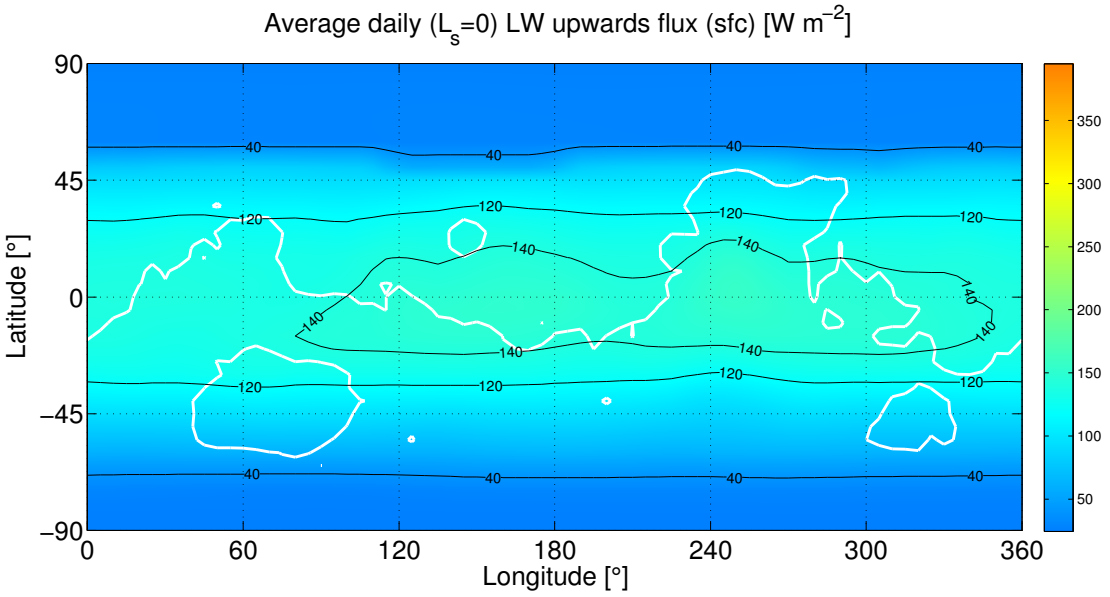


Figure B.14: Average daily LW upwards flux (surface)

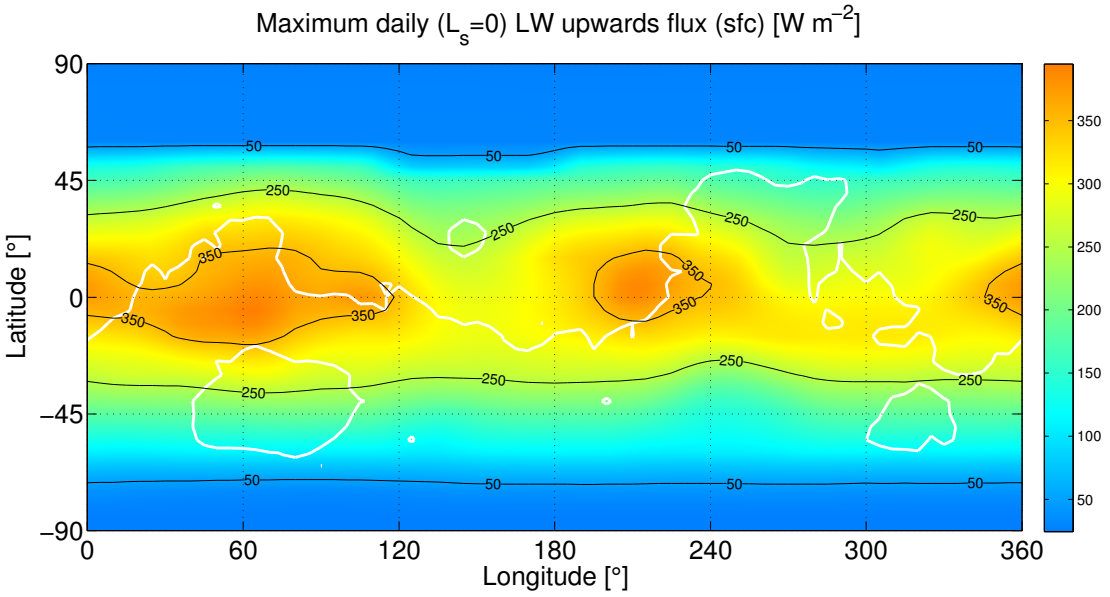


Figure B.15: Maximum daily LW upwards flux (surface)

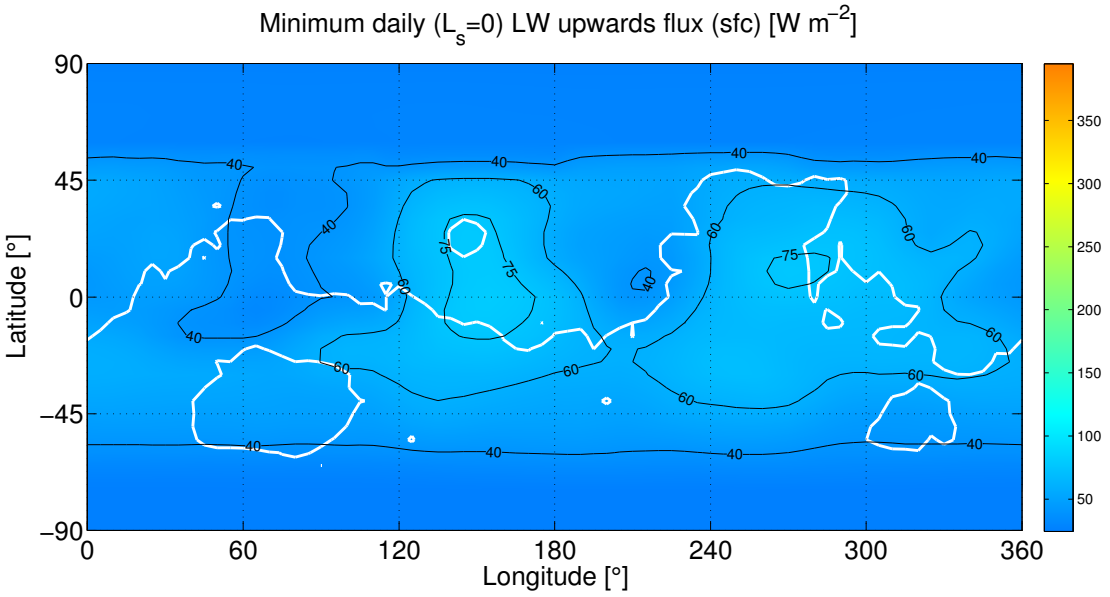


Figure B.16: Minimum daily LW upwards flux (surface)

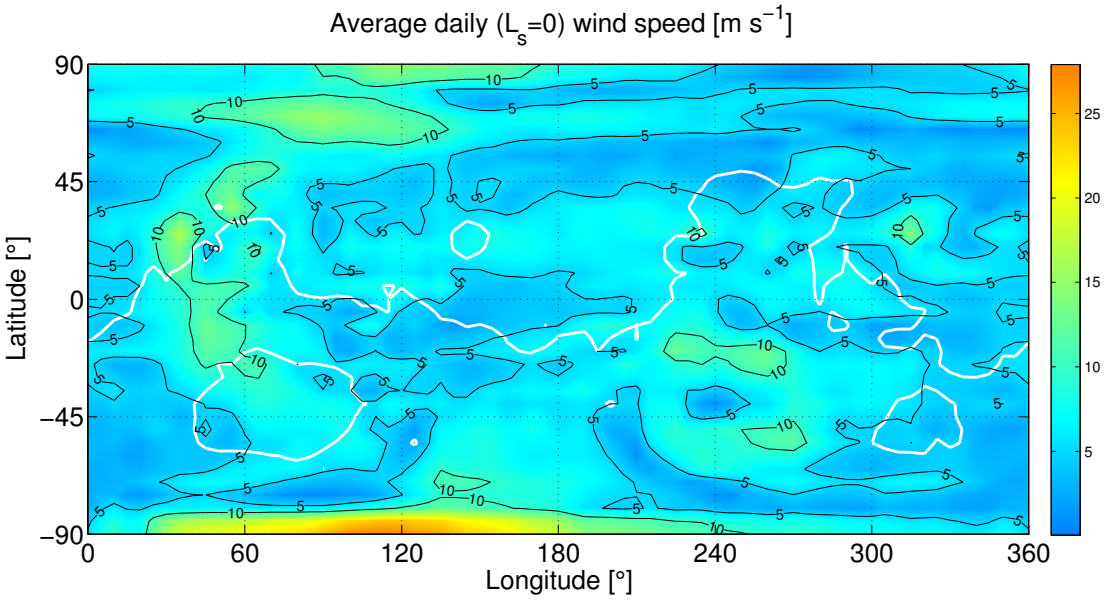


Figure B.17: Average daily wind speed

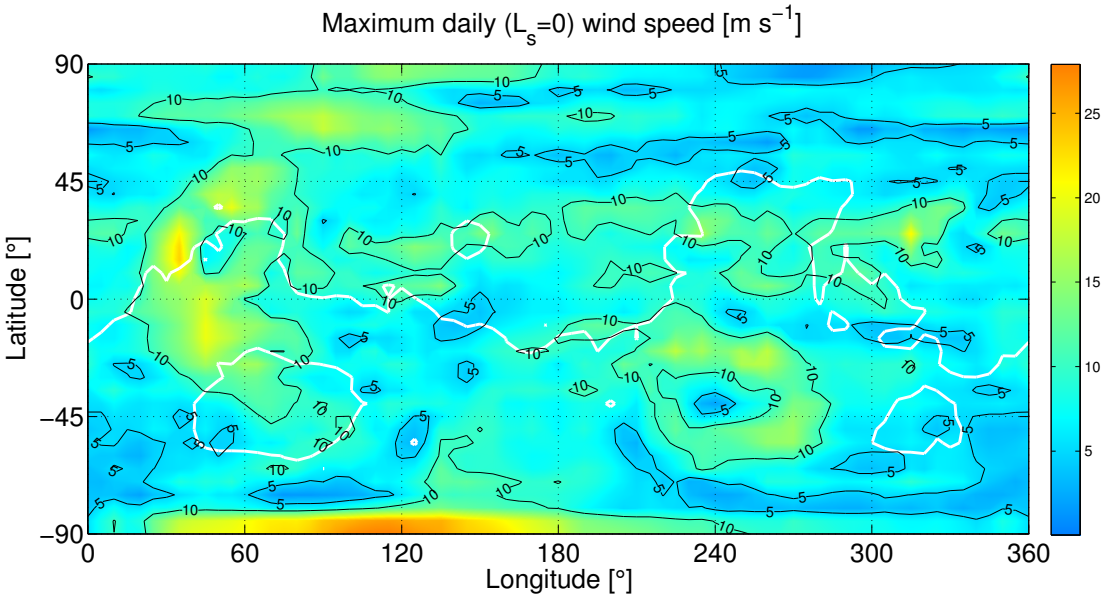


Figure B.18: Maximum daily wind speed

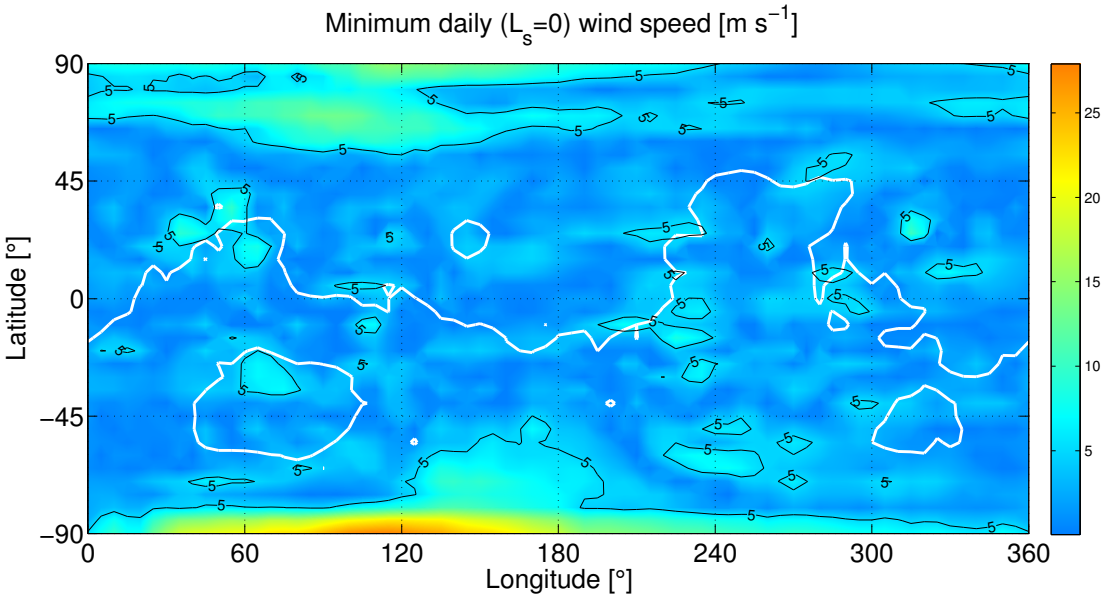


Figure B.19: Minimum daily wind speed

## B.2 Summer solstice

The results for the (northern) Summer solstice ($L_s$=90°) are presented below.

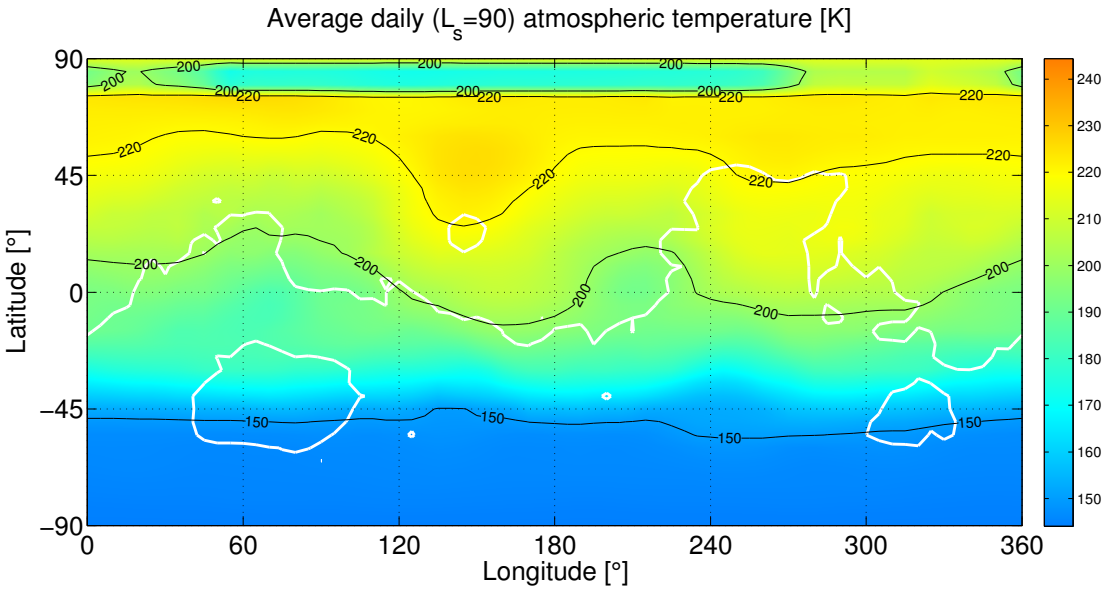


Figure B.20: Average daily atmospheric temperature

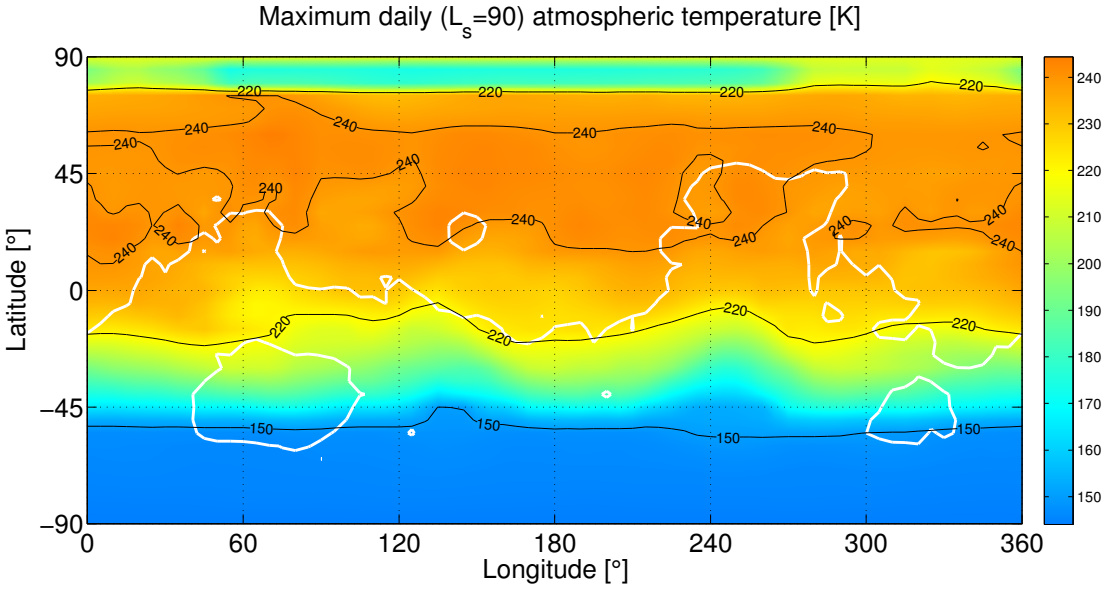


Figure B.21: Maximum daily atmospheric temperature

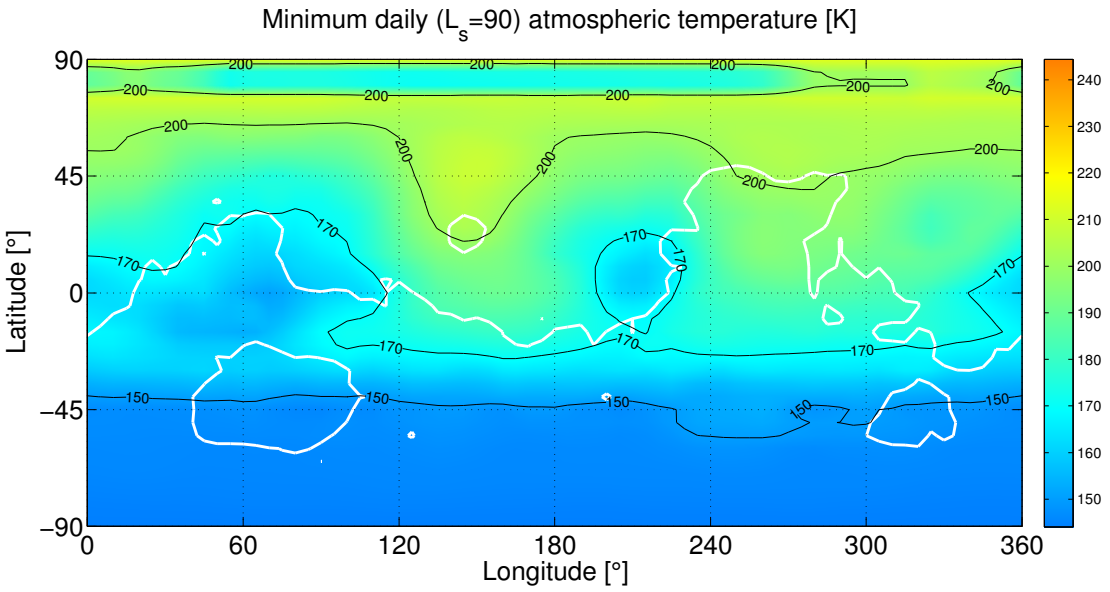


Figure B.22: Minimum daily atmospheric temperature

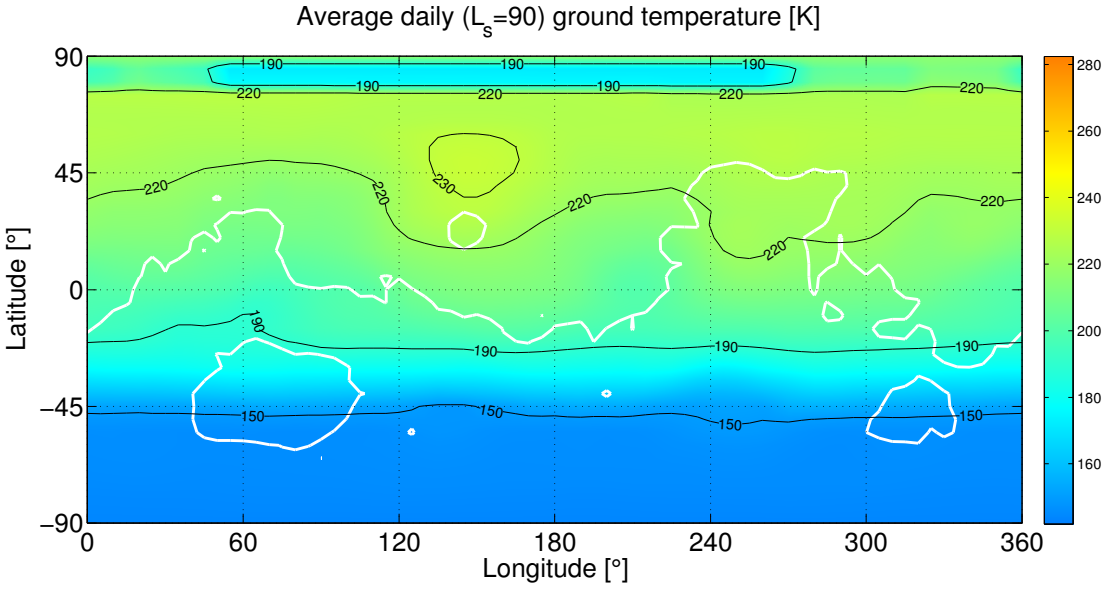


Figure B.23: Average daily ground temperature

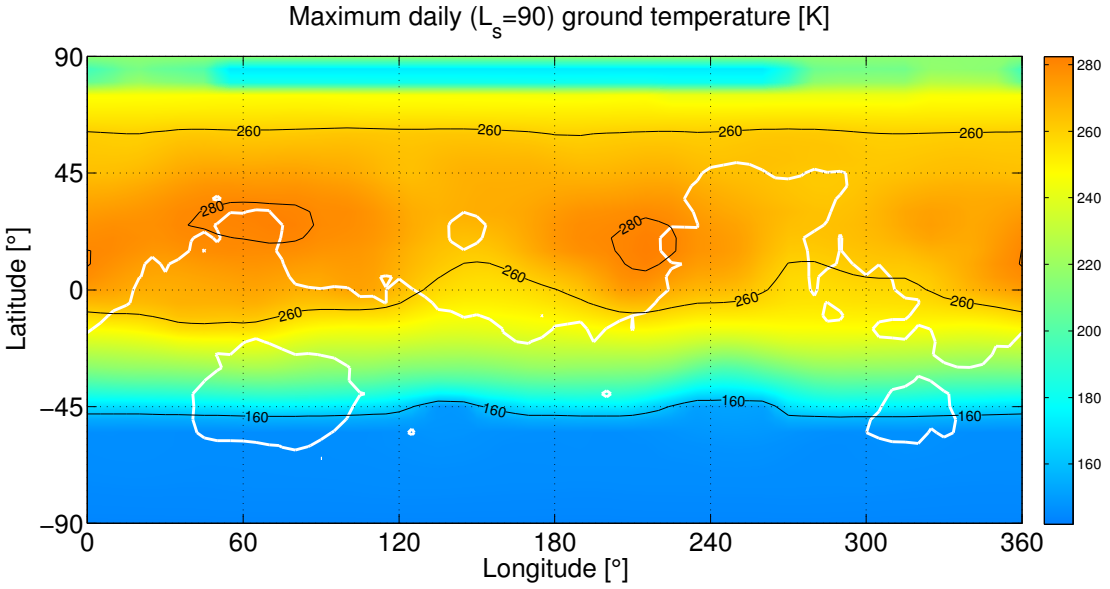


Figure B.24: Maximum daily ground temperature

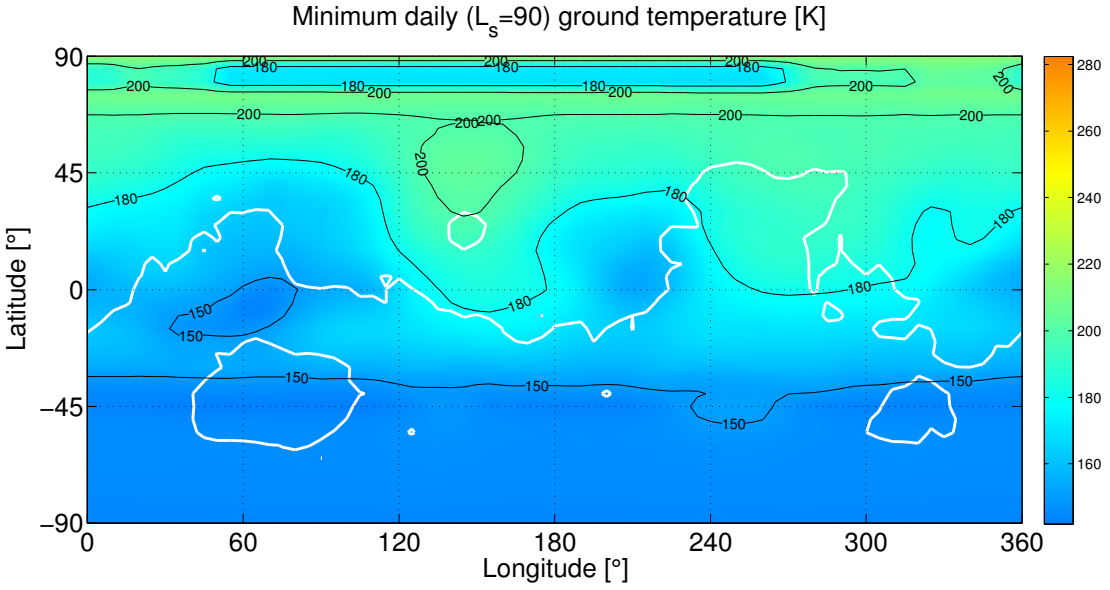


Figure B.25: Minimum daily ground temperature

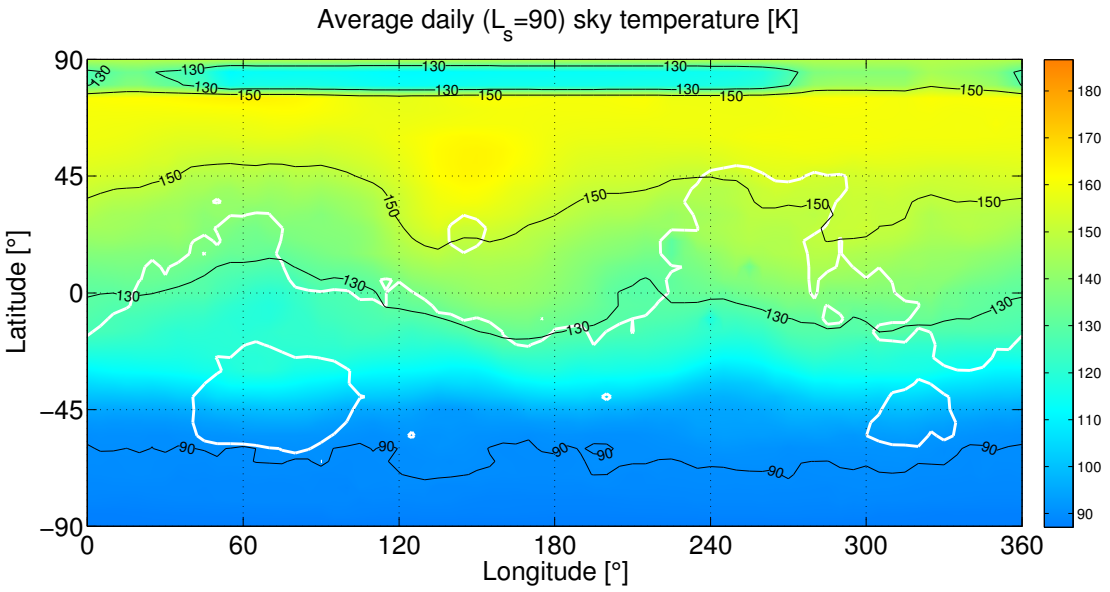


Figure B.26: Average daily sky temperature

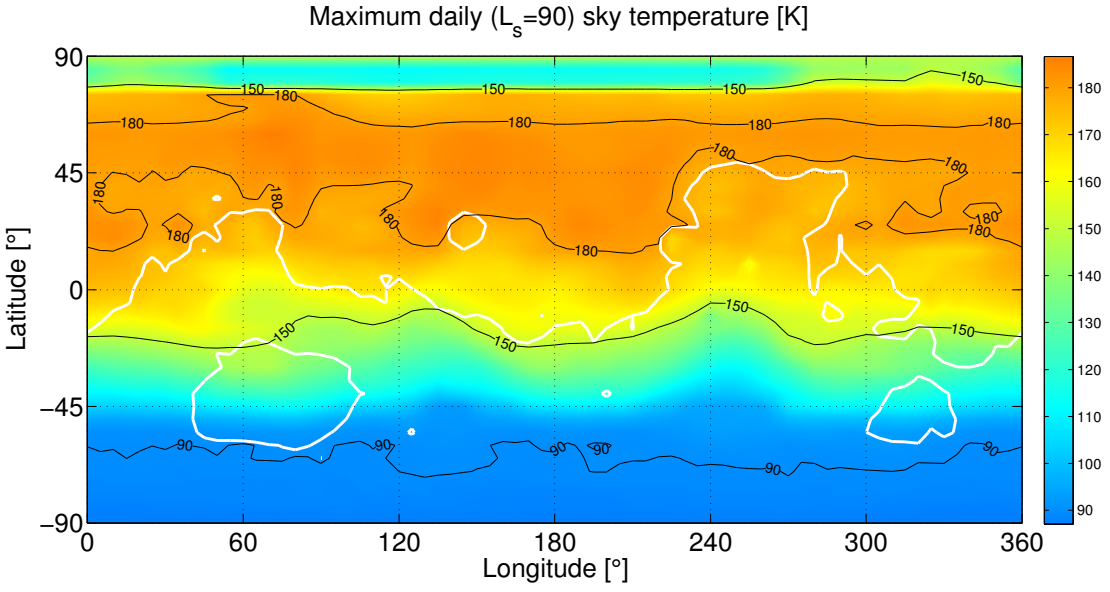


Figure B.27: Maximum daily sky temperature

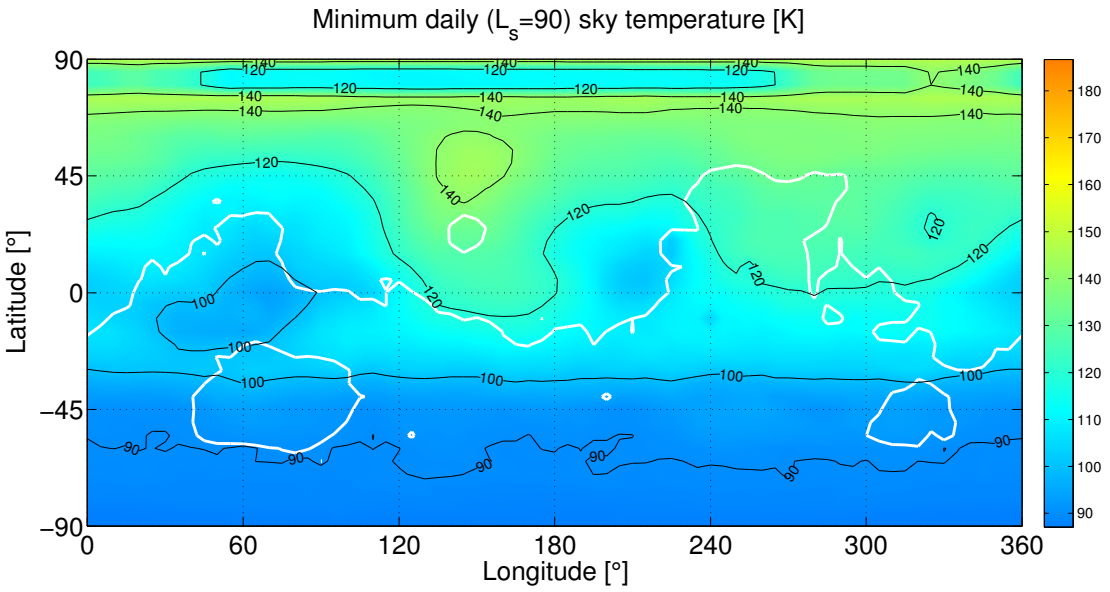


Figure B.28: Minimum daily sky temperature

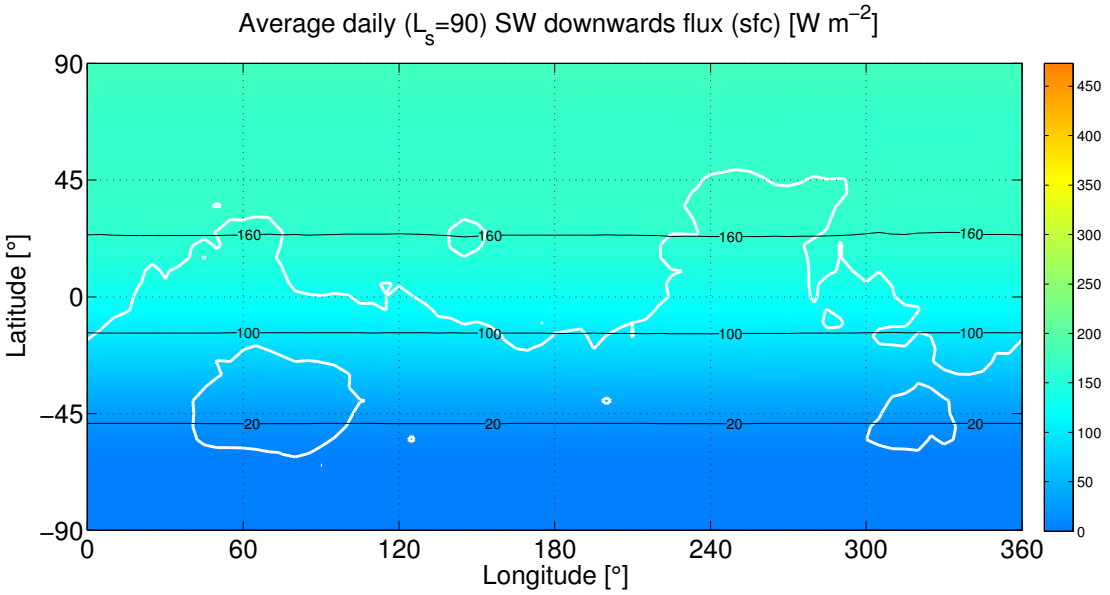


Figure B.29: Average daily SW downwards flux (surface)

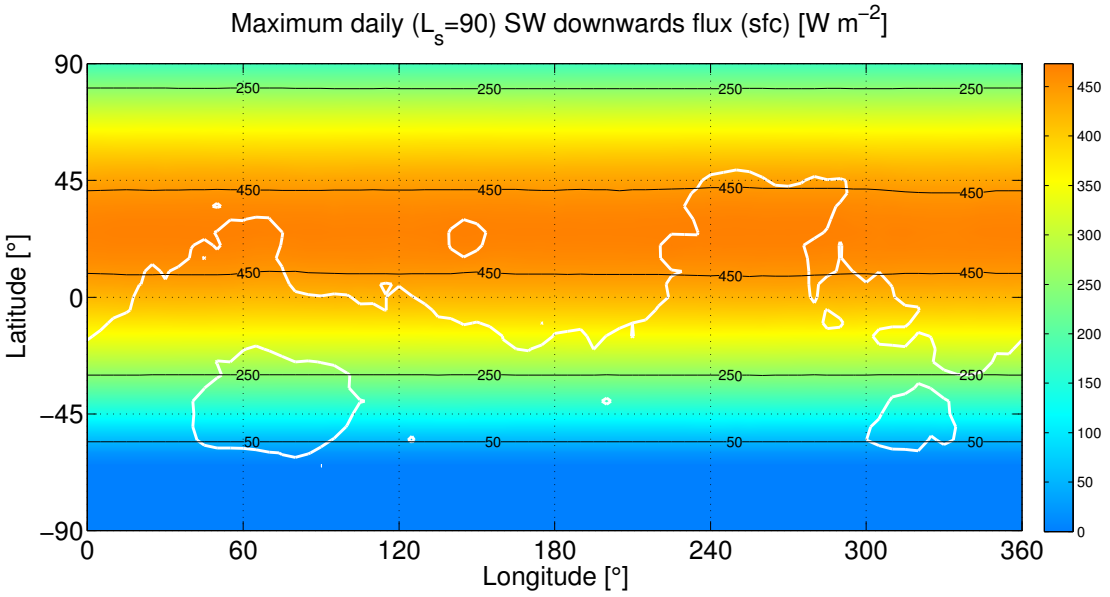


Figure B.30: Maximum daily SW downwards flux (surface)

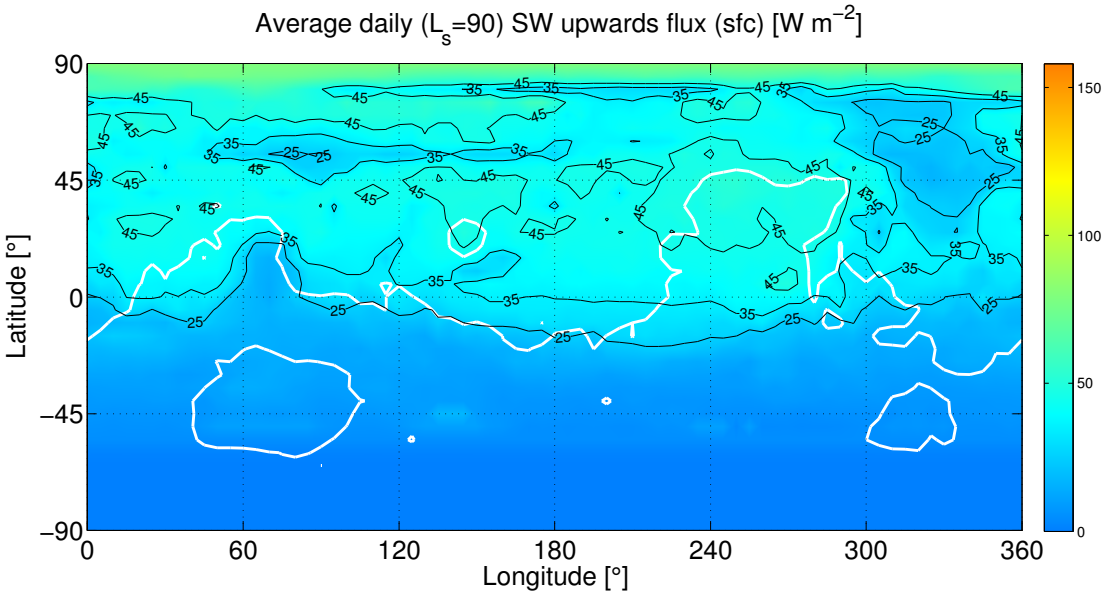


Figure B.31: Average daily SW upwards flux (surface)

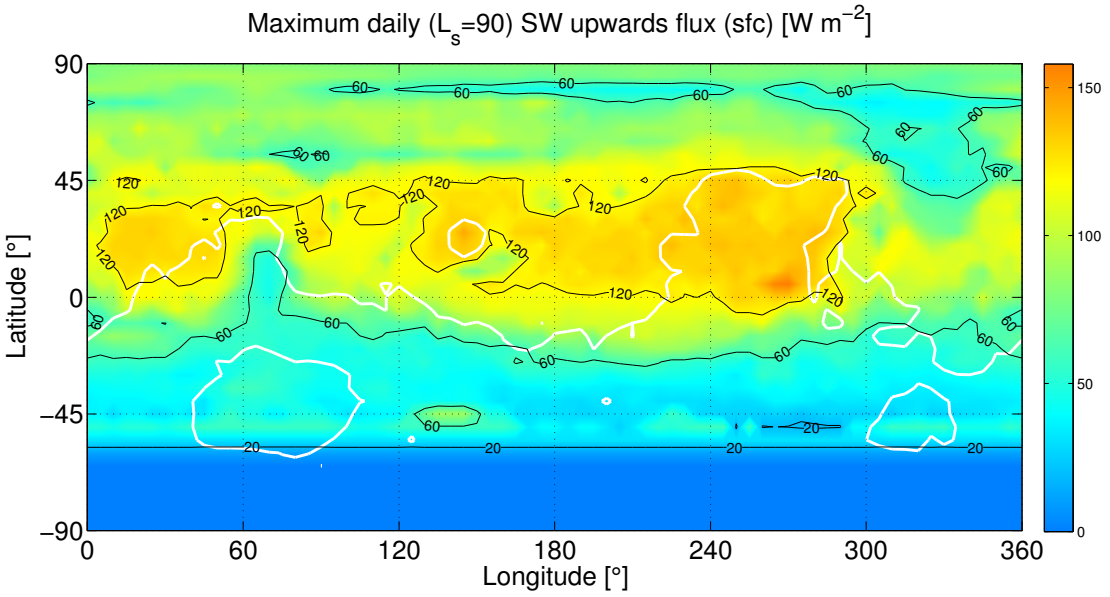


Figure B.32: Maximum daily SW upwards flux (surface)

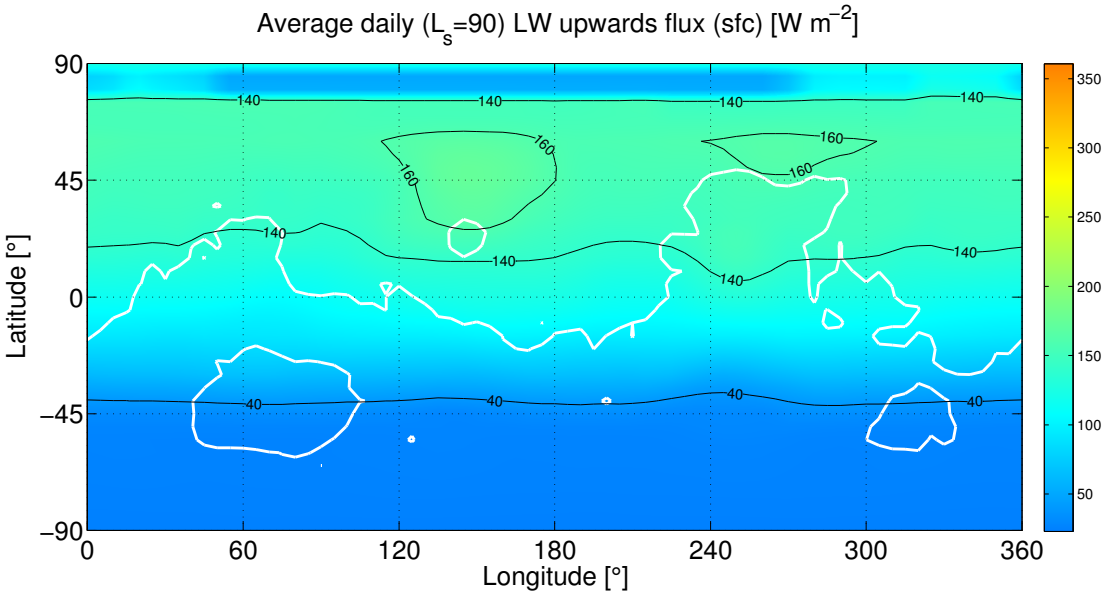


Figure B.33: Average daily LW upwards flux (surface)

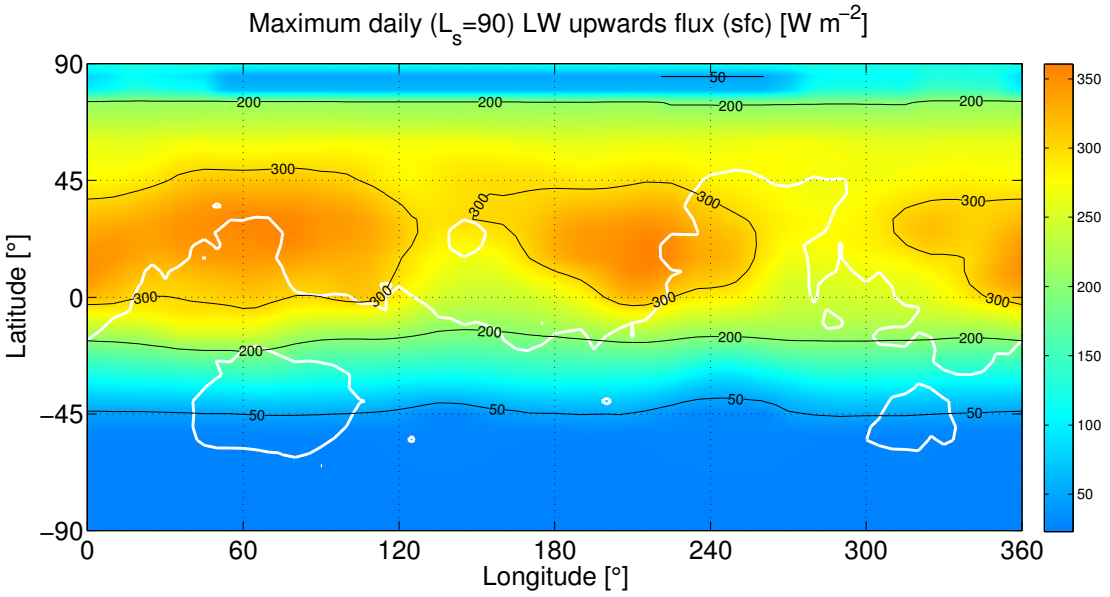


Figure B.34: Maximum daily LW upwards flux (surface)

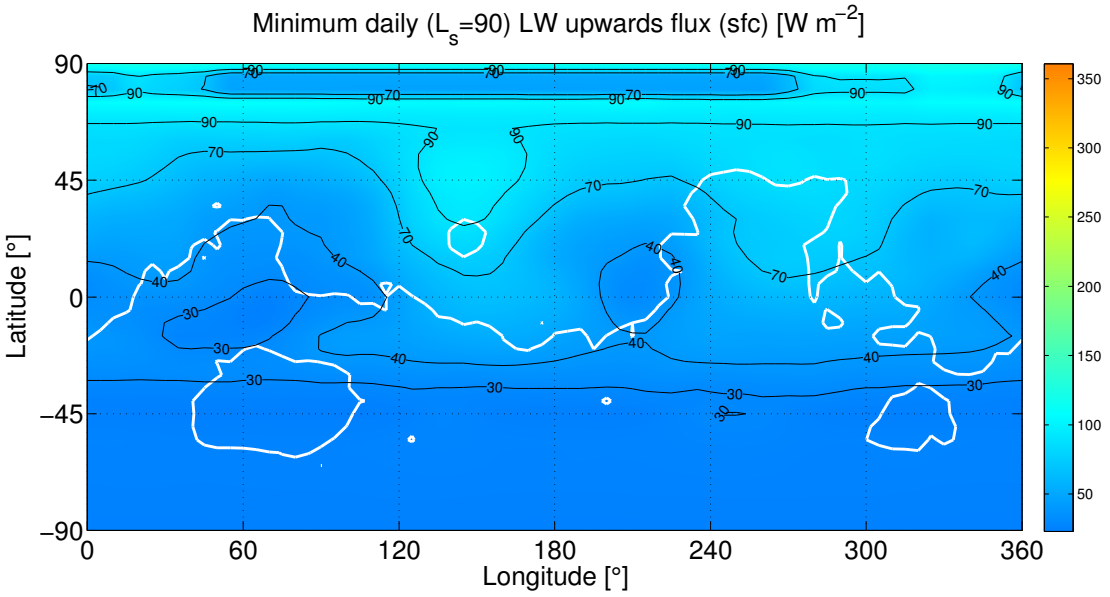


Figure B.35: Minimum daily LW upwards flux (surface)

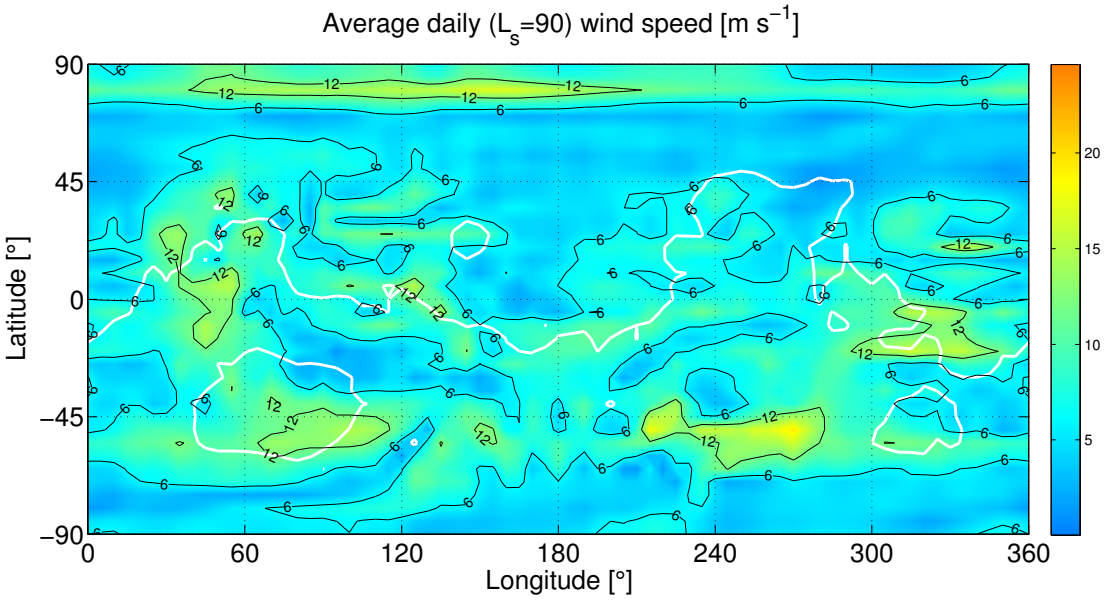


Figure B.36: Average daily wind speed

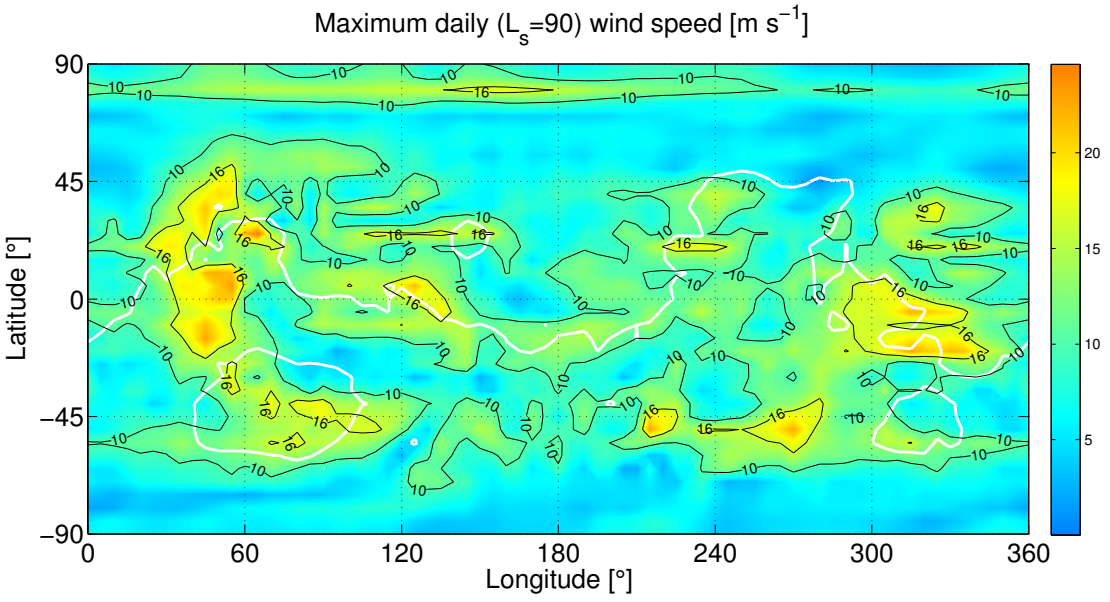


Figure B.37: Maximum daily wind speed

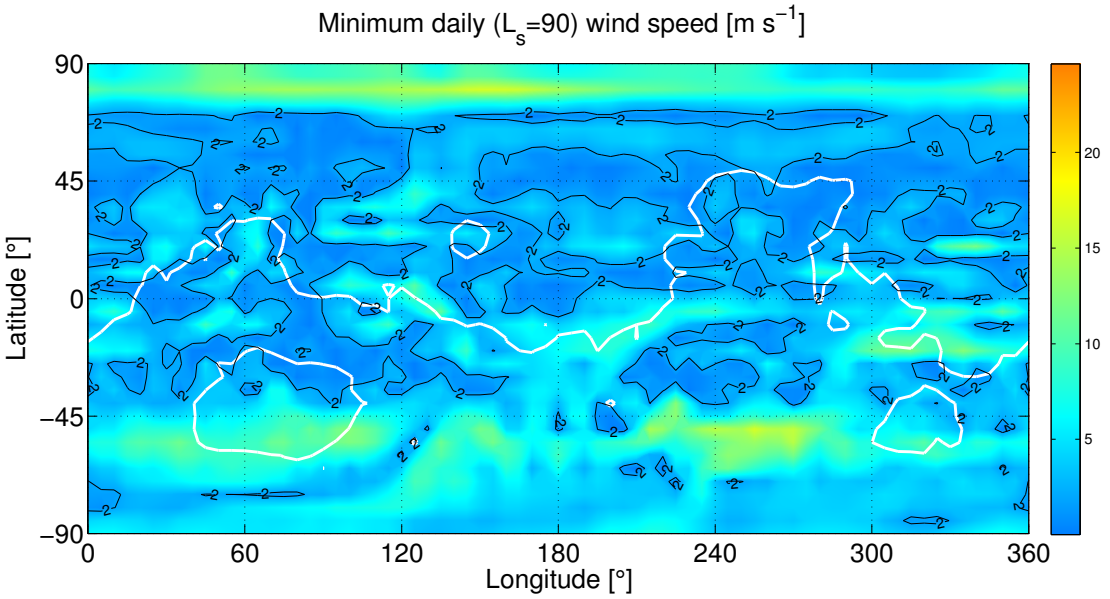


Figure B.38: Minimum daily wind speed

## B.3 Fall equinox

The results for the (northern) Fall equinox ($L_s$=180°) are presented below.

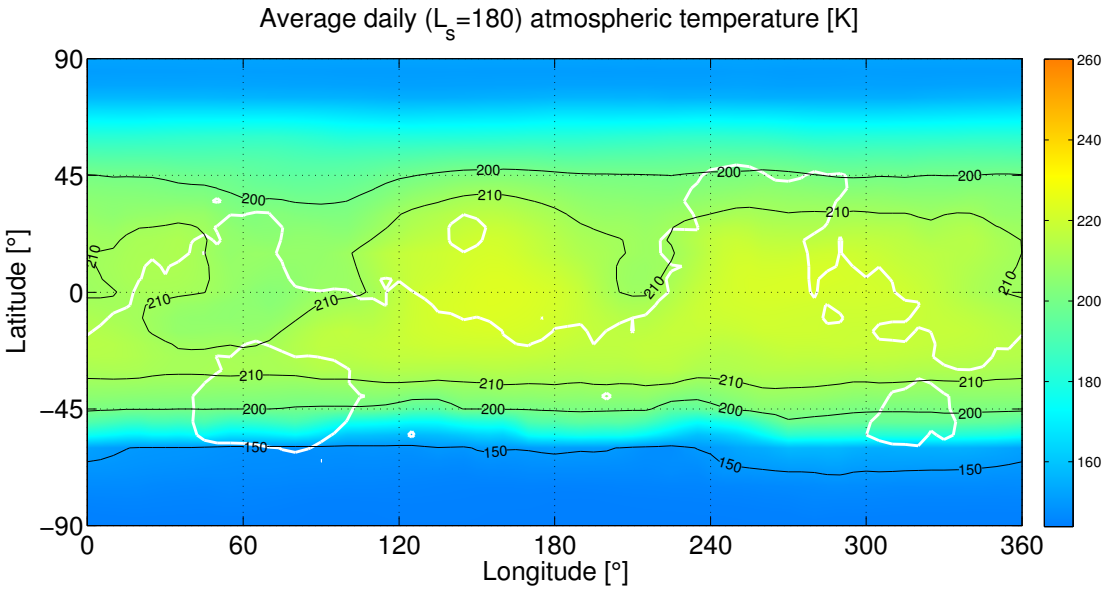


Figure B.39: Average daily atmospheric temperature

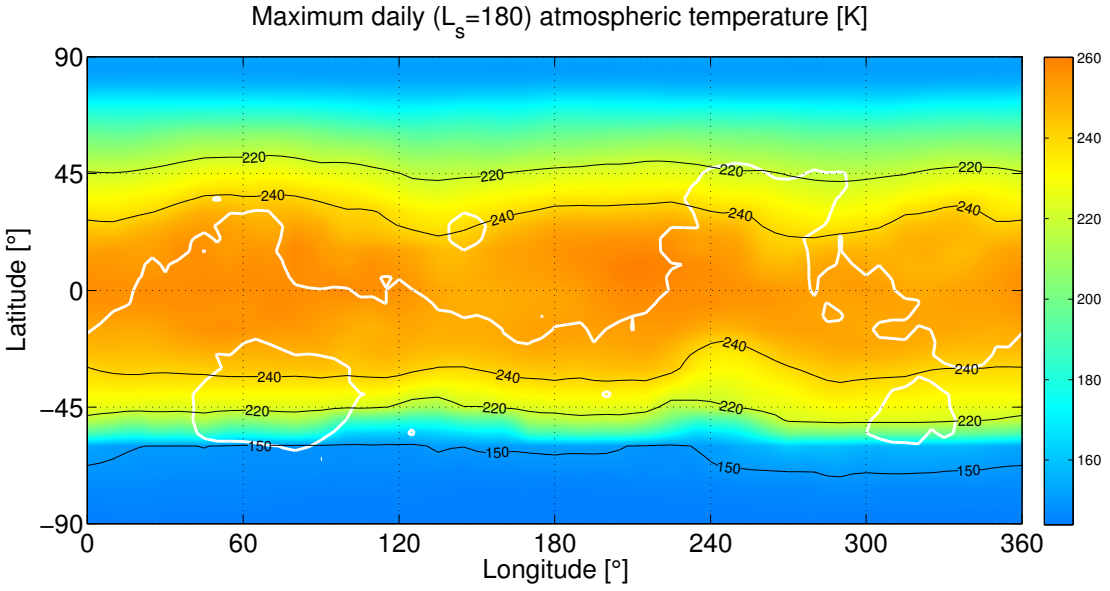


Figure B.40: Maximum daily atmospheric temperature

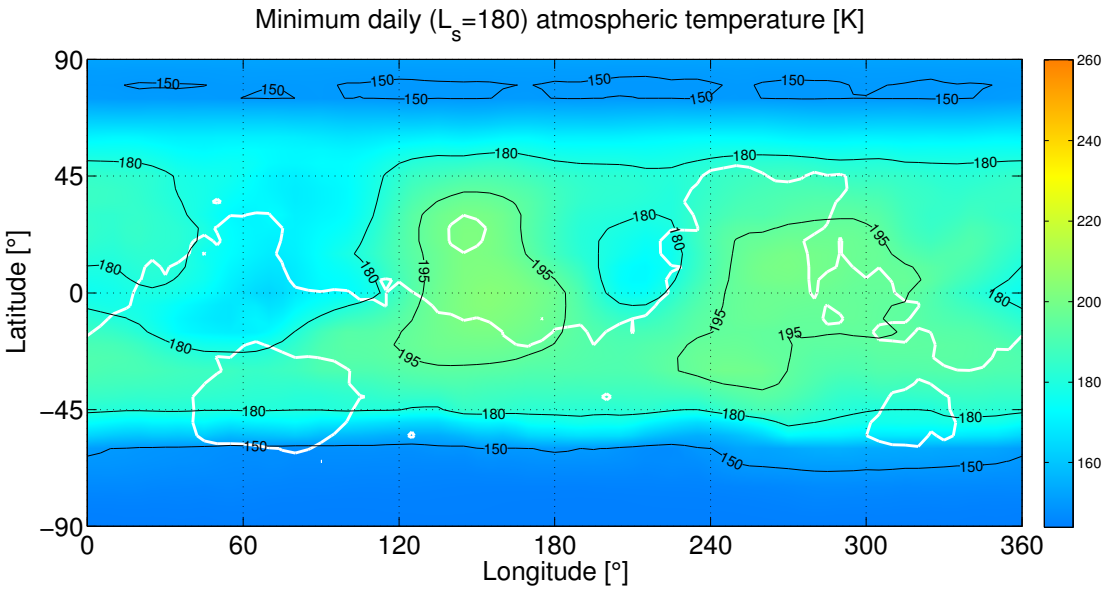


Figure B.41: Minimum daily atmospheric temperature

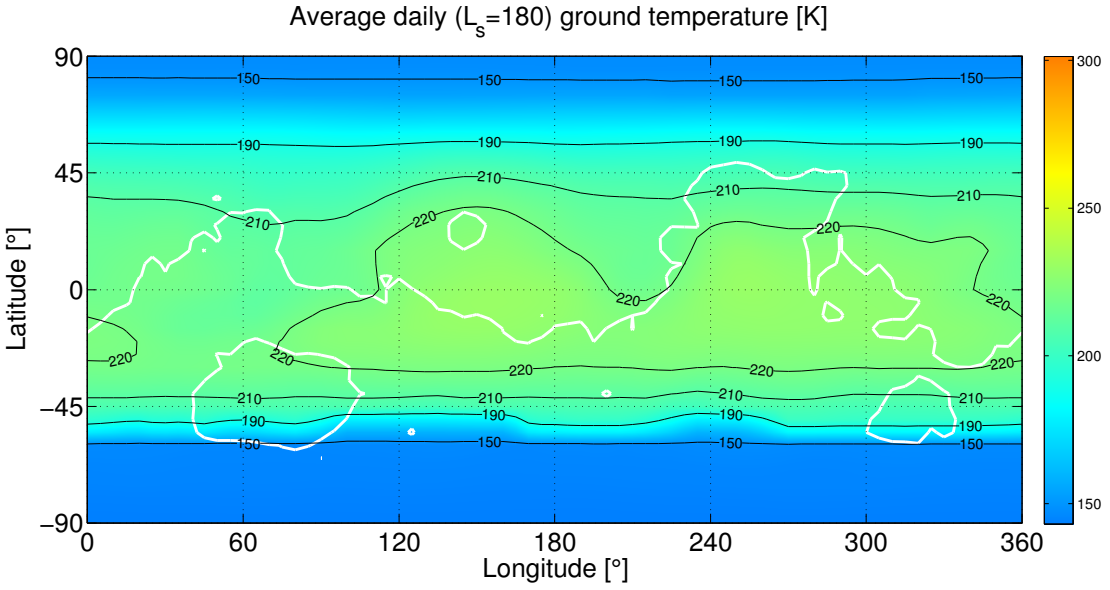


Figure B.42: Average daily ground temperature

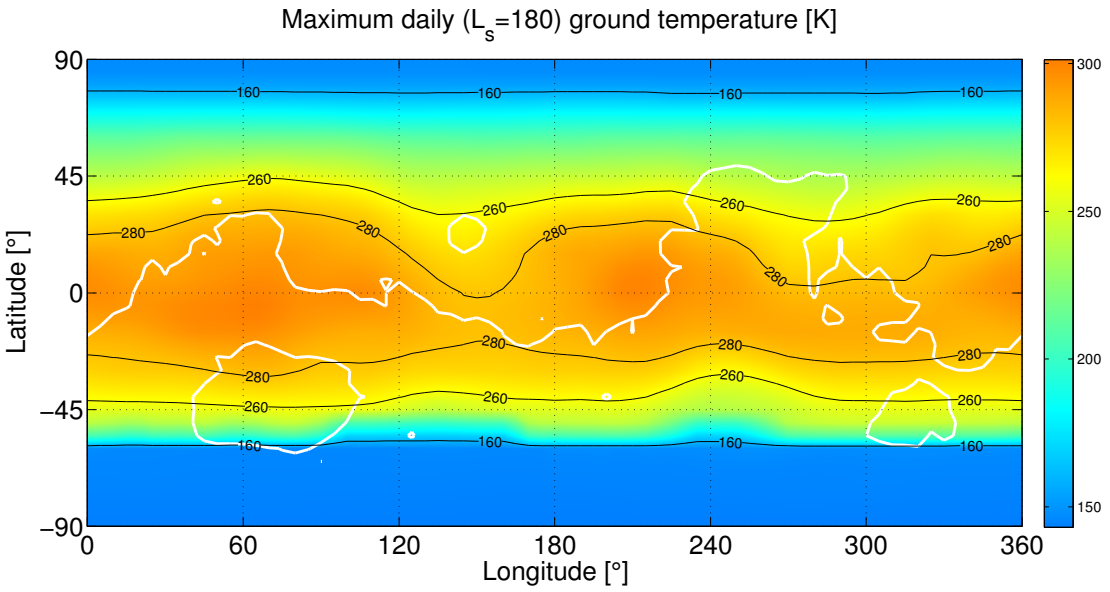


Figure B.43: Maximum daily ground temperature

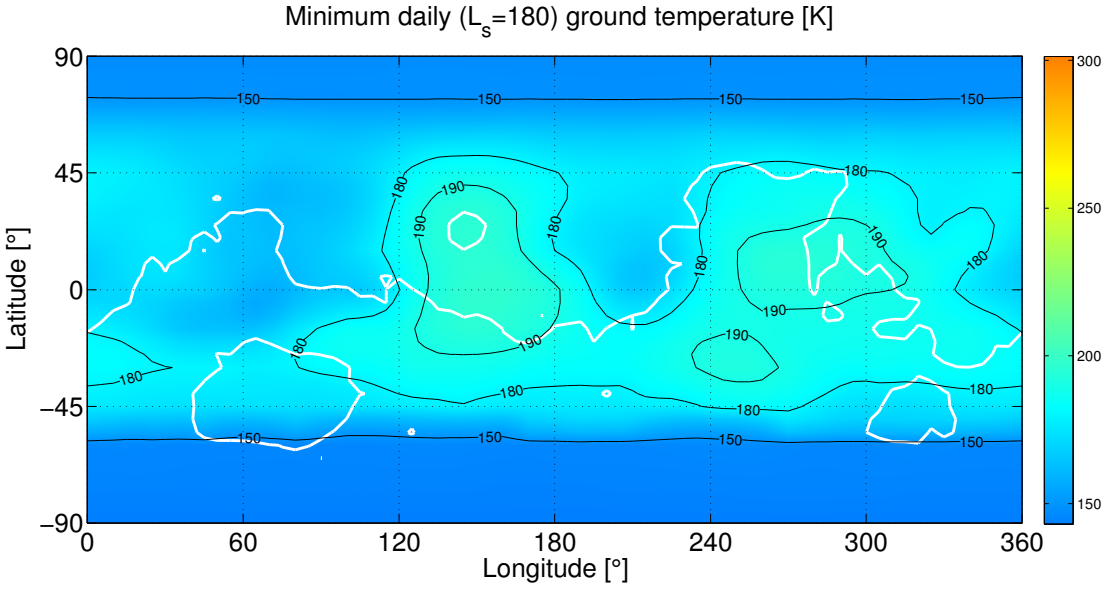


Figure B.44: Minimum daily ground temperature

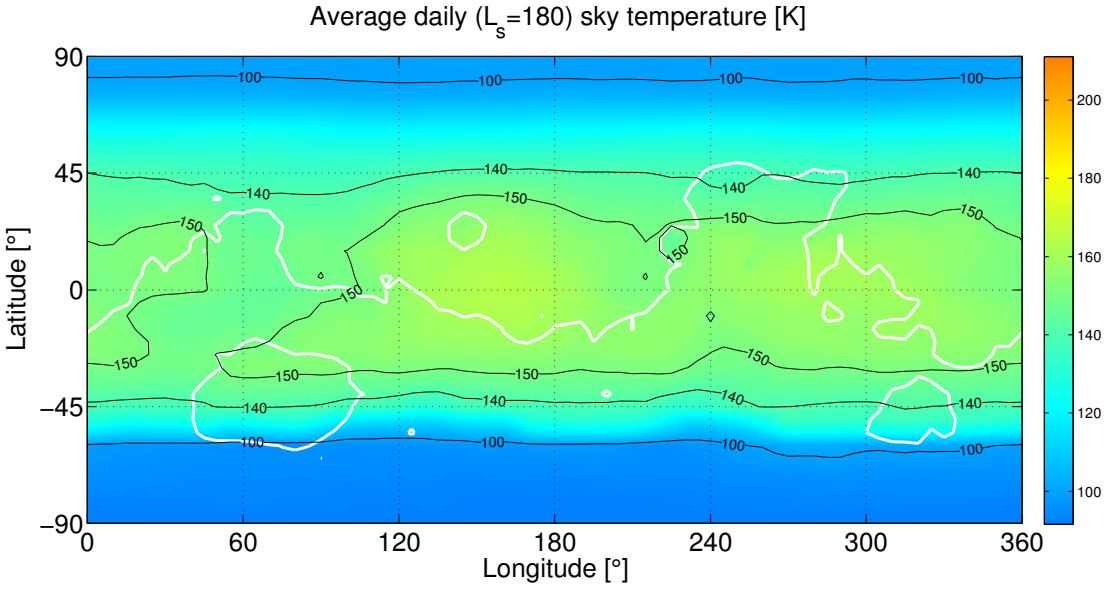


Figure B.45: Average daily sky temperature

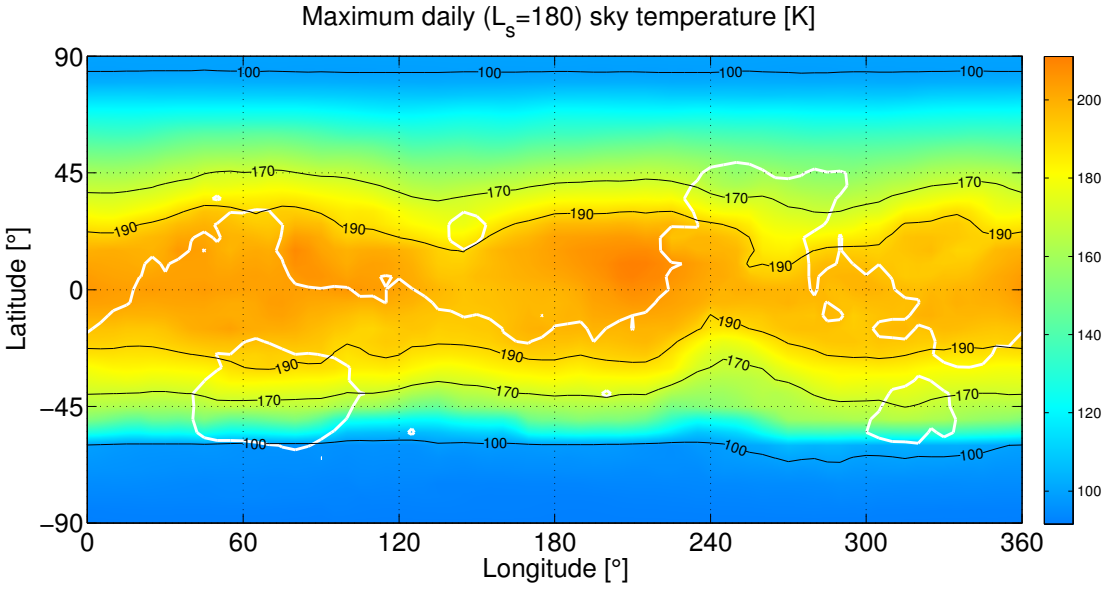


Figure B.46: Maximum daily sky temperature

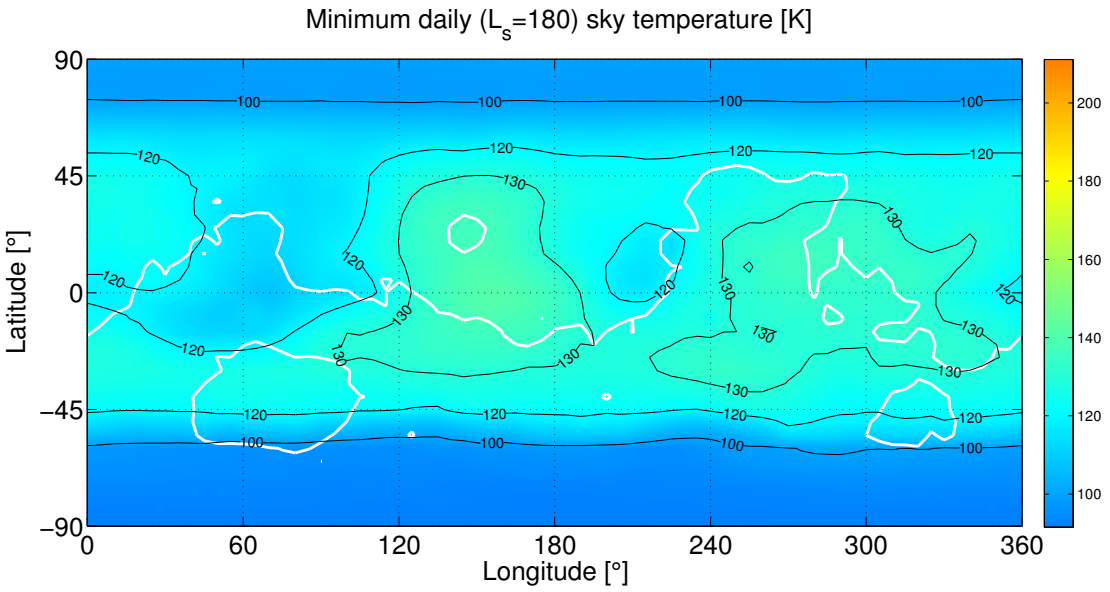


Figure B.47: Minimum daily sky temperature

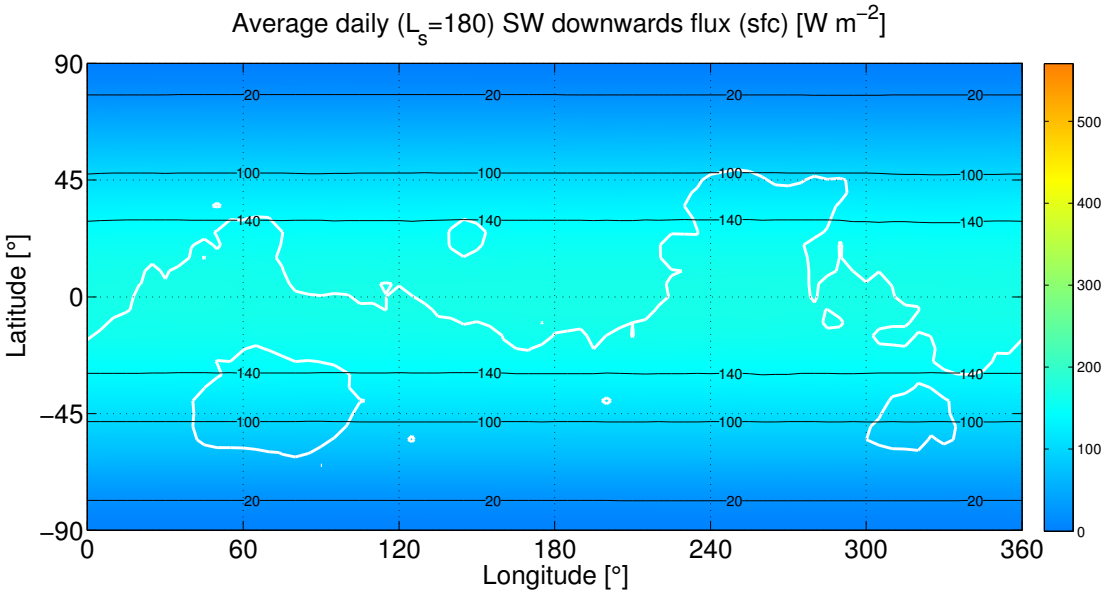


Figure B.48: Average daily SW downwards flux (surface)

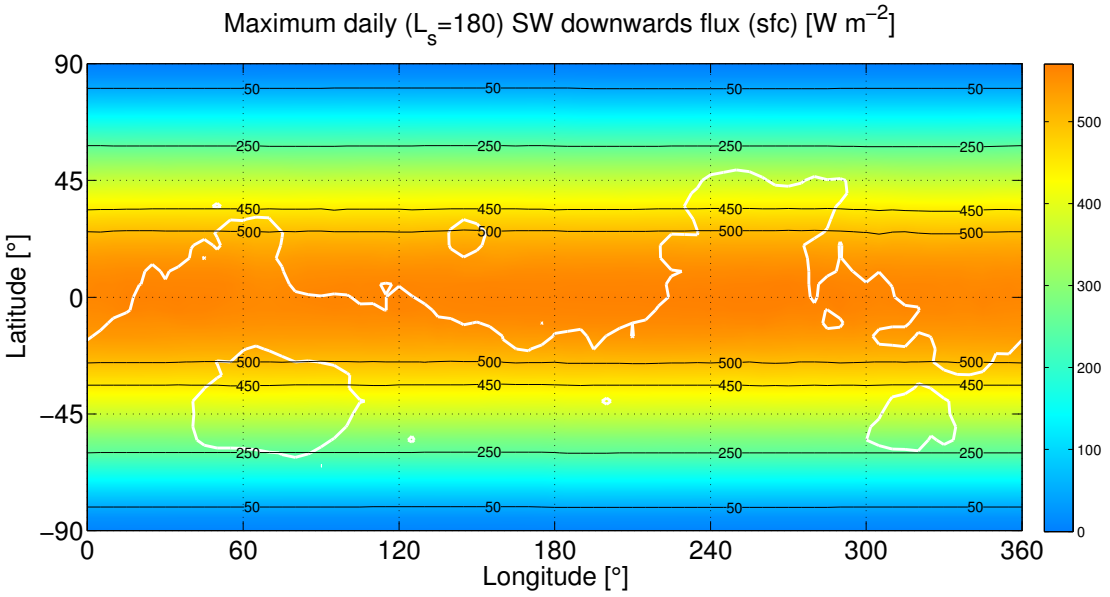


Figure B.49: Maximum daily SW downwards flux (surface)

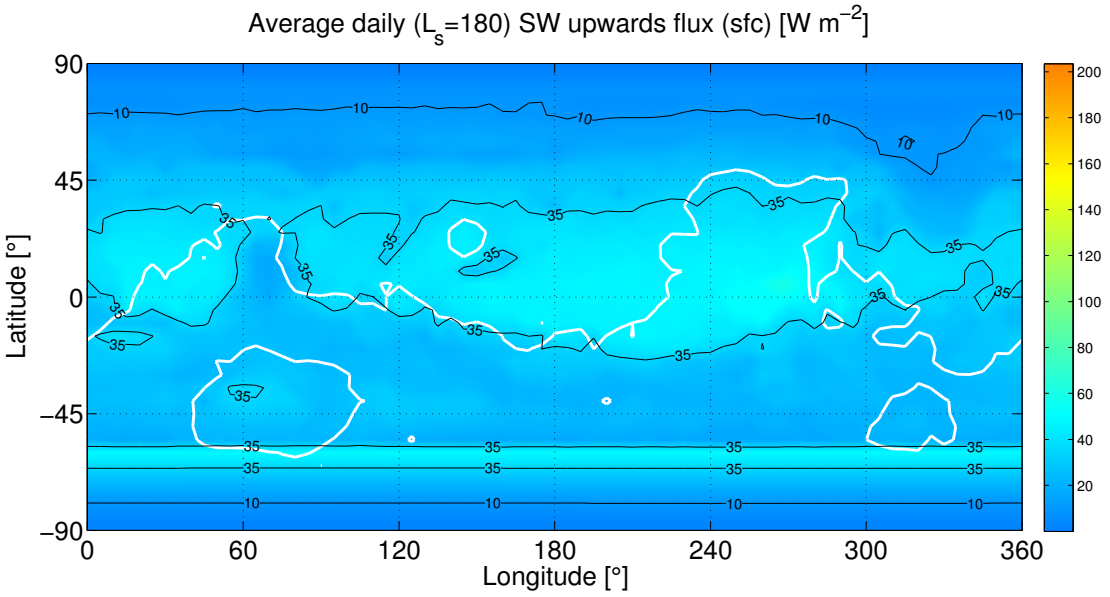


Figure B.50: Average daily SW upwards flux (surface)

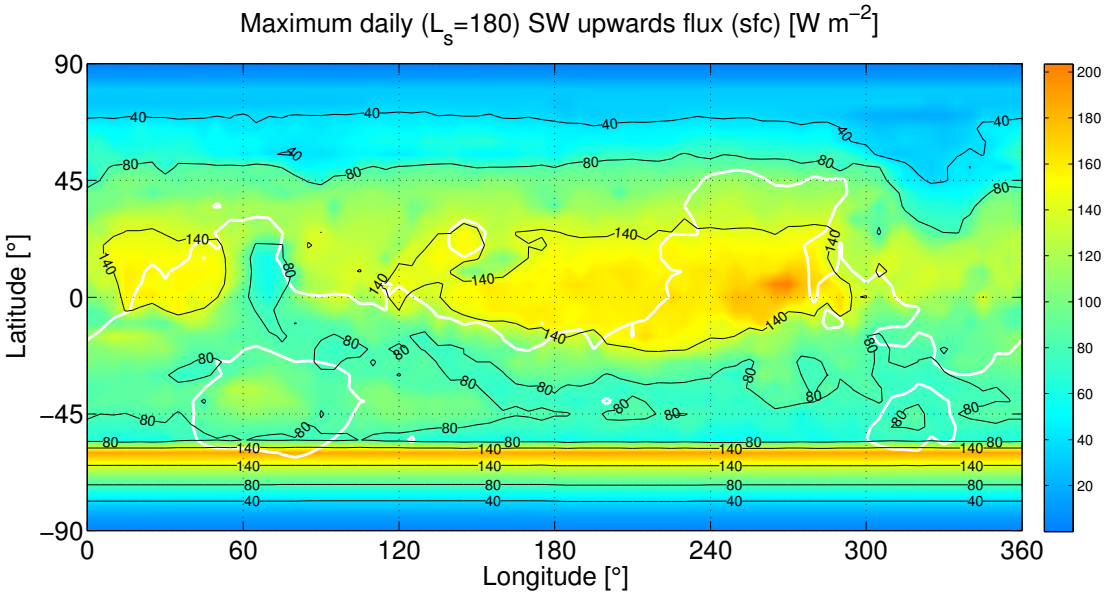


Figure B.51: Maximum daily SW upwards flux (surface)

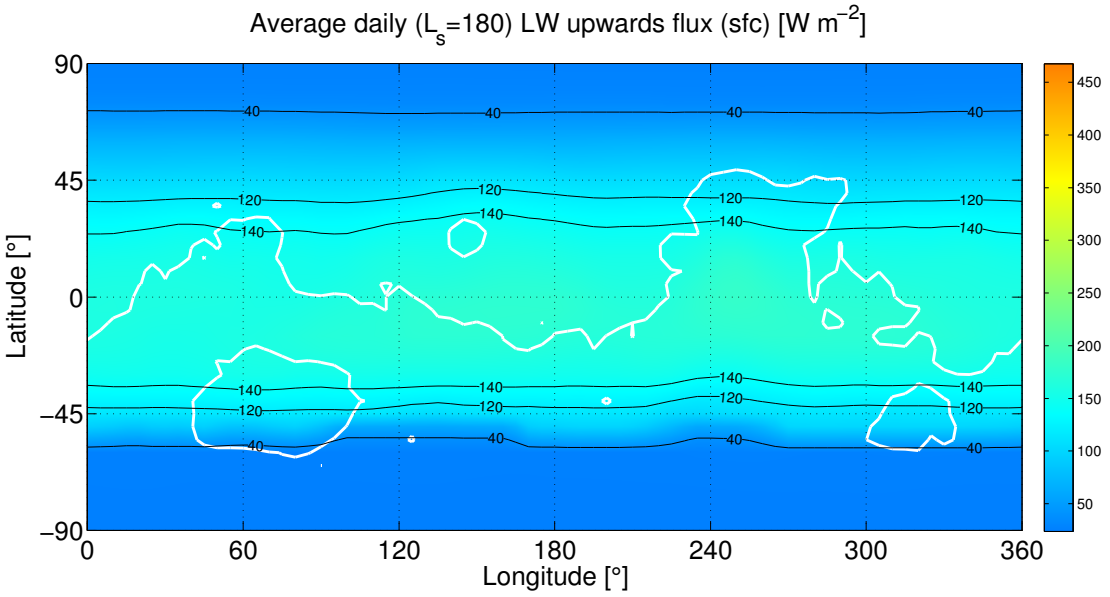


Figure B.52: Average daily LW upwards flux (surface)

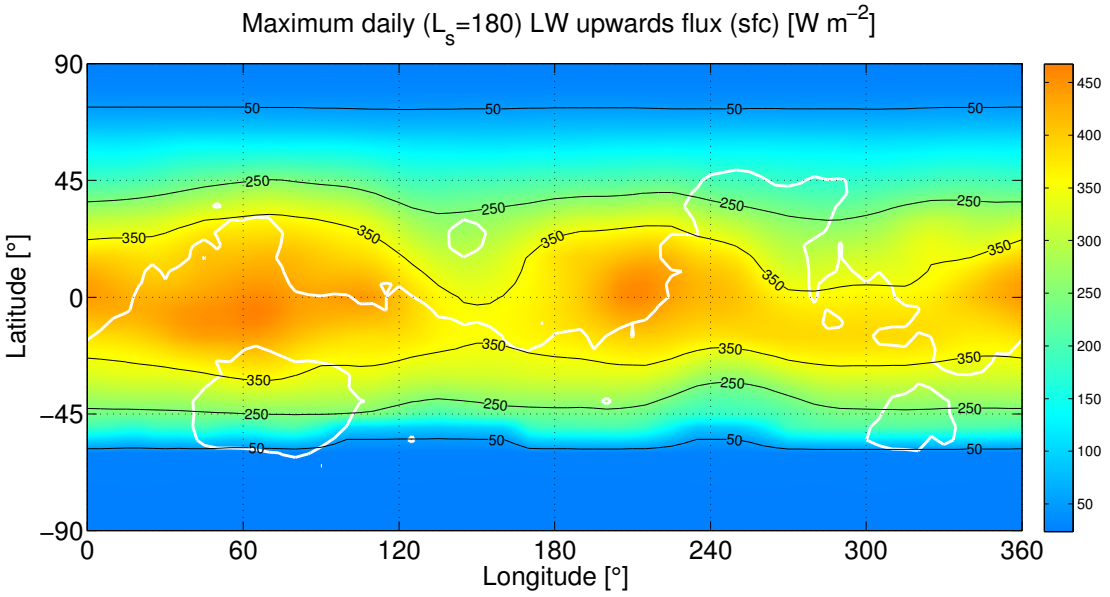


Figure B.53: Maximum daily LW upwards flux (surface)

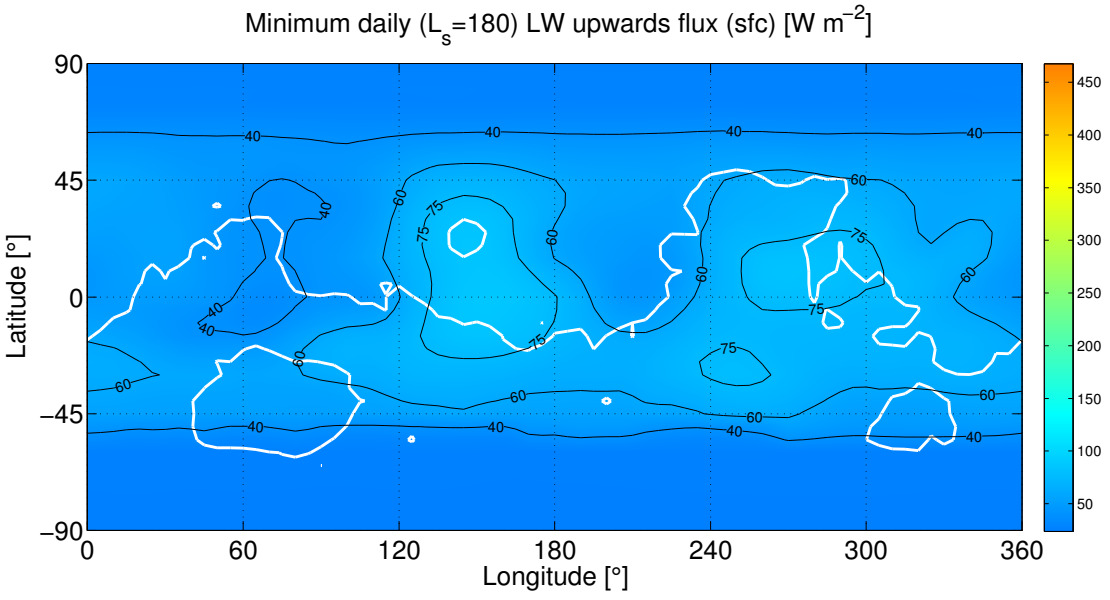


Figure B.54: Minimum daily LW upwards flux (surface)

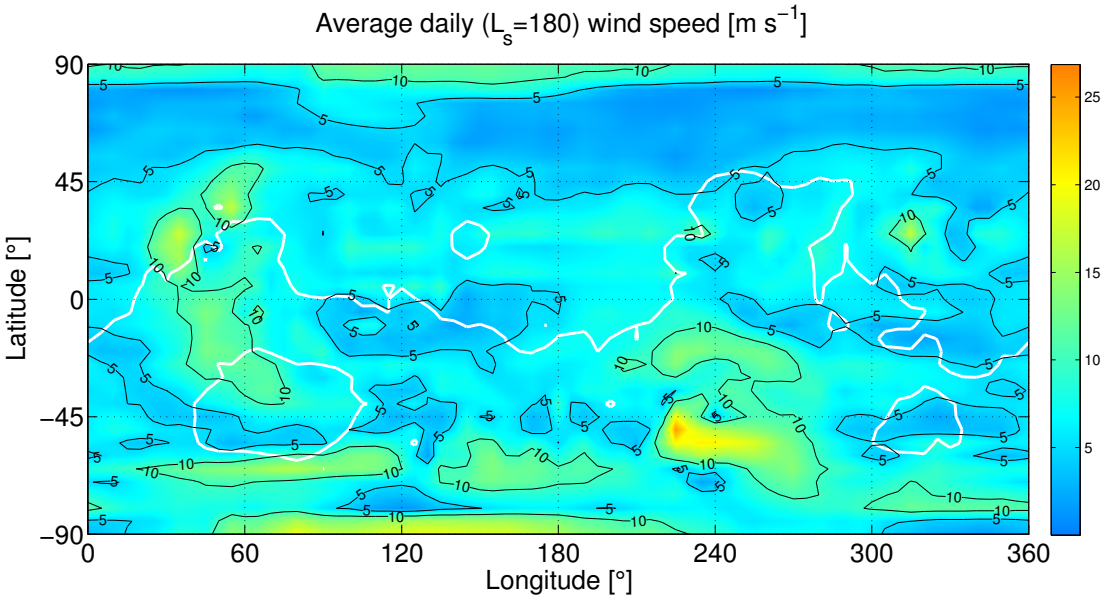


Figure B.55: Average daily wind speed

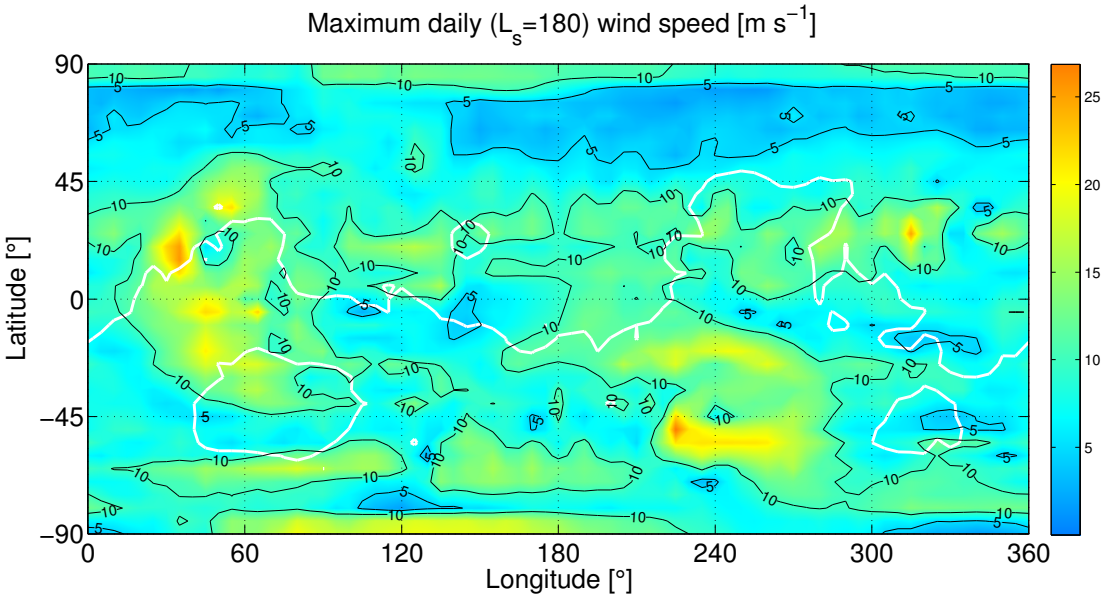


Figure B.56: Maximum daily wind speed

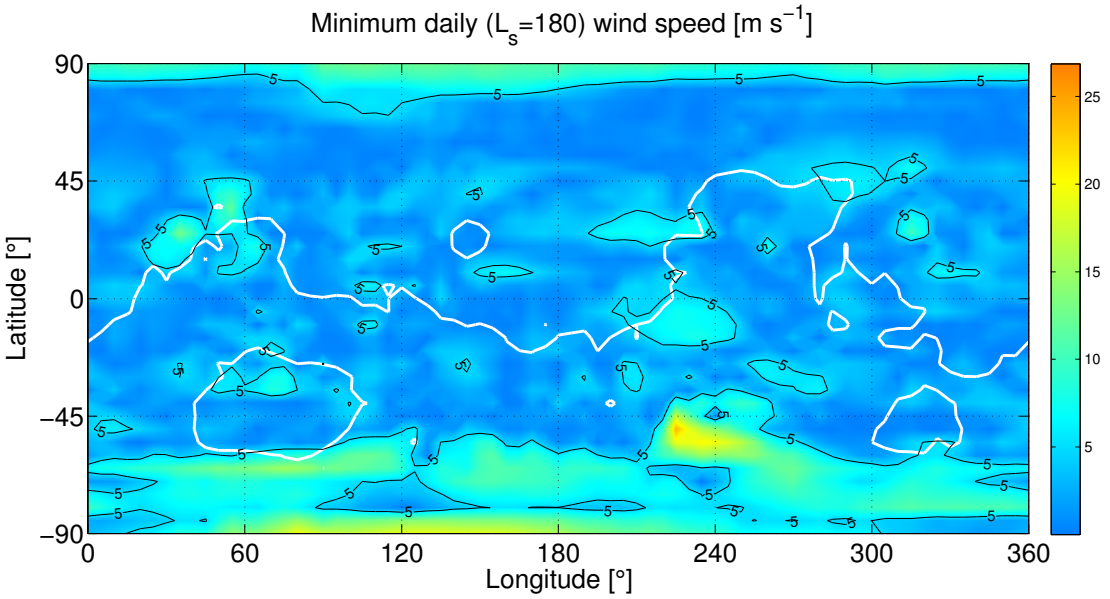


Figure B.57: Minimum daily wind speed

## B.4 Winter solstice

The results for the (northern) Winter solstice ($L_s$=270°) are presented below.

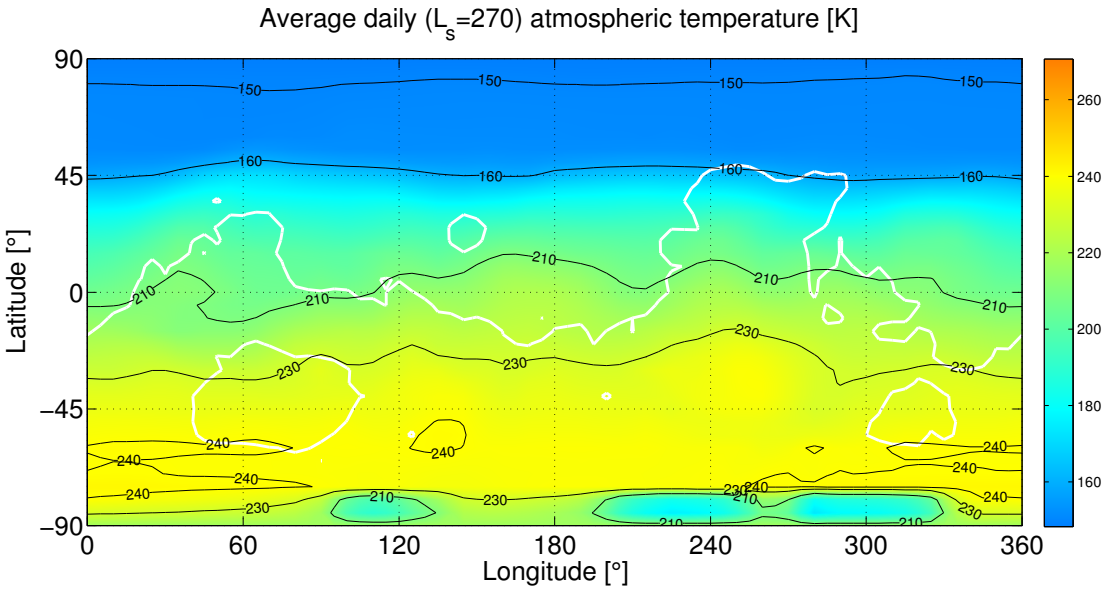


Figure B.58: Average daily atmospheric temperature

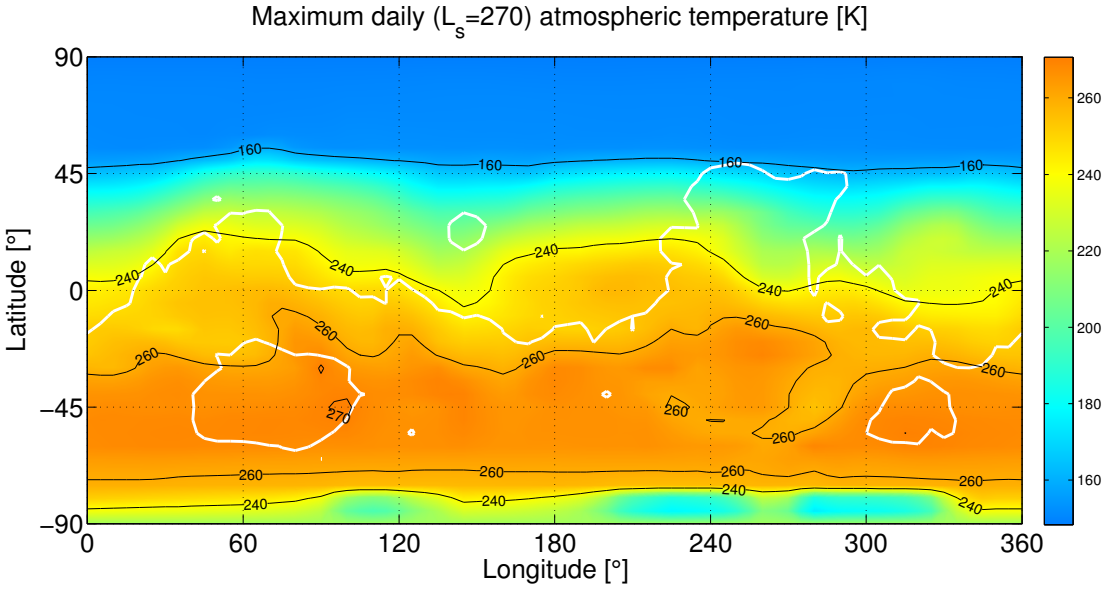


Figure B.59: Maximum daily atmospheric temperature

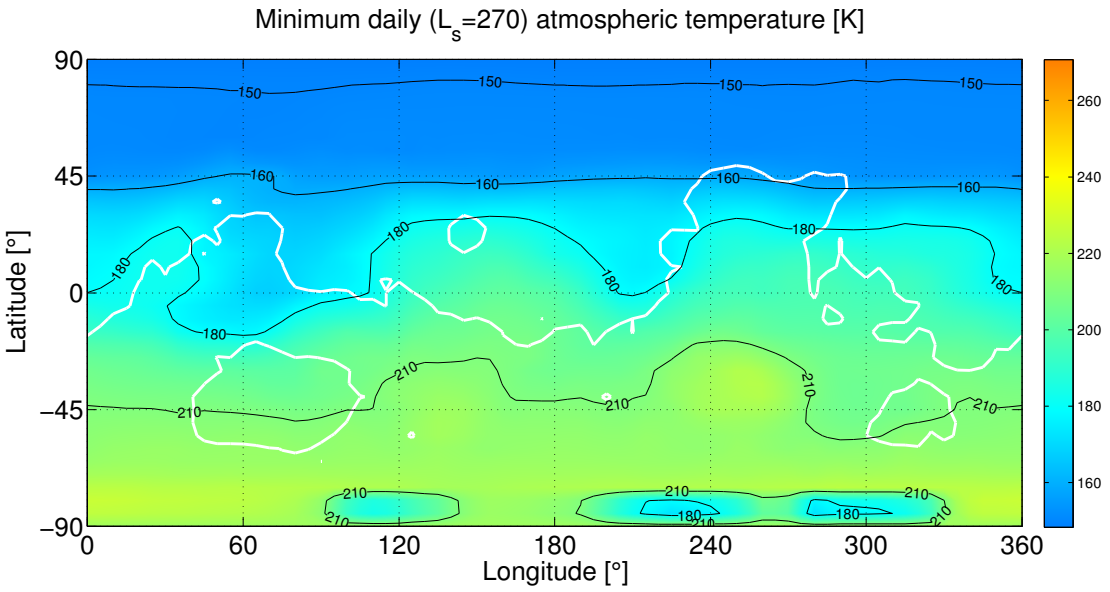


Figure B.60: Minimum daily atmospheric temperature

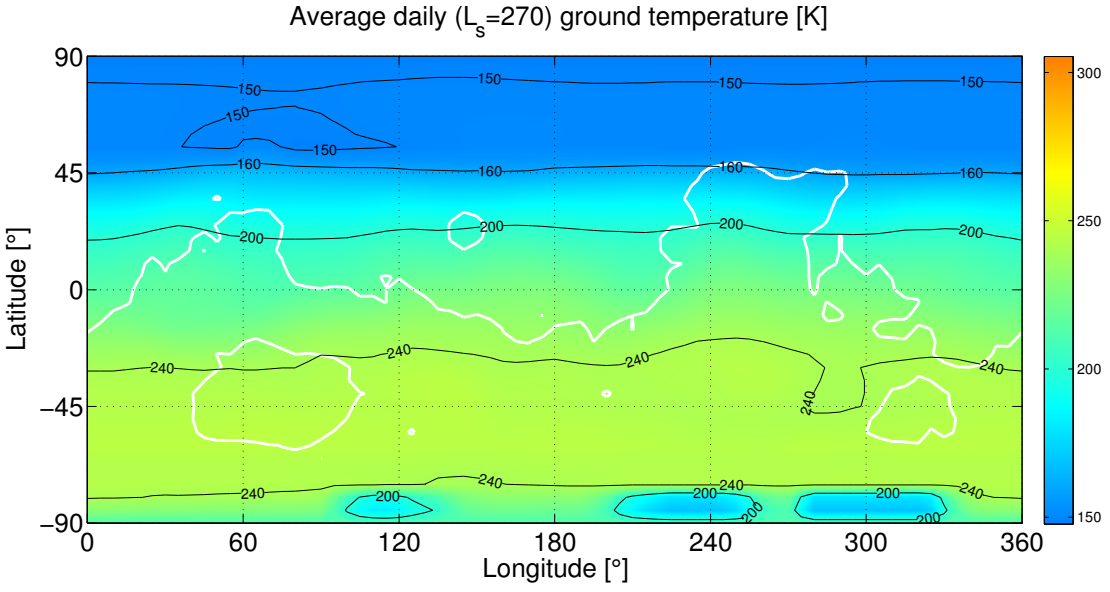


Figure B.61: Average daily ground temperature

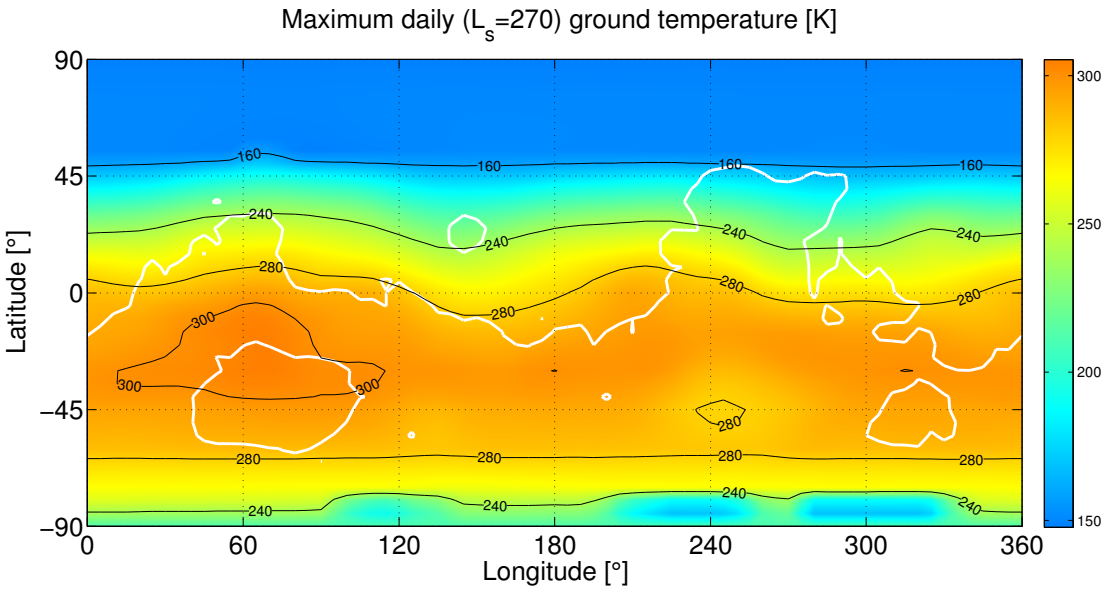


Figure B.62: Maximum daily ground temperature

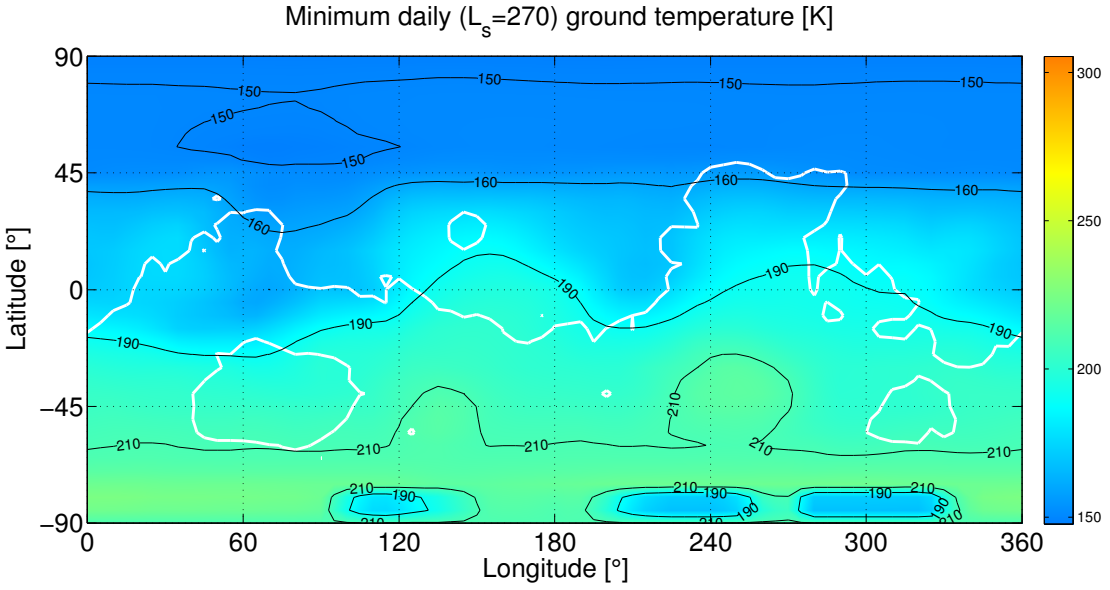


Figure B.63: Minimum daily ground temperature

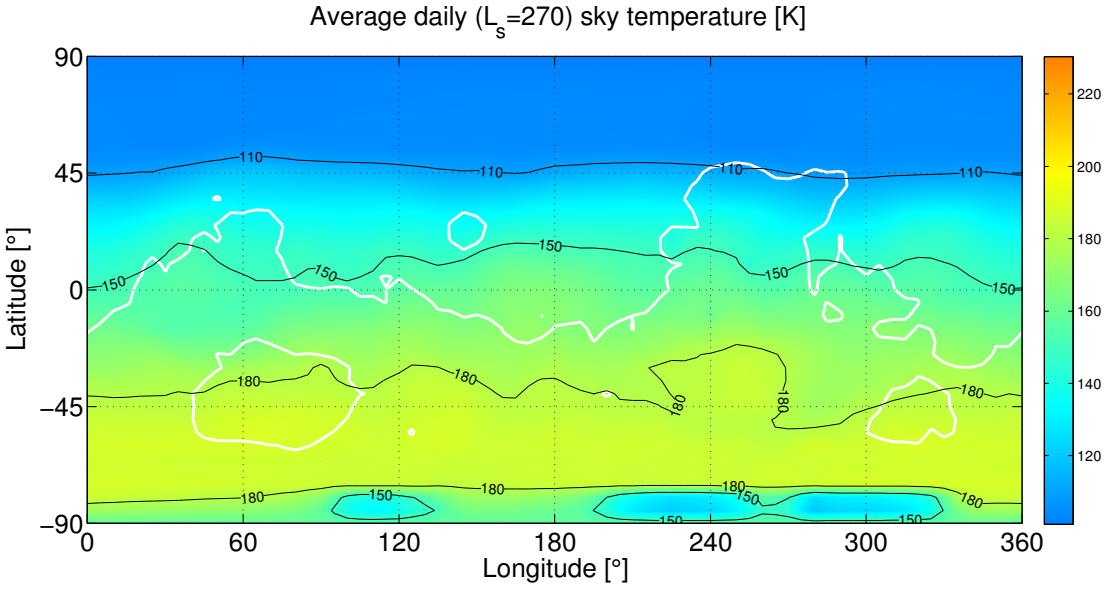


Figure B.64: Average daily sky temperature

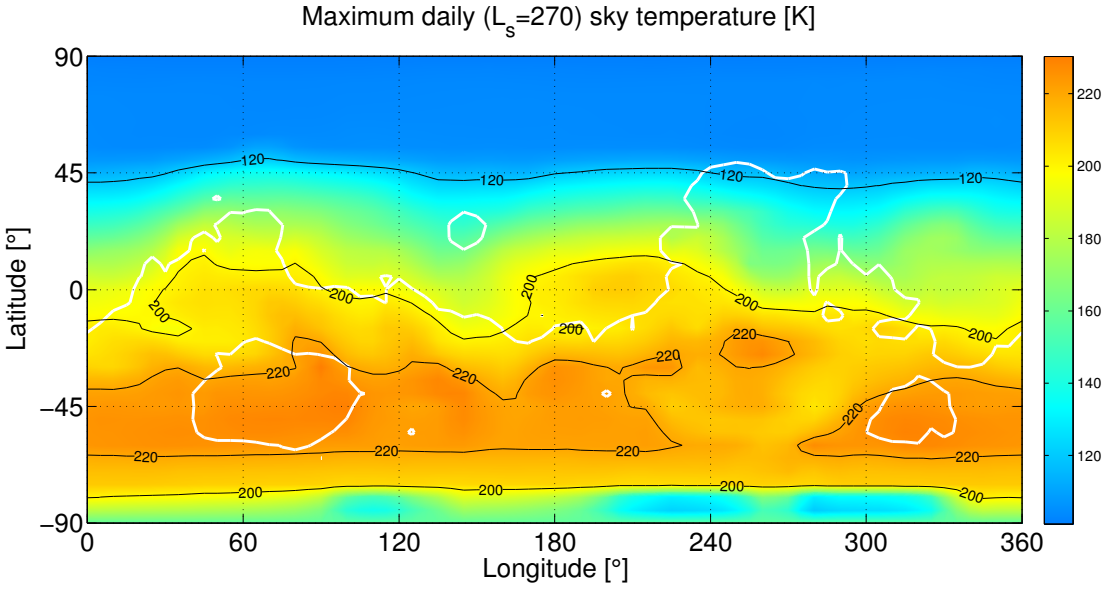


Figure B.65: Maximum daily sky temperature

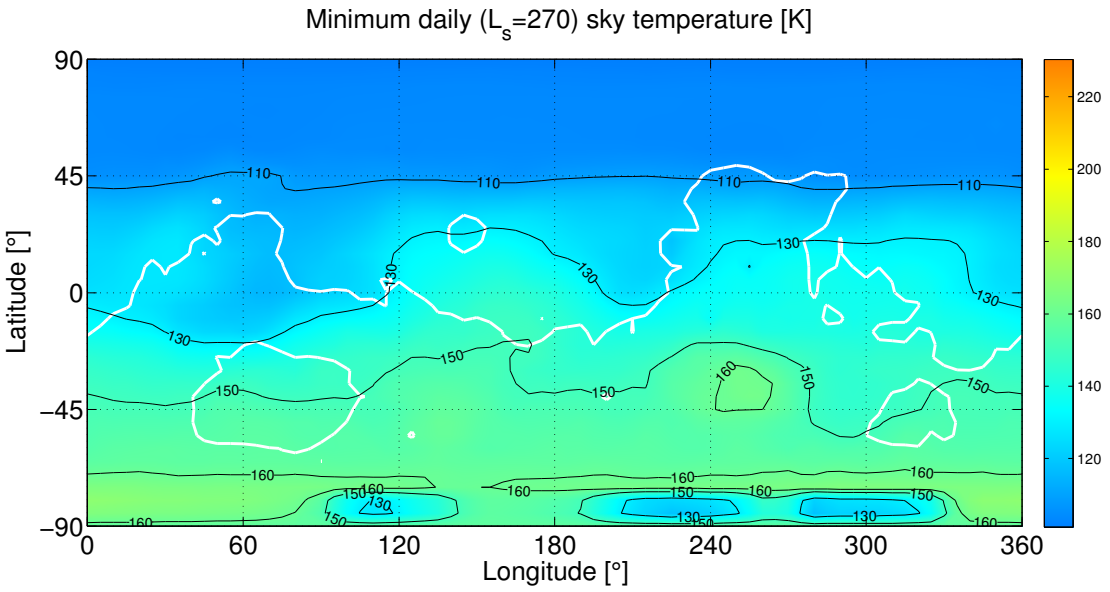


Figure B.66: Minimum daily sky temperature

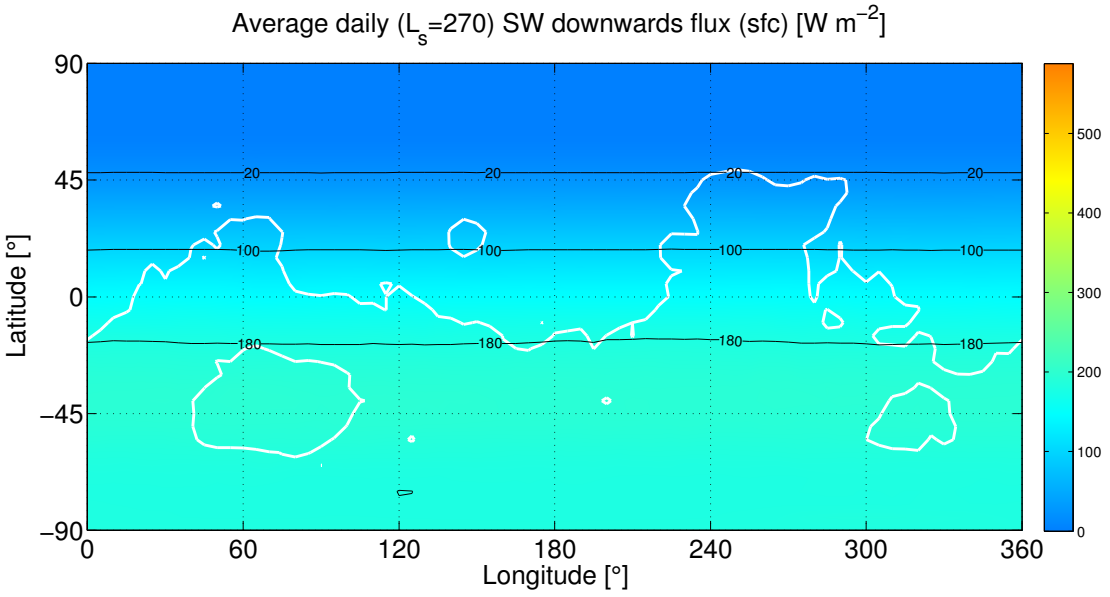


Figure B.67: Average daily SW downwards flux (surface)

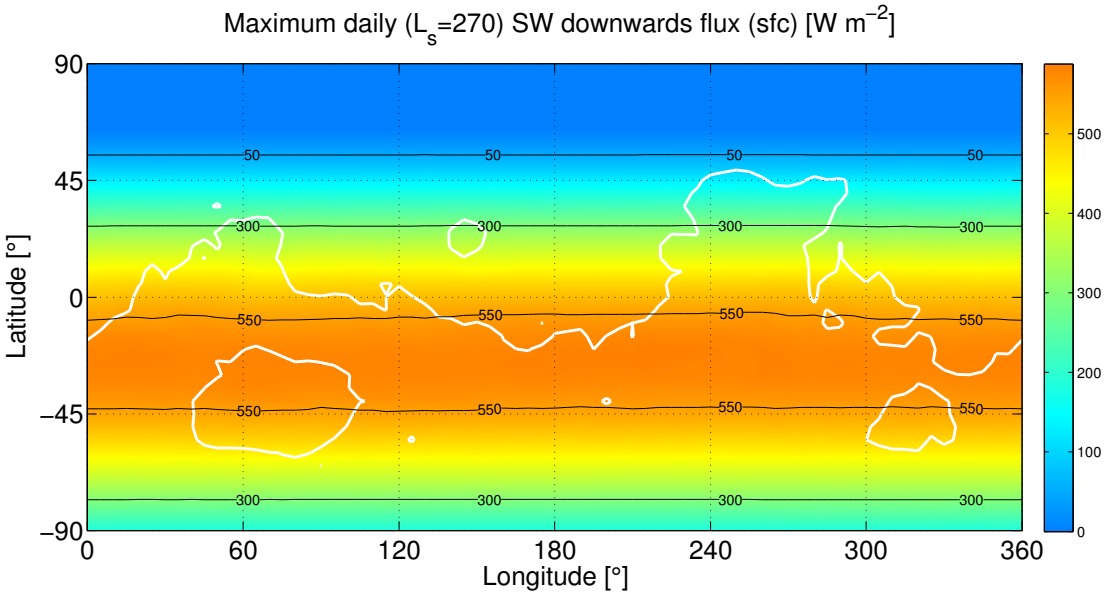


Figure B.68: Maximum daily SW downwards flux (surface)

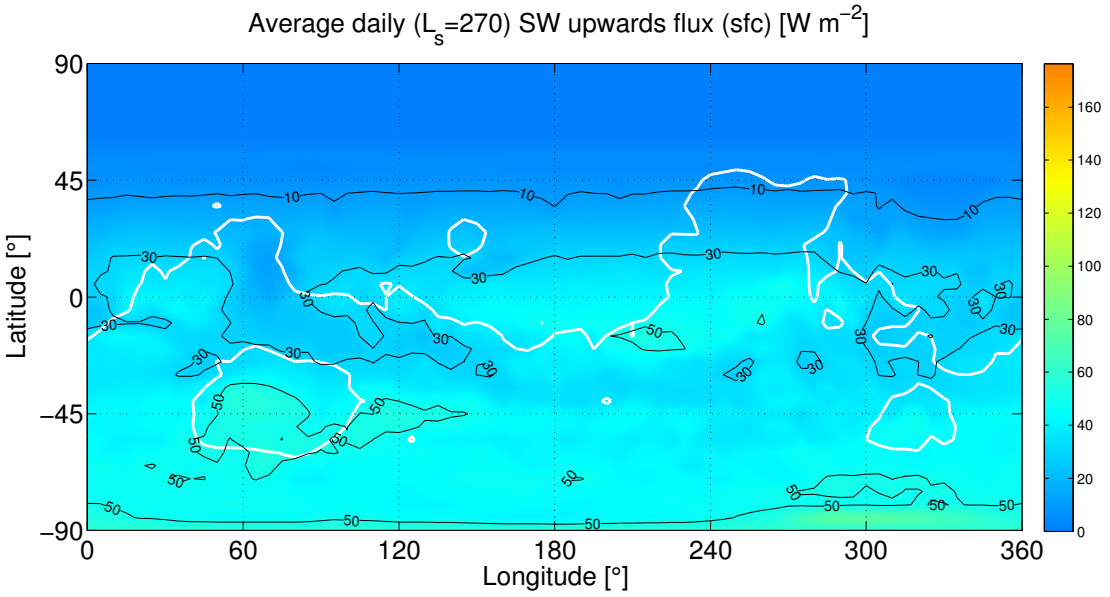


Figure B.69: Average daily SW upwards flux (surface)

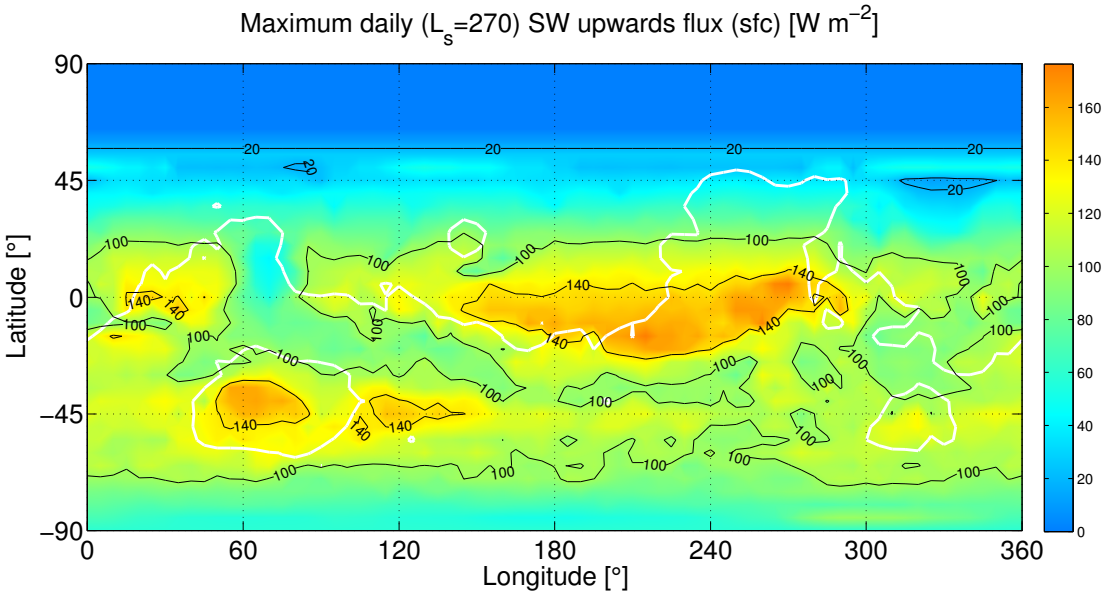


Figure B.70: Maximum daily SW upwards flux (surface)

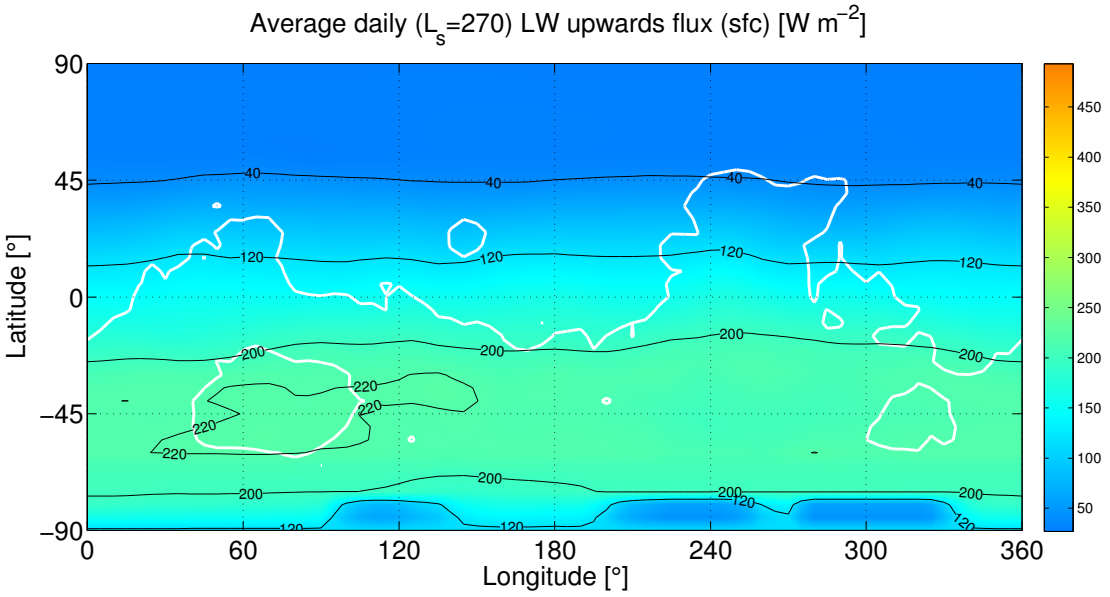


Figure B.71: Average daily LW upwards flux (surface)

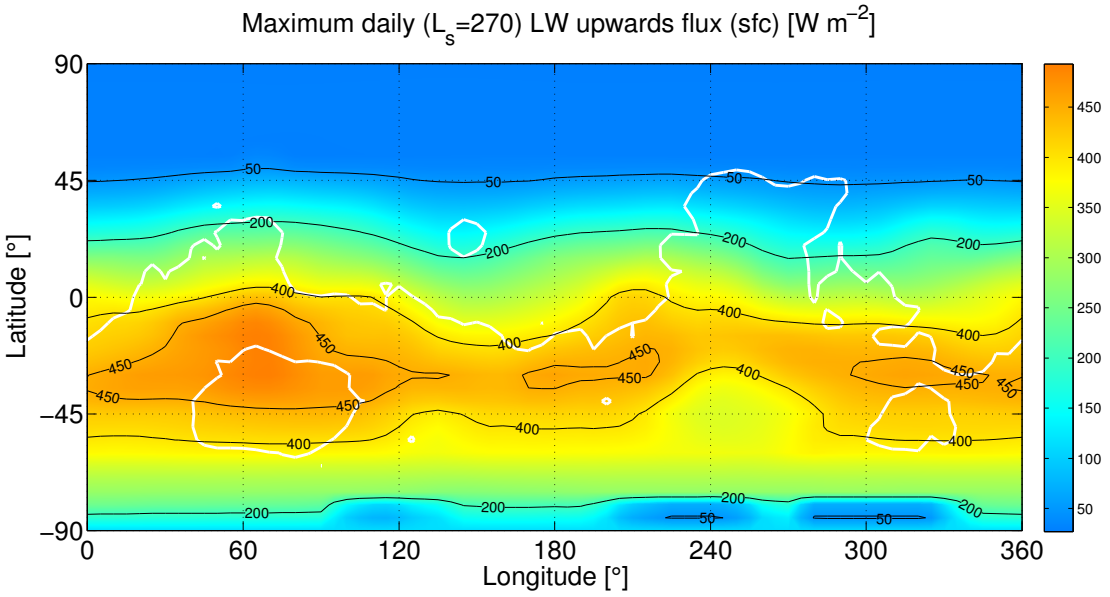


Figure B.72: Maximum daily LW upwards flux (surface)

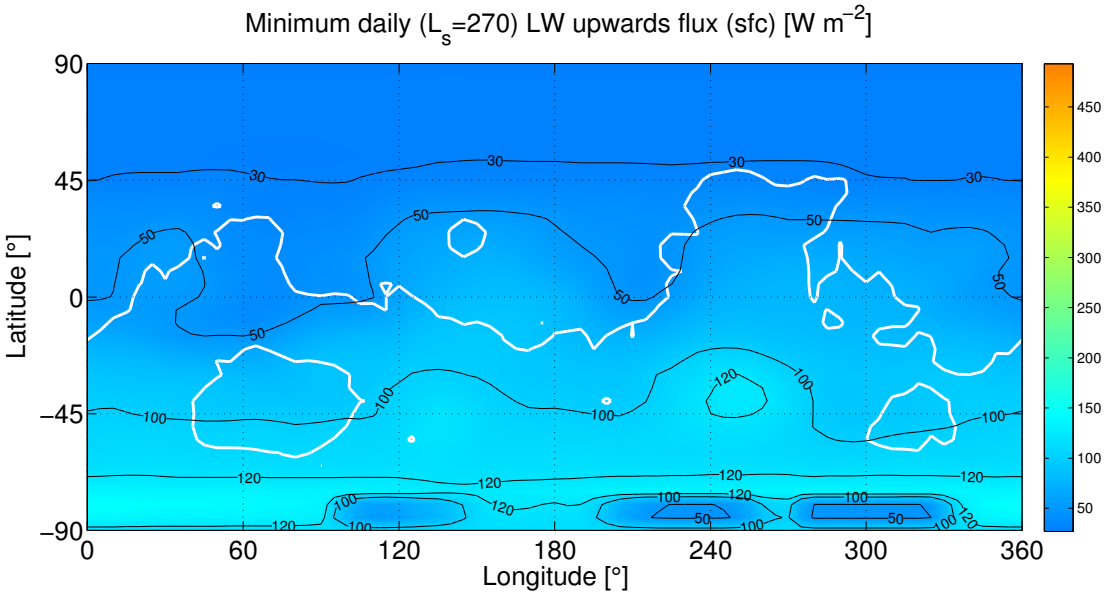


Figure B.73: Minimum daily LW upwards flux (surface)

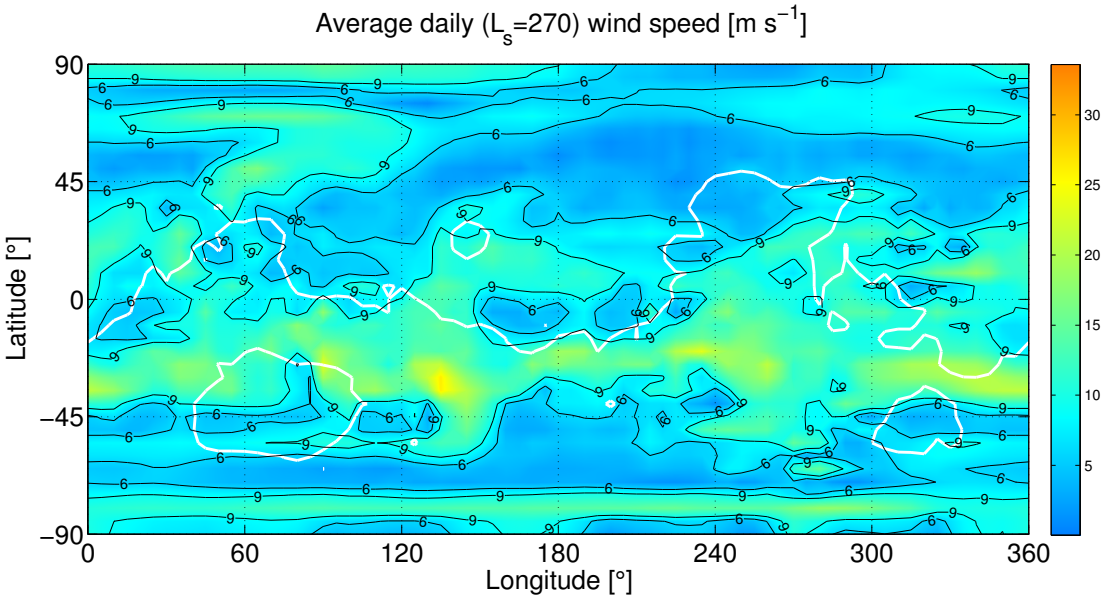


Figure B.74: Average daily wind speed

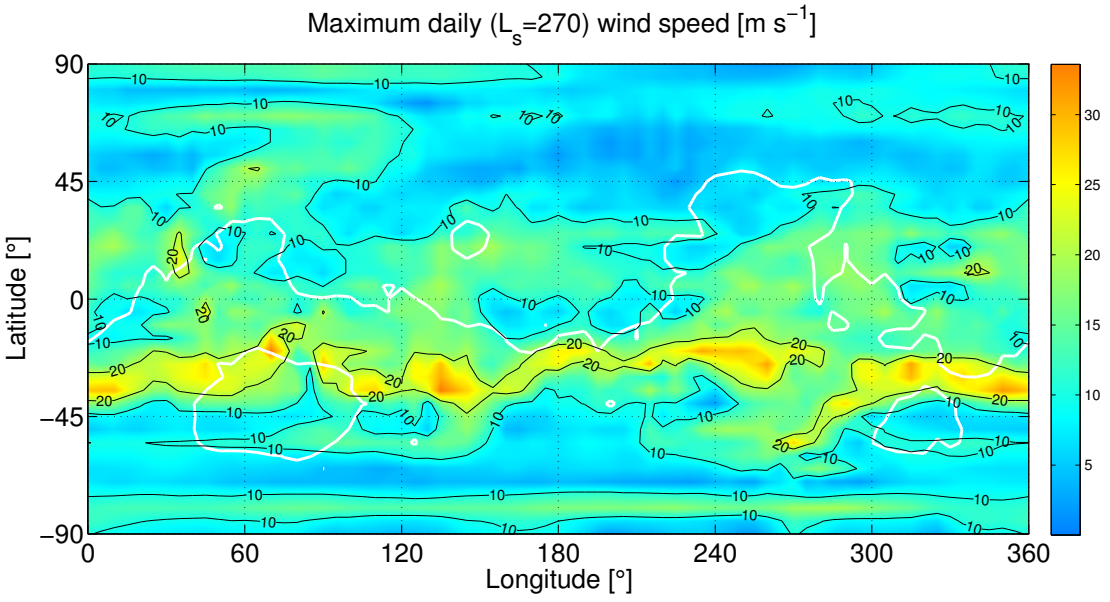


Figure B.75: Maximum daily wind speed

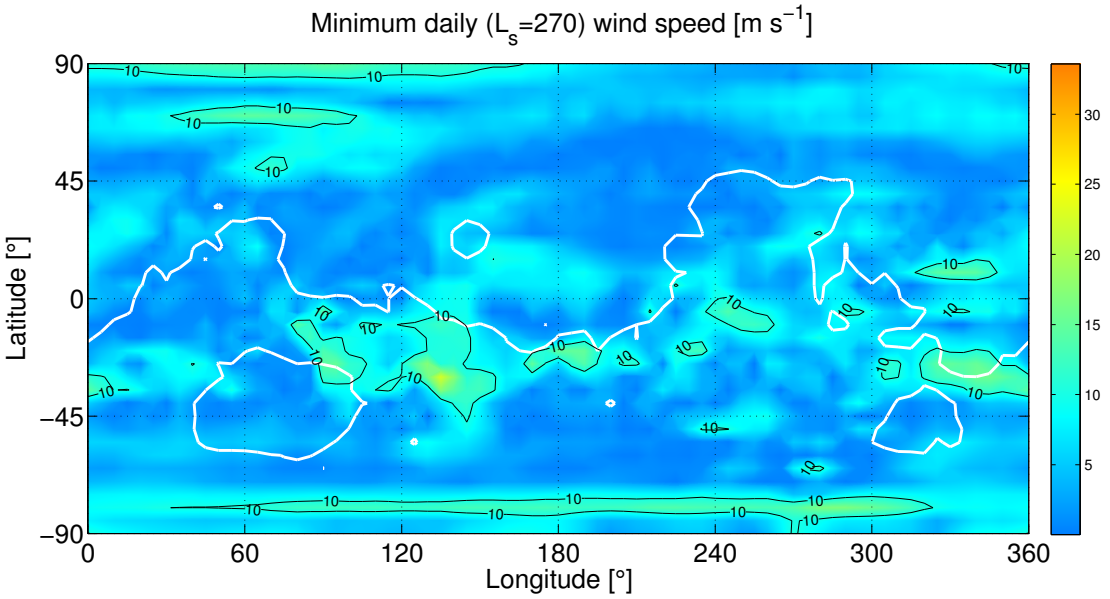


Figure B.76: Minimum daily wind speed

## B.5 Annual simulation

The results for the annual simulation are presented below.

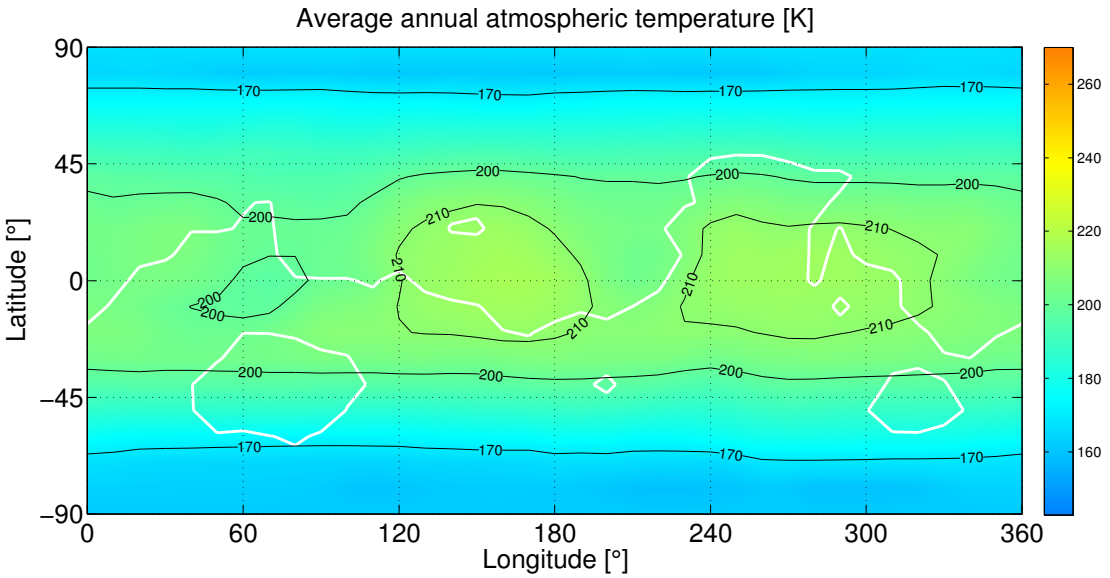


Figure B.77: Average annual atmospheric temperature

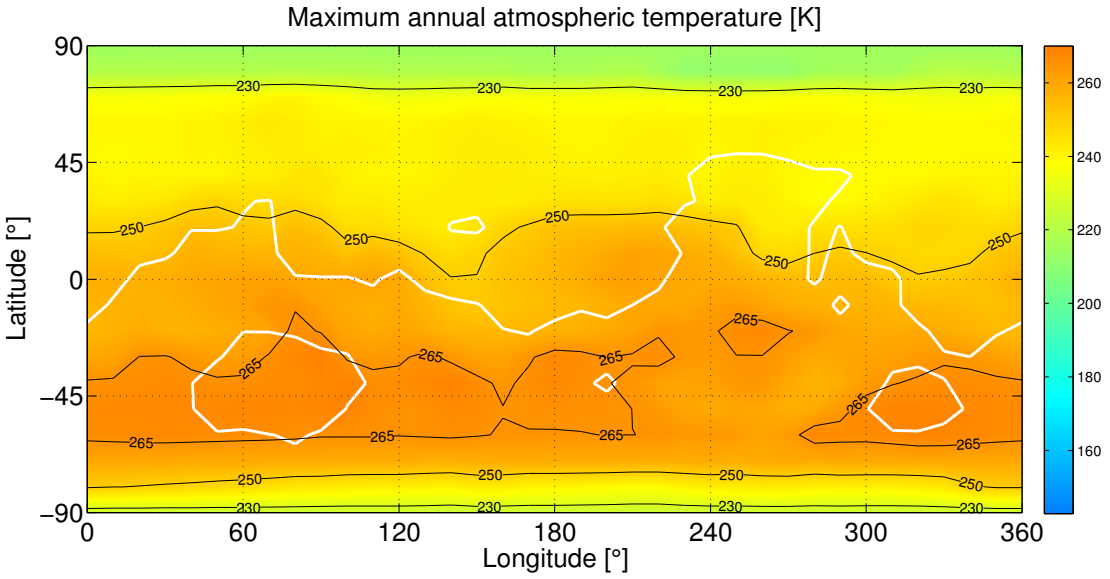


Figure B.78: Maximum annual atmospheric temperature

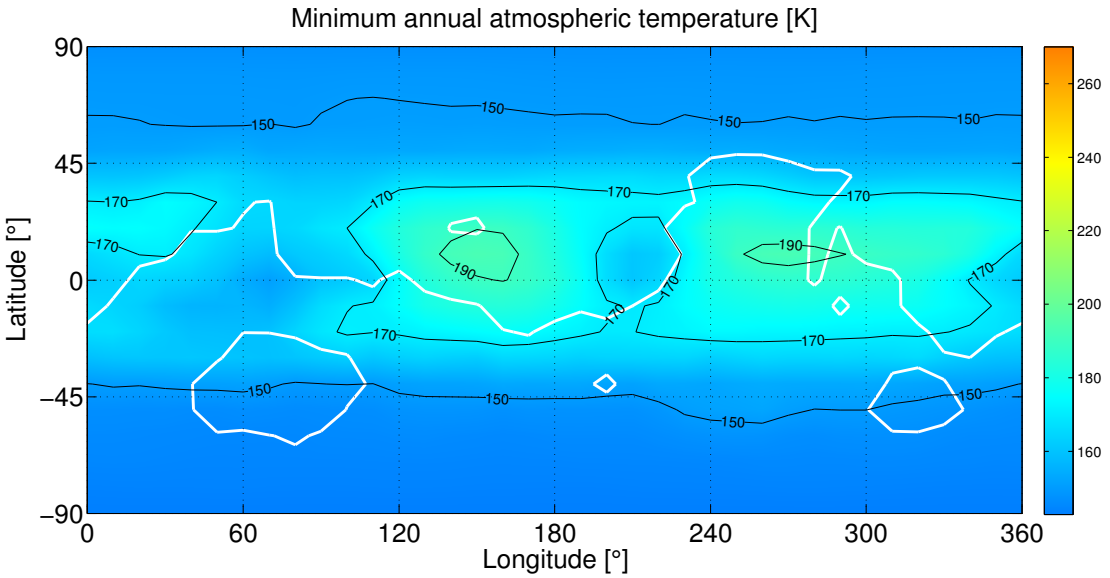


Figure B.79: Minimum annual atmospheric temperature

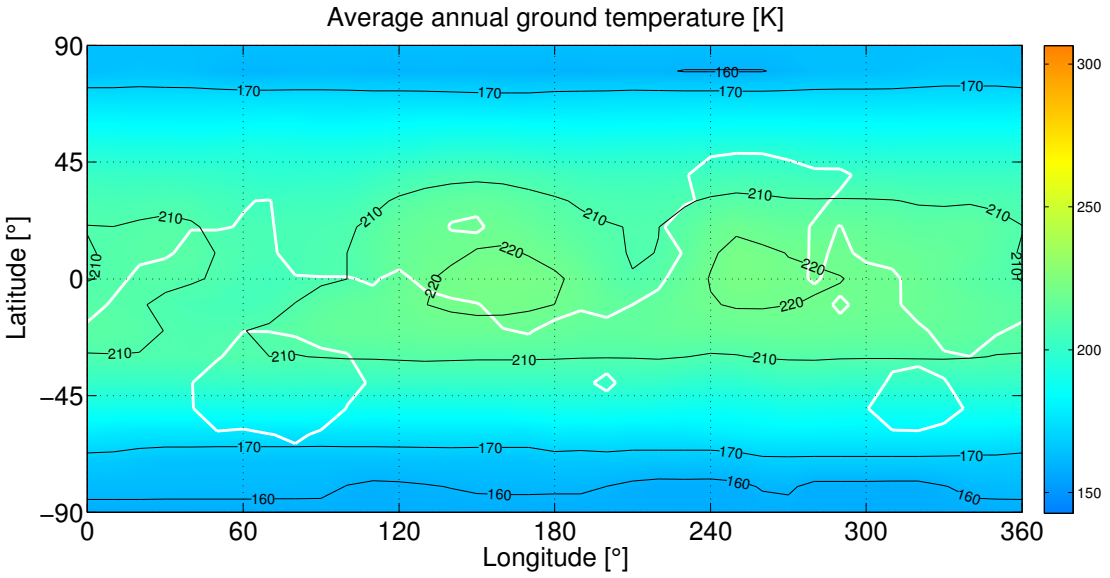


Figure B.80: Average annual ground temperature

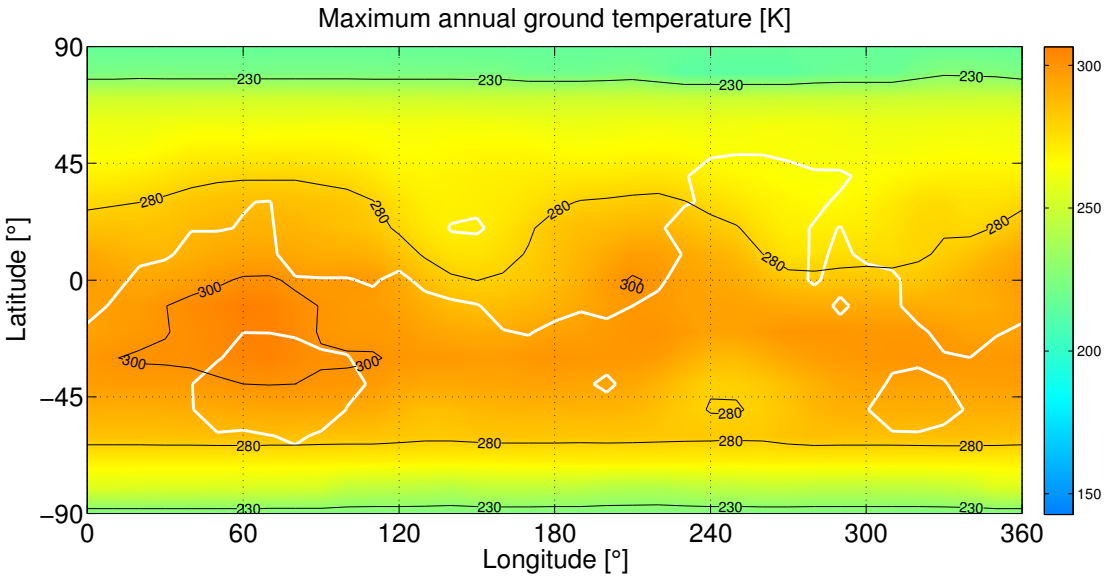


Figure B.81: Maximum annual ground temperature

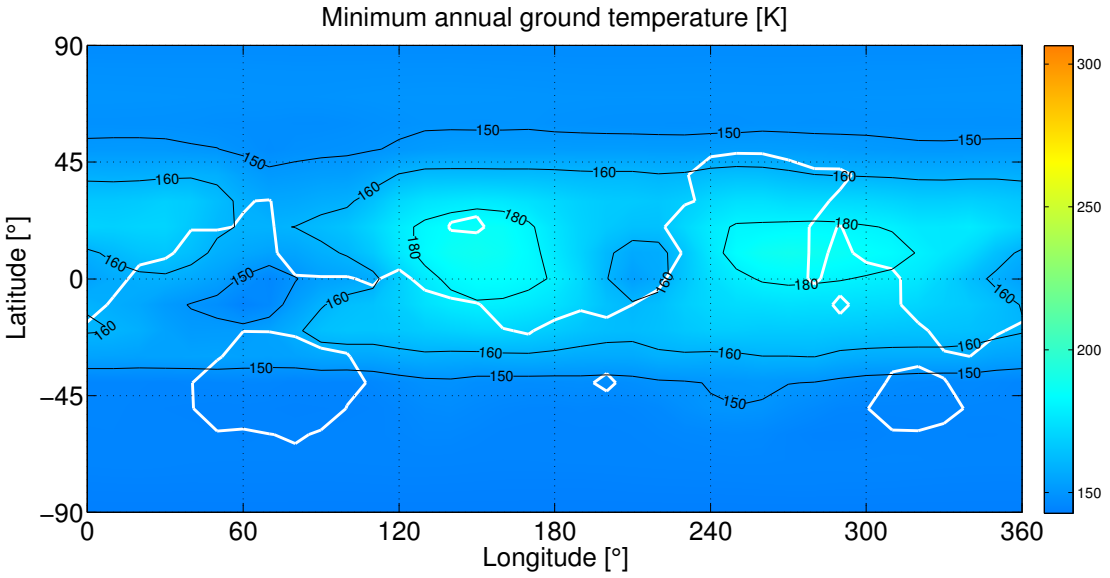


Figure B.82: Minimum annual ground temperature

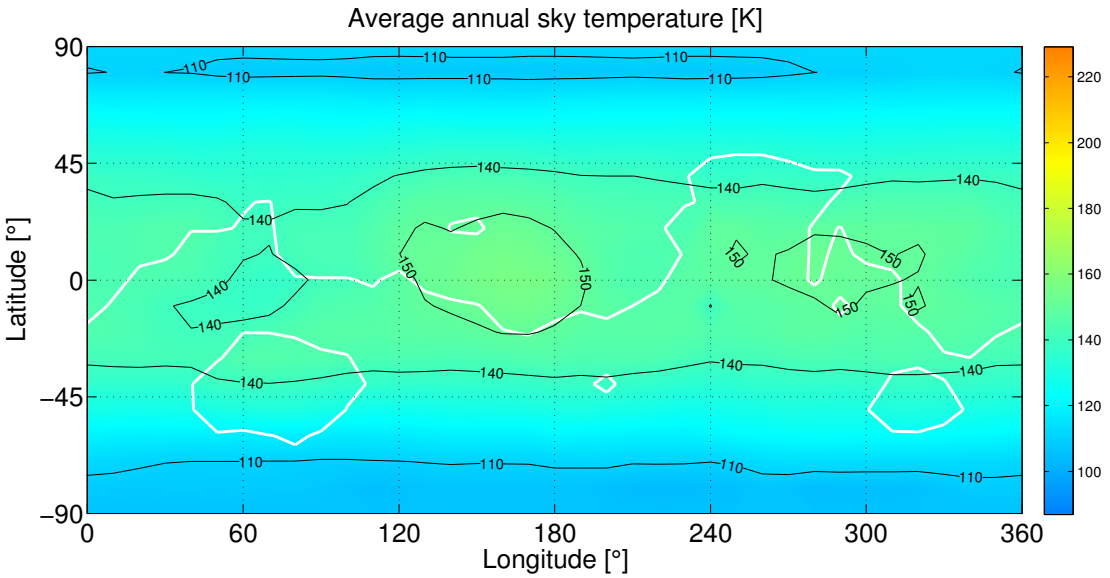


Figure B.83: Average annual sky temperature

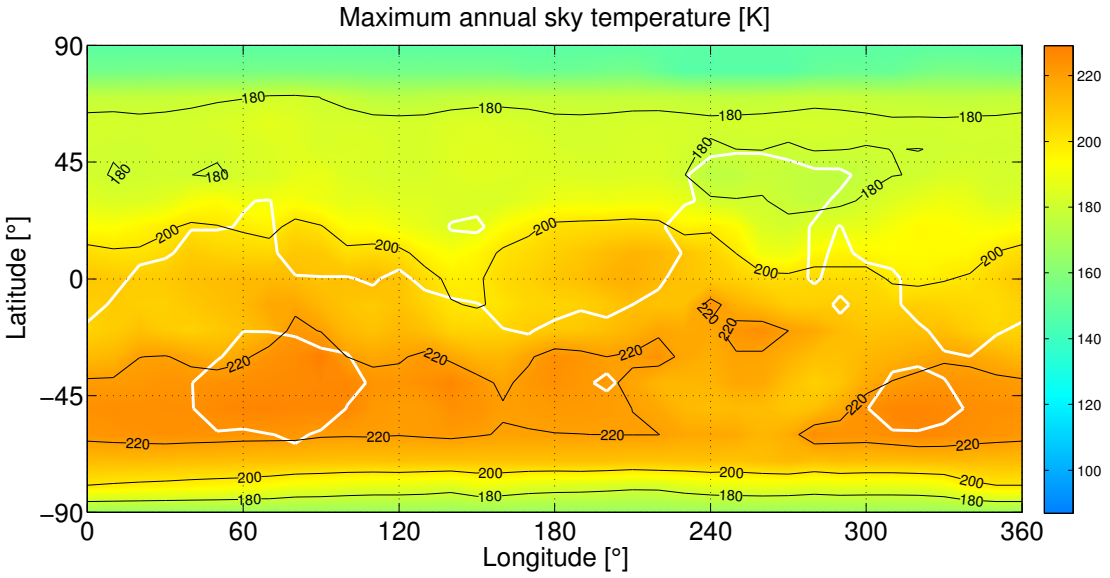


Figure B.84: Maximum annual sky temperature

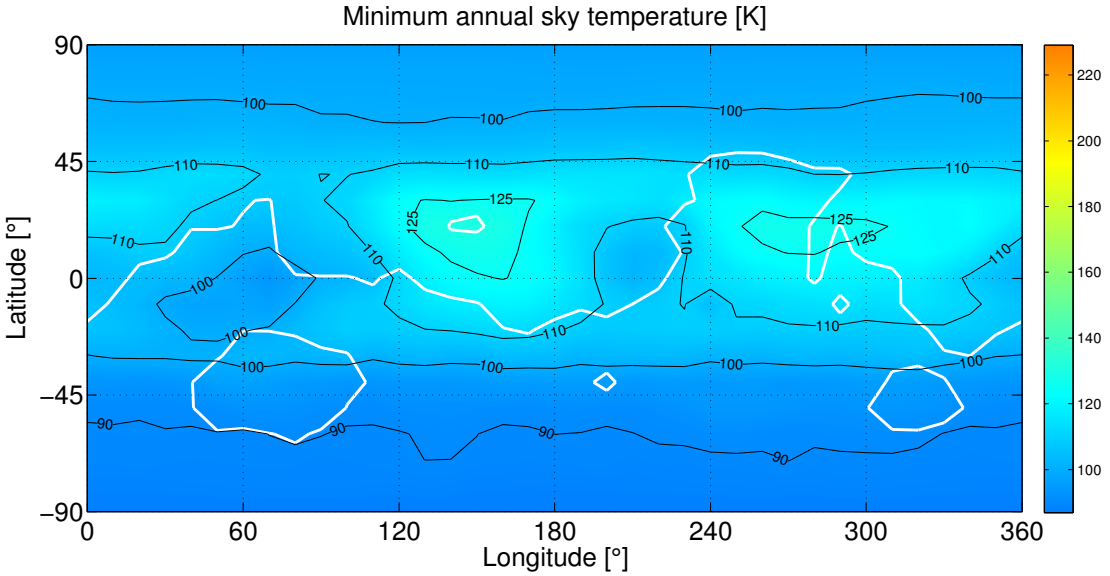


Figure B.85: Minimum annual sky temperature

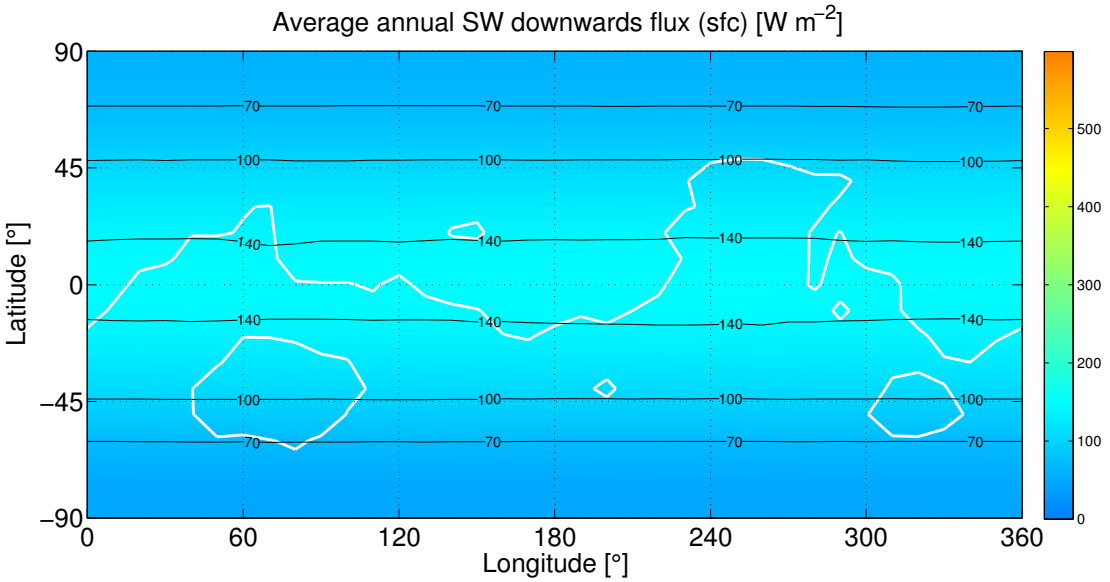


Figure B.86: Average annual SW downwards flux (surface)

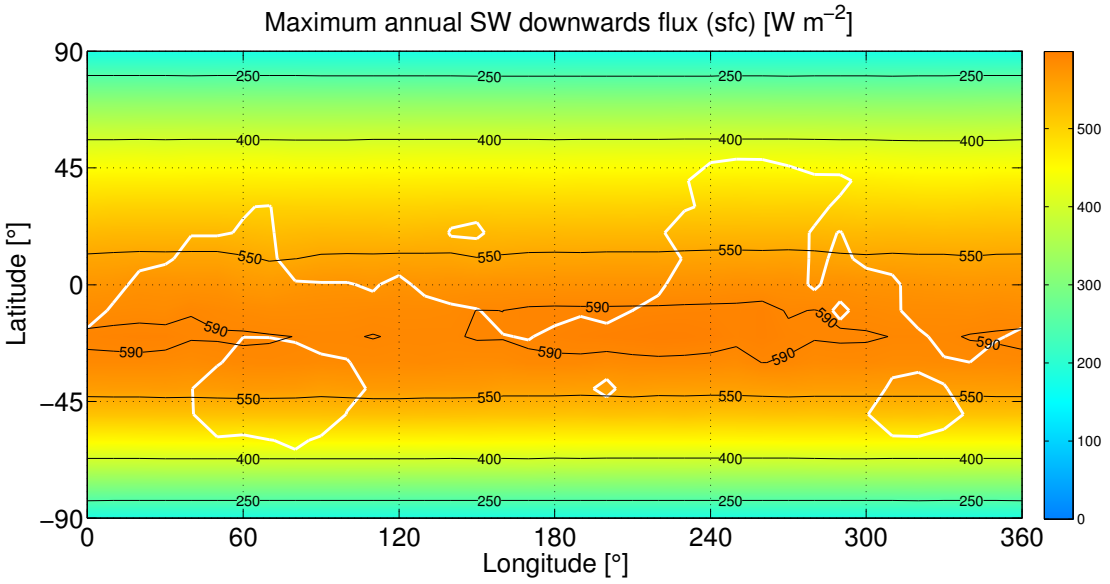


Figure B.87: Maximum annual SW downwards flux (surface)

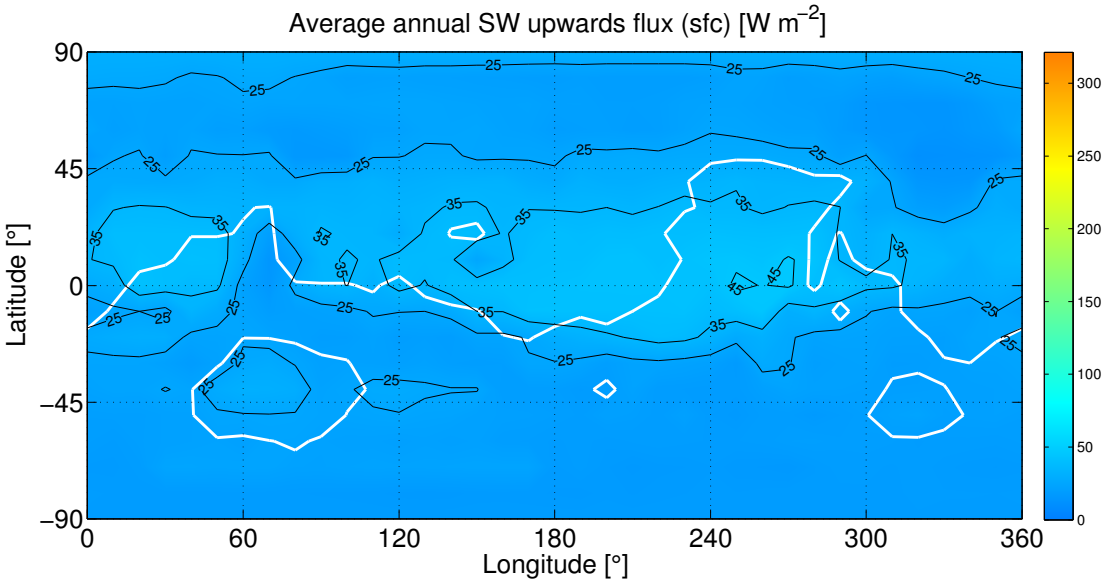


Figure B.88: Average annual SW upwards flux (surface)

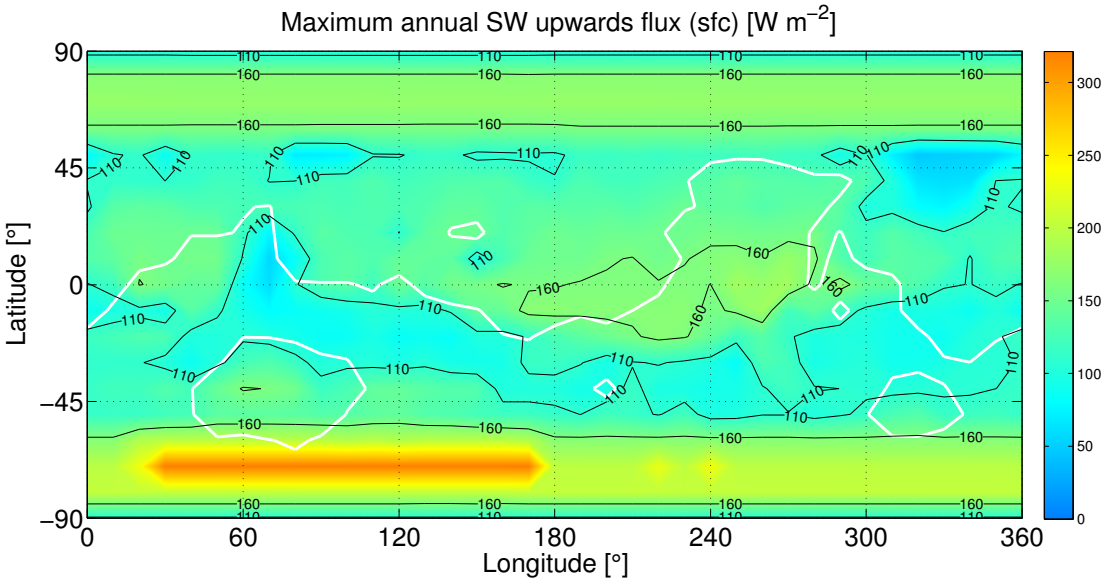


Figure B.89: Maximum annual SW upwards flux (surface)

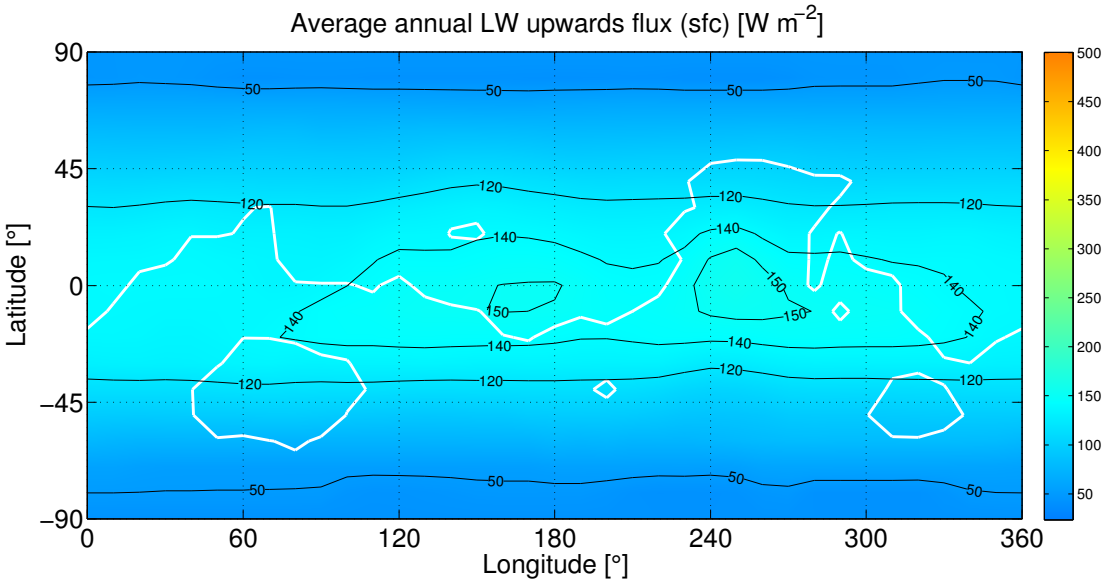


Figure B.90: Average annual LW upwards flux (surface)

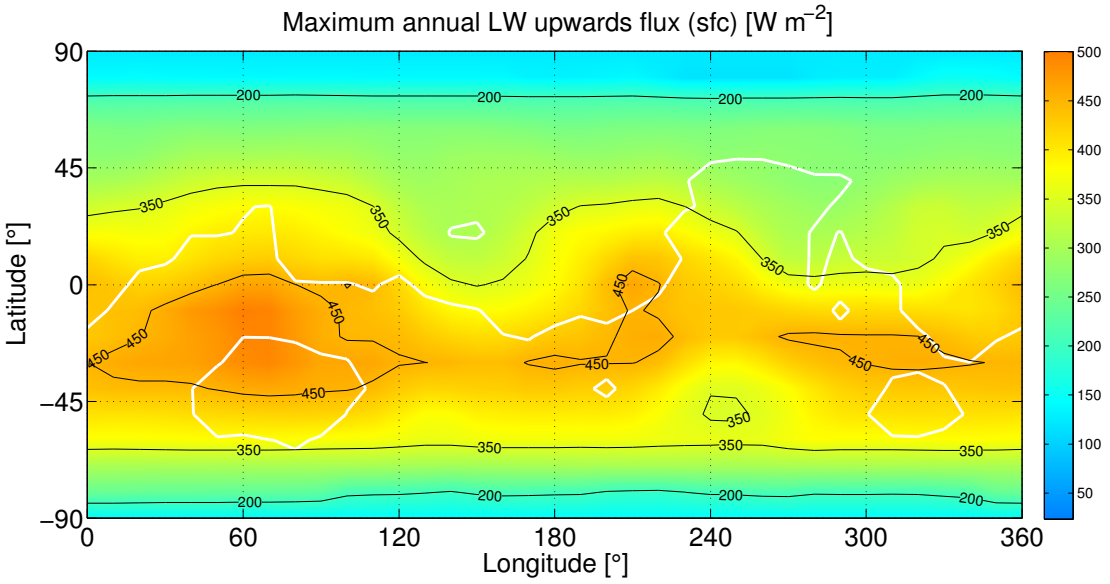


Figure B.91: Maximum annual LW upwards flux (surface)

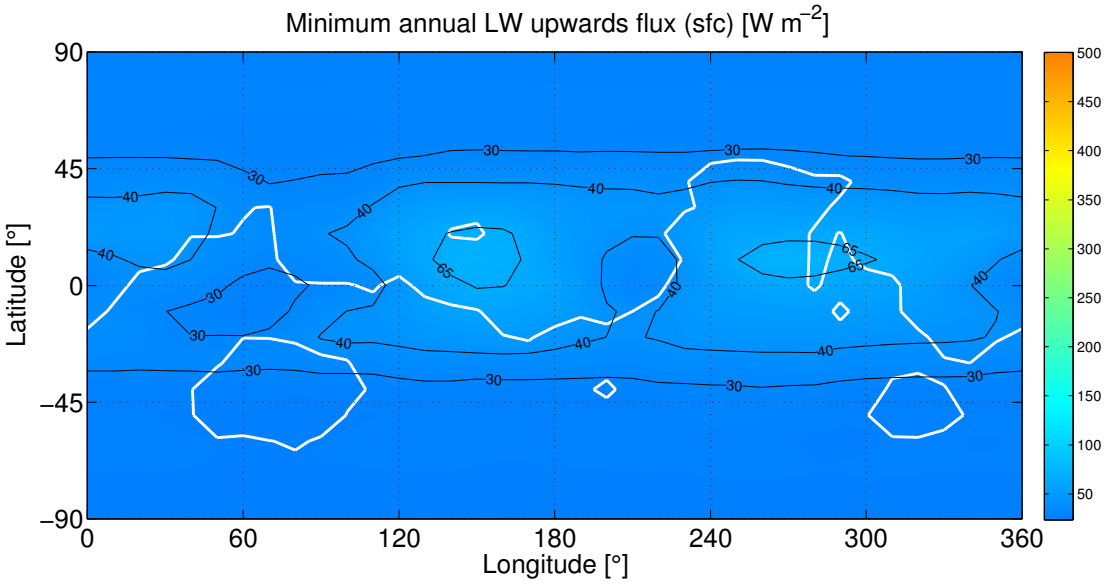


Figure B.92: Minimum annual LW upwards flux (surface)

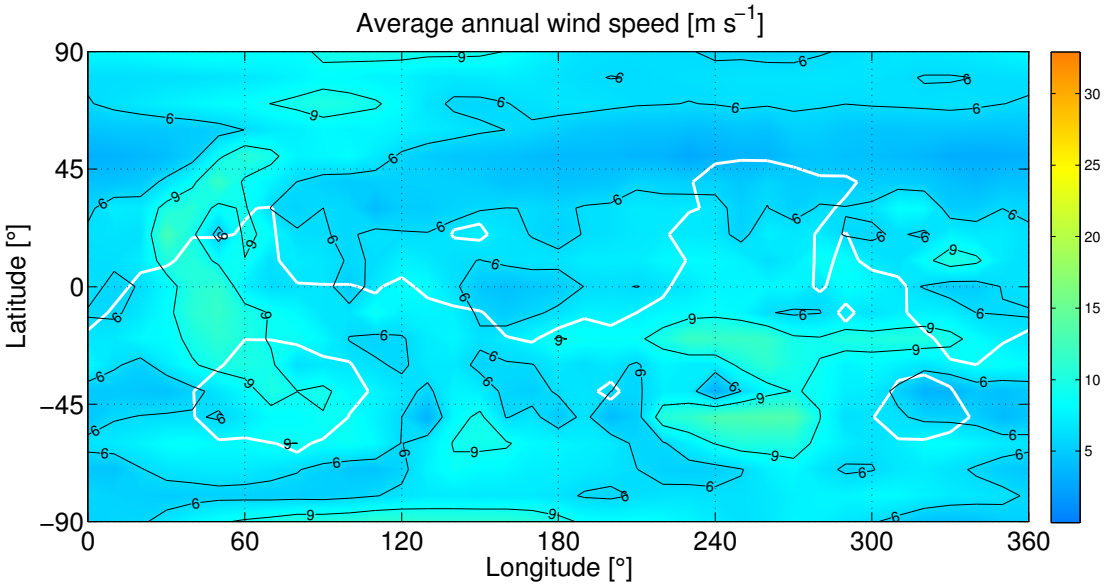


Figure B.93: Average annual wind speed

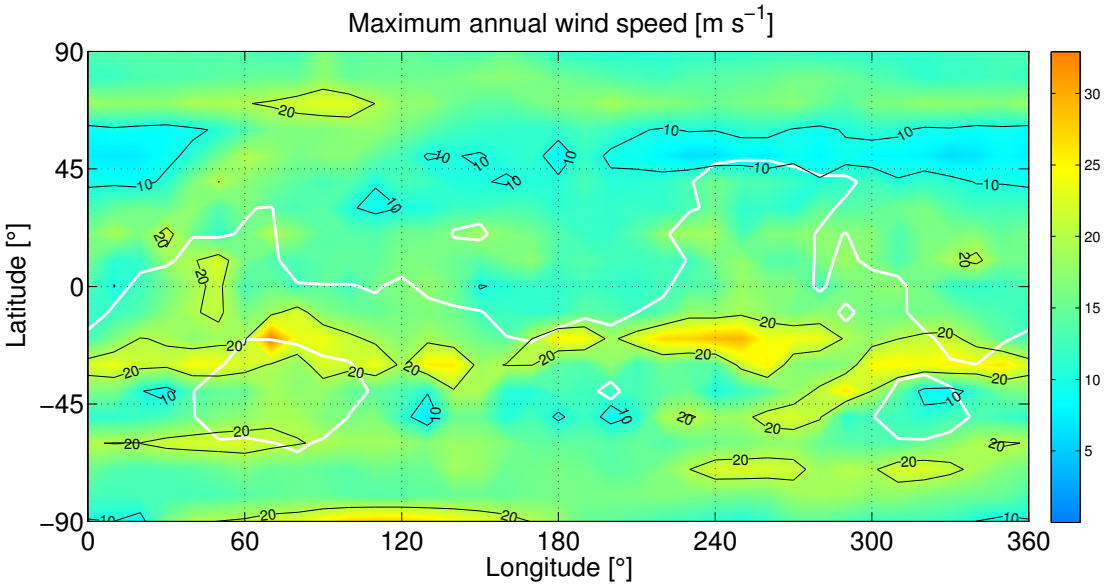


Figure B.94: Maximum annual wind speed

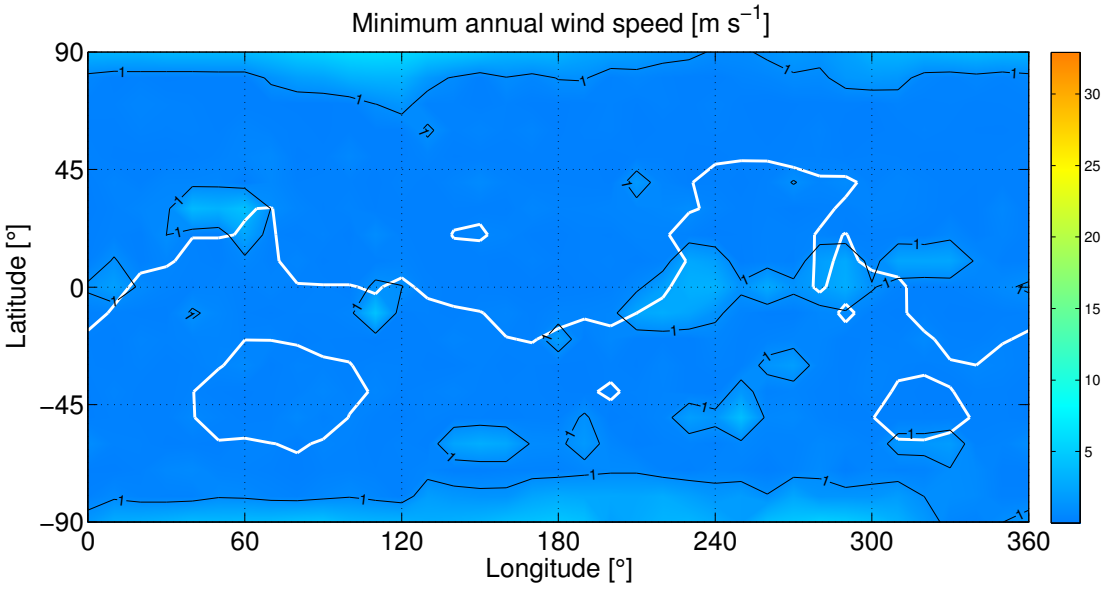


Figure B.95: Minimum annual wind speed

# Appendix C

# Budget

In this section we present the budget of the *Study of the Martian environment for application to the design of a greenhouse*. The man hours as well as the hardware and software resources required to carry out the study are illustrated in Table C.1. Approximately seven months were spent on the project, two of which on a part-time basis and the rest working full time. This amounts to 532 man hours: if we assign a price per hour of 15€, the total cost of the engineering work can be estimated in 8000€. Due to the extensive processing time required by the project, the power consumption has also been included in the budget: with approximately 1200 simulation hours, the electric power consumed corresponds to a cost of 130€. The hardware and software employed during the study sum up to a cost of 5600€. An overhead of 10% has been applied to the man hours and to the processing time. No overhead has been applied to hardware and software expenses, as their cost is considered to be already fixed. The total is close to 14600€.

| Concept | h | €/h | Cost (€) |
|---|---|---|---|
| State of the art | | | |
| Preliminary analysis | 15 | 15 | 225 |
| Missions | 60 | 15 | 900 |
| Models | 45 | 15 | 675 |
| Subtotal of state of the art | 120 | 15 | 1800 |
| Code Implementation | | | |
| TES/MSG Data | 12 | 15 | 180 |
| MarsGRAM model | 90 | 15 | 1350 |
| MarsRAD model | 45 | 15 | 675 |
| Pollack model | 30 | 15 | 450 |
| Dycus model | 10 | 15 | 150 |
| Divine model | 5 | 15 | 75 |
| Auxiliary functions | 60 | 15 | 900 |
| Subtotal of implementation | 252 | 15 | 3780 |
| Writing of the project report | 160 | 15 | 2400 |
| **Subtotal of worked hours** | **532** | **15** | **7980** |
| Overhead (10%) | 54 | 15 | 810 |
| Simulation (Power consumption) | | | |
| TES/MSG Data | 2 | 0.11 | 0.22 |
| 2D Maps | 405 | 0.11 | 44.55 |
| Climate Maps | 63 | 0.11 | 6.93 |
| Location in Time | 714 | 0.11 | 78.54 |
| Auxiliary simulations | 10 | 0.11 | 1.1 |
| **Subtotal of simulation hours** | **1194** | **0.11** | **131.34** |
| Overhead (10%) | 120 | 0.11 | 13.2 |
| Hardware | | | |
| PC (Intel Core i7 860 @ 2.80GHz) | | | 1100 |
| Laptop (Intel Core i7 3540M @ 3.00GHz) | | | 1300 |
| MacBook Air (Intel Core i7 @ 1.7GHz) | | | 1600 |
| **Subtotal of hardware components** | | | **4000** |
| Software | | | |
| Matlab 8.1 R2013a (UNIX) | | | 500 |
| Matlab 8.3 R2014a (Win64) | | | 500 |
| Microsoft Windows 8 (Student) | | | 0 |
| Microsoft Windows Server 2012 (Student) | | | 0 |
| Microsoft Visual Studio 2012 (Student) | | | 0 |
| Intel Fortran Composer XE 2013 | | | 622.57 |
| Microsoft Office 2013 (Student) | | | 0 |
| TeXlive 2013 + Texmaker 4.1.1 | | | 0 |
| **Subtotal of software licenses** | | | **1622.57** |
| **Total** | **586** | | **14600** |

Table C.1: Budget of the *Study of the Martian environment for application to the design of a greenhouse*.

# Bibliography


[1] A. Zak. A complete list of the world's launch attempts in the direction of mars, March 2014. URL http://www.russianspaceweb.com/spacecraft_planetary_mars.html.

[2] D. R. Williams. Chronology of mars exploration, November 2013. URL http://nssdc.gsfc.nasa.gov/planetary/chronology_mars.html.

[3] NASA (Ed.). Mars exploration program overview, 2012. URL http://mars.jpl.nasa.gov/programmissions/science/.

[4] NASA (Ed.). Viking. February 1975. URL http://mars.jpl.nasa.gov/newsroom/presskits/viking.pdf.

[5] NASA (Ed.). Viking 1 lander information, January 2005. URL http://nssdc.gsfc.nasa.gov/planetary/viking1landata.html.

[6] NASA (Ed.). Viking 1 lander description, 2005. URL http://nssdc.gsfc.nasa.gov/nmc/masterCatalog.do?sc=1975-075C.

[7] R. J. Wilson and Mark I. R. The martian atmosphere during the viking mission, i: Infrared measurements of atmospheric temperatures revisited. *Icarus*, 145, 2000. doi: 10.1006/icar.2000.6378.

[8] NASA (Ed.). Viking project information. viking mission to mars, December 2006. URL http://nssdc.gsfc.nasa.gov/planetary/viking.html.

[9] JPL (Ed.). Mars pathfinder mission objectives, July 1997. URL http://mars.jpl.nasa.gov/MPF/mpf/mission_obj.html.

[10] JPL (Ed.). Mars pathfinder science results, atmosphere profile and structure, July 1999. URL http://mars.jpl.nasa.gov/MPF/science/atmospheric.html.

[11] JPL (Ed.). Mars pathfinder proposal information package, February 1997. URL http://www-k12.atmos.washington.edu/k12/mars/MPF_short_facts.html.

[12] JPL (Ed.). Mars pathfinder science results, alpha proton x-ray spectrometer (apxs), July 1999. URL http://mars.jpl.nasa.gov/MPF/science/mineralogy.html.

[13] JPL (Ed.). Mars pathfinder science results, surface material properties, July 1999. URL http://mars.jpl.nasa.gov/MPF/science/surface.html.

[14] D. Savage, G. Webster, and K. Edgett. Delta-fan on mars suggests ancient rivers were persistent, November 2003. URL http://www.nasa.gov/home/hqnews/2003/nov/HQ_03364_MGS_delta.html.

[15] NASA, JPL, and Arizona State University (Eds.). Final count of tes spectra collected during the aerobraking, mapping, and extended phases of mgs, 2008. URL http://tes.asu.edu/about.

[16] NASA, JPL, and Arizona State University (Eds.). Global mineral maps produced from tes data, 2005. URL http://tes.asu.edu/discoveries/2.

[17] B. J. Conrath, J. C. Pearl, M. D. Smith, et al. Mars global surveyor thermal emission spectrometer (tes) observations: Atmospheric temperatures during aerobraking and science phasing. *Journal of Geophysical Research: Planets*, 105, 2000. doi: $10.1029/1999\mathrm{je}001095$.

[18] N. E. Putzig, M. T. Mellon, K. A. Kretke, et al. Global thermal inertia and surface properties of mars from the mgs mapping mission. *Icarus*, 173, 2005. doi: $10.1016/\mathrm{j.icarus}.2004.08.017$.

[19] NASA, JPL, and Arizona State University (Eds.). Tes observed the atmosphere's thermal structure warms and cools according to season and distance from the sun, 2001. URL http://tes.asu.edu/discoveries/13.

[20] NASA, JPL, and Arizona State University (Eds.). Tes provided the first systematic study of martian weather. 2004. URL http://tes.asu.edu/discoveries/6.

[21] NASA, JPL, and Arizona State University (Eds.). Tes mapped the atmosphere's global circulation for three mars years, 2004. URL http://tes.asu.edu/discoveries/10.

[22] NASA, JPL, and Arizona State University (Eds.). Tes discovered that warm dust in the atmosphere prevents water-ice clouds, 2002. URL http://tes.asu.edu/discoveries/14.

[23] NASA, JPL, and Arizona State University (Eds.). Tes monitored the growth and decay of the 2001 global dust storm, 2002. URL http://tes.asu.edu/discoveries/8.

[24] NASA, JPL, and Arizona State University (Eds.). Tes traced the abrupt disappearance of the seasonal polar caps, 2000. URL http://tes.asu.edu/discoveries/12.

[25] NASA, JPL, and Arizona State University (Eds.). Tes discovered that jets of dusty gas produce dark markings on the south polar cap, 2006. URL http://tes.asu.edu/discoveries/5.

[26] R. Simpson. Mars global surveyor mission information, May 2008. URL http://pds-geosciences.wustl.edu/missions/mgs/catalog/mission.txt.

[27] NASA and JPL (Eds.). Mars odyssey mission objectives, 2006. URL http://mars.jpl.nasa.gov/odyssey/mission/science/objectives/.

[28] NASA (Ed.). 2001 mars odyssey arrival press kit, October 2001. URL http://phoenix.lpl.arizona.edu/science04.php.

[29] NASA, JPL, Caltech, and Arizona State University (Eds.). Themis mars atmosphere dust maps, August 2012. URL http://themis.mars.asu.edu/dust_maps.

[30] NASA, JPL, Caltech, and Arizona State University (Eds.). Themis finds a landing site for phoenix, May 2008. URL http://themis.asu.edu/node/5403.

[31] NASA (Ed.). Rover landing site chosen, December 2005. URL http://themis.asu.edu/node/5390.

[32] NASA, JPL, Caltech, and Arizona State University (Eds.). Themis data suggest early gale crater targets for rover, August 2012. URL http://themis.asu.edu/node/5990.

[33] P. B. Saganti, F. A. Cucinotta, J. W. Wilson, et al. Radiation climate map for analyzing risks to astronauts on the mars surface from galactic cosmic rays. *Space Science Reviews*, 110, 2004. doi: 10.1023/b:spac.0000021010.20082.1a.

[34] ESA (Ed.). Mars express mission objectives, August 2003. URL http://sci.esa.int/jump.cfm?oid=31023.

[35] ESA (Ed.). Mars express orbiter instruments, February 2010. URL http://sci.esa.int/jump.cfm?oid=31033.

[36] ESA (Ed.). Water at martian south pole, March 2004. URL http://www.esa.int/Our_Activities/Space_Science/Mars_Express/Water_at_Martian_south_pole.

[37] V. Formisano. Detection of methane in the atmosphere of mars. *Science*, 306, 2004. doi: 10.1126/science.1101732.

[38] ESA (Ed.). Mars express factsheet, May 2013. URL http://www.esa.int/esaSC/SEMTV8374OD_0_spk.html.

[39] ESA (Ed.). New views of the martian ionosphere, November 2012. URL http://sci.esa.int/jump.cfm?oid=51056.

[40] ESA (Ed.). A seasonal ozone layer over the martian south pole, September 2013. URL http://sci.esa.int/jump.cfm?oid=52881.

[41] NASA and JPL (Eds.). Mars exploration rover facts. Technical report, October 2004. URL http://www.jpl.nasa.gov/news/fact_sheets/mars03rovers.pdf.

[42] NASA (Ed.). Mars exploration rover launches press kit. Technical report, June 2003. URL http://marsrover.nasa.gov/newsroom/merlaunch.pdf.

[43] J. Callas. A heartfelt goodbye to a spirited mars rover, May 2011. URL http://blogs.jpl.nasa.gov/2011/05/a-heartfelt-goodbye-to-a-spirited-mars-rover/.

[44] D. Coulter. Sand-trapped mars rover makes big discovery, December 2009. URL http://news.wustl.edu/news/Pages/15257.aspx.

[45] NASA (Ed.). Mars exploration rover landings press kit. Technical report, January 2004. URL http://marsrover.nasa.gov/newsroom/merlandings.pdf.

[46] P. Withers and M. D. Smith. Atmospheric entry profiles from the mars exploration rovers spirit and opportunity. *Icarus*, 185, 2006. doi: 10.1016/j.icarus.2006.06.013.

[47] R. V. Morris, D. W. Ming, R. Gellert, et al. The hydrothermal system at home plate in gusev crater, mars: Formation of high silica material by acid-sulfate alteration of basalt. 2008. URL `http://www.lpi.usra.edu/meetings/lpsc2008/pdf/2208.pdf`.

[48] M. S. Rice, Bell III J. F., E. A. Cloutis, A. Wang, S. W. Ruff, M. A. Craig, D. T. Bailey, J. R. Johnson, P. A. de Souza Jr., and W. H. Farrand. Silica-rich deposits and hydrated minerals at gusev crater, mars: Vis-nir spectral characterization and regional mapping. *Icarus*, 205, 2010. doi: 10.1016/j.icarus.2009.03.035.

[49] W. H. Farrand et al. Multispectral reflectance of rocks in the columbia hills examined by the mars exploration rover spirit: Cumberland ridge to home plate. 2007. URL `http://www.lpi.usra.edu/meetings/lpsc2007/pdf/1957.pdf`.

[50] A. Wang et al. Coexistence of si-rich and s-rich materials at gusev crater, columbia hills. 2008. URL `http://www.lpi.usra.edu/meetings/lpsc2008/pdf/2186.pdf`.

[51] A. Castano et al. Autonomous detection of dust devils and clouds on mars. *Machine Vision and Applications*, 19:467–482, 2008. URL `DOI:10.1007/s00138-007-0081-3`.

[52] M. D. Smith, M. J. Wolff, N. Spanovich, et al. Mars Exploration Rovers Mini-TES Atmospheric Results (Invited). In *AAS/Division for Planetary Sciences Meeting Abstracts #36*, volume 36 of *Bulletin of the American Astronomical Society*, page 1129, November 2004.

[53] A. Molina, M. A. de Pablo, and M. Ramos. Studying martian permafrost from surface temperature data of mini-tes, spirit mer mission. In *Ambientes periglaciares, permafrost y variabilidad climática*, pages 197–204. Blanco J.J. and de Pablo Hernández M.A. and Ramos Sainz M. (Eds.), 2010.

[54] R. E. Arvidson, S. W. Squyres, and S. L. Murchie. Mars exploration rover opportunity mission: recent results for meridiani planum. volume 42, 2011.

[55] C. Schröder et al. Meteorites on mars observed with the mars exploration rovers. December 2007.

[56] NASA (Ed.). Mars reconnaissance orbiter mission objectives, July 2005. URL http://www.nasa.gov/mission_pages/MRO/mission/science-objectives.html.

[57] NASA (Ed.). Mars reconnaissance orbiter instruments, 2005. URL http://mars.jpl.nasa.gov/mro/mission/science/objectives/.

[58] NASA (Ed.). Nasa mars orbiter speeds past data milestone, March 2010. URL http://www.jpl.nasa.gov/news/news.php?release=2010-073.

[59] NASA, JPL, and University of Arizona (Eds.). Mission 2020: A candidate landing site in gusev crater, April 2014. URL http://hirise.lpl.arizona.edu/ESP_035164_1655.

[60] E. Lakdawalla. Mars climate sounder confirms a martian weather prediction, October 2011. URL http://www.planetary.org/blogs/emily-lakdawalla/2011/3234.html.

[61] D. Kass. Mars climate sounder watches mars weather to prepare for curiosity landing, September 2010. URL http://www.planetary.org/blogs/guest-blogs/update_20100929.html.

[62] J. J. Plaut, A. Safaeinili, J. W. Holt, et al. Radar evidence for ice in lobate debris aprons in the mid-northern latitudes of mars. *Geophysical Research Letters*, 36, 2009. doi: 10.1029/2008gl036379.

[63] NASA (Ed.). Phoenix mars mission. Technical report, November 2005. URL http://phoenix.lpl.arizona.edu/pdf/fact_sheet.pdf.

[64] NASA (Ed.). Phoenix analyst's notebook, 2011. URL http://an.rsl.wustl.edu/phx/solbrowser/browserFr.aspx?tab=misssumm.

[65] NASA and LPL (Eds.). Phoenix scientific measurements, 2005. URL http://phoenix.lpl.arizona.edu/science04.php.

[66] P. H. Smith et al. H2o at the phoenix landing site. *Science*, 325(5936):58–61, July 2009. doi: 10.1126/science.1172339.

[67] J. A. Witeway et al. Mars water-ice clouds and precipitation. *Science*, 325(5936), July 2009. doi: 10.1126/science.1172344.

[68] NASA and LPL (Eds.). Nasa phoenix results point to martian climate cycles, July 2009. URL http://phoenix.lpl.arizona.edu/07_02_09_pr.php.

[69] L. Komguem et al. Phoenix lidar measurements of mars atmospheric dust. *Icarus*, 223:649–653, February 2013.

[70] R. E. Arvidson, R. G. Bonitz, M. L. Robinson, J. L. Carsten, and R. A. Volpe. Results from the mars phoenix lander robotic arm experiment. *Journal of Geophysical Research: Planets*, 114, 2009. doi: 10.1029/2009je003408.

[71] S. C. Cull et al. Concentrated perchlorate at the mars phoenix landing site: Evidence for thin film liquid water on mars. *Geophysical Research Letters*, 37 (L22203), 2010.

[72] L. K. Tamppari, D. Bass, B. Cantor, et al. Phoenix and mro coordinated atmospheric measurements. *Journal of Geophysical Research: Planets*, 115, 2010. doi: 10.1029/2009je003415.

[73] NASA and JPL (Eds.). Mars science laboratory landing site selection, 2012. URL http://mars.jpl.nasa.gov/msl/mission/timeline/prelaunch/landingsiteselection/.

[74] NASA and JPL (Eds.). Mars science laboratory mission objectives, 2012. URL http://mars.jpl.nasa.gov/msl/mission/science/objectives/.

[75] G. Webster et al. Mars science laboratory landing press kit, July 2012.

[76] R. Navarro-González. Initial results from the mars science laboratory: 100 sols. April 2013.

[77] M. Genzer et al. Mars water-ice clouds and precipitation. *Geophysical Research Abstracts*, 15(3870), 2013.

[78] J. Pla-Garcia et al. Preliminary interpretation of the meteorological environment through mars science laboratory rover environmental monitoring station observations and mesoscale modeling, November 2013.

[79] F. J. Martín-Torres, M.-P. Zorzano, C. Armiens, et al. Highlights from the rover environmental monitoring station (rems) on board the mars science laboratory: New windows for atmospheric research on mars. In F. Forget and M. Millour, editors, *Mars Atmosphere: Modelling and Observation, 5th International Workshop*, page 1103, January 2014.

[80] V. E. Hamilton, A. R. Vasavada, R. M. Haberle, et al. Preliminary results from the mars science laboratory rems ground temperature sensor at rocknest. In *Lunar and Planetary Science Conference*, volume 44 of *Lunar and Planetary Science Conference*, page 1364, March 2013.

[81] J. H. Jones, P. B. Niles, C. R. Webster, et al. Preliminary interpretations of atmospheric stable isotopes and argon from mars science laboratory (sam). In *Lunar and Planetary Science Conference*, volume 44 of *Lunar and Planetary Science Conference*, page 2781, March 2013.

[82] D. L. Bish, D. F. Blake, D. T. Vaniman, et al. X-ray diffraction results from mars science laboratory: Mineralogy of rocknest at gale crater. *Science*, 341(6153), September 2013. doi: $10.1126/\mathrm{science}.1238932$.

[83] J. Grotzinger, D. Blake, J. Crisp, et al. Mars science laboratory: Results from bradbury landing to glenelg. In *EGU General Assembly Conference Abstracts*, volume 15 of *EGU General Assembly Conference Abstracts*, page 11735, April 2013.

[84] D. M. Hassler. Measuring the radiation environment on mars, 2013.

[85] J. V. Hamilton et al. Simultaneous msl rems and mars odyssey themis ground temperature measurements in gale crater, mars. *Geophysical Research Abstracts*, 16(3134), 2014.

[86] C. Leovy and Y. Mintz. Numerical simulation of the atmospheric circulation and climate of mars. *Journal of Atmospheric Sciences*, 26:1167–1190, 1969. doi: $10.1175/1520\text{-}0469(1969)026{<}1167{:}\mathrm{NSOTAC}{>}2.0.\mathrm{CO};2$.

[87] R. M. Haberle, C. P. McKay, J. B. Pollack, et al. *Atmospheric Effects on the Utility of Solar Power on Mars*, page 845. 1993.

[88] J. B. Pollack, R. M. Haberle, J. Schaeffer, et al. Simulations of the general circulation of the martian atmosphere. i - polar processes. *Journal of Geophysical Research*, 95(B2):1447–1473, February 1990. doi: $10.1029/\mathrm{JB095iB02p01447}$.

[89] R. D. Dycus. The meteorite flux at the surface of mars. *Publications of the Astronomical Society of the Pacific*, 81:399, August 1969. doi: $10.1086/128793$.

[90] N. Divine. Five populations of interplanetary meteoroids. *Journal of Geophysical Research*, 98:17029–17048, September 1993. doi: $10.1029/93\mathrm{JE}01203$.

[91] M. Alexander. Mars transportation environment definition document. TM-2001 (210935), March 2001.

[92] P. A. Bland and T. B. Smith. Meteorite accumulations on mars. *Icarus*, 144: 21–26, March 2000. doi: $10.1006/\mathrm{icar}.1999.6253$.

[93] H. McNamara, B. Jones, R. Suggs, et al. Meteoroid engineering model (mem): A meteoroid model for the inner solar system. *Earth Moon and Planets*, 95:123–139, December 2004. doi: $10.1007/\mathrm{s}11038\text{-}005\text{-}9044\text{-}8$.

[94] C. G. Justus and D. L. Johnson. Mars global reference atmospheric model 2001 version (mars-gram 2001): Users guide. (210961), April 2001.

[95] R. M. Haberle, J. L. Hollingsworth, A. Colaprete, et al. The nasa/ames mars general circulation model: Model improvements and comparison with observations. Technical report, January 2003.

[96] S.W. Bougher, S. Engel, and P. Withers. The ncar mars thermospheric general circulation model: a review. Technical report, January 2003.

[97] J. H. Joseph, W. J. Wiscombe, and J. A. Weinman. The delta-eddington approximation for radiative flux transfer. *Journal of Atmospheric Sciences*, 33:2452–2459, December 1976. doi: $10.1175/1520\text{-}0469(1976)033{<}2452{:}\mathrm{TDEAFR}{>}2.0.\mathrm{CO};2$.

[98] H. Savijarvi. Radiative fluxes on a dustfree mars. *Contributions to Atmospheric Physics/Beitraege zur Physik Atmosphaere*, 64:103–112, May 1991.

[99] K. A. Kozarev, N. A. Schwadron, et al. The earth-moon-mars radiation environment module (emmrem): Framework and current developments. In I. Zhelyazkov,

editor, *American Institute of Physics Conference Series*, volume 1121 of *American Institute of Physics Conference Series*, pages 164–168, April 2009. doi: 10.1063/1.3137938.

[100] N. Schwadron et al. Earth-moon-mars radiation environment module (emmrem). Technical Report 1001, June 2006.

[101] J. W. Wilson, F. F. Badavi, F. A. Cucinotta, et al. Hzetrn: Description of a free-space ion and nucleon transport and shielding computer program. *NASA STI/Recon Technical Report N*, 95:28530, May 1995.

[102] T. M. Miller and L. W. Townsend. Heavy ion collision event generator for the 3d monte carlo transport code hetc. June 2006.

[103] LMD, OU, IAA, ESA, and CNES (Eds.). The mars climate database projects, 1997. URL `http://www-mars.lmd.jussieu.fr/`.

[104] R. T. Clancy, B. J. Sandor, M. J. Wolff, et al. An intercomparison of ground-based millimeter, mgs tes, and viking atmospheric temperature measurements: Seasonal and interannual variability of temperatures and dust loading in the global mars atmosphere. *Journal of Geophysical Research: Planets*, 105, 2000. doi: 10.1029/1999je001089.

[105] D. Rapp. *Solar Energy on Mars*, volume 1, pages 16–17. December 2004.

[106] M. Allison. Accurate analytic representations of solar time and seasons on mars with applications to the pathfinder/surveyor missions. *Geophysical Research Letters*, 24:1967, August 1997. doi: 10.1029/97GL01950.

[107] J. Feynman, A. Ruzmaikin, and V. Berdichevsky. The jpl proton fluence model: an update. *Journal of Atmospheric and Solar-Terrestrial Physics*, 64:1679–1686, November 2002. doi: 10.1016/S1364-6826(02)00118-9.

[108] P. B. Saganti, F. A. Cucinotta, J. W. Wilson, et al. Radiation climate map for analyzing risks to astronauts on the mars surface from galactic cosmic rays. *Space Science Reviews*, 110:143–156, January 2004. doi: 10.1023/B:SPAC.0000021010.20082.1a.